Mohd Jamil Mohamed Mokhtarudin

Wolfson College

Supervised by

Assoc. Prof. Stephen J. Payne

Mathematical Modelling of Cerebral Ischaemia-Reperfusion Injury

A thesis submitted for the degree of Doctor of Philosophy

Michaelmas Term, 2016

Abstract

Restoring cerebral blood flow using reperfusion treatment is a common method in treating ischaemic stroke. Reperfusion treatment should be given within 4.5 hours from stroke onset. However, reperfusion beyond this time window poses the risk of reperfusion injuries such as intracranial haemorrhage and cerebral tissue swelling. The focus of this thesis is to study the effect of cerebral tissue swelling after reperfusion as it can occur in a few hours after the treatment. Cerebral tissue swelling may cause brain structure movement and cerebral microvessel compression; the latter may then lead to secondary ischaemia occurrence.

In this thesis, two mathematical models are presented. The first model investigates the effect of ischaemia-reperfusion in the formation of cerebral tissue swelling. This model provides the understanding of suitable reperfusion conditions to reduce the effect of tissue swelling and also becomes the basis for the subsequent model. Meanwhile, the second model studies the role of a water-transporting protein, aquaporin-4 in ischaemia-reperfusion and its potential as part of treatments for cerebral tissue swelling. In addition, the ionic concentration may change during ischaemia which may be a factor contributing to cerebral tissue swelling. Thus, the effect of ionic concentration on the swelling formation is also investigated.

Finally, validations of these models are achieved by developing patient-specific geometries from available ischaemic stroke patient MRI data and utilising finite element analysis. Comparison between the simulation results and the MRI data is done by quantifying the brain ventricles movement during cerebral tissue swelling.

Acknowledgement

In the name of God, the Most Beneficent, the Most Merciful. Praise and thanks be to God, Lord of all the worlds.

Writing this page; although was the hardest of all pages in this thesis, was also satisfying, knowing that I am finally nearing the end of the journey of DPhil research. I should give credit to a number of people, who have made this journey possible.

I would first of all like to thank my supervisor, Stephen Payne, who encouraged me to apply for DPhil studentship 3 years ago, and then guided me through the whole process. His teaching, support, and helping; especially in improving my writings, have been gratefully received.

My parents, family, and my beloved wife, Habibah, who have provided exceptional support, unconditional love, and patience throughout this embarkation, deserve the most credit. I am also greatly indebted my best friend, Abbas, who have been all ears to my problems and was always giving the best advice.

I would also like to thank the members of Physiological Understanding through Modelling (PUMMA) group. George, Wahbi, and Flora (plus me make the "Final Four") as excellent colleagues and thank you for being the best company to start and end this journey together. Other past and present members include Chang, for helping me with the MRI data and possible future collaboration; Ean, for your advice on using ELMER; Chris, Simao, Adam and to all the others.

I must also thank, not to mention, to others who have made my life in Oxford a pleasure. Spending most of my Wednesdays with the Oxford Gamelan Society members; rehearsing, performing in many concerts, and of course socialising, would not have been possible without the permission from Peter Smith and Jonathan Robert to join the group. Thanks must go to those in Wolfson College, IBME, Oxford, Malaysia, and fellow friends around the world, who directly or indirectly helped me through the past 3 years.

My final thanks and prayer go to the One, that He may accept this thesis and may forgive me its possible errors, which all are due to none but myself, and that He may allow it to be beneficial to anyone seeking advantage from this thesis.

Dissemination

Peer-Reviewed Journal Papers (2 published)

- Mokhtarudin, M.J.M. and Payne, S.J. The study of the function of AQP4 in cerebral ischemia-reperfusion injury using poroelastic theory. International Journal for Numerical Methods in Biomedical Engineering, accepted 6th March 2016.

- Mokhtarudin, M.J.M. and Payne, S.J. Mathematical model of the effect of ischemia-reperfusion on brain capillary collapse and tissue swelling. Mathematical Biosciences, 263: 111-120, 2015.

Conference Presentations and Posters (2)

- M. J. M. Mokhtarudin, S. J. Payne (2016, September), Investigating the Importance of Ionic Concentration on Ischaemic Cerebral Tissue Swelling using Donnan Equilibrium. (Eds.). Paper presented at MEIbioeng 16, University of Oxford (Oxford), United Kingdom.

- M. J. M. Mokhtarudin, S. J. Payne (2015, July). The study of the function of AQP4 in cerebral ischaemia-reperfusion injury using poroelastic theory. P. Nithiarasu, E. Budyn (Eds.). Paper presented at 4th International Conference on Computational & Mathematical Biomedical Engineering, Ecole Normale Superieure de Cachan (Paris), France.

Workshops and Summer Schools

- EMS-ESMTB Summer School Mathematical Biology of Tissue Mechanics, Leiden, Netherlands (25th-29th July, 2016).

- 7th Summer School on Biomechanics of Soft Tissues: Multiscale Modeling, Simulation and Applications, Graz University of Technology, Austria (4th-8th July, 2016).

Table of Contents

List of Abbreviations

.stl	StereoLithography
ADC	Apparent diffusion coefficient
AQP	Aquaporin
AQP4	Aquaporin-4
BBB	Blood-brain barrier
CBF	Cerebral blood flow
CNS	Central nervous system
CPM	Cellular Potts Model
CPP	Cerebral perfusion pressure
CT	Computed tomography
CSF	Cerebrospinal fluid
CVR	Cerebrovascular resistance
DALYs	Disability-adjusted life years
DLU	Displacement-length units
DMMB	1,9 dimethylmethylene blue
DS	Decompressive surgery
DWI	Diffusion-weighted MRI
ECASS	European Cooperative Acute Stroke Study
ECS	Extracellular space
FCD	Fixed charge density
FDA	Food and Drug Administration
FEA	Finite element analysis
FLAIR	Fluid-attenuated inversion recovery
FUT	Follow-up time
GAG	Glycosaminoglycan
Gd-DTPA	Gadopentetate dimeglumine
IA	Intraarterial
ICP	Intracranial pressure
ICS	Intracranial space
ISF	Interstitial fluid
IV	Intravenous
LPS	Lipopolysaccharide
LU	Length units
MAP	Mean arterial pressure
MCAO	Middle cerebral artery occlusion
MERCI	Mechanical Embolus Removal in Cerebral Ischemia

MMP	Matrix metalloproteinase
MRI	Magnetic resonance imaging
mRNA	Messenger ribonucleic acid
mRS	Modified Rankin Scale
NIHSS	National Institutes of Health Stroke Scale
NVU	Neurovascular unit
ODE	Ordinary differential equation
PDE	Partial differential equation
PKC	Protein kinase C
pHWI	pH-weighted MRI
PT	Presentation time
PU	Pressure units
PWI	Perfusion-weighted MRI
rtPA	Recombinant tissue plasminogen activator
TU	Time units

List of Figures

List of Tables

Chapter 1

Introduction

1.1 Brain Stroke and Treatments

Stroke has been ranked as the second major cause of death worldwide in 2010 by the Global Burden of Diseases, Injuries, and Risk Factors Study (Lozano et al., 2012) contributing to about 10% of the overall deaths in that year. In a study that measures the years of life lost due to premature mortality and years lived with disability due to various types of diseases and injuries, also collectively known as disability-adjusted life years (DALYs) (Murray et al., 2012), it was found that stroke placed third after ischaemic heart disease and lower respiratory infections. This study shows that stroke does not only cause death, but it may also cause lifelong damage to the victim. Stroke incidence and mortality rates over the year 1990 to 2010 vary depending on the country. It was found that the incidence decreases within high-income countries, while the contrary has been shown within low-income and middle-income countries (Feigin et al., 2014). This is likely to be due to good healthcare services and various stroke prevention programmes enforced within the high-income countries (Mendis et al., 2015). Despite these facts, the study done by World Health Organization (2014) found that stroke still ranked second as a leading cause of death in 2012 and that this is unlikely to change until the year 2030.

Strokes can be classified into two main types; ischaemic stroke and haemorrhagic stroke, where each constitutes about 67.3-80.5% and 6.5-19.6% of the overall occurrence, the remainder being unclassified (Feigin et al., 2003). Ischaemic stroke happens due to the obstruction of a cerebral blood vessel by the deposition of fat or a blood clot. On the other hand, haemorrhagic stroke occurs when a cerebral blood vessel weakens and

ruptures, eventually causing leakage of blood into the tissue surrounding the rupture. From here onwards, the study will focus on ischaemic stroke as it is more common than haemorrhagic stroke, despite studies showing that haemorrhagic stroke presents a higher mortality rate than ischaemic stroke (Andersen et al., 2009).

About 70% of patients diagnosed with ischaemic stroke have a thrombus blocking a major brain vessel, while the remainder either have a blockage in small arteries (microvessels), a blockage of blood vessels due to a blood clot (embolism) or a constriction of blood vessels (stenosis) (Furlan et al., 2003). The main clinical goal in treating ischaemic stroke is to restore the cerebral blood flow (CBF) to the affected cerebral tissue region within a short timescale and this process is called reperfusion therapy. Current reperfusion methods aim to remove the blood clot, either by insertion of a mechanical device into the vessels (Smith et al., 2005) or by using recombinant tissue plasminogen activator (rtPA) (Haley Jr et al., 1993).

Mechanical revascularisation devices including embolectomy and thrombectomy are highly efficient in treating a thrombus in large cerebral vessels. The use of rtPA to dissolve a thrombus in these vessels is relatively impractical due to the large size of any blood clot that obstructs these vessels (Jansen et al., 1995). Mechanical Embolus Removal in Cerebral Ischemia (MERCI) is one example of a revascularisation device. A balloon catheter is inserted into the affected vessel and the balloon is inflated to prevent blood flow from interrupting the removal process. Then, the retriever is moved through the catheter, wrapped around the clot and removed together with the catheter (Smith et al., 2008). Figure 1.1 shows an example of catheterisation process. About 50% of patients with an occlusion in large vessels were successfully revascularised through the usage of MERCI within 8 hours after stroke onset (Smith et al., 2005). However, the shear forces

exerted on the vessels lumen by the catheter during the removal process may pose a risk of vessel injury and eventually cause haemorrhage (Akins et al., 2014).

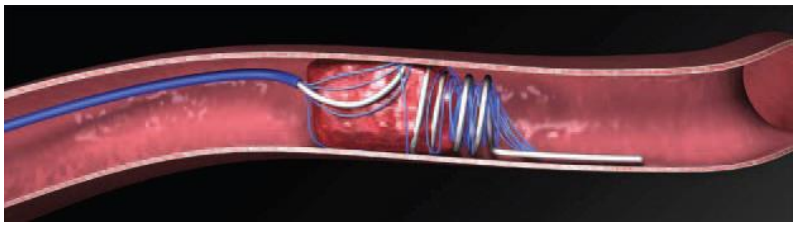

Figure 1.1: Example of MERCI devices in which the retriever wraps around the clot before being removed from the vessel. Taken from (Smith et al., 2008).

Treatment of ischemic stroke using rtPA, on the other hand, is usually done within a 3-hour time window of stroke onset (Hacke et al., 2004) and its efficacy within this time window has been approved by The Food and Drug Administration (FDA) in June 2006 based on the results of randomised clinical trials done by The National Institute of Neurological Disorders and Stroke rt-PA Stroke Study Group (1995). However, many recent studies here shown the potential of the treatment to go beyond this time window (Lansberg et al., 2009; Sandercock et al., 2012). The time window of rtPA has been shown to be greater in a study involving patients undergoing magnetic resonance imaging (MRI) and computed tomography (CT) imaging prior to the treatment (Schellinger et al., 2007). The time limitation imposed on the treatment of rtPA on stroke patients is due to the potential risk of haemorrhagic complications. As a consequence of this, only a small number of stroke patients are treated with rtPA (Barber et al., 2001).

Determining the eligibility of a stroke patient for reperfusion treatment depends on the knowledge of the time of stroke onset. The time from symptoms onset to hospital arrival of is usually not recorded or not known for a majority of stroke patients (George et al., 2009). In addition, strokes also can occur at night between 12 a.m. to 6 a.m., which is during sleep (Marshall, 1977), putting the patients outside of the time window and consequently not eligible for reperfusion treatments. About 16 to 27% of stroke patients

wake up from sleep with stroke symptoms (Fink et al., 2002; Jiménez-Conde et al., 2007; Serena et al., 2003). Therefore, it is still a big challenge for clinicians to decide the suitability of treatments for stroke patients with unknown onset time so as to reduce the risk of post treatment injuries.

1.2 Medical Imaging for Cerebral Ischaemia Investigation

Medical imaging is a technique used to visualise the interior of the human body. CT and MRI are two of the most common medical imaging procedures for evaluating stroke patients. The decision on which options to use depends on the availability of the imaging modality, risk to the patient, cost and expertise. The goal of these procedures is to obtain a detailed image of the brain of the patient, which displays the location of the infarct, type of stroke and other useful information before a treatment procedure can be performed.

CT is widely used in stroke patients to verify the presence of intracranial haemorrhage infarction (Lodder, 1984). It is also used to show the initial signs of cerebral stroke in patients and the efficacy of providing thrombolytic treatment to them (Barber et al., 2000; von Kummer, Rudiger et al., 1997) due to it being a fast procedure and readily available in many hospitals (Barber et al., 2005). The development of perfusion CT for the assessment of CBF (Koenig et al., 1998; Mayer et al., 2000), which can be used in predicting the development of ischaemic infarction, makes it a feasible imaging tool in stroke cases.

During the early development of MRI, its efficacy was not as promising as compared to CT (Mohr et al., 1995), although it was proven to provide better sensitivity in experimental stroke models in animals followed by 4 hours of reperfusion (Brant-Zawadzki et al., 1986; Mintorovitch et al., 1991). Despite this, the development of MRI

that is sensitive to the diffusion of water in the cerebral tissue, also known as diffusion-weighted MRI (DWI), could potentially determine the cerebral tissue with energy failure and ion concentration homeostasis, which indicates the region of ischaemic tissue (Busza et al., 1992). In a study of the efficacy of DWI within 6 hours from the onset of stroke, it was shown that it provides better sensitivity in identifying infarcts compared to conventional CT and MRI (Barber et al., 1999; Gonzalez et al., 1999). DWI also gives more accurate and more sensitive detection than a CT scan in a middle cerebral artery occlusion (MCAO) lesion (Lansberg et al., 2000). However, CT and DWI show small differences in the ability in visualising early ischaemic infarct when using quantitative scoring system ASPECTS (Barber et al., 2005), thus proving that CT is more reliable than MRI as the former is a faster method and also more accessible.

On the other hand, perfusion-weighted MRI (PWI) is another MRI technology that can visualise tissue perfusion, which is very important in determining the region of cerebral tissue that is still viable (Detre et al., 1992). Combining DWI and PWI allows the identification of the region within the cerebral infarct that is still recoverable and determination of the benefit of the thrombolytic treatment to patients (Keir et al., 2000). The lesion detected by DWI measures the irreversible damage of the tissue; meanwhile the lesion detected by PWI measures the tissue region that has reduced CBF. The PWI lesion is usually larger than the DWI lesion during the early stroke onset (Baird et al., 1997) and the mismatch between these lesions, which is known as the penumbra (Astrup et al., 1981), can help to identify the tissue region that still is viable to be saved by thrombolytic treatment (Prichard et al., 1999).

The PWI-DWI mismatch provides only an approximation of the region of the salvageable tissue. The development of pH-weighted MRI (pHWI) that can detect the tissue with reduced pH value allows for the identification of abnormal tissue region (Sun

et al., 2007). Tissue will become acidic or decrease in pH when its metabolism is disrupted by a lack of energy and oxygen, and carbon dioxide accumulation, which usually occurs when the blood flow is impaired. Hence, by using this fact, pHWI can be used in conjunction with DWI and PWI (Sun et al., 2010). Figure 1.2 shows the region of mismatch between the three different MRI techniques. The pink-yellow mismatch represents the area of tissue region with reduced CBF, meanwhile the black-yellow mismatch represents the minimum area of the penumbra (Sun et al., 2007). Combination of the three MRI techniques may improve the measurement of potential salvageable cerebral tissue before a thrombolytic treatment is employed.

Figure 1.2: Example of ischemic cerebral tissue region that shows the areas with ADC, CBF and pHWI deficit detected using DWI, PWI and pHWI MRI, respectively. Taken from (Sun et al., 2007).

1.3 Brain Swelling After Ischaemia-Reperfusion

Although reperfusion is used to recover the CBF to the affected tissue region and to reduce the infarct area, some stroke patients may suffer several possible injuries termed reperfusion injury (Molina et al., 2005). Examples of such injuries are intracranial haemorrhage as demonstrated by delayed thrombolysis (The NINDS t-PA Stroke Study Group, 1997) and catheterisation (Akins et al., 2014), cerebral tissue damage as a result of several pathophysiological processes during ischaemia (Dirnagl et al., 1999), and brain tissue swelling due to oedema or accumulation of fluid in the tissue (Ayata et al., 2002). The causes of these injuries are multifactorial and are interdependent, involving blood-brain barrier injury (Yang et al., 1994) that can cause oedema, an increase in matrix

metalloproteinase (MMP) activities that degrade extracellular matrix integrity (Wang et al., 2004), and the formation of oxygen free radicals that can damage the tissues (Floyd, 1990; Traystman et al., 1991) to name a few. The developments of haemorrhagic and brain oedema after ischaemia-reperfusion are major risks that need special supervision by clinicians for stroke patients. The focus of this thesis is to study the effect of brain tissue swelling due to oedema as a result of ischaemia-reperfusion injury.

Brain tissue swelling or the accumulation of oedematous fluid usually occurs within a few hours after stroke reperfusion and has been shown to continue to worsen up to the first 5 days after the stroke onset (Shaw et al., 1959) with about 80% mortality rate (Hacke et al., 1996). Several early experimental studies have demonstrated that oedema formation depends on the duration of ischaemia (Heiss et al., 1997; Ito et al., 1979; Traupe et al., 1982). However, the formation of brain oedema solely relies on the fluid within the blood vessels, in which if there is no reperfusion after ischaemia, then oedema will not occur; a concept known as “no flow-no oedema” (Hossmann, 1976). Oedema formation due to cerebral ischaemia is initially due to the intracellular fluid accumulation (cytotoxic oedema) and later followed by the accumulation of fluid within the extracellular space (ECS) (vasogenic oedema) (Kimelberg, 2004). The accumulation of fluid in the ECS will cause the tissue to expand and to swell and also result in an increase in intracranial pressure (ICP) (Donkin et al., 2010).

The formation of brain oedema also results in a phenomenon known as the space-occupying effect and the first report of such a case can be found in (Menzies, 1893). This phenomenon causes the shift of the structure in the midline of the brain that divides the two cerebral hemispheres such as the ventricles of the brain. This can readily be seen through the use of sonography (Gerriets et al., 1999; Stolz et al., 1999), which is suitable for patients who are unable to undergo CT scanning (Gerriets et al., 2001). This

phenomenon results in the formation of brain herniation (Frank, 1995), which usually occurs in about 78% of patients with MCAO (Hacke et al., 1996). In the European Cooperative Acute Stroke Study (ECASS), brain herniation was the most common cause of death 7 days from ischaemia-reperfusion treatments (Hacke et al., 1995).

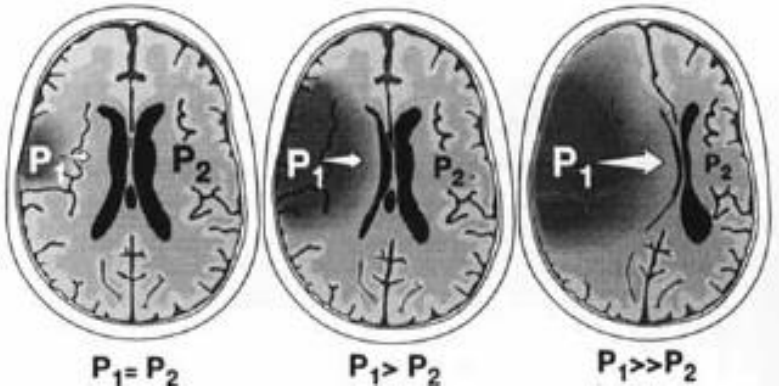

Figure 1.3: Example of the formation of brain herniation due to space-occupying effect of oedema. Pressure in the left side of the brain, P_1 is bigger than the right side, P_2, thus causing a midline shift to the right side of the brain. Taken from (Frank, 1995).

Figure 1.3 shows a schematic of the formation of brain herniation. The elevation of ICP in the region of swollen cerebral tissue causes brain herniation and may also result in cerebral vascular compression (Frank, 1995). A minimum ICP value of 30 mmHg was found to cause the occurrence of brain herniation, which usually developed within 2 to 5 days after brain oedema (Steiner et al., 2001). The compression effect of the swollen brain on cerebral vessels may reduce CBF and this has been shown in an experimental study on dogs (Miller et al., 1973). The compression of cerebral vessels after ischemia-reperfusion can result in a phenomenon called no-reflow (Ames et al., 1968), in which certain vessels remain blocked even after reperfusion and this has been proved in an early study (Chiang et al., 1968) using light and electron microscopes on rabbits. The occurrence of this phenomenon may lead to secondary ischaemia (Lindenberg, 1955).

Several treatments for brain oedema are available which include osmotherapeutic and surgical treatments. Decompressive surgery (DS) is a surgical procedure that removes

a certain part of the skull to create space that allows the swollen brain tissue to expand (Cushing, 1905), thus being effective in relieving ICP, preventing herniation and improving cerebral perfusion pressure (CPP), especially after MCAO (Amorim et al., 2014; Naugebauer et al., 2014; Soinne et al., 2014). Several recent randomized controlled trials have suggested that DS can reduce the mortality and improve patient functional outcome if done within 48 hours of stroke onset (Hofmeijer et al., 2009; Vahedi et al., 2007); however, the decision to perform this operation depends on the individual assumptions of every patient. Despite its effectiveness, DS poses several complications, usually post-surgery, such as risk of mortality (Honeybul, 2008), herniation through the surgical site (Yang et al., 2008), subdural effusion (Aarabi et al., 2006; Yang et al., 2008), syndrome of the trephined (illustrated in Figure 1.4) (Fodstad et al., 1984; Joseph et al., 2009; Yamaura et al., 1977), hydrocephalus, and epilepsy (Kan et al., 2006).

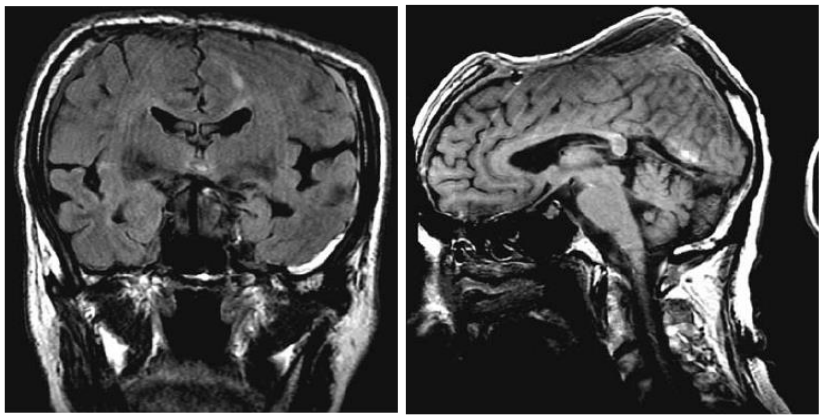

Figure 1.4: Syndrome of the trephined, which occurs at the site of DS as a result of external compressive forces on the brain. Taken from (Akins et al., 2008).

Osmotherapy, on the other hand, is another alternative in treating brain oedema. It is the use of osmotically active substances such as mannitol, glycerol and sorbitol (Nau, 2000) to reduce the tissue water content by creating an osmotic gradient between the tissue compartments and the vasculature (Zornow, 1996), which will reduce the volume of the swollen brain tissue and subsequently reduce the elevated ICP. The rate of ICP

reduction relies upon the volume of the brain, the severity of blood-brain barrier damage, the initial value of ICP and also the amount of prescription used (Steiner et al., 2001). Mannitol is the most widely used osmotherapeutic agent in controlling rising ICP following brain stroke (Adams et al., 1994; Hacke et al., 2000), despite its advantages in cerebral oedema having yet to be proven clinically (Candelise et al., 1975; Santambrogio et al., 1978) with not enough randomized trials to support its usage (Bereczki et al., 2000). Figure 1.5 summarise the available treatments for stroke and brain oedema.

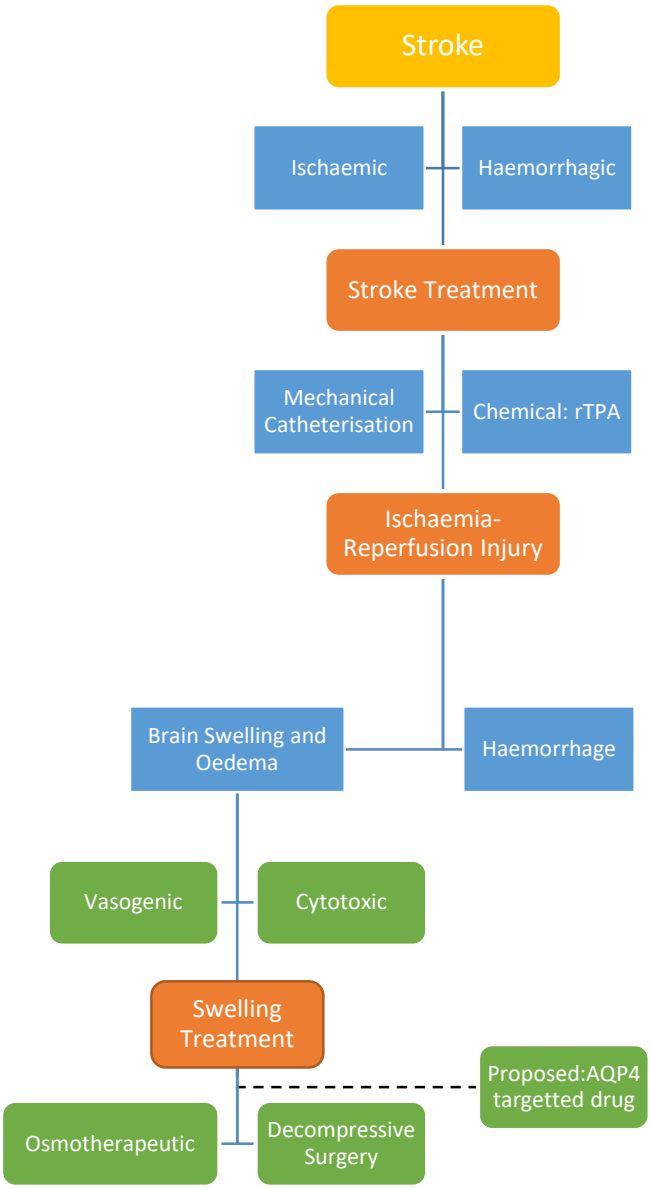

Figure 1.5: Types of stroke, the outcomes, and the treatments available.

Aside from the available treatments for brain oedema, several animal studies have been done on aquaporin-4 (AQP4) that is found in the central nervous system as a target for future drug development in reducing cerebral oedema (Papadopoulos et al., 2008). AQP4 is a water channel protein that plays a part in brain oedema formation and elimination (Marmarou, 2007). It was found, through numerous experiments, that inhibition of AQP4 function has the potential to minimise cytotoxic oedema (Papadopoulos et al., 2007) and also may alleviate the formation of vasogenic oedema if the cerebral ischaemia is prolonged (Amiry-Moghaddam et al., 2003).

1.4 Motivation and Thesis Objective

Despite the availability of various treatments for cerebral ischaemic stroke, there are still problems regarding the effectiveness of applying these treatments to patients. Some reasons are the lack of understanding of the mechanism of the formation of ischaemic stroke, how the infarct develops and how the recovery process happens. In order to learn about the mechanism, large numbers of experiments involving both animals and humans will be required, which are expensive and time-consuming (Araujo et al., 2004). Hence, mathematical models are often developed to test hypotheses regarding a particular aspect of a biological process in ischaemic stroke and be very useful in providing (1) understanding of that particular biological problem; (2) mathematical representation of experimental results; (3) suggestions for appropriate experiments to clarify the biological mechanism; and (4) realistic predictions of similar problems without having to carry out clinical experiments (Swanson et al., 2003).

The primary objective of this thesis is to develop a mathematical model to further understand the progression of cerebral tissue swelling due to vasogenic oedema formation after ischaemia-reperfusion. However, developing mathematical models to understand

this is not easy because there are many possible mechanisms involved and these are usually interrelated. Some of the earliest mathematical models such as those of (Nagashima et al., 1990; Rapoport, 1978) have been used to understand the formation of vasogenic oedema. The model developed in this thesis includes additional mechanisms that were not included in previous works such as the mechanical properties of the cerebral tissue and microvessels, the effect of various molecule sizes on the filtration force, the effect of tissue swelling on the compression of microvessels leading to the no-reflow phenomenon, and the role of AQP4 and ionic concentration of cerebral tissue on tissue swelling.

1.5 Thesis Organisation

The thesis will be further divided into 7 more chapters. Chapter 2 reviews the literature related to the topic of the thesis. This includes reviews on the physiological background of brain tissue and the theoretical background of existing mathematical models. Meanwhile, the main focus of Chapter 3 is the development of a 1D mathematical model that describes the formation of vasogenic oedema as a result of blood reperfusion after ischaemia. This model provides the foundation model for the subsequent chapters in the thesis.

A mathematical model of the function of AQP4 after ischaemia-reperfusion is studied in Chapter 4. This is done by extending the model developed in Chapter 3 by adding an AQP4 model, which allows the water to move within the different compartments in the cerebral tissue. However, one of the major concerns of this model is the assumption of constant ionic concentration of the cerebral tissue. This issue is addressed in Chapter 5, in which the model is further extended by including the Donnan

equilibrium to describe the importance of the variability in the ionic concentrations of the cerebral tissue.

Chapter 6 describes the implementation of the models developed in the previous chapters for 2D and 3D finite element analysis (FEA). A simplified brain geometry is developed to simulate the brain swelling after ischaemic-reperfusion. This chapter provides a general idea on what to expect on the models before using actual patient images for FEA, which is done in Chapter 7. This chapter provides insights to the ability of the models developed for predicting the brain tissue swelling. Lastly, in Chapter 8, a summary for all findings and suggestions for future work are presented.

Chapter 2

Literature Review

Sections 2.3.2, 2.3.4, and 2.3.6 have appeared as part of **Mokhtarudin, M.J.M.** and Payne, S.J. "Mathematical model of the effect of ischemia-reperfusion on brain capillary collapse and tissue swelling" *Mathematical Biosciences*, 263: 111-120, 2015.

Meanwhile, section 2.2.5 has appeared as part of **Mokhtarudin, M.J.M.** and Payne, S.J. "The study of the function of AQP4 in cerebral ischemia-reperfusion injury using poroelastic theory" *International Journal for Numerical Methods in Biomedical Engineering*, doi: 10.1002/cnm.2784.

2.1 Introduction

In this chapter, the fundamental anatomy and physiology of brain parenchyma, the brain capillary endothelium and the blood-brain barrier (BBB) breakdown, the formation of brain oedema and its effect on intracranial pressure (ICP), and the aquaporin-4 (AQP4) water protein channel, will all be described. This will be followed by the description of basic mathematical fundamentals regarding tissue mechanics, capillary filtration, osmotic pressure and Donnan equilibrium, and vessel tube law, which will be used later to formulate the mathematical model in this thesis.

2.2 Background Physiology

In this section, the underlying cerebral physiology is described. Firstly, the neurovascular unit (NVU) that makes up cerebral tissue, its function in forming the BBB that covers the cerebral microvessels, and the BBB breakdown mechanism are presented. Then, the importance of maintaining ICP and how BBB breakdown can lead to vasogenic

oedema are also described. Lastly, a description of the aquaporin channel family will be described with the primary focus on the function of AQP4 in the formation and elimination of brain oedema.

2.2.1 Neurovascular Unit and Blood-Brain Barrier

The NVU consists of glial cells (mainly the astrocytes), neurons, and microvessels. The astrocyte is a star-shaped cell and makes contact with microvessels, neurons and pia mater via astrocyte foot processes. Meanwhile, the neuron is a cell that is able to respond to an electrical stimulus and to transmit it through the nervous system. Lastly, microvessels are responsible for microcirculation in the body and distribution of blood, containing nutrients, throughout the tissues. Astrocytes are mainly involved in the structural support of neurons, maintenance of microvessel endothelial integrity, and also help in the regulation of ionic concentrations in the extracellular space (Tortora et al., 2009). Neurons may also be involved in the regulation of blood flow in the microvessels (Hawkins et al., 2005).

In the brain, the endothelial wall of the microvessels possesses a selective permeability towards molecules and ions that can pass through it and this forms a special barrier called the BBB, which separates the blood from the brain extracellular fluid. This barrier only allows certain molecules to pass through it such as water, oxygen, carbon dioxide, glucose and amino acids, while preventing the movement of toxic molecules and neurotransmitters that can damage the brain tissue. The BBB is also important in maintaining brain homeostasis and providing an optimal microenvironment (Abbott et al., 2010).

Figure 2.1 shows the structure of the BBB and the presence of the associated cells, which makes the brain capillary vessels different from the capillaries of other peripheral

organs. The endothelial cell of the brain capillary has different anatomical structure compared to other peripheral capillaries. The presence of a tight junction (also known as zonulae occludens) between the cerebral endothelial cells acts as a diffusion barrier which limits the movement of molecules and ions through the capillary (Kniesel et al., 2000). The BBB also lacks fenestrations between the endothelial cells, which suggests that the exchange of solutes through brain capillary is restricted (Fenstermacher et al., 1988). In addition to the anatomical and structural differences, the brain endothelium is also different from those found in other peripheral organs in terms of its activity. The study done by Sedlakova et al. (1999) on the BBB in the rabbit found that it has low pinocytotic activity, thus restricting the movement of molecules and ions across it. Meanwhile, an early study done by Oldendorf et al. (1977) found that the cerebral endothelial cells possess a high amount of mitochondria compared to other peripheral endothelial cells, providing energy to maintain ionic concentration between the blood plasma and brain extracellular fluid (Fenstermacher et al., 1988) and also to maintain the structure of the brain capillary endothelial cells (Oldendorf et al., 1977).

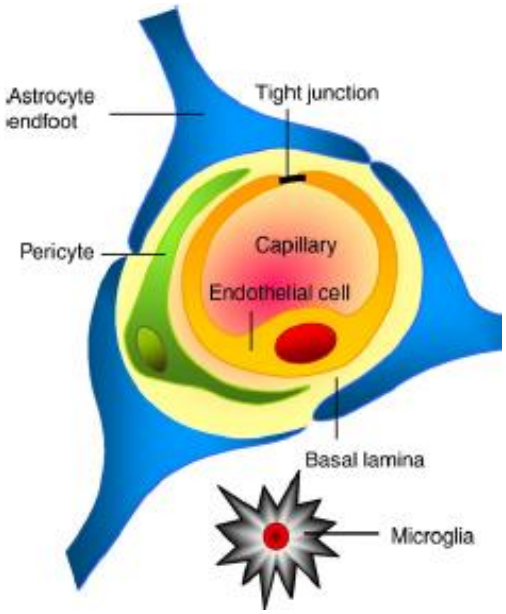

Figure 2.1: The structure of the BBB and associated cells. Taken from (Abbott et al., 2010).

Other structures that form the BBB are basal lamina, pericytes and the astrocyte endfeet. The basal lamina is a 30 – 40 nm thick membrane which serves as a macromolecule filter, microvessel support, and cell migration controller (Perlmutter et al., 1990). Meanwhile, pericytes are thought possibly to be responsible for sustaining the BBB permeability, regulating blood flow and helping in the formation of new vessels (Krueger et al., 2010). The astrocyte foot processes that surround the capillary help to maintain BBB properties (Janzer, 1993). Lastly, the microglia near the BBB are involved in the immune response of the brain (Abbott et al., 2010).

A study performed by Li et al. (2010) showed that the hydraulic permeability of cerebral capillary vessels is very small, being about 10^{-11} m/s.cmH_2O, compared with other capillary vessels, for which it is about 10^{-9} m/s.cmH_2O (Levick et al., 2010). However, many pathological conditions may increase the permeability of the BBB through a number of different mechanisms and these remain poorly understood (Greenwood, 1991).

2.2.2 Blood-Brain Barrier Breakdown

Disruption of the BBB may be caused by many brain pathologies such as stroke, infection, multiple sclerosis, Alzheimer's disease, Parkinson's disease, epilepsy, tumours, and other brain injuries (Abbott et al., 2006). In the case of ischemic stroke, there is a reduction in cerebral blood flow (CBF) that causes oxygen deprivation to the brain tissue. This creates a series of molecular processes that produces toxic proteases and free radicals, which are involved in damaging the NVU and opening the BBB (Yang et al., 2011). A detailed review of the cellular and molecular processes of BBB breakdown can be found in (Yang et al., 2011).

The duration of BBB opening following an ischemic stroke depends on the duration of the attack, the duration and amount of reperfusion, and the concentration of plasma glucose (Greenwood, 1991). Rapid reperfusion has advantages and disadvantages as it restores oxygen delivery to the brain but it also may cause sudden oxidative stress (Aoki et al., 2002). Reperfusion can also cause a biphasic opening of the BBB. The BBB starts to break down about two hours after an ischemic attack (Brouns et al., 2009) but this is still reversible with reperfusion, where the BBB disruption is repairable by the surrounding cells. However, about 24 to 72 hours after the attack, reperfusion can cause irreversible damage to the BBB (Yang et al., 2011).

A study done by Tomás-Camardiel et al. (2005) on the time-course of BBB breakdown on rats using lipopolysaccharide (LPS) to induce BBB disruption found that the BBB started to break down 6 hours after the induction of LPS, reaching maximum disruption after 24 hours. The BBB breakdown then started to be repaired by the tissue 48 hours after blood reperfusion and was completely restored 14 days after the LPS induction. In another study with regard to post-ischaemia leakiness of the BBB of rats done by Abo-Ramadan et al. (2009), it is found that the transfer rate constant, K_i, of gadopentetate dimeglumine (Gd-DTPA) through the BBB opening increases for about 12 hours after ischemia and then decreases, reaching approximately zero at week 5. Figure 2.2 shows the variation of K_i with time after ischaemia. The value of K_i were determined using Patlak plot equations (Patlak et al., 1985), which is a graphical method of measuring the unidirectional flux of a test substance with varying concentration through any membrane system (Patlak et al., 1983). In that study, it was also found that K_i increases linearly with the ischemic lesion size.

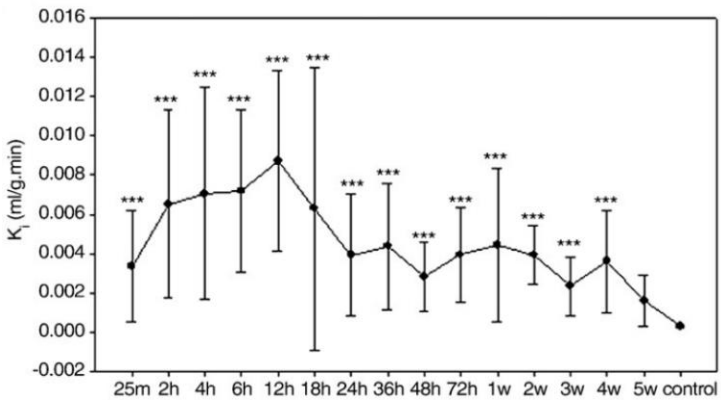

Figure 2.2: BBB transfer rate constant, K_i trend with time up to 5 weeks post-ischemia measured. *** indicate $p < 0.001$ in Kruskal-Wallis test between the respective time point and control test samples. Taken from (Abo-Ramadan et al., 2009).

2.2.3 Intracranial Pressure and Monitoring

ICP is the pressure inside the skull. The value of ICP depends on age (Czosnyka et al., 2005), CBF and autoregulation (Bouma et al., 1992), body posture, and many other factors. The ICP also depends on the head position, where it has been shown that the ICP is reduced when a person is in the sitting position with the head making a 30 degree elevation from the original supine position (Ng et al., 2004). Usually, the ICP for a healthy adult in a supine position is around 7 to 15 mmHg (Steiner et al., 2006). In a study of patients with brain oedema after cerebral infarction, continuous monitoring of the ICP level showed that those with ICP above 15 mmHg incurred brain death despite medical treatment to reduce the ICP (Ropper et al., 1984).

Within the space inside the skull or intracranial space (ICS) composed of three components which are the brain tissue, the blood, and the cerebrospinal fluid (CSF), the volume of these components is constant at all time. The increase in the volume of any one of these components must be compensated for by a decrease in the volume of another compartment so that the volume remains constant, or else the ICP will increase. The relationship between the volume of CSF, the volume of blood and the volume of the brain

tissue with ICP is governed by the Monro-Kellie doctrine (Mokri, 2001). This compensatory mechanism can be used to describe how ICP is maintained within the brain.

Elevation of ICP can lead to serious damage to the brain by reducing the CBF. ICP and CBF are related by the eqn. (2.1):

$$\mathrm{CPP} = \mathrm{MAP} - \mathrm{ICP} = \mathrm{CBF} \cdot \mathrm{CVR}, \tag{2.1}$$

where CPP is cerebral perfusion pressure and MAP is the mean arterial pressure or the average blood pressure of an individual. Here, CPP represents the pressure gradient that drives CBF into the brain. Meanwhile CVR is the cerebrovascular resistance and it is dependent on various physiological variables such as cerebral metabolic rate for oxygen and glucose and partial pressure of carbon dioxide in arterial blood (White et al., 2008). CVR also depends on the size of the arteriolar opening, where it has been shown that cerebral ischaemia may cause the constriction of the vessels, thus eventually increasing the CVR (Siemkowicz, 1980). From eqn. (2.1), an increment in ICP will cause a reduction in CBF into the arteries and may initiate microvessel collapse due to the resulting increase in brain tissue pressure (Steiner et al., 2006).

Maintaining BBB function is important to sustain normal ICP and cerebral homeostasis (Unterberg et al., 2004). An increase in BBB permeability may cause brain oedema, which in turn may affect brain tissue pressure and violate the Monro-Kellie doctrine. The normal BBB is often governed by small pores that only allow small molecules to pass through (Rippe et al., 1994), thus increasing its permeability which allows plasma proteins to pass through into the interstitial space, eventually causing brain oedema and leading to an increase of the ICP.

2.2.4 Vasogenic and Cytotoxic Oedema

One of the consequences of BBB breakdown is vasogenic oedema. As the BBB breaks down, its permeability increases, allowing protein plasma to filtrate through the capillary into the interstitial space (Kimelberg, 2004; Unterberg et al., 2004). This later creates an osmotic gradient which causes excess water movement from the capillary into the interstitial space, resulting in vasogenic oedema. Vasogenic oedema causes a water content expansion in the brain tissue space, brain tissue swelling and also an increase in the ICP (Donkin et al., 2010) as illustrated in Figure 2.3.

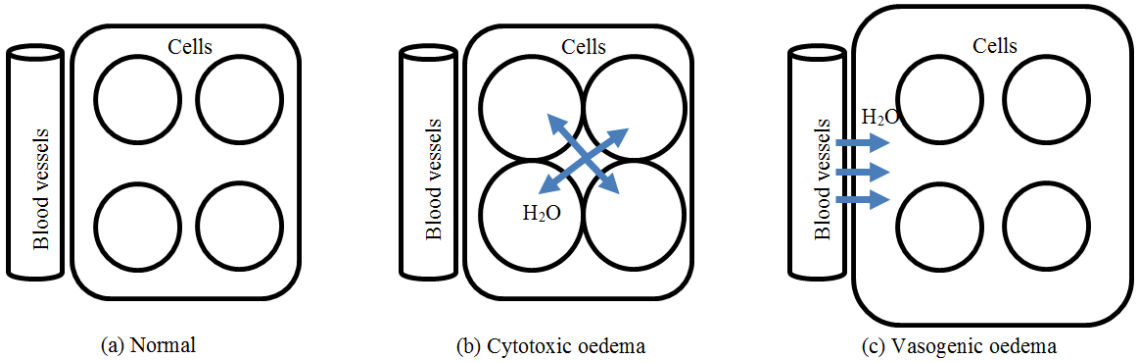

Figure 2.3: Formation of the major types of oedema: (a) normal condition; (b) cytotoxic oedema occurs when the water accumulates from extracellular space into the cells due to osmotic pressure imbalance; (c) vasogenic oedema occurs when the water from blood vessels enters the extracellular space due to BBB disruption.

Brain tissue oedema may cause compression of the microvascular bed, which can lead to focal ischemic stroke (del Zoppo et al., 2003). Vasogenic oedema clearance occurs in three possible mechanisms, which are: (1) bulk flow due to pressure gradients from extracellular space to CSF (Reulen et al., 1977; Reulen et al., 1978); (2) oedema fluid protein reuptake by the astrocyte and breakdown through lysosomal digestion (Fotheringham et al., 2000; Wolman et al., 1981); and (3) reverse vesicular transport of oedematous fluid protein through the endothelium, although this is found only in some cerebral microvasculatures (Vorbrodt et al., 1985). One current hypothesis for vasogenic oedema resolution is via the role of AQP4 water channels that are present in the BBB,

but the actual mechanisms remain unknown (Tourdias et al., 2011); this will be discussed in detail in the next section.

Meanwhile, another type of oedema, usually coexisting with vasogenic oedema, is known as cytotoxic oedema. This involves the accumulation of water in the astrocyte and neuron (Unterberg et al., 2004) but is mostly seen to occur in the astrocyte (Kimelberg, 2004). Being different from vasogenic oedema, cytotoxic oedema occurs not due to BBB disruption or an increase in the BBB permeability, but due to the imbalance of osmotically active solutes between the astrocyte and the extracellular space. Three mechanisms may be involved, which are: (1) increase in the permeability of the cells towards sodium (Na^+) and potassium (K^+) ions; (2) failure of ion-pumps after energy depletion following prolonged ischemia; and (3) continuous uptake of osmotically active solutes by the cells (Unterberg et al., 2004). These mechanisms cause an imbalance in ionic concentrations between the astrocyte and the extracellular space, which result in the disruption of water homeostasis of the astrocyte. The ionic concentration imbalance is due to the impairment of ATP production in the astrocyte after ischaemic stroke (Zador et al., 2009).

Astrocyte swelling is usually seen to occur as an early event in many cerebral diseases, particularly in ischaemic stroke (Kimelberg, 1995; Papadopoulos et al., 2007). During ischemia, the occluded cerebral vessels reduce the cellular functions, especially in water homeostasis that further result in astrocyte swelling or cytotoxic oedema. If ischemia is prolonged, the BBB starts to breakdown and vasogenic oedema starts to occur (Zador et al., 2009). Hence, the clearance of cytotoxic oedema is thought to follow the same routes as in vasogenic oedema. The excess water that is initially in the astrocyte may move to the extracellular space at a later stage of cerebral disease when the cell starts

to degenerate. The water then may be removed via the same paths as in vasogenic oedema (Papadopoulos et al., 2007).

2.2.5 Cerebral Capillary Compression

Brain tissue swelling can cause brain herniation or the movement of the brain midline structure (Frank, 1995). The effect of brain tissue swelling, together with brain herniation may result in the compression of microvessels within the brain (del Zoppo et al., 2003), which subsequently resulting in the deficit of CBF through the affected regions. The compression of microvessels creates the no-reflow phenomenon (Ames et al., 1968), where certain vessels remain blocked after reperfusion treatments and this may lead to the occurrence of secondary ischaemia (Lindenberg, 1955).

However, the occurrence of this phenomenon is not solely due to brain tissue swelling (Fischer et al., 1977), but in fact, it is multifactorial, which includes vascular factors (eg: endothelial damage), blood factors (eg: blood viscosity, platelet and erythrocyte aggregation), and cardiovascular factors (eg: venous blockage, blood pressure) (Hossmann, 1997). Another possible factor is the abrupt changes of the tone of the smooth muscle of the microvessels during ischaemia followed by reperfusion (Todd et al., 1986). This is proven in the study of the capillary flow velocities using ischaemic-reperfused gerbils (Hauck et al., 2004). In this thesis, however, only the effect of brain tissue swelling on the brain microvessels compression will be studied.

2.2.6 Aquaporin-4 and Its Function in Brain Oedema

Aquaporin (AQP) is an integral membrane transport protein with its main function in the transportation of water. It was first discovered by Agre and colleagues in a study of human erythrocyte membranes (Preston et al., 1991), and has led to the discovery of many AQPs in animal and plant cells. There are 14 known types of AQP discovered thus

far in humans and rodents, however in the brain, there are three main AQPs that can be found which are AQP1, AQP4 and AQP9 (Papadopoulos et al., 2013).

The AQP originally found by Agre was named AQP1 (Knepper et al., 2004). In the brain, AQP1 plays a role in the production and secretion of CSF (Oshio et al., 2005) and can be found in the apical membrane of the choroid plexus (Nielsen et al., 1993), in the circumventricular organs (i.e. specialised areas of the brain without BBB) and is almost absent in the cerebral microvessels (Wilson et al., 2010). Meanwhile, AQP4 is found mostly in the astrocyte processes, which are located at the subpial astrocyte processes that form the subarachnoid central nervous system (CNS)-CSF interface, at the basolateral membrane of ependymal cells and subependymal astrocyte processes between the ventricle CNS-CSF interface, and at the perivascular astrocytes that form the CNS-blood interface or the BBB (Nielsen et al., 1997; Rash et al., 1998). Experiments done by Manley et al. (2004) on AQP4-null mice showed a reduction in astrocyte water permeability, suggesting a role for AQP4 in astrocyte water permeability. Lastly, AQP9 has been found in the glial cells in forebrain and in the endothelial cells of pial vessels, although it is rather weakly expressed (Badaut et al., 2004). Among all of these AQP, AQP4 is the major water protein channel expressed in the brain (Papadopoulos et al., 2004).

Being the most abundant in the brain, AQP4 plays an important role in water movement between the compartments in the brain, especially in CNS-related diseases such as traumatic brain injury, ischaemia and tumour, which contributes to brain oedema or swelling formation and elimination (Marmarou, 2007). Many experiments have been done to study the expression of AQP4 during these diseases and its role in brain oedema. For example, the study done by Vizuete et al. (1999) found that the expression of the messenger ribonucleic acid (mRNA) of AQP4 depends on the disruption of the BBB and

AQP4 may have a role in maintaining brain water homeostasis. The deletion of AQP4 is thought to supress the formation of brain cytotoxic oedema as shown in the studies on the AQP4-null mice during brain water intoxication (Verkman et al., 2000), ischaemic stroke (Verkman et al., 2000) and meningitis (Papadopoulos et al., 2005). However, the role of AQP4 is reversed in the model of vasogenic oedema during brain intraparenchymal fluid infusion, focal cortical freeze injury, tumour (Papadopoulos et al., 2004), brain contusion (Saadoun et al., 2003) and brain abscess (Bloch et al., 2005), in which its presence actually helps to reduce this type of oedema. Thus, it can be concluded that the role played by AQP4 depends on the type of oedema present.

During early ischaemic stroke, deletion of AQP4 will slow down the rate of water flow into the brain, particularly in the astrocyte. This is because at the initial stage of ischemia, cytotoxic oedema occurs and the BBB remains intact (Papadopoulos et al., 2007). If ischemia continues and BBB starts to break down, then water will filtrate into the extracellular space, which causes vasogenic oedema. Deletion of AQP4 at this stage of ischemia however, may interfere with the elimination of oedematous fluid (Amiry-Moghaddam et al., 2003). The time-course study of BBB disruption done by (Tomás-Camardiel et al., 2005) found that there is a strong AQP4 expression which coincides with the onset of BBB breakdown and when the BBB starts to restore. These results suggest that AQP4 is responsible for the formation of early cytotoxic oedema and the elimination of late vasogenic oedema. The study done by Taniguchi et al. (2000) on the time-course of AQP4 expression suggested a similar conclusion, where the expression of AQP4 was validated by monitoring the brain oedema formation and resolution using magnetic resonance imaging (MRI).

There are two possible theories (Papadopoulos et al., 2013) for oedema clearance via AQP4, which are: (1) water is cleared through the AQP4 interfaces as explained

above, driven by osmotic gradients (Agre, 2006); and (2) water is cleared along perivenous spaces and is removed into cervical lymphatics, facilitated by AQP4 (Iliff et al., 2012). However, the osmotic gradients between the astrocyte and extracellular space and CSF, respectively, will oppose the flow of water through AQP4 from these clearance routes (Papadopoulos et al., 2013). In addition, the clearance process could take a considerable amount of time (Ohata et al., 1990).

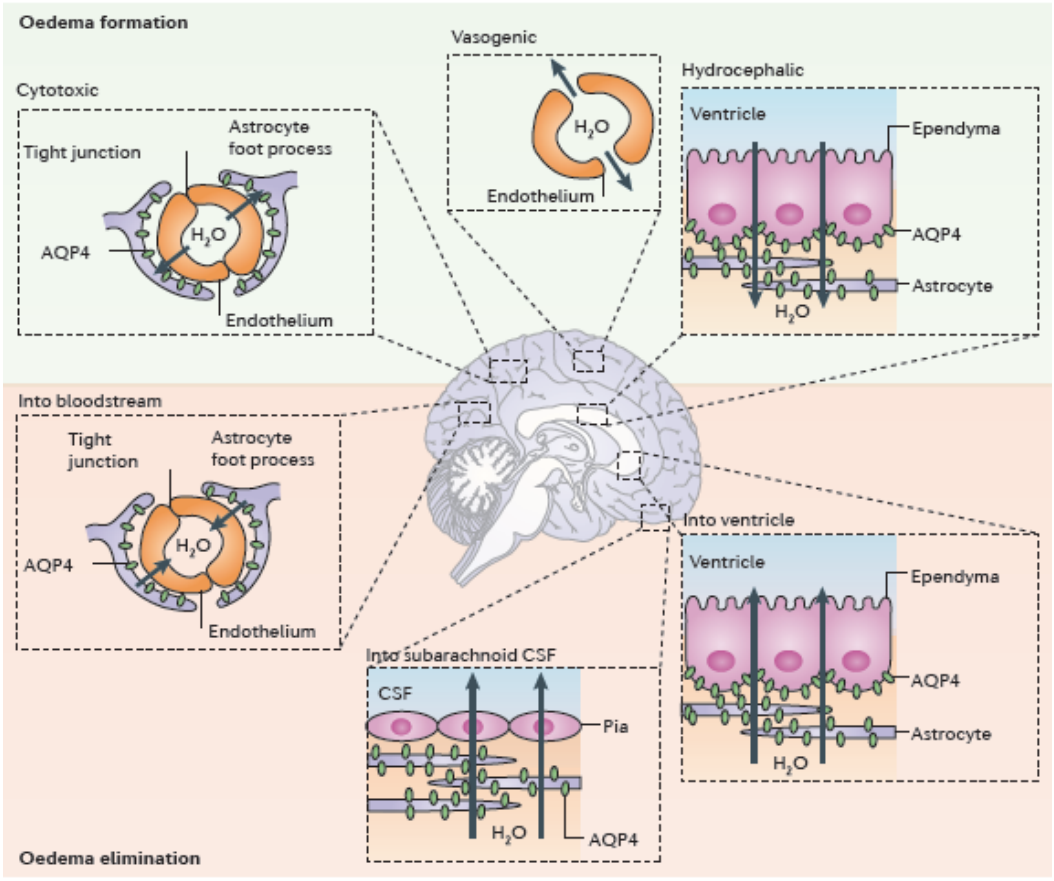

Figure 2.4: Routes of brain oedema formation and elimination. Taken from (Papadopoulos et al., 2013).

Figure 2.4 summarises the different types of brain oedema and the involvement of AQP4 in their formation and elimination. Note that, in the figure, there is another type of oedema, which is not the focus of this study, hydrocephalic oedema. It is the accumulation of CSF from the brain ventricle into the brain interstitial space and AQP4 is also thought to play a role in its formation.

2.3 Mathematical Model

This section describes the mathematical theories involved in the development of the models to describe ischaemia-reperfusion injury. Two important theories that were used mostly throughout this thesis are poroelastic theory, which will be used later to model the cerebral tissue mechanics, and the filtration equation, which is important in describing the water filtration from capillaries into the interstitial space due to BBB breakdown.

In addition to the theories mentioned above, there are several physical laws that should be explored, considering their importance in describing the cerebral tissue mechanics and fluid dynamics. These include the Donnan equilibrium, cellular volume regulation, and vascular collapse model, which will all be described thoroughly in the following sections.

2.3.1 Tissue Mechanics and Poroelastic Theory

When a pressure gradient develops within the tissue due to water filtration, for instance, the interstitial space expands and tissue will deform. This deformation depends on the tissue elastic properties. One of the most common approaches to study brain tissue deformation is the use of poroelastic theory, which is suitable for modelling long term fluid movement processes (Kyriacou et al., 2002) such as water filtration into the brain interstitial space. This theory has been widely used in many studies regarding brain tissue such as those in the hydrocephalus (Smillie et al., 2005; Taylor et al., 2004; Tully et al., 2011), neurosurgery (Miga et al., 2000; Miller, 1999), brain chemotherapeutic infusion (Basser, 1992) and others.

Poroelastic theory was first introduced in modelling soil consolidation, which is a process of gradual settlement of soil under loading (Biot, 1941). The concept was initiated based on the works by von Terzaghi in 1925 but was further generalised into three-dimensional form by (Biot, 1941; Terzaghi, 1943). Terzaghi assumed that soil particles are bound together by the interaction of a solid matrix and a fluid, usually water, present in the porous structure. This theory is based on the following assumptions (Terzaghi, 1943): (1) the material is isotropic and homogeneous; (2) the soil is completely saturated; (3) the soil and water in the pores are incompressible; (4) there is a linear stress-strain relationship; (5) relatively small strains; and (6) water flow through the porous structure is governed by Darcy's Law. This initial development of the theory however, was only for quasi-static processes that occur slowly with negligible inertial effects.

Further generalisations were made (Biot, 1956, 1961, 1962) to incorporate the dynamical behaviour of the porous structure such as the fluid phase acceleration and gravitational forces. Further re-derivations were made (Zienkiewicz, 1982) and also by (Green et al., 1969), of which the latter is commonly known as mixture theory, to provide alternative formulations to the constitutive model of the porous solid. Furthermore, the theory was further developed to study the behaviour of fractured rocks that have a double porosity and permeability (Aifantis, 1980) and was later generalised to include multiple porosity and permeability (Bai, 1993). The concept of multiple porosity and dynamic behaviour in the poroelastic theory was then applied to study water transport in the cerebral space during hydrocephalus (Tully et al., 2011).

Therefore, this theory is suitable to model brain tissue by assuming the brain tissue to be a homogeneous and linearly elastic material containing water and blood in a porous structure. In addition, this theory will also be used to study water transport within the

different compartments within the brain tissue, namely the astrocyte, neuron, ECS and capillary by implementing the multiple porosity theory.

2.3.2 Mathematical Framework of Poroelastic Theory

Figure 2.5 shows a block of tissue containing two different porosities containing fluids A and B, and a solid matrix. The porosity is defined as the volume of a phase divided by the total volume of the system:

$$\mathrm{n^a} = \frac{\mathrm{dV^a}}{\mathrm{dV}}, \tag{2.2}$$

where the superscript $a = 1, \dots, A$ represents the different fluid networks with different values of porosity present in the system (Bai, 1993), which in the case of Figure 2.5, equate to fluids A and B. The solid matrix and fluid phase displacements can be denoted as u_i and ${u_i}^a$ respectively. In this theory, the relative fluid displacement is given as (Biot, 1962):

$$\omega_i^a = n^a(u_i^a - u_i). \tag{2.3}$$

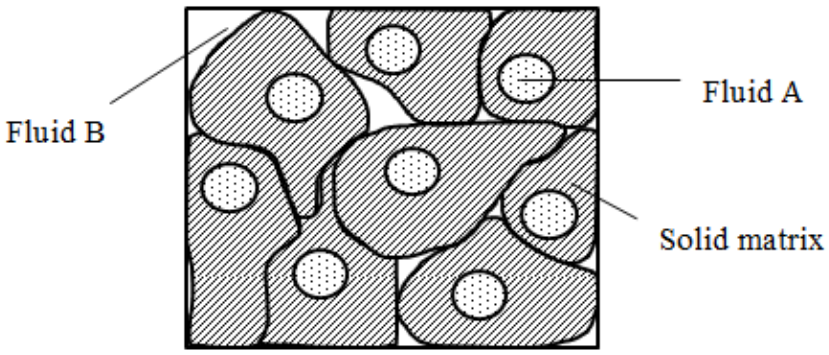

Figure 2.5: An example of a block with two porosities present.

The theory starts by considering the solid phase equilibrium equation first. Terzaghi's principle states that when a porous medium is subjected to a stress, it is opposed by the pressure of each fluid network present (Terzaghi, 1943) as given by:

$$\sigma_{ij} = \sigma'_{ij} - \sum_{a=1}^{A} \alpha^a P^a \delta_{ij}, \tag{2.4}$$

where σ_{ij} and σ'_{ij} are the total and effective stresses in the solid matrix respectively, α is the Biot parameter (Biot et al., 1957), P is the fluid pressure and δ_{ij} represents the Kronecker delta. In this analysis, the subscript i and j have the values depending on the dimension of the space, and the comma in between them represents the divergence operation over the variables for which it is subscripted. For an isotropic and linearly elastic material, the effective stress can be related to the strain by:

$$\sigma'_{ij} = 2G\left(\varepsilon_{ij} + \frac{v}{1-2v}\varepsilon_{ii}\right), \tag{2.5}$$

where G is the shear modulus and v is the Poisson's ratio. The strain-displacement relationship is given by:

$$\varepsilon_{ij} = \frac{1}{2}\left(u_{i,j} + u_{j,i}\right). \tag{2.6}$$

In equilibrium of momentum, the divergence of eqn. (2.4) must be zero. However, in the presence of local body forces such as gravity and accounting for fluid acceleration, the divergence of the total stress is given by:

$$\sigma_{ij,j} + \rho(b_i - \ddot{u}_i) = \sum_{a=1}^{A} \rho^a(\ddot{\omega}_i^a + \dot{\omega}_j^a \dot{\omega}_{i,j}^a), \tag{2.7}$$

where $\rho = \sum_{a=1}^{A} n^a \rho^a + (1-n)\rho^s$ is the total density of the system, $n = \sum_{a=1}^{A} n^a$ is the total volume fraction of the combined fluid networks, ρ^s is the density of the solid phase, and b_i are the local body forces. The solid displacement is described in the Lagrangian frame of reference while the fluid velocities are described in the Eulerian frame of reference relative to the solid matrix (Zienkiewicz et al., 1990; Zienkiewicz et al., 1984). By substituting eqns. (2.4), (2.5), and (2.6) into eqn. (2.7), the equation for the solid phase can be expressed as:

$$G\nabla^2 u_i + \frac{G}{1-2v}\nabla(\nabla \cdot u_i) - \sum_{a=1}^{A} \alpha^a \nabla P^a - \sum_{a=1}^{A} \rho^a \left(\ddot{\omega}_i^a + \dot{\omega}_j^a \cdot \nabla \dot{\omega}_i^a\right) + \rho(b_i - \ddot{u}_i) = 0 \tag{2.8}$$

For the fluid networks, the fluid flow of fluid phase a can be described by mass conservation (Zienkiewicz et al., 1990):

$$\frac{1}{Q^a}\dot{P}^a + \alpha^a \dot{\varepsilon}_{ii} + \dot{\omega}_{i,i}^a - \sum_{a,b=1,b\neq a}^{A} \dot{S}_{b\to a} = -\frac{\dot{\rho}^a}{\rho}\omega_i^a, \tag{2.9}$$

where $\dot{S}_{b\to a}$ represents the rate of fluid transfer from fluid network b to fluid network a. The term Q^a is known as the relative compressibility of the fluid network and can be expressed as:

$$\frac{1}{Q^a} = \frac{\alpha^a - n^a}{K^S} + \frac{n^a}{K^a}, \tag{2.10}$$

where K^s and K^a are the bulk moduli for the solid matrix and fluid network respectively. In addition, each fluid network can also be described using equilibrium of momentum, which is given by the sum of the divergence of the fluid pressure, the viscous drag force R^a, and the external forces, and is equal to the acceleration of the fluid network relative to the solid matrix as shown below:

$$\rho(b_i - \ddot{u}_i) - P_{,i}^a - R_i^a = \frac{\rho^a}{n^a}\left(\ddot{\omega}_i^a + \dot{\omega}_j^a \dot{\omega}_{i,j}^a\right). \tag{2.11}$$

The term R_i^a can be described by Darcy's Law, which is given by:

$$R_i^a = \frac{\dot{\omega}_i^a}{k^a}, \tag{2.12}$$

where the term k^a is known as the permeability of the fluid network, which is usually assumed to be isotropic and which can then be represented by a single value (Zienkiewicz et al., 1990).

Substituting eqn. (2.12) into (2.11), substituting into eqn. (2.9) and expressing in ∇ notation gives:

$$\frac{1}{Q^a}\dot{P}^a + \alpha^a \nabla \cdot \dot{u}_i + k^a \rho^a \nabla \cdot (b_i - \ddot{u}_i) - k^a \nabla^2 P^a - \frac{k^a \rho^a}{n^a} \nabla \cdot \left(\ddot{\omega}_i^a + \dot{\omega}_j^a \cdot \nabla \dot{\omega}_i^a\right) - \sum_{a,b=1,b\neq a}^{A} \dot{S}_{b\to a} + \frac{\dot{\rho}^a}{\rho} \omega_i^a = 0, \tag{2.13}$$

Equations (2.8) and (2.13) form the set of equations that can be used to solve for the fluid pressure and solid displacement of the system. The term $\dot{S}_{b\to a}$ is very useful because it can be used to represent the amount of water transfer between the different compartments present within the system. For example, it has been used to describe the water transport between the different fluid networks present in a four-network cerebral model (Tully et al., 2011).

2.3.3 Cellular Volume Regulation and Membrane Elasticity

Cell volume changes are important to allow cells to function mechanically such as in cell proliferation, cell migration and also in cell death. The volume changes due to the pressures developed between the intracellular and extracellular spaces, in which it can drive water either in or out of the cell. A cell volume and pressure regulation model that incorporate the surface membrane elasticity has been developed by Jiang et al. (2013). Such a model is important in describing the mechanical changes of cerebral cells such as astrocyte and neuron due to water filtration after ischaemia.

The water flux J_{water} through the cell is given by a simple equation relating hydrostatic, ΔP, and osmotic pressure, $\Delta\Pi$, differences across the membrane as:

$$J_{\text{water}} = F(\Delta P - \Delta\Pi), \tag{2.14}$$

where F represents the rate constant of water through a particular membrane, which determines the permeability of the membrane towards water. This model looks similar to the filtration model, which will be described in the later section, although it is without the

reflection coefficient, σ, term, which is specific for molecule and ion filtration across a membrane.

Assuming that water moves across the cell surface area, then the total water transfer across the cell membrane, $\dot{S}_{\text{membrane}}$ is given by:

$$\dot{S}_{\text{membrane}} = J_{\text{water}} A_i, \tag{2.15}$$

where A_i is the deformed surface area of the cell, which can be related with the original surface area, A_o and elastic modulus, E_c of the cell membrane by an elastic cortex model implemented directly from (Clark et al., 2011) as given below:

$$\sigma = \frac{E_c}{2}\left(\frac{A_i}{A_o} - 1\right) + \mu_c \frac{1}{A_i}\frac{dA_i}{dt} - \sigma_a, \tag{2.16}$$

The elastic cortex model was derived to represent a spherical plasma membrane protrusion which is usually observed during cell movement and apoptosis (Tinevez et al., 2009). In eqn. (2.16), the first and second terms on the right-hand side represent the passive stress and shear stress with cell viscosity, μ_c, respectively, meanwhile the last term is the active stress due to the contraction of the membrane.

To simplify the cell elastic model, the contribution of shear stress and active stress towards the elasticity of the cell membrane is often neglected. This is because the shear stress due to the viscosity of the cell is smaller than the passive stress (Jiang et al., 2013) and energy deprivation after a prolonged cerebral ischaemia may disrupt the electrical propagation in astrocytes (Panickar et al., 2005).

2.3.4 Filtration Equation

The filtration equation is important in modelling the filtration of ions and protein plasma from the blood into the cerebral tissue after BBB breakdown. Capillary filtration was first described by (Starling, 1896), who stated that the fluid movement across the

capillary wall depends on the difference between the hydrostatic and osmotic pressures between the blood and interstitial fluid (ISF). Hydrostatic pressure is the pressure that is exerted by a fluid at rest. Meanwhile, osmotic pressure is the pressure exerted by the difference between the concentrations of solutes present in the fluid, which will be explained in detail in the Section 2.3.5.

The filtration flux, J_{VA}, can be described by eqn. (2.17):

$$J_{VA} = L_p \left[(P_b - P_w) - \sum_{m=1}^{M} \left(\sigma (\Pi_b - \Pi_w) \right)_m \right], \tag{2.17}$$

where L_p is the hydraulic permeability of the capillary wall, P is the hydrostatic pressure with the subscripts b and w representing the blood and ISF (water) phases respectively, and Π is the osmotic pressure for each water-soluble solute, m, present in the blood plasma and ISF. The filtration flux has a similar form of equation as (2.14) but it has an extra reflection coefficient term, σ which is in the range of 0 to 1, with $\sigma = 1$ meaning that no solute can pass through the capillary wall.

In steady state, the ISF protein concentration, C_w, is not a fixed value but dynamically varying and can be related to the solute flux, J_S, and water flux through $C_w = J_S / J_{VA}$ (Levick et al., 2010). The blood plasma protein concentration, together with the definition of C_w, can be used to express Π_w in terms of Π_b as given by:

$$\Pi_b - \Pi_w = \sigma \Pi_b \frac{1 - e^{-Pe}}{1 - \sigma e^{-Pe}}, \tag{2.18}$$

where:

$$Pe = \frac{J_{VA}(1 - \sigma)h}{D} \tag{2.19}$$

is the Péclet number with h and D denoting the wall thickness and diffusion coefficient, respectively. By substituting eqn. (2.18) into eqn. (2.17), the filtration flux can be found to be:

$$J_{VA} = L_p \left[(P_b - P_w) - \sum_{m=1}^{M} \left(\sigma^2 \Pi_b \frac{1 - e^{-Pe}}{1 - \sigma e^{-Pe}} \right)_m \right], \tag{2.20}$$

In a normal capillary wall, there exist both small and large pores which allow the flow of solutes such as ions and proteins through the wall (Rippe et al., 1994). Equation (2.20) can be extended by adding filtration terms for both small and large pores as shown below:

$$J_{VA} = \sum_{l=1}^{L} L_{p_l} \left[(P_b - P_w) - \sum_{m=1}^{M} \left(\sigma^2 \Pi_b \frac{1 - e^{-Pe}}{1 - \sigma e^{-Pe}} \right)_{l,m} \right], \tag{2.21}$$

where l represents the different pore sizes present on the wall. In the experiment done by Preston et al. (1997) in the rat BBB after ischemia, it was suggested that there are large pores present in the BBB. The filtration equation can be modified to model the filtration behaviour of a pathological BBB by giving appropriate value of the reflection coefficients of proteins and ions, which can be assumed to be 0.93 and 0 respectively for both pore sizes (Su, 2011). Thus, eqn. (2.21) becomes:

$$\begin{aligned} J_{VA} = L_{p_S} & \left[(P_b - P_w) - \sum_{m=1}^{M} \left(\sigma^2 \Pi_b \frac{1 - e^{-Pe}}{1 - \sigma e^{-Pe}} \right)_{\text{protein},S} \right] \\ & + L_{p_L} \left[(P_b - P_w) - \sum_{m=1}^{M} \left(\sigma^2 \Pi_b \frac{1 - e^{-Pe}}{1 - \sigma e^{-Pe}} \right)_{\text{protein},L} \right], \end{aligned} \tag{2.22}$$

where the subscript L and S represent the large and small pores present in breakdown BBB.

Since the reflection coefficients for both pores can be assumed to be the same (Su, 2011), the equation can be simplified to:

$$J_{VA} = L_p \left[(P_b - P_w) - \left(\sigma^2 \Pi_b \frac{1 - e^{-Pe}}{1 - \sigma e^{-Pe}} \right) \right], \tag{2.23}$$

where L_p is the combined hydraulic permeability for small and large pores. The value of L_p for normal BBB is estimated to be about 2.0×10^{-9} cm/s.cmH_2O (Fraser et al., 1990)

and during ischemia, the value can increase more than 100 times the normal value (Hakamata et al., 1995).

2.3.5 Osmotic Pressure and Donnan Equilibrium

In two regions filled with solutions that are separated by a semi-permeable membrane, the process governing the movement of the solvent molecules through this membrane in the direction from the region with higher solvent concentration is called osmosis. This movement is due to the development of osmotic pressure within the regions that drives the solvent through the membrane. Osmotic pressure depends on the solute concentration within the region and also the surrounding temperature (Eyster, 1943).

For an ideal solution with low concentration, the osmotic pressure, Π, can be described using the Morse equation (Amiji et al., 2003) as given below:

$$\Pi = p_{osm} = iRTc, \tag{2.24}$$

where T and c are the surrounding temperature and the concentration of the solute, respectively, meanwhile R is the gas constant. The dimensionless constant i is known as the van't Hoff factor, which represents the number of ions dissociated from one mole of an ionic solution. For weak electrolytes such as carboxylic acids, the van't Hoff factor has a value of 1. This relationship has become the basis for obtaining eqn. (2.18) as derived comprehensively in (Levick et al., 2010).

Cell ISF contains many free moving ions such as Na^+, K^+, $Ca^{2+}$and HCO_3^- that can contribute to the electrochemical behaviour of the cell. In addition to these ions, the cell also contains macromolecules such as DNA and proteins that have fixed negative charges. These charges are collectively termed as fixed charge density (FCD). The presence of FCD in healthy tissue does not cause water movement due to the difference

in ionic concentration between intra- and extracellular spaces because the movement of ions is controlled by the active ion channels (Leaf, 1959). However, when the tissue is damaged due to ischaemia and the cell membrane starts not to function as normal, this will cause an influx of ions from the ECS into the cell to balance out the effect of FCD charges and will create an osmotic pressure difference that might lead to tissue swelling. This process is known as the Donnan effect (Donnan, 1924).

The effect of FCD can be modelled using the Donnan equilibrium (Cowin et al., 2009). Donnan equilibrium has been studied in various mathematical models of biological tissues such as the cerebral tissue (Drapaca et al., 2012; Elkin et al., 2010; Lang et al., 2014), aorta (Azeloglu et al., 2008), and intervertebral disc tissue (Frijns et al., 1997). Denoting FCD as c^{fc} and according to the electroneutrality conditions, the sums of ionic concentrations within the tissue and the external environment are given as:

$$c_i^+ - c_i^- - c^{fc} = 0, \tag{2.25}$$

$$c_o^+ - c_o^- = 0, \tag{2.26}$$

where the subscripts i and o represent the internal and external environment, respectively, meanwhile the superscripts $+$ and $-$ represent the positive (cation) and negative (anion) charged ions, respectively. Equation (2.26) shows that the concentrations of cation and anion in the external environment are equal and, to simplify the analysis, these concentrations are equated to a constant external concentration, c_o. The activity of the substance in the ionic solution is given by:

$$a_{(a)} = f_{(a)} c_{(a)}, \tag{2.27}$$

which describes the deviation of the substance from its ideal behaviour with f the activity coefficient and the subscript (a) represents either the internal or external environment. For an ideal solution, $f = 1$.

The Donnan equilibrium can be described by the equilibrium of the electrochemical potentials between the internal and external solutions. For a mixture of cations and anions, the equilibriums of the electrochemical potentials are given as:

$$\mu_i^+ = \mu_o^+, \tag{2.28}$$

$$\mu_i^- = \mu_o^-, \tag{2.29}$$

Here, μ is the electrochemical potential of each constituent of the mixture. These chemical potentials have the following relationships:

$$\mu_{(a)}^+ = \mu_{(a)}^{+,\mathrm{ref}} + \frac{1}{\bar{V}^+}\left(RT \ln a_{(a)}^+ + F\xi_{(a)}\right), \tag{2.30}$$

$$\mu_{(a)}^- = \mu_{(a)}^{-,\mathrm{ref}} + \frac{1}{\bar{V}^-}\left(RT \ln a_{(a)}^- - F\xi_{(a)}\right), \tag{2.31}$$

where F is Faraday's constant, $\bar{V}$ is the partial molar volume of the substance and ξ is the electrical potential of the solution.

Substituting the eqns. (2.30) and (2.31) into the equilibrium of electrochemical potential to obtain the relationship below:

$$a_i^+ a_i^- = a_o^+ a_o^-, \tag{2.32}$$

From the equation above, substituting the eqn. (2.27) to obtain another condition of electroneutrality below:

$$c_i^+ c_i^- = f^2 c_o^2, \tag{2.33}$$

where $f^2 = \frac{f_o^+ f_o^-}{f_i^+ f_i^-}$. Solving the eqns. (2.27) and (2.33) simultaneously to obtain c_i^+ and c_i^- in terms of c_o and c^{fc}.

$$2c_i^+ = c^{fc} + \sqrt{c^{fc^2} + 4f^2 c_o^2}, \tag{2.34}$$

$$2c_i^- = -c^{fc} + \sqrt{c^{fc^2} + 4f^2 c_o^2}, \tag{2.35}$$

The osmotic pressure, Δp_{osm}, can be calculated using eqn. (2.24) in which the concentration, c is equal to the sum of osmotically active ions, as given below:

$$\Delta p_{osm} = p_i - p_o = RT\left[\sqrt{c^{fc^2} + c^{*2}} - c^*\right], \tag{2.36}$$

and equation above is only applicable for the case of ideal solution with $c^* = 2c_o$. Although FCD also have charges, they are osmotically inactive (Kurbel, 2008) and are thus excluded from the summation.

2.3.6 Vascular Collapse and Tube Law

One of the effects of an increase in ICP is vessel collapse. Vessel collapse can occur when there is a decrease in the transmural pressure across the vessel wall. The formation of vessel collapse causes the narrowing of the vessels and may restrict CBF to the brain tissue (Siemkowicz, 1980), a phenomenon known as no-reflow (Ames et al., 1968). This phenomenon is thought to occur due to the difference in the transmural pressure in the cerebral vessels.

The transmural pressure can be related to the change in the cross-sectional area of the vessel as given by (Baish et al., 1997):

$$P_b - P_w = E\left(\frac{A_i}{A_o}\right)^k - P_c, \tag{2.37}$$

where E is the capillary wall stiffness, A_i and A_o are the deformed and baseline cross-sectional areas respectively, P_c is the critical pressure that causes collapse, and k is an exponent. At baseline conditions, $P_b - \bar{P} = E - P_c$, hence eqn. (2.37) can be rewritten as:

$$\frac{A_i}{A_o} = \left(1 + \frac{\bar{P} - P_w}{E}\right)^{1/k}. \tag{2.38}$$

Equation (2.38) assumes that the vessel collapse occurs without any change in perimeter (Drzewiecki et al., 1997). Figure 2.6 shows the changes in cross-sectional area for changes in the transmural pressure. For positive values of transmural pressure, the

vessel retains its circular cross-sectional area. When transmural pressure becomes increasingly negative, the tube flattens and eventually collapses.

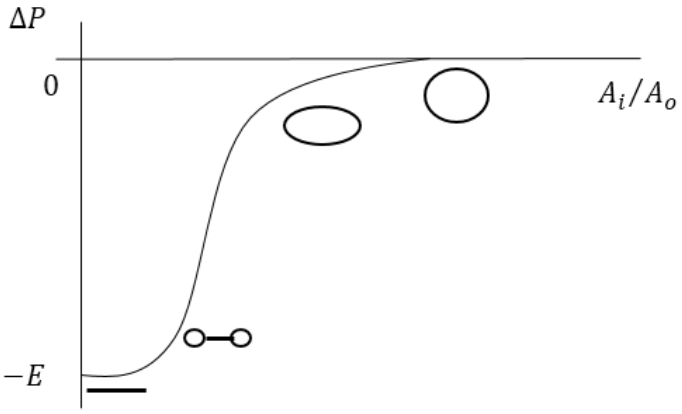

Figure 2.6: The transmural pressure and ratio of cross-sectional area relationship of the tube law. Modified from (Jensen et al., 1989).

2.4 Summary

Cerebral microvessels have an endothelium that forms a BBB that protects the tissue from many brain tissue diseases. The opening of BBB after ischaemic stroke allows filtration of fluid from blood into the interstitial space that can consequently form vasogenic oedema. Accumulation of oedematous fluid can result in an increase in ICP and cause tissue swelling, both of which will compress the cerebral vessels. In addition, ischaemic stroke also will cause the cells to swell due to the imbalance in the ionic concentrations and this is known as cytotoxic oedema.

The formation of vasogenic oedema can be modelled using a capillary filtration model and its effect of cerebral tissue swelling can be modelled using poroelastic theory. The Donnan equilibrium can be used to describe the ion imbalance in cells, which can affect the osmotic pressure difference between the cells and the ECS. The cerebral vessel properties can be simplified by implementing the tube law.

Chapter 3

Mathematical Model of the Effect of Ischaemia-Reperfusion on Brain Capillary and Tissue Swelling

---

The work presented in this chapter has appeared as **Mokhtarudin, M.J.M.** and Payne, S.J. "Mathematical model of the effect of ischemia-reperfusion on brain capillary collapse and tissue swelling" *Mathematical Biosciences*, 263: 111-120, 2015.

3.1 Introduction

Vasogenic oedema occurs when the tight junction structure of the blood-brain barrier (BBB) breaks down after cerebral ischaemia, allowing the filtration of plasma proteins and ions from the blood circulation into the cerebral tissue. The fluid starts to accumulate in the brain tissue resulting in tissue swelling and increases the intracranial pressure (ICP). These might cause the compression of cerebral microvessels and impede the cerebral blood flow although after blood reperfusion (Chiang et al., 1968). This is also known as the no-reflow phenomenon (Ames et al., 1968).

In this chapter, a model is developed to study the effect of reperfusion on the formation of oedema and tissue swelling and how these two can cause brain vessels to collapse. Formation of vasogenic oedema is modelled using the filtration equation in which the differences in transmural pressure across the cerebral capillaries cause water to filtrate into the tissue interstitial space. Accumulation of water in this space will cause tissue displacement, which is modelled using poroelastic theory. Lastly, vessel collapse

is modelled using the tube law of microvessels that relates transmural pressure to changes in vessels cross-sectional area. The model developed here also becomes the foundation for the other models in subsequent chapters.

3.2 Proposed Model[1]

Consider a very small volume of cerebral tissue, which contains a distribution of capillary vessels with different sizes and mechanical properties. In this model, it is assumed that water filtrates from the blood vessels into the cerebral interstitial space through the capillary wall. To best illustrate the filtration process, consider a single capillary as shown in Figure 3.1. After stroke occurrence, the lack of oxygen creates a series of molecular cascade that destroys the surrounding endothelial cells of the cerebral blood vessels and causes the BBB breakdown (Yang et al., 2011), thus increasing the BBB permeability. When blood flows through the cerebral capillaries after reperfusion, ions and some protein plasma can filtrate through the interstitial space via the BBB. The reperfusion creates an osmotic pressure difference between the interstitial space and the capillary, which causes water flux into the tissue space. Accumulation of water inside the interstitial space can cause tissue displacement. Furthermore, the pressure difference between interstitial space and capillary will cause vessel collapse.

The capillaries are assumed to be distributed homogeneously inside the cerebral tissue and the permeability of the normal BBB is assumed to be approximately zero, to simplify the proposed mathematical model. The brain tissue is assumed to be elastic, homogeneous and isotropic, and the model treats white and grey matter as mechanically the same.

[1] Readers that are not interested in the full derivation of the model can skip the sections 3.2.1 to 3.2.4 and go straight to section 3.3.

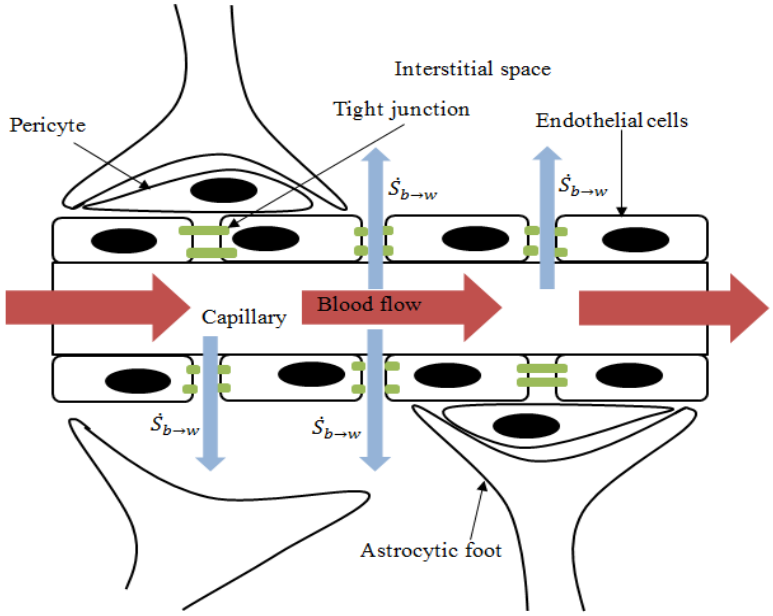

Figure 3.1: Capillary filtration after BBB breakdown, showing water filtration flux through the endothelium of the capillary with damaged tight junctions. $\dot{S}_{b\to w}$ represents the water movement from blood capillaries into the cerebral tissues via capillary filtration.

In this model, the water flux into the cerebral tissue due to BBB breakdown is represented by the term $\dot{S}_{b\to w}$, as shown in the Figure 3.1. This term is applicable to damaged tissues only. In normal tissues, this term equals zero. The details of the derivation of $\dot{S}_{b\to w}$ is in the section 3.2.1. The accumulation of water in the cerebral tissue will cause it to swell and potentially cause the microvessels to be compressed. The derivations of microvessels compression and tissue swelling are in the sections 3.2.2 and 3.2.3, respectively. Lastly, section 3.2.4 will describe the non-dimensionalisation of the equations.

3.2.1 Capillary Filtration

It is assumed that water filtration, $\dot{S}_{b\to w}$ occurs across the surface area of each vessel within a small volume of cerebral tissue and that this can be approximated by an integration of water flux, J_{VA}, at each point in space over the distribution of vessel

circumferences, $p(c)$, for each vessel of constant length, L_c, in a given volume as shown below:

$$\dot{S}_{b\to w} = \frac{dN}{dV}\int_0^\infty J_{VA} L_c p(c) dc, \tag{3.1}$$

where the subscripts b and w represent the blood and water phases respectively. The term $\frac{dN}{dV}$ is a scaling factor that represents the number of vessels N in a given volume V. The baseline volume fraction of the blood is:

$$\bar{n}_b = \frac{dN}{dV}\pi {R_c}^2 L_c, \tag{3.2}$$

where R_c is the baseline value of vessel radius. The term J_{VA} is independent of vessel size and can thus be taken out from the integral (3.1). Substituting eqn. (3.2) into (3.1) gives:

$$\dot{S}_{b\to w} = J_{VA}\frac{\bar{n}_b}{\pi {R_c}^2}\int_0^\infty p(c) dc, \tag{3.3}$$

The integral above can be simplified by assuming that the vessel perimeter does not change as the wall deforms, hence:

$$\int_0^\infty p(c) dc, = 2\pi R_c f, \tag{3.4}$$

where f represents the fraction of vessels that remain open at each point because it is assumed that water flux occurs only whilst the vessel is still opens. Thus, eqn. (3.3) reduces to:

$$\dot{S}_{b\to w} = J_{VA}\frac{2\bar{n}_b}{R_c} f, \tag{3.5}$$

The water filtration flux from pathological brain capillaries into the interstitial space, which has been described in Chapter 2, can be modelled using the modified Starling principle:

$$J_{VA} = L_{p_S}\left[(P_b - P_w) - \sum_{m=1}^{M}\left(\sigma^2\Pi_b\frac{1-e^{-Pe}}{1-\sigma e^{-Pe}}\right)_{\text{protein},S}\right] + L_{p_L}\left[(P_b - P_w) - \sum_{m=1}^{M}\left(\sigma^2\Pi_b\frac{1-e^{-Pe}}{1-\sigma e^{-Pe}}\right)_{\text{protein},L}\right], \tag{3.6}$$

where P_b is the blood pressure, L_p is the hydraulic permeability, σ is the reflection coefficient, and Π_b is the osmotic pressure in the capillary. The subscript S and L represent the small and large pores present in the BBB during breakdown. The Péclet number, Pe is given by:

$$Pe_j = \frac{J_{VA}(1-\sigma_j)h}{D}, \tag{3.7}$$

with h and D represent the capillary wall thickness and diffusion coefficient respectively and the subscript j denotes either small or large pores. Equation (3.6) can be simplified since the reflection coefficients for both small and large pores are assumed to be the same, to give a composite filtration model as shown below:

$$J_{VA} = L_p\left[(P_b - P_w) - \left(\sigma^2\Pi_b\frac{1-e^{-Pe}}{1-\sigma e^{-Pe}}\right)\right], \tag{3.8}$$

where L_p now represents the combined hydraulic permeability for both small and large pores. This equation is highly nonlinear and can be further simplified by assuming $Pe \ll 1$, as will be justified later in Section 3.2.4 and taking the first order approximation using Taylor series expansion to yield:

$$J_{VA} = L_p[(P_b - P_w) - \sigma\Pi_b\,]. \tag{3.9}$$

Substituting eqn. (3.9) into (3.5) gives the final capillary filtration model used here:

$$\dot{S}_{b\to w} = 2\bar{n}_b\frac{L_p}{R_c}f[(P_b - P_w) - \sigma\Pi_b\,]. \tag{3.10}$$

3.2.2 Vessel Wall Model

Vessels are assumed to collapse when there is a transmural pressure difference and to occur without any change in the perimeter. The transmural pressure across the wall is related to the change in the cross-sectional area of the vessel as described in Chapter 2:

$$\frac{A_i}{A_o} = \left(1 + \frac{\overline{P} - P_w}{E}\right)^{1/k}. \tag{3.11}$$

where $\bar{P}$ is the ICP, P_w is the interstitial pressure, E is the capillary wall stiffness, A_i and A_o are the deformed and baseline cross-sectional areas respectively, and k is an exponent.

3.2.3 Tissue Displacement

The system consisting of the brain tissue, brain capillary, interstitial fluid (ISF) and water filtration can be described using poroelastic theory as previously discussed in Chapter 2. This can be used to solve for the tissue displacement and fluid phase pressures, which are given by:

$$G\nabla^2 u_i + \frac{G}{1-2v}\nabla(\nabla \cdot u_i) - \sum_{a=1}^{A} \alpha^a \nabla P^a - \sum_{a=1}^{A} \rho^a\left(\ddot{\omega}_i^a + \dot{\omega}_j^a \cdot \nabla \dot{\omega}_i^a\right) + \rho(b_i - \ddot{u}_i) = 0 \tag{3.12}$$

$$\frac{1}{Q^a}\dot{P}^a + \alpha^a \nabla \cdot \dot{u}_i + k^a \rho^a \nabla \cdot (b_i - \ddot{u}_i) - k^a \nabla^2 P^a - \frac{k^a \rho^a}{n^a}\nabla \cdot \left(\ddot{\omega}_i^a + \dot{\omega}_j^a \cdot \nabla \dot{\omega}_i^a\right) - \sum_{a,b=1, b\neq a}^{A} \dot{S}_{b\to a} + \frac{\dot{\rho}^a}{\rho}\omega_i^a = 0, \tag{3.13}$$

where u_i is the solid phase displacement with b_i representing the external forces acted on the system, while ω_i^a and P^a are the fluid phase displacement and pressure respectively with the superscript $a = 1, \ldots, A$ representing the different fluid phases present in the system. The terms G, v and ρ represent the shear modulus, Poisson's ratio and the total density of the system while α^a, Q^a, $k^a\left(=\frac{\kappa^a}{\mu^a}\right)$, ρ^a, and n^a represent the Biot parameter,

relative compressibility, permeability, density and volume fraction of each fluid phase. The term $\dot{S}_{b\to a}$ is the rate of fluid transfer from one fluid phase to another.

These equations are highly nonlinear. However, in biological flows such as water filtration into the cerebral tissue, the fluid acceleration are low and can be neglected (Tully et al., 2011). Further, the fluid densities are assumed constant throughout the process. It is also assumed that the tissue displacement is a slow process so that the time derivative of the solid phase displacement can be neglected. The effect of external forces on the system is very small and can be neglected. For the one-dimensional case and assuming spherical symmetry, the equations can thus be simplified to:

$$G\nabla^2 u + \frac{G}{1-2v}\nabla(\nabla\cdot u) - \sum_{a=1}^{A}\alpha^a \nabla P^a = 0, \tag{3.14}$$

$$\frac{1}{Q^a}\dot{P}^a - k^a\nabla^2 P^a - \sum_{a,b=1,b\neq a}^{A}\dot{S}_{b\to a} = 0, \tag{3.15}$$

In the model proposed here, three phases are involved which are the solid brain tissue phase and two fluid phases, blood and water. Thus, the system of equations can be written out fully as:

$$\nabla^2 u - \frac{2}{r^2}u = \frac{1-2v}{2G(1-v)}\left(\alpha_b\frac{\partial P_b}{\partial r} + \alpha_w\frac{\partial P_w}{\partial r}\right), \tag{3.16}$$

$$\frac{1}{Q_b}\frac{\partial P_b}{\partial t} - k_b\nabla^2 P_b + \dot{S}_{b\to w} = 0, \tag{3.17}$$

$$\frac{1}{Q_w}\frac{\partial P_w}{\partial t} - k_w\nabla^2 P_w - \dot{S}_{b\to w} = 0, \tag{3.18}$$

A positive value of $\dot{S}_{b\to w}$ represents the direction of the movement of water from the blood capillaries into the interstitial space, while a negative value represents the reverse direction.

3.2.4 Non-dimensionalisation

The system of equations above can be further simplified through the use of non-dimensionalisation. Assuming that the characteristic lengths for the tissue displacement u and distance r are L_u and L respectively, the baseline value for all the pressures is $\bar{P}$, and the characteristic time for time t is T, the equations can be non-dimensionalised as follows:

$$\tilde{\nabla}^2 u - \frac{2}{\tilde{r}^2}\tilde{u} = \frac{L}{L_u}\frac{\bar{P}(1-2v)}{2G(1-v)}\left(\alpha_b \frac{\partial \widetilde{P}_b}{\partial \tilde{r}} + \alpha_w \frac{\partial \widetilde{P}_w}{\partial \tilde{r}}\right), \tag{3.19}$$

$$\frac{L^2}{Q_b k_b T}\frac{\partial \tilde{P}_b}{\partial \tilde{t}} - \tilde{\nabla}^2 \tilde{P}_b + 2\bar{n}_b \left(\frac{L_p L^2}{R_c k_b}\right) f\left[\left(\tilde{P}_b - \tilde{P}_w\right) - \sigma \tilde{\Pi}_b\right] = 0, \tag{3.20}$$

$$\frac{L^2}{Q_w k_w T}\frac{\partial \tilde{P}_w}{\partial \tilde{t}} - \tilde{\nabla}^2 \tilde{P}_w - 2\bar{n}_b \left(\frac{L_p L^2}{R_c k_w}\right) f\left[\left(\tilde{P}_b - \tilde{P}_w\right) - \sigma \tilde{\Pi}_b\right] = 0, \tag{3.21}$$

where the tilde (~) symbol is used to represent the non-dimensionalised variables. Without loss of generality, by setting the coefficient on the right-hand side of eqn. (3.19) equal to one, the relationship between the two characteristic lengths becomes:

$$L_u = \frac{\bar{P}(1-2v)}{2G(1-v)} L. \tag{3.22}$$

Either one of the coefficients in the round bracket of eqns. (3.20) and (3.21) can also be set equal to one to determine a suitable characteristic length. Using the parameter values given in Table 3.2, the characteristic length chosen here is:

$$L = \sqrt{\frac{R_c k_w}{L_p}}, \tag{3.23}$$

which gives a value of 0.779 mm, which is reasonable for brain tissue which has a length of the order of millimetres. Similarly, either one of the coefficients of the time derivative of pressures in eqns. (3.20) and (3.21) can also be set to one to give a characteristic time:

$$T = \frac{R_c}{L_p Q_w} \tag{3.24}$$

which gives a value of 51.4 s, which is reasonable for a process that occurs over a timescale of minutes.

It can be noted that the ratio of the permeability of blood k_b to the permeability of water k_w is much larger than one:

$$\frac{k_b}{k_w} = \frac{\kappa_b/\mu_b}{\kappa_w/\mu_w} \gg 1, \tag{3.25}$$

implying that all coefficients in eqn. (3.20) with k_b as their denominator are approximately zero and can be neglected, leaving only $\tilde{\nabla}^2 \tilde{P}_b = 0$, which means blood pressure is effectively constant throughout space and equal to the baseline value of blood pressure, $\bar{P}_b$. Therefore, the system of equations can now be reduced to only two equations by removing all differential forms of $\tilde{P}_b$, as shown below:

$$0 = \tilde{\nabla}^2 u - \frac{2}{\tilde{r}^2}\tilde{u} - \frac{\partial \tilde{P}_w}{\partial \tilde{r}}, \tag{3.26}$$

$$\frac{\partial \tilde{P}_w}{\partial \tilde{t}} = \tilde{\nabla}^2 \tilde{P}_w + 2\bar{n}_b f\left[\left(\tilde{P}_b - \tilde{P}_w\right) - \sigma \tilde{\Pi}_b\right], \tag{3.27}$$

The coefficient α_w can thus be included into a slightly revised relationship for characteristic length (3.22):

$$L_u = \frac{\alpha_w \bar{P}(1-2v)}{2G(1-v)} L, \tag{3.28}$$

to give a revised value of 1.105 mm. These equations can now be used to solve for tissue displacement and interstitial water pressure.

Lastly, non-dimensionalising the Péclet number yields:

$$Pe = \tilde{J}_{VA}\beta, \tag{3.29}$$

where:

$$\beta = \frac{\bar{J}_{VA}(1-\sigma)h}{D} \tag{3.30}$$

and $\bar{J}_{VA}$ represents the characteristic water filtration flux, with value in the order of 10^{-9} m/s. The capillary wall thickness, h has a value of 0.5 μm, while the diffusion coefficient of protein, D has a value of 5.62×10^{-6} m^2/s (Zhang et al., 2006). This gives a value of $\beta \approx 10^{-11}$, thus $Pe \ll 1$.

3.3 Numerical Procedures and Model Parameters

This section is divided into 3 subsections. Firstly, the summary of the model is presented. In the summary, the equations of the model are listed and the behaviour of the model when the brain tissue is under normal and damaged conditions is discussed. Secondly, the numerical procedures used for the model such as the initial and boundary conditions are explained in detail. Lastly, the model parameters are listed in a table and their significant are discussed.

3.3.1 Summary of the Model

The list of equations, in non-dimensionalised form, for the model is as listed in the Table 3.1. Under the baseline condition, it is assumed that the BBB remains intact, in which case there is no breakdown occurrence and subsequently no water flux into the cerebral tissue. Therefore, this can be modelled by letting the capillary filtration $\tilde{S}_{b\to w}$ equals to zero. Hence, the tissue water pressure, $\tilde{P}_w$ will remain at the baseline value of the ICP and no tissue swelling can happen.

Meanwhile, for damaged tissue or in the core zone of the ischaemia, the BBB breakdown is assumed to occur. Upon reperfusion, some of the protein and ions can filtrate the BBB causes water flux into the cerebral tissue leading to the tissue swelling. To simulate this, the capillary filtration is no longer zero but has the form shown in Table 3.1.

Table 3.1: List of equations for the proposed model.

Equations	**Tissue Condition**	**Capillary Filtration, $\tilde{S}_{b\to w}$**
$0 = \tilde{\nabla}^2 u - \frac{2}{\tilde{r}^2}\tilde{u} - \frac{\partial \tilde{P}_w}{\partial \tilde{r}}$, $\frac{\partial \tilde{P}_w}{\partial \tilde{t}} = \tilde{\nabla}^2 \tilde{P}_w + \tilde{\dot{S}}_{b\to w}$.	Normal Tissue (Baseline)	$\tilde{\dot{S}}_{b\to w} = 0$
	Damage tissue (in the core zone)	$\tilde{\dot{S}}_{b\to w} = 2\bar{n}_b f\left[\left(\tilde{P}_b - \tilde{P}_w\right) - \sigma\tilde{\Pi}_b\right]$

3.3.2 Numerical Procedures

The boundary conditions are set both at the origin (zero flux in all variables) and at a far boundary, where the variables return to the baseline values, as given:

$$\frac{\partial}{\partial \tilde{r}}(\tilde{u}, \tilde{P}_w)\Big|_{\tilde{r}=0} = 0, \tag{3.31}$$

$$\tilde{u}(\tilde{R}, \tilde{t}) \to 0, \tag{3.32}$$

$$\tilde{P}_w(\tilde{R}, \tilde{t}) \to \tilde{\bar{P}} = 1. \tag{3.33}$$

Meanwhile, the initial conditions at $\tilde{t} = 0$ are as shown:

$$\tilde{u}(\tilde{r}, 0) = 0, \tag{3.34}$$

$$\tilde{P}_w(\tilde{r}, 0) = \tilde{\bar{P}} = 1, \tag{3.35}$$

where the initial pressure is assumed to be equal to its baseline value and the tissue initially has zero displacement. The initial temporal gradient of pressure is given by:

$$\frac{\partial \tilde{P}_w}{\partial \tilde{t}}\Big|_{\tilde{t}=0} = \bar{n}_b[(\tilde{P}_b - \sigma\tilde{\Pi}_b) - 1\,]. \tag{3.36}$$

A collapse front will exist at the points where the pressure is equal to a critical value given by:

$$\tilde{P}_c = 1 + \tilde{E}. \tag{3.37}$$

Once pressure has reached this critical value, the differential equation reduces to:

$$\frac{\partial \tilde{P}_c}{\partial \tilde{t}} = \tilde{\nabla}^2 \tilde{P}_c, \tag{3.38}$$

which is a linear diffusion equation. After pressure has reached its critical value, there is no further water leakage from the collapse vessels. The collapse process is assumed here to be irreversible.

The brain volume is about 1130 to 1260 cm^3 (Cosgrove et al., 2007), implying that the radius is somewhere around 65 to 67 mm, assuming that the brain is a perfect sphere. This means that the outer boundary is found in between 83.5 to 86 length units (LU). Hence, a maximum length range of $\tilde{R} = 100$ LU is chosen, representing the solid boundary of the skull. The core zone, $\tilde{r} = \tilde{r}_c$; the region of BBB breakdown, is initially set to be of radius 4 LU (3.116 mm), unless otherwise stated. In the other regions, capillary filtration is assumed to not occur to represent normal tissue. The eqns. (3.26) and (3.27) (or in the Table 3.1) are solved using a standard non-linear parabolic-elliptic partial differential equation (PDE) solver in MATLAB.

3.3.3 Model Parameters

The shear modulus G of cerebral tissue can be calculated from the value of tissue Young's modulus E_T and Poisson's ratio v from the relationship:

$$G = \frac{E_T}{2(1+v)}. \tag{3.39}$$

The value of E_T is not well known, thus is taken here from the case of hydrocephalic conditions, which are assumed to occur slowly and producing relatively larger E_T compared to those found during neurosurgical processes, which produce smaller values of E_T (Tully et al., 2011). Meanwhile, the value of v is taken from the rough estimate of (Drake et al., 1996).

Table 3.2: List of parameters and their baseline value for the proposed model.

Parameter	**Value**	**Reference(s)**
Poisson's ratio, v	0.35	(Drake et al., 1996)
Shear modulus, G	216.3 Pa	Calculated using $E_T = 584$ Pa (Taylor et al., 2004) and eqn. (3.39)
Permeability of blood, κ_b	1.0×10^{-10} m^2	(Tully et al., 2011)
Viscosity of blood, μ_b	3.6×10^{-3} Pa.s	(Su, 2011)
Biot parameter for blood network, α_b	1	(Tully et al., 2011)
Relative compressibility of blood, Q_b	669.0 Pa	Using eqn. (3.40), (3.41), and $K_b = 1.0 \times 10^{10}$ Pa (Masugata et al., 1998)
Permeability of water, κ_w	3.6×10^{-15} m^2	(Su, 2011)
Viscosity of water, μ_w	1.0×10^{-3} Pa.s	Value for water at 20 ˚C
Biot parameter for water network, α_w	1	(Tully et al., 2011)
Relative compressibility of water, Q_w	3244 Pa	Using eqn. (3.40), (3.41), $n_w = 0.8$ and $K_w = 2.2 \times 10^9$ Pa
Hydraulic permeability, L_p	2.9×10^{-9} m/s.cmH_2O or 3.0×10^{-11} m/s.Pa	(Su, 2011)
Reflection coefficient, σ	0.93	(Su, 2011)
Capillary osmotic pressure, Π_b	2445 Pa or 25 cmH_2O	(Su, 2011)
Blood pressure, $\bar{P}_b$	4389 Pa or 33 mmHg	(Lucas, 2013)
Baseline value of pressure, $\bar{P}$	1330 Pa or 10 mmHg	(Payne, 2006)
Typical capillary radius, R_c	5×10^{-6}m	(Cassot et al., 2006)
Capillary wall stiffness, E	864.5 Pa or 6.5 mmHg	(Baish et al., 1997)
Baseline value of blood volume fraction, $\bar{n}_b$	0.03	(Ito et al., 2001)

There are four parameters that represent the characteristics of the fluid networks. They are the permeability κ^a, viscosity μ^a, Biot parameter α^a, and relative compressibility Q^a. The first three parameter values are taken directly from literature, while the values of Q^a are calculated from (Bai, 1993; Zienkiewicz et al., 1990; Zienkiewicz et al., 1984):

$$\frac{1}{Q^a} = \frac{\alpha^a - n^a}{K^S} + \frac{n^a}{K^a}, \tag{3.40}$$

where K^S and K^a are the bulk moduli for the solid and fluid phases respectively. The tissue bulk modulus can be calculated from:

$$K^S = \frac{2G(1+v)}{3(1-2v)}. \tag{3.41}$$

The bulk modulus for blood is taken from (Masugata et al., 1998), where the blood is assumed slightly compressible. Other parameters are taken directly from literature as shown in Table 3.2.

The system of eqns. (3.26) and (3.27) is used to solve for interstitial pressure and tissue displacement. The function f, which represents the fraction of vessels that remain open at each point in space and time, is approximated here using a sigmoid function:

$$f = \frac{1}{2}\left(1 + \tanh\left(\frac{1 + \frac{\bar{P} - P_w}{E}}{\epsilon}\right)\right), \tag{3.42}$$

where the term $\epsilon = 0.01$ is a scaling factor. This is used to ensure that the value of f can be either one (vessels open) or zero (vessels close), but that there is a small transition between these two states in order to ensure numerical stability.

3.4 Results

Figure 3.2 shows the changes in tissue displacement and interstitial pressure with time and radius. The water pressure initially increases sharply and reaches the maximum pressure at about 2200 time units (TU) (1.3 days) after constant reperfusion. The maximum pressure is 1.198 pressure units (PU) (11.98 mmHg), which is below the critical pressure (1.65 PU or 16.5 mmHg). This indicates that the vessels do not collapse at the baseline conditions. Meanwhile, the tissue displacement increases slowly compared to the rise in the water pressure. The maximum tissue displacement is 0.240 displacement-

length units (DLU) (0.265 mm), which occurs at distance 8.8 LU (6.69 mm) at time 5000 TU. This suggests that the tissue spreads as the interstitial pressure increases due to water filtration, but that this occurs slowly.

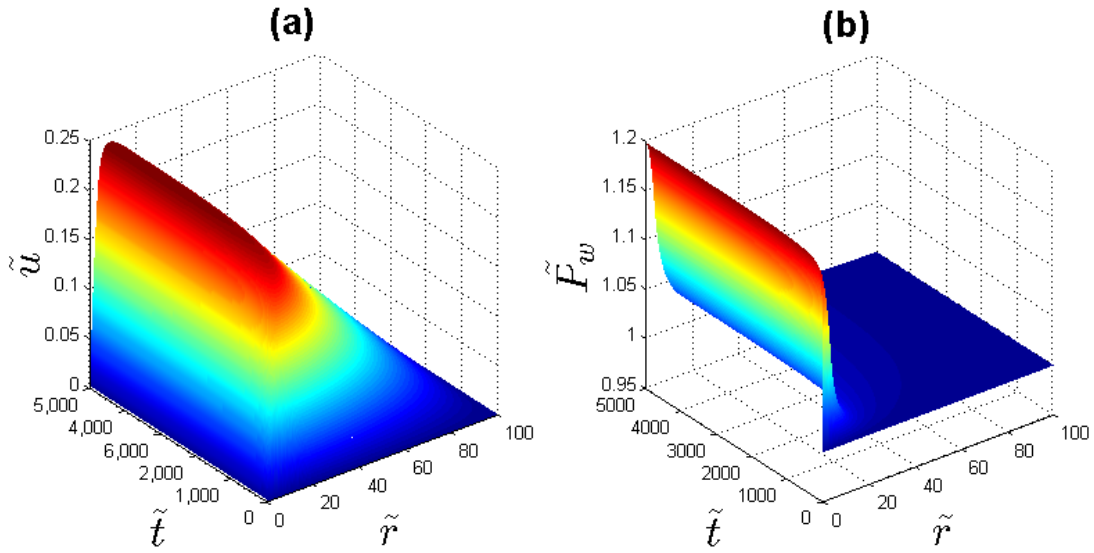

Figure 3.2: Time courses of vessel behaviour using baseline parameters values: (a) tissue displacement; (b) interstitial water pressure.

When $\tilde{r}_c$ is varied while other parameter values are set at baseline conditions, the results shown in Figure 3.3 are obtained. The pressure reaches a maximum value at 1.58 PU (15.80 mmHg), which is slightly below the critical value (16.50 mmHg), indicating that vessels will never collapse at the baseline conditions. The normal value of ICP is in the range 7 to 15 mmHg (Steiner et al., 2006). However, ICP values of more than 20 mmHg should be monitored as high ICP increases the chances of mortality (Balestreri et al., 2006). On the other hand, the tissue displacement increases, reaching a maximum value at about 7.5 DLU (8.288 mm) at core radius of about 50 LU (38.95 mm). The position of maximum displacement increases sharply at a core radius less than 5 LU (3.895 mm) but then increases almost linearly, reaching a maximum value of about 53 LU (41.29 mm).

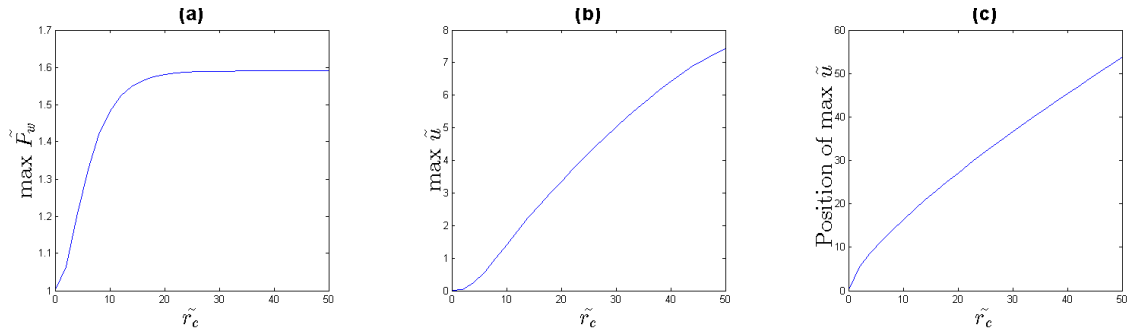

Figure 3.3: Vessel behaviour using baseline parameters values with varying core radius: (a) maximum pressure; (b) maximum displacement; (c) position of maximum displacement.

There are other parameters that will affect the behaviour of the model, the most important of which are the capillary stiffness E, blood pressure P_b, reflection coefficient σ and capillary osmotic pressure Π. The driving pressure, given by eqn. (3.36) must be positive to allow capillary filtration to occur. Hence, the ranges of blood pressure and osmotic pressure that will cause water flux into tissue space are $P_b > 27.10$ mmHg and $\Pi_b < 33.63$ cmH_2O, assuming baseline values for other variables.

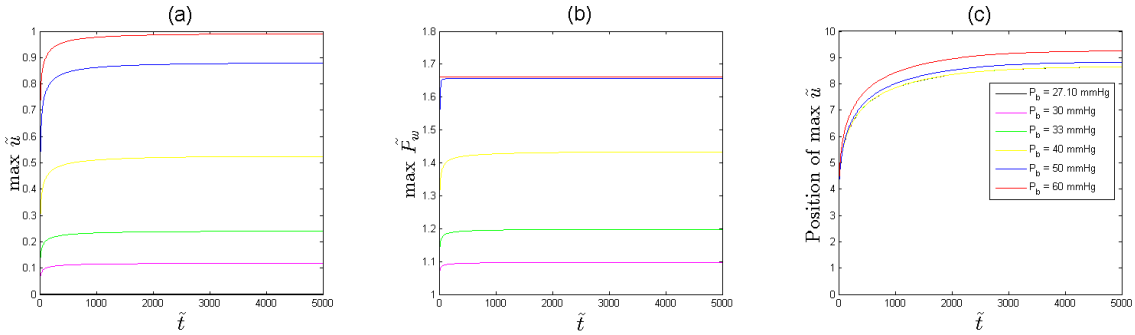

Figure 3.4: Time courses of vessel behaviour using baseline values with varying P_b: (a) maximum displacement; (b) maximum pressure; (c) position of maximum displacement.

Figure 3.4 shows the change in maximum displacement and its position and maximum pressure against time when P_b is varied. Maximum water pressure increases reaching a plateau when P_b increases. Collapse occurs for both $P_b = 50$ and 60 mmHg as shown in Figure 3.4(b). For $P_b = 50$ mmHg, the rise in water pressure to reach the critical value is slow, about 41 TU (0.6 hours) after reperfusion. Meanwhile, for $P_b = 60$ mmHg, the rise in water pressure is quick, taking about 6.5 TU (5.6 minutes) to reach the

critical pressure. The higher the reperfusion pressure, the faster the vessel collapse occurs. Furthermore, the maximum displacement also increases when P_b increases and reaches a maximum value of 0.99 DLU (1.094 mm) at $P_b = 60$ mmHg with the position of maximum displacement found at 9.26 LU (7.214 mm). Tissue is displaced as P_b increases to give space for the amount of water flux into the interstitial space. For other values of P_b that do not cause collapse, the position of maximum displacement shows similar values and trends. As P_b increases and the vessels start to collapse, the position of maximum displacement also starts to increase.

Figure 3.5 shows the results obtained when σ is varied while other parameters are kept at baseline values. The maximum displacement and maximum pressure both increase as σ decreases. When $\sigma = 0$, vessels collapse occurs and the time of collapse occurrence is about 39.3 TU (0.56 hours) after reperfusion. Zero σ means all protein plasma can filtrate through the capillary BBB and this decreases the osmotic pressure inside the interstitial space, which allows more water to flow into it. The maximum tissue displacement when $\sigma = 0$ is 0.8805 DLU (0.9730 mm) which occurs at 4.83 LU (3.763 mm) from the core radius. For the other values of σ, the position of maximum displacement is found to be roughly the same. Another interesting result is that at $\sigma = 1$, where there is a total blockage of protein plasma into the interstitial space, there is still an increase in tissue displacement and water pressure. This is due to the difference in blood and water pressures that causes water to filtrate into the interstitial space. However, a balance between too high and too low value of reperfusion pressure is important to avoid the risk of vessel collapse.

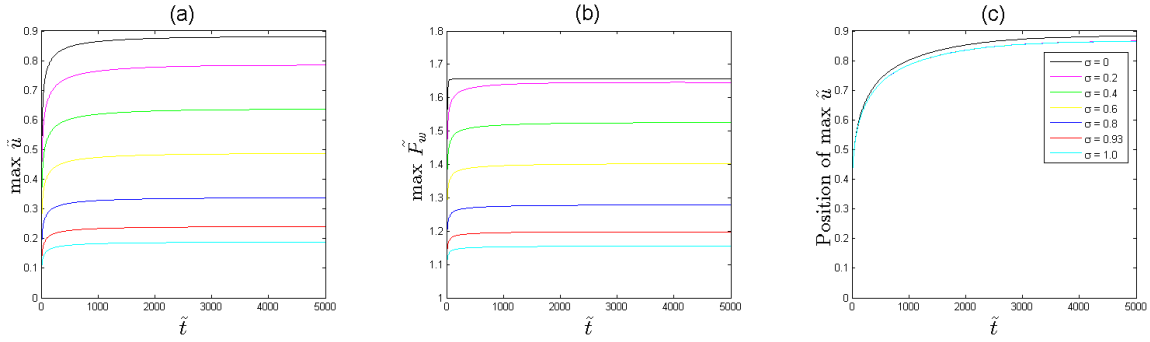

Figure 3.5: Time course of vessel behaviour using baseline values with varying σ: (a) maximum displacement; (b) maximum pressure; (c) position of maximum displacement.

The results for varying Π are as shown in Figure 3.6. The maximum displacement and maximum pressure both increase when Π decreases. Vessel collapse occurs when $\Pi = 0$, showing that water filtration occurs due to the difference in blood and water pressures only. The occurrence of vessel collapse is about 39.3 TU (0.56 hours) after reperfusion, similar to the results when $\sigma = 0$. The maximum displacement during collapse is the same as when $\sigma = 0$, i.e. 0.8805 DLU (0.9730 mm). The position of maximum displacement when $\Pi = 0$ is at 8.83 LU (6.879 mm), meanwhile for other values of Π, the position of maximum displacement is the same. Giving reperfusion containing a high concentration of protein plasma can provide a high Π value, but too high a value of Π can also cause vessel collapse.

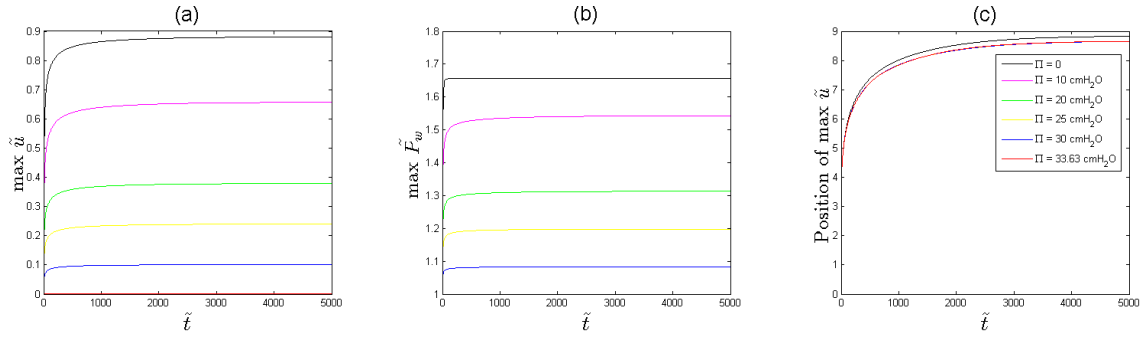

Figure 3.6: Time courses of vessel behaviour using baseline values with varying Π: (a) maximum displacement; (b) maximum pressure; (c) position of maximum displacement.

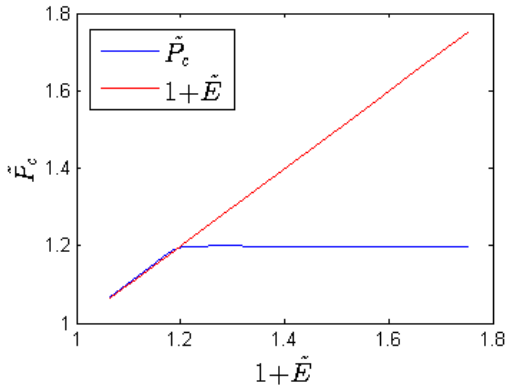

Figure 3.7: Relationship between critical pressure and capillary stiffness.

Figure 3.7 shows the critical pressure-capillary stiffness relationship obtained when E is varied while other parameters are kept at baseline conditions. Collapse will occur when water pressure reaches the critical value given by eqn. (3.37). In Figure 3.7, the minimum E before collapse occurs is estimated to be 0.1983 $\left(\tilde{E} = 1.1983 - 1\right)$ PU (263.74 Pa), as shown by the intersection between the two lines. Any capillaries with stiffness higher than this may have less chance to collapse. The maximum P_c reached when E is varied is 1.1993 PU (1595 Pa) and this remains constant for higher E values. From this result, it shows that having low capillary stiffness can cause vessel collapse.

3.5 Discussion

This section is divided into three subsections, namely: (1) Model Feature; which discusses the model assumptions and justification; (2) Clinical Significant; which discusses the results importance in clinical settings; and (3) Future Improvement; which discusses possible improvements on the model to increase the accuracy.

3.5.1 Model Features

The model proposed here has been used to predict the occurrence of vessel collapse when reperfusion is carried out for patients after ischemic stroke. A low value of hydraulic permeability of the normal BBB and cerebral blood flow (CBF) autoregulation

both maintain water flow into the interstitial space and hence regulate brain volume (Doczi, 1993). Hence, assuming that there is no net water flux through the BBB is reasonable because the water flow is tightly regulated. After an ischemic attack, BBB breakdown can occur and increase its permeability. The hydraulic permeability of the pathological BBB was estimated to be 10^{-9} m/s.cmH_2O (Li et al., 2010), which is about 100 times larger than normal (Hakamata et al., 1995). In this study, the hydraulic permeability used is 2.9×10^{-9} m/s.cmH_2O, taken from (Su, 2011). Meanwhile, the reflection coefficient σ in the model is taken specifically for protein plasma. It is assumed that the value of σ for ions is zero, which means that all ions can freely enter the interstitial space when BBB breakdown occurs. Both of the σ values are taken to be the same as the properties of peripheral capillaries because when the BBB breaks down, its properties are assumed to be the same as those in peripheral capillaries (Su, 2011).

A reduction in BBB permeability after ischemic attack causes water flux into the cerebral tissue space when reperfusion is applied. This is shown by the results where the interstitial pressure increases when the reperfusion pressure increases. This is also shown by cerebral tissue displacement, which reflects the occurrence of tissue swelling. The increase in both the tissue interstitial pressure and displacement causes capillaries to collapse. From the results shown here, it is found that vessel collapse occurs at high reperfusion pressure, low blood osmotic pressure, low BBB reflection coefficient and also at low capillary stiffness. It should be noted here that collapse is assumed to occur when the term f becomes zero. This term is an approximation of the integration in eqn. (3.4), assuming that all vessels have the same dimensions and mechanical properties. To investigate the effect of different vessels properties would require setting up a full integral for that equation. The effect of BBB breakdown on the mechanical properties of cerebral capillaries may also affect the collapse occurrence. There are no data available for

cerebral capillary stiffness and hence, an approximation is made by taking the capillary stiffness value from (Baish et al., 1997), which, it should be noted, was a study on tumour microcirculation.

3.5.2 Clinical Significant

This model is able to predict brain tissue swelling after ischaemia-reperfusion. It is also used to study the influence of cerebral tissue swelling on the formation of secondary ischaemia through microvessels compression. Accumulation of fluid in the tissue extracellular space will cause brain tissue swelling and the increase in the ICP (Donkin et al., 2010). The swollen brain tissue may result in the compression of cerebral microvessels, which may reduce the CBF and potentially lead to secondary ischaemia (Ames et al., 1968; Chiang et al., 1968; Miller et al., 1973).

From the results, it is predicted that there are several factors that can influence the occurrence of capillary vessels collapse during cerebral ischaemia-reperfusion. These are the blood reperfusion pressure (Figure 3.4), cerebral capillary permeability (represented by the reflection coefficient σ in Figure 3.5), blood reperfusion osmotic pressure or concentration (Figure 3.6), and cerebral capillary stiffness (Figure 3.7). The model predicted that vessel collapse can occur when: (1) a high value of reperfusion pressure ($P_b > 50$ mmHg) is given; (2) the reperfused blood is diluted, which increases the amount of water that can pass through the BBB into the tissue space; (3) a very low plasma protein reflection coefficient, which allows for easier entrance of plasma protein into the tissue extracellular space; and (4) when the cerebral capillary stiffness is low ($E < 263.74$ Pa), for example in elderly patients.

Brain tissue swelling is not the only factor that can result in the microvessels compression, but in fact, this is a multifactorial pathophysiology, which includes blood

factors such as blood viscosity, cardiovascular factors such as venous congestion (Hossmann, 1997), and activation of coagulation agents and leukocyte aggregation (del Zoppo et al., 2003). From the results of the model, microvessels compression can be avoided using reperfusion blood with low plasma protein and concentrated. An ischaemia-reperfusion therapeutic strategy known as blood conditioning (Pan et al., 2007) has been previously developed by filtering the arterial blood out of the patient to reduce the level of leukocyte and platelet to a level that can prevent the occurrence of secondary ischaemia through vessels endothelial depletion. The blood is then returned to the circulation through a catheter. Using a similar strategy, the blood may be made concentrated by reducing the amount of blood water content. Therefore, the model provides a general clinical guideline for a careful and thorough ischaemia-reperfusion treatment planning although these factors are not yet proven in any clinical studies.

3.5.3 Future Improvement

The model proposed here does not consider the contribution of local cerebral autoregulation, which may have an effect on controlling transmural pressure. Generally, cerebral autoregulation impairment occurs after stroke and its recovery may take up to 3 months (Aries et al., 2010). Impairment of local autoregulation in the infarcted region will likely intensify the reperfusion injury (Reinhard et al., 2012). However, it is still not very clear whether there is disruption to local cerebral autoregulation after ischemic stroke (Jordan et al., 2012). Including the dynamics of cerebral autoregulation in future may provide a better understanding of vessel collapse occurrence.

An assumption of the homogeneity of cerebral tissue is made here for the purpose of model simplification. In reality, the white matter possesses a higher tissue compliance than grey matter, which allows it to easily expand when water filtrates (Kimelberg, 2004).

Vasogenic oedema occurs most commonly in the white matter and this is due to the structural differences, where white matter is more homogeneous while grey matter is more twisted (Klatzo, 1987). In the study done by Kuroiwa et al. (1994), it was found that swelling of the white matter due to vasogenic oedema is anisotropic, which depends on the nerve fibres orientation (Kuroiwa et al., 1990). Incorporation of the anisotropy of white matter into the current model would be a worthwhile for further investigation (Basser, 1992; Shahim et al., 2010; Stoverud et al., 2012).

Another aspect worth studying is the vasogenic oedema resolution. The oedematous fluid will move out into the ventricles and subarachnoid spaces via glia limitans, into the capillary endothelium via the astrocytic foot or by metabolic degradation (Papadopoulos et al., 2004; Tourdias et al., 2011). The presence of aquaporin-4 (AQP4) channels in the glia limitans and astrocytic foot (Papadopoulos et al., 2004) facilitate the removal of the oedematous fluid. However, AQP4 also plays a role in the formation of cytotoxic oedema that causes intracellular swelling, which does not result in an increase in ICP and brain tissue swelling (Donkin et al., 2010). Modification of the current model through inclusion of the role of AQP4 might provide new insight towards the occurrence of reperfusion injury.

There are many other causes of the no-reflow phenomenon, including elevated blood viscosity (Fischer et al., 1979), oxidative stress (Aoki et al., 2002; Yang et al., 2011), leukocyte adhesion (Donkin et al., 2010; Huang et al., 2006) and post-ischemic hypotension (Hossmann, 1997). During ischemia, erythrocytes and platelets accumulate in the cerebral vessels, which will impede cerebral blood flow (Hossmann, 1997). In addition, restoration of oxygen after ischemia may create oxygen free radicals and initiate complex cascade activations of metalloproteinase (MMP) that will cause irreversible damage to the cerebral vessel endothelium (Yang et al., 2011). In a study done by del

Zoppo et al. (1991), within the first 4 hours of middle cerebral artery occlusion (MCAO), leukocytes were found to adhere to the cerebral vessels endothelium, which may also block the blood flow. Hence, extending the model by including the various factors described above will help in the understanding of the no-reflow phenomenon. However, this model is the first to describe the occurrence of reperfusion injury after ischemic stroke through the development of vasogenic oedema and vessel collapse.

3.6 Summary

The model proposed in this chapter has been used to study reperfusion after ischemic stroke in terms of the occurrence of the no-reflow phenomenon. A capillary filtration model was used to describe the influx of water from capillary vessels into the brain interstitial space. Poroelastic theory was used to describe the effect of water filtration on the formation of tissue swelling.

The increase in interstitial pressure and tissue swelling are hypothesized to cause vessel collapse. Vessel collapse is thought to cause the no-reflow phenomenon, which contributes to secondary ischemia. The model predicts that vessel collapse can occur at high value of reperfusion pressure, low blood osmotic pressure, high cerebral capillary permeability and low cerebral capillary stiffness. This model could be used to predict a suitable reperfusion pressure and to quantify the tissue swelling area in the cerebral tissue after reperfusion.

Chapter 4

The Study of the Function of Aquaporin-4 in Cerebral Ischaemia-Reperfusion Injury using Poroelastic Theory

---

The work presented in this chapter has appeared as **Mokhtarudin, M.J.M.** and Payne, S.J. (2015) "The study of the function of AQP4 in cerebral ischaemia-reperfusion injury using poroelastic theory", Paper presented at 4th International Conference on Computational & Mathematical Biomedical Engineering.

This work has also appeared in **Mokhtarudin, M.J.M.** and Payne, S.J. "The study of the function of AQP4 in cerebral ischemia-reperfusion injury using poroelastic theory" *International Journal for Numerical Methods in Biomedical Engineering*, doi: 10.1002/cnm.2784.

4.1 Introduction

In this chapter, the effect of aquaporin-4 (AQP4) in cerebral swelling after ischemia-reperfusion is studied. It is thought that AQP4 may play a role in both the formation and elimination of brain oedema. AQP4 is a water-transporting protein, which can be found in the brain at the following three locations: (1) in the subpial astrocyte processes between the subarachnoid cerebrospinal fluid (CSF) and the central nervous system (CNS); (2) in the perivascular astrocyte processes, which can be found at the blood-brain barrier (BBB); and (3) in the basolateral membrane of ependymal cells and subependymal astrocyte processes between the ventricle CNS-CSF interface (Papadopoulos et al., 2013). Many experiments have been done to study the expression of AQP4 during CNS-related diseases and its role in brain oedema, especially in ischaemic stroke. During early ischaemic stroke where cytotoxic oedema usually occurs,

deletion of AQP4 will slow down the rate of water flow into the brain, particularly into the astrocyte (Papadopoulos et al., 2007). If ischemia continues and the BBB starts to breakdown, water will filtrate into the extracellular space (ECS), causing vasogenic oedema. The absence of AQP4 at this stage of ischemia, however, may interfere with the elimination of oedematous fluid (Amiry-Moghaddam et al., 2003).

The model developed in Chapter 3 is now modified to incorporate the effect of AQP4 by assuming that the cerebral space is made up of four fluid compartments namely the astrocyte, neuron, ECS, and blood microvessels, with the brain tissue as the solid matrix. AQP4 are located in the astrocyte, which allows the movement of water between the astrocyte and the cerebral capillary and ECS, respectively. These will be modelled using the multiple-network poroelastic theory proposed by Tully et al. (2011).

4.2 Modification of Previous Model[2]

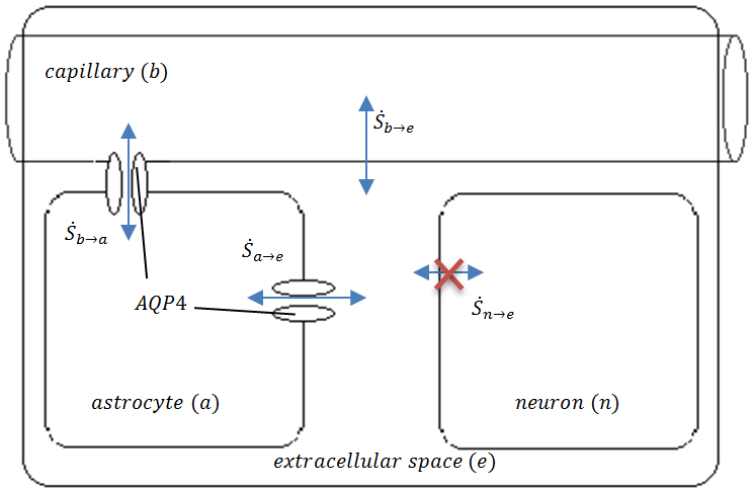

Figure 4.1: Locations of AQP4 in the astrocyte which allows water transfer between astrocyte and capillary and ECS, respectively.

After persistent ischaemia, the BBB starts to break down and this may cause filtration of proteins and ions from the reperfused blood. The filtration may create a

[2] Readers who are not interested in the full derivation of the model can skip the sections 4.2.1 till 4.2.3 and go straight to section 4.3 for the model summary.

pressure gradient that causes water accumulation into the ECS. In the previous model, the cerebral space was assumed to be made of two fluid compartments, namely the ECS and the capillary vessels with the brain tissue as the solid matrix, and this was modelled using poroelastic theory. Here, the model is slightly modified to include two more fluid compartments as proposed by Cloutier et al. (2009), these being the astrocytes and neurons. Water transfer is only allowed between the extracellular fluid into the astrocyte via parenchymal AQP4, between the capillary into the astrocyte via perivascular AQP4 and also via capillary filtration into the ECS due to the BBB breakdown, these being represented by $\dot{S}_{a\to e}$, $\dot{S}_{b\to a}$, and $\dot{S}_{b\to e}$, respectively. Meanwhile, the net water transfer into the neuron, $\dot{S}_{n\to e}$ is assumed to be zero since it has no AQP4 embedded to it. Figure 4.1 shows a schematic of these processes.

4.2.1 Multiporosity Network Model

In this model, there are five phases involved which are the brain tissue and four fluid phases: blood, ECS, astrocyte and neuron. The various phases and the fluid transfers between them can be described using multiple-network poroelastic theory. These compartments are denoted as a, n, b, and e for the astrocyte, neuron, capillary vessels and ECS, respectively. Assuming one-dimensional spherical symmetry, the system of equations of the processes can be written fully as:

$$\nabla^2 u - \frac{2}{r^2}u = \frac{1-2v}{2G(1-v)}\left(\alpha_e \frac{\partial P_e}{\partial r} + \alpha_a \frac{\partial P_a}{\partial r} + \alpha_n \frac{\partial P_n}{\partial r} + \alpha_b \frac{\partial P_b}{\partial r}\right), \tag{4.1}$$

$$\frac{1}{Q_e}\frac{\partial P_e}{\partial t} = k_e \nabla^2 P_e + \dot{S}_{b\to e} + \dot{S}_{a\to e} + \dot{S}_{n\to e}, \tag{4.2}$$

$$\frac{1}{Q_a}\frac{\partial P_a}{\partial t} = k_a \nabla^2 P_a - \dot{S}_{a\to e} + \dot{S}_{b\to a}, \tag{4.3}$$

$$\frac{1}{Q_n}\frac{\partial P_n}{\partial t} = k_n \nabla^2 P_n - \dot{S}_{n\to e}, \tag{4.4}$$

$$\frac{1}{Q_b}\frac{\partial P_b}{\partial t} = k_b \nabla^2 P_b - \dot{S}_{b\to e} - \dot{S}_{b\to a}, \tag{4.5}$$

The terms P, α, Q, and k represent the hydrostatic pressure, Biot constant, relative compressibility and permeability for the fluid phases, respectively; meanwhile the terms u, v and G represent the tissue displacement, Poisson's ratio and shear modulus of the brain tissue respectively.

In addition, using previous results obtained in Chapter 3 regarding the homogeneity of blood pressure throughout the space, the system of equations can be reduced to:

$$0 = \nabla^2 u - \frac{2}{r^2}u - \frac{1-2v}{2G(1-v)}\left(\alpha_e \frac{\partial P_e}{\partial r} + \alpha_a \frac{\partial P_a}{\partial r} + \alpha_n \frac{\partial P_n}{\partial r}\right), \tag{4.6}$$

$$\frac{1}{Q_e}\frac{\partial P_e}{\partial t} = k_e \nabla^2 P_e + \dot{S}_{b\to e} + \dot{S}_{a\to e}, \tag{4.7}$$

$$\frac{1}{Q_a}\frac{\partial P_a}{\partial t} = k_a \nabla^2 P_a - \dot{S}_{a\to e} + \dot{S}_{b\to a}, \tag{4.8}$$

$$\frac{1}{Q_n}\frac{\partial P_n}{\partial t} = k_n \nabla^2 P_n. \tag{4.9}$$

4.2.2 Water Transfer between Compartments

The water from the capillary is transferred either into the astrocyte via perivascular AQP4 or into the ECS via filtration after BBB breakdown. The water flow into the ECS by capillary filtration due to the BBB breakdown, which has been described in Chapter 3, is given by:

$$\dot{S}_{b\to e} = 2\bar{n}_b \frac{L_p}{R_c}\left(\frac{L_e}{L_c}\right) f[(P_b - P_e) - \sigma \Pi_b\,], \tag{4.10}$$

which has a slight modification to include an additional term, $\frac{L_e}{L_c}$, to represent the ratio of the surface area of the capillary that is in contact with the ECS. The terms $\bar{n}_b$, L_p, R_c, σ, and Π_b are the baseline volume fraction of blood, hydraulic permeability, radius of capillary, reflection coefficient and osmotic pressure of the capillary, respectively.

Meanwhile, the term f represents the fraction of vessels that remain open at each point of space and time, which is approximated by a sigmoid function

Meanwhile, the water transfer from the capillary into the astrocyte via AQP4 can be derived using a similar fashion as used in deriving the capillary filtration above, given by:

$$\dot{S}_{b\to a} = \frac{2\bar{n}_b}{R_c}\left(\frac{L_a}{L_c}\right) f {J_{VA}}^{b\to a}, \tag{4.11}$$

where the term $\frac{L_a}{L_c}$ is the ratio of the surface area of capillary that make contact with the astrocyte endfoot. The term ${J_{VA}}^{b\to a}$ is the water flux from the capillary into the astrocyte via perivascular AQP4, which is given by the difference between the hydrostatic and osmotic pressure gradients as:

$${J_{VA}}^{b\to a} = F n_{AQP4b}[P_b - P_a - (\Pi_b - \Pi_a)\,], \tag{4.12}$$

where $F = \frac{M}{RT} k_{AQP4}$ is the hydraulic permeability through AQP4 (Jiang et al., 2013), with M the molar volume of water, RT the product of gas constant and body temperature, and k_{AQP4} is the permeability rate through AQP4 into the astrocyte. Meanwhile, the term Π_a is the osmotic pressure in the astrocyte and n_{AQP4b} represents the fraction of AQP4 present in the astrocyte that makes connection with the capillary. Substituting eqn. (4.12) in to (4.11) gives:

$$\dot{S}_{b\to a} = 2 n_{AQP4b} \bar{n}_b \frac{F}{R_c}\left(\frac{L_a}{L_c}\right) f[P_b - P_a - (\Pi_b - \Pi_a)\,], \tag{4.13}$$

The water transfer through parenchymal AQP4 can be described by the total water flux from astrocyte into ECS, ${J_{VA}}^{a\to e}$, through the deformed astrocyte surface area, A_a, as shown below:

$$\dot{S}_{a\to e} = \left(\frac{dN_a}{\mathrm{dV}}\right) {J_{VA}}^{a\to e} A_a, \tag{4.14}$$

where $\frac{dN_a}{dV}$ represents the number of astrocyte N_a in a given volume V. The term ${J_{VA}}^{a\to e}$ has a similar form to eqn. (4.12), which is given by:

$${J_{VA}}^{a\to e} = F n_{AQP4e}[P_a - P_e - (\Pi_a - \Pi_e)\,], \tag{4.15}$$

with the term n_{AQP4e} here representing the fraction of parenchymal AQP4 present in the astrocyte and Π_e the osmotic pressure of the ECS.

The initial and deformed surface areas of the astrocyte can be related using the constitutive law of a spherical cell as proposed by (Jiang et al., 2013) as shown below:

$$P_a - P_e = \frac{E_a}{2}\left(\frac{A_a}{\bar{A}_a} - 1\right), \tag{4.16}$$

which relates the pressure difference between the astrocyte and the ECS with the change in the surface areas. The terms E_a and $\bar{A}_a$ are the elastic modulus and initial surface area of the astrocyte, respectively. Meanwhile, the baseline volume fraction of astrocyte is:

$$\bar{n}_a = \frac{d(N_a V_a)}{dV}, \tag{4.17}$$

where V_a is the volume of the astrocyte. Substituting eqns. (4.15) to (4.17) into (4.14) gives:

$$\dot{S}_{a\to e} = F n_{AQP4e}\left(\frac{\bar{A}_a \bar{n}_a}{V_a}\right)\left[\frac{2}{E_a}(P_a - P_e) + 1\right][P_a - P_e - (\Pi_a - \Pi_e)\,]. \tag{4.18}$$

4.2.3 Non-dimensionalisation

The system of equations (4.6) to (4.9) can be written in full to include the water transfer equations as shown:

$$0 = \nabla^2 u - \frac{2}{r^2}u - \frac{1-2v}{2G(1-v)}\left(\alpha_e \frac{\partial P_e}{\partial r} + \alpha_a \frac{\partial P_a}{\partial r} + \alpha_n \frac{\partial P_n}{\partial r}\right), \tag{4.19}$$

$$\frac{1}{Q_e}\frac{\partial P_e}{\partial t} = k_e\nabla^2 P_e + 2\bar{n}_b\frac{L_p}{R_c}\left(\frac{L_e}{L_c}\right)f[(P_b - P_e) - \sigma\Pi_b\,] + Fn_{AQP4e}\left(\frac{\bar{A}_a\bar{n}_a}{V_a}\right)\left[\frac{2}{E_a}(P_a - P_e) + 1\right][P_a - P_e - (\Pi_a - \Pi_e)\,], \tag{4.20}$$

$$\frac{1}{Q_a}\frac{\partial P_a}{\partial t} = k_a\nabla^2 P_a - Fn_{AQP4e}\left(\frac{\bar{A}_a\bar{n}_a}{V_a}\right)\left[\frac{2}{E_a}(P_a - P_e) + 1\right][P_a - P_e - (\Pi_a - \Pi_e)\,] + 2n_{AQP4b}\bar{n}_b\frac{F}{R_c}\left(\frac{L_a}{L_c}\right)f[P_b - P_a - (\Pi_b - \Pi_a)\,], \tag{4.21}$$

$$\frac{1}{Q_n}\frac{\partial P_n}{\partial t} = k_n\nabla^2 P_n. \tag{4.22}$$

The permeability of the fluid in the astrocyte, neuron and ECS are taken to be the same, assuming that each compartment is made up mainly of water. Hence, $k_a = k_n = k_e = k_w = \frac{\kappa_w}{\mu_w}$, in which $\kappa_w = 3.6 \times 10^{-15}$ m^2 and $\mu_w = 1.0 \times 10^{-3}$ Pa s are the permeability and viscosity of water, respectively.

Also, by letting the characteristic lengths for the tissue displacement u and distance r to be L_u and L respectively, the baseline value for all the pressures $\bar{P}$, and the characteristic time T, the above equations can be non-dimensionalised as shown by equations below. Here, the tilde (~) symbol is used to represent the non-dimensionalised variables.

$$\tilde{\nabla}^2\tilde{u} - \frac{2}{\tilde{r}^2}\tilde{u} = \left(\frac{L\bar{P}}{L_u}\frac{1-2v}{2G(1-v)}\right)\left(\alpha_e\frac{\partial\tilde{P}_e}{\partial\tilde{r}} + \alpha_a\frac{\partial\tilde{P}_a}{\partial\tilde{r}} + \alpha_n\frac{\partial\tilde{P}_n}{\partial\tilde{r}}\right), \tag{4.23}$$

$$\frac{L^2}{Q_e T k_e}\frac{\partial\tilde{P}_e}{\partial\tilde{t}} = \tilde{\nabla}^2\tilde{P}_e + 2\bar{n}_b f\left(\frac{L^2}{k_e}\frac{L_p}{R_c}\right)\left(\frac{L_e}{L_c}\right)\left[\left(\tilde{P}_b - \tilde{P}_e\right) - \sigma\tilde{\Pi}_b\,\right] + n_{AQP4e}\left(\frac{L^2F}{k_e}\frac{\bar{A}_a\bar{n}_a}{V_a}\right)\left[\frac{2}{E_a}(P_a - P_e) + 1\right]\left[\tilde{P}_a - \tilde{P}_e - \left(\tilde{\Pi}_a - \tilde{\Pi}_e\right)\,\right], \tag{4.24}$$

$$\frac{L^2}{Q_a T k_e}\frac{\partial\tilde{P}_a}{\partial\tilde{t}} = \tilde{\nabla}^2\tilde{P}_a - n_{AQP4e}\left(\frac{L^2F}{k_e}\frac{\bar{A}_a\bar{n}_a}{V_a}\right)\left[\frac{2}{E_a}(P_a - P_e) + 1\right] \cdot\left[\tilde{P}_a - \tilde{P}_e - \left(\tilde{\Pi}_a - \tilde{\Pi}_e\right)\,\right] + 2n_{AQP4b}\bar{n}_b f\left(\frac{L^2}{k_e}\frac{\mathrm{F}}{R_c}\right)\left(\frac{L_a}{L_c}\right)\left[\tilde{P}_b - \tilde{P}_a - \left(\tilde{\Pi}_b - \tilde{\Pi}_a\right)\,\right], \tag{4.25}$$

$$\frac{L^2}{Q_n T k_e}\frac{\partial\tilde{P}_n}{\partial\tilde{t}} = \tilde{\nabla}^2\tilde{P}_n. \tag{4.26}$$

The coefficients in the round bracket of eqns. (4.24) and (4.25) could be used to determine the characteristic length by setting them to be equal to one. However, the characteristic length for the distance r is chosen here to be:

$$L = \sqrt{\frac{R_c k_e}{L_p}}, \tag{4.27}$$

in which $R_c = 5.0 \times 10^{-6}$ m and $L_p = 3.0 \times 10^{-11}$ m/s Pa , giving a value of 0.779 mm, which is reasonable for brain tissue. Setting the coefficient in the bracket on the right-hand side of eqn. (4.23) equal to one, the characteristic length for displacement u is given by:

$$L_u = \frac{\bar{P}(1-2v)}{2G(1-v)} L. \tag{4.28}$$

which has the value of 1.105 mm when setting $\bar{P} = 1330$ Pa, $G = 216.3$ Pa and $v = 0.35$. Meanwhile, the characteristic time is chosen to be:

$$T = \frac{L^2}{K^s k_e} \tag{4.29}$$

by setting the coefficient of the time derivative of pressures in eqns. (4.24), (4.25), and (4.26) equal to one and using the fact that the relative compressibility Q of each fluid has different values but is directly proportional to the bulk modulus of the tissue, K^s (Zienkiewicz et al., 1984). This will give the value of the characteristic time to be 260 s, which is about 5 times higher than that obtained in Chapter 3.

4.3 Model Summary

The equations used to describe the model proposed here are as listed in the Table 4.1.In the normal tissue, two assumptions are considered: (1) the BBB remains intact; hence no capillary filtration can occur. Thus, $\tilde{\dot{S}}_{b\to e} = 0$; and (2) the net water movement through AQP4 is assumed zero, i.e. $\tilde{\dot{S}}_{a\to e} = \tilde{\dot{S}}_{b\to a} = 0$. Therefore, in this case, the ECS,

the astrocyte, and the neuron pressures would remain at the baseline pressure value of the ICP, $\tilde{\bar{P}} = 1$.

Meanwhile, in the damaged tissue, these assumptions are no longer valid. The capillary filtration and water movement through AQP4 terms are now not equal to zero but have the forms as shown in Table 4.1.

Table 4.1: List of equations for the proposed AQP4 model.

Equations	**Tissue Condition**	**Water movement terms**
$\tilde{\nabla}^2\tilde{u} - \frac{2}{\tilde{r}^2}\tilde{u} = \left(\frac{L\bar{P}}{L_u}\frac{1-2v}{2G(1-v)}\right) \cdot \left(\alpha_e\frac{\partial\tilde{P}_e}{\partial\tilde{r}} + \alpha_a\frac{\partial\tilde{P}_a}{\partial\tilde{r}} + \alpha_n\frac{\partial\tilde{P}_n}{\partial\tilde{r}}\right)$, $\frac{1}{Q_e}\frac{\partial\tilde{P}_e}{\partial\tilde{t}} = \tilde{\nabla}^2\tilde{P}_e + \tilde{\dot{S}}_{b\to e} + \tilde{\dot{S}}_{a\to e}$, $\frac{1}{Q_a}\frac{\partial\tilde{P}_a}{\partial\tilde{t}} = \tilde{\nabla}^2\tilde{P}_a - \tilde{\dot{S}}_{a\to e} + \tilde{\dot{S}}_{b\to a}$, $\frac{1}{Q_n}\frac{\partial\tilde{P}_n}{\partial\tilde{t}} = \tilde{\nabla}^2\tilde{P}_n$.	Normal Tissue (Baseline)	$\tilde{\dot{S}}_{b\to e} = \tilde{\dot{S}}_{a\to e} = \tilde{\dot{S}}_{b\to a} = 0$
	Infarct (in the core zone)	$\tilde{\dot{S}}_{b\to e} = 2\bar{n}_b f\left(\frac{L_e}{L_c}\right)\left[(\tilde{P}_b - \tilde{P}_e) - \sigma\tilde{\Pi}_b\right]$, $\tilde{\dot{S}}_{a\to e} = n_{AQP4e}\left(\frac{R_c F}{L_p}\frac{\bar{A}_a\bar{n}_a}{V_a}\right)\left[\frac{2}{E_a}(P_a - P_e) + 1\right] \cdot \left[\tilde{P}_a - \tilde{P}_e - (\tilde{\Pi}_a - \tilde{\Pi}_e)\right]$, $\tilde{\dot{S}}_{b\to a} = 2n_{AQP4b}\bar{n}_b f\left(\frac{\mathrm{F}}{L_p}\right)\left(\frac{L_a}{L_c}\right) \cdot \left[\tilde{P}_b - \tilde{P}_a - (\tilde{\Pi}_b - \tilde{\Pi}_a)\right]$.

4.4 Numerical Procedures

The initial conditions for all variables are as shown:

$$\tilde{u}(\tilde{r}, 0) = 0, \tag{4.30}$$

$$\tilde{P}_e(\tilde{r}, 0) = 1, \tag{4.31}$$

$$\tilde{P}_a(\tilde{r}, 0) = 1, \tag{4.32}$$

$$\tilde{P}_n(\tilde{r}, 0) = 1, \tag{4.33}$$

where the initial pressure of ECS is assumed to be equal to the baseline value of intracranial pressure (ICP), $\bar{P}$ and the tissue is initially stationary. Further, the initial volumes of the astrocyte and neuron are assumed to be maintained, meaning that the intercellular and extracellular pressures are initially the same. Hence the initial pressures for both of them are also equal to the baseline value. Meanwhile, boundary conditions at

the origin are set so that the flux is zero in all variables, with all variables returning to baseline values at a far boundary $\tilde{R}$, as given by:

$$\frac{\partial}{\partial \tilde{r}}\left(\tilde{u}, \tilde{P}_e, \tilde{P}_a, \tilde{P}_n\right)\Big|_{\tilde{r}=0} = 0 \tag{4.34}$$

$$\tilde{u}(\widetilde{R}, \tilde{t}) \to 0, \tag{4.35}$$

$$\widetilde{P}_e(\widetilde{R}, \tilde{t}) \to 1, \tag{4.36}$$

$$\widetilde{P}_a(\widetilde{R}, \tilde{t}) \to 1, \tag{4.37}$$

$$\widetilde{P}_n(\widetilde{R}, \tilde{t}) \to 1, \tag{4.38}$$

The maximum length range, $\tilde{R} = 100$ length unit (LU) (77.9 mm) is used to represent the skull radius. The system of eqns. (4.23) to (4.26) is solved using the built-in MATLAB solver for a 1D parabolic-elliptic PDE. Throughout the 1D analysis, a core radius $\tilde{r}_c = 8$ LU (6.232 mm) will be used to represent the radius of cerebral tissue affected by ischaemia, unless otherwise stated.

4.5 Model Parameters

The system of eqns. (4.23) to (4.26) introduces many additional parameters on top of those introduced in Chapter 3 and these are as listed in Table 4.2. Some parameters are taken from estimations. For instance, the Biot parameter should have a value in the range of $n^a \leq \alpha^a \leq 1$, where n^a is the porosity of the fluid network a (Biot et al., 1957). This parameter indicates how the change in the fluid pressure is transferred to the solid phase, with a value smaller than one meaning that the fluid is not able to compensate with the load exerted on it and is transferred to the solid phase. The values of α^a are all taken to be equal to 1, similar to the work done by Tully et al. (2011). In their studies, the values of α^a for the blood networks for healthy brain condition in a multiple network poroelastic model were estimated by replicating the results of a single network poroelastic model (Tully et al., 2009). However, to use the model developed here to replicate the result of a

single network poroelastic model as previously done is not possible because of the earlier assumption of the volume fraction of water in ECS, $n_w = 0.8$, which is different from the current assumption of $\bar{n}_e = 0.2$.

Table 4.2: List of additional parameters for the modified model.

Parameter	**Value**	**Reference(s)**
Molar volume of liquid water, M	18.02×10^{-6} m^3/mol	Standard value for water
Gas constant and temperature, RT	2577.3 J/mol	Physical constant
Ratio of surface area of capillary surrounded by astrocyte, $\frac{L_a}{L_c}$	0.80	(Janzer, 1993)
Initial surface area of the astrocyte, $\bar{A}_a$	2.5×10^{-9} m^2	(Williams et al., 1980)
Volume of astrocyte, V_a	5.7×10^{-16} m^3	(Williams et al., 1980)
Astrocyte permeability through aquaporin-4, k_{AQP4}	5.0×10^{-4} m/s	(Solenov et al., 2003)
Volume fraction of astrocyte, $\bar{n}_a$	0.25	(Cloutier et al., 2009)
Biot parameter for astrocyte, α_a	1	(Tully et al., 2011)
Elasticity of the surface layer of astrocyte, E_a	40 kPa	(Yamane et al., 2000)
Baseline ion concentration of astrocyte, $[S_c]_a$	301.0 mM	(Orlowski et al., 2013)
Volume fraction of ECS, $\bar{n}_e$	0.20	(Cloutier et al., 2009)
Baseline ion concentration of ECS, $[S_c]_e$	296.0 mM	(Orlowski et al., 2013)
Volume fraction of neuron, $\bar{n}_n$	0.45	(Cloutier et al., 2009)
Biot parameter for neuron, α_n	1	(Tully et al., 2011)

Other parameters estimated are the baseline ion concentrations of astrocyte and ECS, which are used to determine the osmotic pressure for the astrocytes and ECS:

$$\Pi_m = RT \sum_{c=1}^{C} [S_c]_m, \tag{4.39}$$

where the terms $[S_c]_m$ are the ionic concentrations in each of the fluid compartments m, with $c = 1, \dots, C$, being the ions that were considered in the determination of the osmotic pressure. These include Na^+, K^+, Ca^{2+}, Cl^-, $HCO_3{}^-$, and other non-permeable anions in the intracellular space. The values for the ionic concentration in astrocytes and the ECS are taken from the calculation done by Orlowski et al. (2013).

4.6 Results

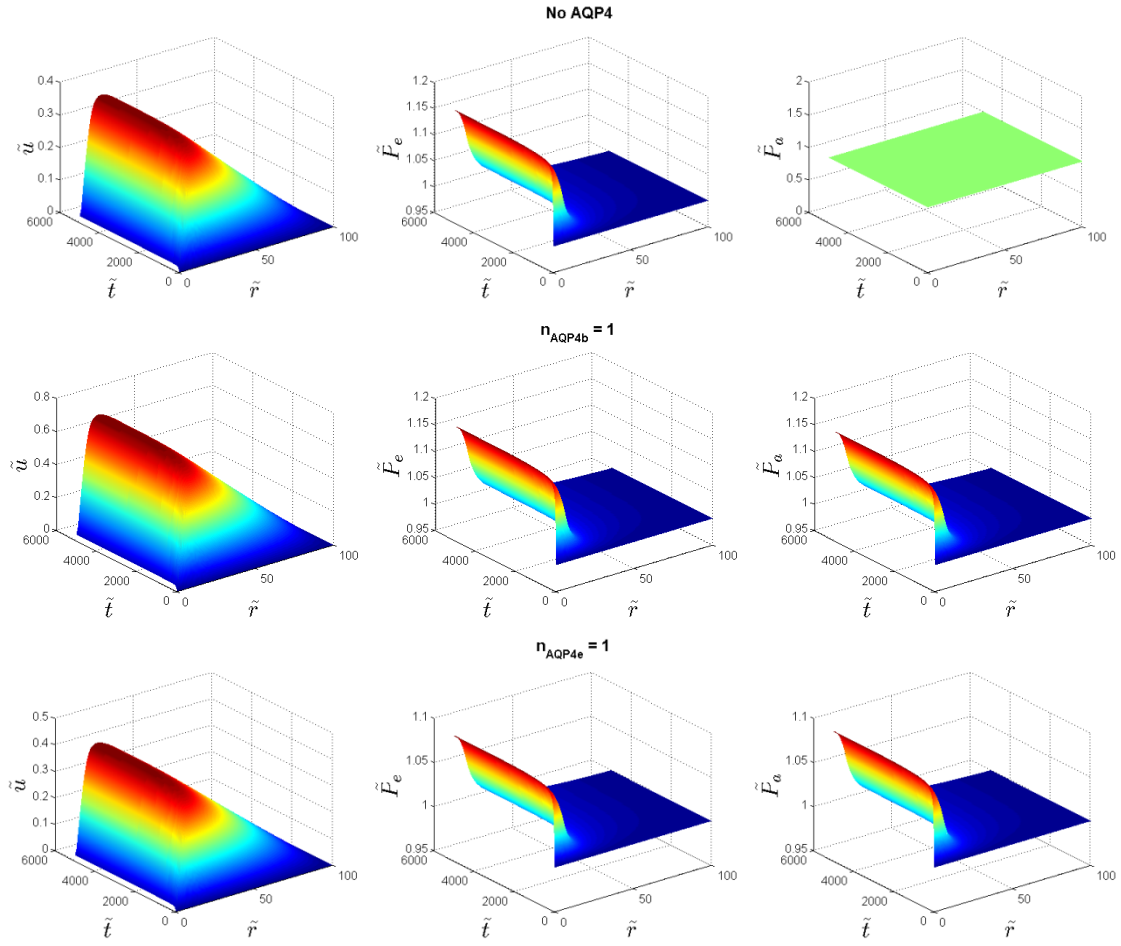

Figure 4.2: Time varying behaviour of the tissue under baseline parameters values with three different AQP4 ratio: (Top) No AQP4; (Middle) $n_{AQP4b} = 1$; (Bottom) $n_{AQP4e} = 1$.

Figure 4.2 shows the changes in the tissue displacements and fluid pressures for three different AQP4 conditions, which are: (1) only perivascular AQP4 present, (2) only parenchymal AQP4, and (3) neither perivascular nor parenchymal AQP4 are present. When there is no AQP4 present, the astrocyte pressure remains at baseline value because there is no path that allows water to come into it and it is already assumed that the net flow of water through the membrane of astrocyte is zero. Meanwhile, the ECS pressure and tissue displacement are at 1.16 pressure units (PU) and 0.373 displacement-length units (DLU), respectively. When only perivascular AQP4 is present, the ECS pressure remains at 1.16 PU while both the astrocyte pressure and tissue displacement increase.

This is because the water is transferred from reperfused blood into both of the fluid compartments causing a combined effect towards an increase in tissue displacement. However, when only parenchymal AQP4 is present, part of the ECS water is transferred into the astrocyte, causing both the astrocyte pressure and tissue displacement to increase. This is, again, due to the combined effect of the pressure increment in both compartments.

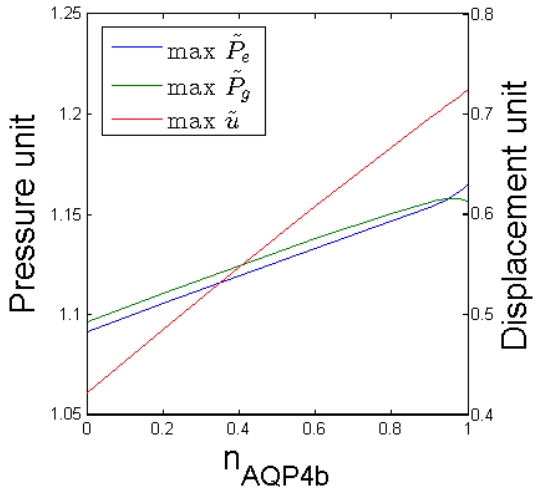

Figure 4.3: Tissue behaviour with varying n_{AQP4b}. The left and right vertical axes represent the pressure and displacement values, respectively.

The behaviour of the fluid compartmental pressures and tissue displacement with varying perivascular AQP4 ratio n_{AQP4b} can be viewed more clearly, as shown in Figure 4.3. As n_{AQP4b} decreases approaching zero, $\tilde{P}_e$ decreases and at the same time, the tissue displacement also decreases. This is because part of the pressure is transferred into the astrocyte by the movement of water via AQP4, thus reducing the vasogenic oedema and ICP. However, this is compensated for by the increase in astrocyte pressure which may cause the astrocyte to swell. Meanwhile, when the value of n_{AQP4b} increases, approaching one, less water will be transferred between the ECS and the astrocyte and most of the water transfer into these two compartments will only come from the reperfused blood in the capillary. In addition, the tissue displacement also increases with increased

perivascular AQP4 due to the combined effect of the pressure build up in both of the fluid compartments.

Figure 4.4 shows the variation of fluid pressures and tissue displacement with the ischaemic core radius for n_{AQP4b} ratios of 0, 0.25, 0.5, 0.75 and 1. At very small core radius values of about 0 to 10 LU, the fluid pressures and tissue displacement have approximately the same values for any AQP4 ratios. However, for a larger core radius, the variations in ECS pressure, astrocyte pressure and tissue displacement with AQP4 ratios is approximately 3.3%, 5.1% and 25.0%, respectively. One exception is for the result of the fluid pressures when only perivascular AQP4 is present. For instance, in the case of ECS pressure, the value is higher for a core radius less than 25 LU compared to the results when there is a certain amount of parenchymal AQP4. For the case of a core radius larger than 25 LU, the ECS pressure reaches almost a constant value of 1.55 PU. Meanwhile, for the case of astrocyte pressure variation with core radius when only perivascular AQP4 is present, the pressure increases almost linearly with increasing core radius before slowly reaching a constant value. The different variations of both of these fluid pressures at $n_{AQP4b} = 1$ compared to other n_{AQP4b} values are probably because they depend solely on the reperfused blood properties.

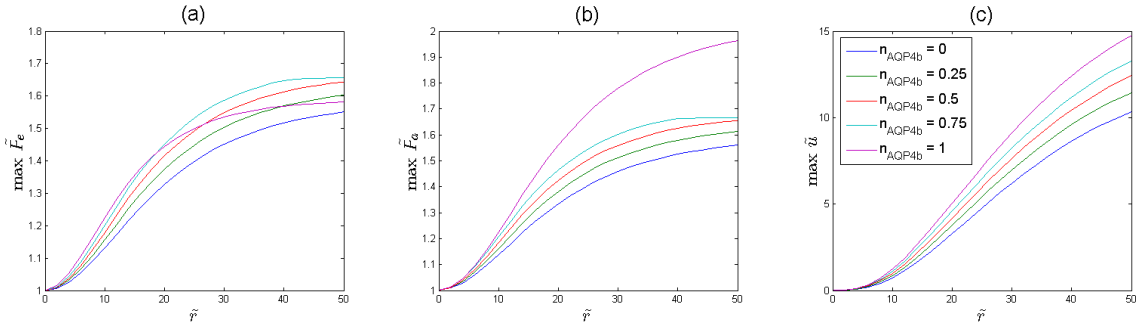

Figure 4.4: Tissue behaviour with varying core radius for 5 different n_{AQP4b} ratios: (a) ECS pressure; (b) astrocyte pressure; and (c) tissue displacement.

Figure 4.5 below shows the behaviour of the fluid pressures and tissue displacement when the ionic concentration of the astrocyte $[S]_a$ is varied from the baseline value. From the result, it can be seen that an increase of $[S]_a$ causes the astrocyte pressure and tissue displacement to increase but not the ECS pressure. For a change of 100 mM in $[S]_a$, the ECS pressure, astrocyte pressure and tissue displacement change by approximately 7.5%, 10.9% and 16.7% respectively.

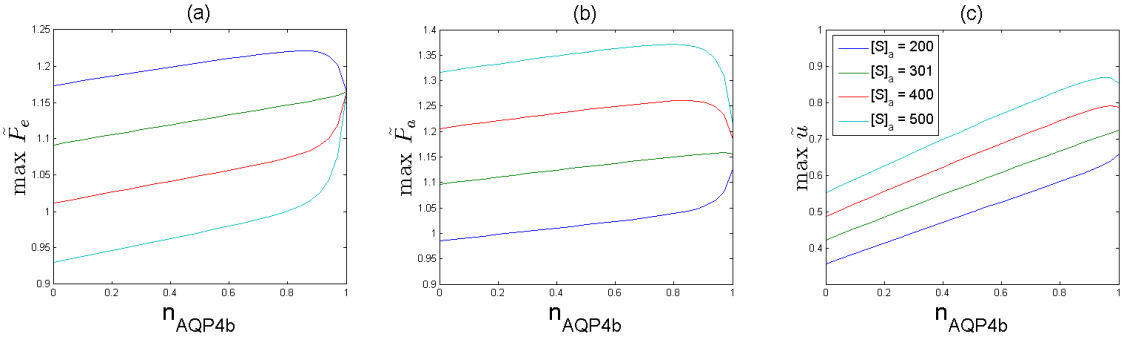

Figure 4.5: Tissue behaviour with varying n_{AQP4b} for 5 different ionic concentrations of astrocyte, $[S]_a$: (a) ECS pressure; (b) astrocyte pressure; and (c) tissue displacement. The unit of the concentrations are in mM.

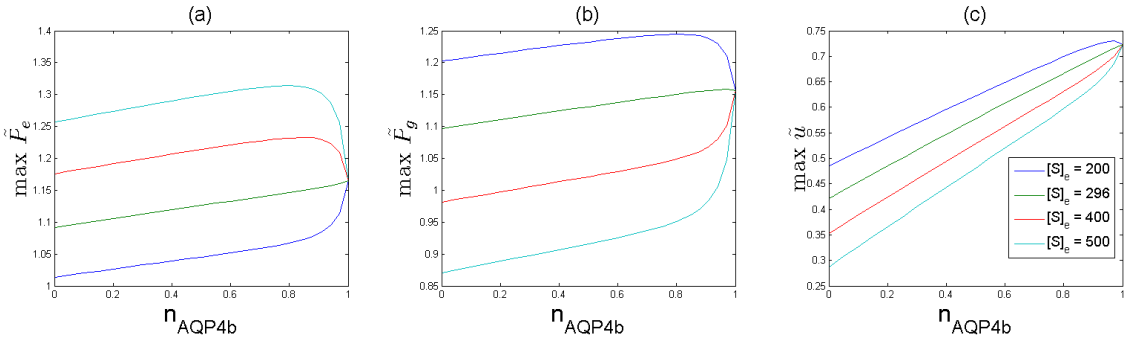

Figure 4.6: Tissue behaviour with varying n_{AQP4b} for 5 different ionic concentrations of ECS, $[S]_e$: (a) ECS pressure; (b) astrocyte pressure; and (c) tissue displacement. The unit of the concentrations are in mM.

Meanwhile, Figure 4.6 shows the tissue behaviour with varying ECS ionic concentration. From this figure, the ECS and astrocyte pressure respectively increase and decrease as the ECS ionic concentration increases from baseline value to 500 mM. Meanwhile, the variation of tissue displacement with n_{AQP4b} shows a linear relationship.

Increasing the ECS concentration by 100 mM shows a decrease in tissue displacement of about 17.6% from the baseline value.

4.7 Discussion

This section will discuss the model in three aspects, namely: (1) Model Features; where the justification of the model assumptions is explained; (2) Clinical Significant; which relates the results obtained with literature and describes their importance; and (3) Future Improvement; that discusses possible modifications on the model to improve the simulations.

4.7.1 Model Features

The model developed here has introduced the astrocyte and the neuron as additional fluid compartments beside the ECS. This reduces the volume fraction of ECS from 80%, which was assumed previously in Chapter 3, to 20%. The previous assumption was made based on the total water percentage in the brain, including water in the ECS, astrocyte and neuron. However, the ECS actually only constitutes about 12-19% of the brain volume (Go, 1997; Nicholson et al., 1998). The presence of astrocytes also plays a role in absorbing some of the water that moves into ECS from reperfused blood. However, this will cause the astrocyte pressure to increase and possibly will cause astrocyte swelling. The advantage of this is the reduction of vasogenic oedema as well as reducing the risk of vessel collapse due to the rise of ECS pressure.

Cerebral oedema generally can be divided into two types: cytotoxic and vasogenic (Unterberg et al., 2004). The former is the intracellular accumulation of water, especially in the astrocytes, due to the loss of electrolyte balance between the astrocyte and ECS. It is usually seen in early cerebral ischaemia when there is low blood flow and the BBB is

still intact (Papadopoulos et al., 2007). It occurs due to there being insufficient energy actively to regulate ionic concentrations. Cytotoxic oedema usually is not accompanied by brain swelling because when the cell swells, it takes up the ECS water through AQP4 and reduces the ECS volume fraction (Donkin et al., 2010), while the brain water volume remains constant. Meanwhile, vasogenic oedema occurs due to the water movement from the vasculature into the ECS, such as the movement of water due to BBB breakdown, which usually happens after ischaemia. This will later result in the increase of brain water content and consequently result in tissue swelling (Donkin et al., 2010). Both types of oedema can also commonly occur simultaneously (Kimelberg, 2004).

The presence of AQP4 has been shown to be involved in the formation of cytotoxic oedema in early ischaemia and elimination of vasogenic oedema after ischaemia (Papadopoulos et al., 2013). Deletion of AQP4 at the early stage of ischaemia may greatly reduce the formation of cytotoxic oedema but deletion of AQP4 at a later stage of ischaemia may hinder the process of vasogenic oedema elimination (Amiry-Moghaddam et al., 2003). In addition, there are also many experimental works that demonstrate the expression of AQP4 to correlate with the repair of BBB breakdown (Tomás-Camardiel et al., 2005; Vizuete et al., 1999), which shows that AQP4 is important in oedema elimination.

4.7.2 Clinical Significant

Table 4.3 summaries the results obtained in Figure 4.2. The model shows that the presence of parenchymal AQP4 does reduce vasogenic oedema, which is shown by the reduction in ECS pressure. However, the astrocyte pressure increases to compensate for this reduction, which will cause astrocyte swelling or cytotoxic oedema. It is also found from this model that the increment in pressure of both of these compartments in the

presence of AQP4 causes significant tissue displacement, compared to the condition when there is no AQP4 present. Therefore, even though vasogenic oedema is reduced in the presence of AQP4, the tissue swelling is not. On the other hand, when no AQP4 is present, tissue swelling is reduced but the ECS pressure remains high, which imposes the risk of capillary collapse and secondary stroke occurrence. When only perivascular AQP4 is presence, the water can move into both astrocyte and ECS from the blood vessels, but the water cannot be transferred between ECS and astrocyte. Hence, the tissue swelling is the largest for this case. In the study done by Amiry-Moghaddam et al. (2003), the deletion of AQP4 at a later stage of ischaemia may inhibit the clearance process of vasogenic oedema, although it helps in reducing cytotoxic oedema. Accumulation of water in astrocyte may cause the cell to rupture, and thus the presence of AQP4 during ischaemia-reperfusion may worsen the function of the brain.

Table 4.3: Generalization of the results of AQP4 model from Figure 4.2.

AQP4 ratio	**Astrocyte Pressure**	**ECS Pressure**	**Tissue swelling**
No AQP4	Remains at baseline	Increases	Occurs the least
Only perivascular AQP4	Increases	Increases equals to the no AQP4 case	Largest among the cases
Only parenchymal AQP4	Increases	ECS pressure increases but less than no AQP4 case	Larger than no AQP4 case

Treating oedema by inhibiting AQP4 function has been proposed by Marmarou (2007). However, as shown in Figure 4.3, regulating the right percentage of AQP4 presence in parenchymal and perivascular astrocytes might effectively reduce the effect of oedema. In addition, from Table 4.3, when only perivascular AQP4 is present, the ECS pressure remains the same as in the case of no AQP4 presence, showing that in this case, water is not able to move between the ECS and the astrocyte. This result also shows that the presence of parenchymal AQP4 is important in transferring some of the water content in the ECS into the astrocyte. Without parenchymal AQP4, the movement of water into

the astrocyte may be very slow if assuming that the only way water can get into the astrocyte is via the membrane phospholipid bilayer. Hence, selective inhibition of either parenchymal or perivascular AQP4 is a promising treatment plan for cerebral oedema.

It should be noted that the actual distribution of AQP4 within the astrocyte membrane is still unknown. From a study into the quantification of AQP4 density using immunogold analysis on retinal glial cells of rats, it was found that the astrocyte endfeet contain 10 times more AQP4 than non-endfoot membranes (Nagelhaus et al., 1998). One special characteristic of perivascular AQP4 is that it is anchored to the astrocyte endfeet by a specific protein called α-syntrophin. The disruption of the gene encoding this protein will cause the loss of only the AQP4 attached on the astrocyte endfeet adjacent to the blood vessels but not those attached to other parts of the astrocyte (Amiry-Moghaddam et al., 2003; Neely et al., 2001). Therefore, a treatment plan to remove specific AQP4 by targeting the α-syntrophin gene could be developed to inhibit the function of perivascular AQP4.

On the other hand, Figure 4.5 and Figure 4.6 show the tissue behaviour obtained for selected values of ECS and astrocyte ionic concentrations. It has been found by Jin et al. (2012) that AQP4 also plays role in the transport of K^+ ions in the brain parenchyma. From the results, it can be concluded that a high ionic concentration of ECS and astrocyte is required to cause a significant cerebral tissue swelling. It should be noted here that this model uses constant value of these ionic concentrations and it represents the total ionic concentration present in the ECS and astrocyte based on estimation done by Orlowski et al. (2013). The importance of the ionic concentration changes will be discussed thoroughly in Chapter 5.

4.7.3 Future Improvement

The pathway of oedema clearance described in this model is only through the AQP4 found in the astrocyte into the blood circulation. AQP4 is mostly found in astrocyte endfeet that surround the capillary, compared to the parenchymal astrocyte (Nagelhaus et al., 2013). Other possible pathways, such as through the ventricles and subarachnoid space into the CSF interfaces, are described by giving a fixed pressure and displacement boundary conditions. Although in this model, part of the ECS pressure is transferred into the astrocyte via AQP4 as a representation of vasogenic oedema clearance, the water cannot be removed from the astrocyte into the blood circulation due to the pressure gradient opposing the water flow into the blood via AQP4. This is in agreement with the suggestion by Papadopoulos et al. (2013) regarding the pressure gradient between the intracellular space and the blood circulation. Oedema also may take a considerable amount of time to be cleared (Ohata et al., 1990), especially when the BBB remains disrupted for a long time while blood is continuously reperfused. Work done by Ohata et al. (1990) found that the clearance of oedema through CSF is predominant compared to other pathways such as through the blood circulation. Hence, imposing varying boundary conditions to the model might provide new insights to the importance of AQP4.

It should also be noted that this model only considers a constant value of ionic concentration in both the astrocyte and the ECS. From the results, there is not much difference in tissue displacement and compartmental pressures when the ionic concentration is varied. However, modifying the model by including a cerebral metabolism model (Orlowski et al., 2011) or a membrane potential model (Endresen et al., 2000) might provide a clearer idea of the effect of ischaemia on the formation of vasogenic oedema after reperfusion. Furthermore, the involvement of AQP4 in ion dynamics, specifically potassium, K^+ ions, in the brain parenchyma has been studied by

Jin et al. (2012). Water transport through AQP4 from the ECS into the astrocyte causes a reduction in ECS volume and thus increases the K^+ concentration in the ECS. This will further increase K^+ uptake by the astrocyte. That study also shows that AQP4 deletion may impair the K^+ uptake by the astrocyte from the ECS. The inclusion of an ionic concentration model may thus provide a better understanding towards cerebral ischaemia-reperfusion.

4.8 Summary

The model developed here has provided a better understanding on the function of AQP4 during ischaemia-reperfusion. The presence of AQP4 during ischaemia-reperfusion injury is shown to help to reduce vasogenic oedema but it is compensated for by the increase in astrocyte pressure, leading to the formation of cytotoxic oedema. AQP4 function inhibition could possibly become a new treatment to reduce brain oedema by targeting either perivascular or parenchymal AQP4, but this technique must be applied appropriately so that the effects of tissue swelling and oedema are balanced.

Chapter 5

The Effect of Changes in Ionic Concentration of Cerebral Tissue in Ischaemia-Reperfusion Injury

---

The work presented in this chapter has appeared as **M. J. M. Mokhtarudin** and S. J. Payne (2016), "Investigating the Importance of Ionic Concentration on Ischaemic Cerebral Tissue Swelling using Donnan Equilibrium" Paper presented at MEIbioeng 16.

5.1 Introduction

Ischaemic stroke interrupts the cerebral blood circulation and can lead to the disruption of neuronal electrical activity, reduction of astrocyte metabolism and an ion homeostasis imbalance in the cerebral tissue. If the interruption is prolonged, it can cause an irreversible damage to the cells; the region in the cerebral tissue that experiences this is known as the ischemic core. The region surrounding this damaged core may contain cells that are still viable and that can still be saved; it is known as the penumbra (Astrup et al., 1981). The penumbra can be identified using a number of advanced magnetic resonance imaging (MRI) techniques and it is also useful to understand the characteristics of the cells such as the ionic concentration changes within this region. In this context, changes in the ionic concentration within the cerebral tissue, primarily the astrocyte, may lead to water movement via osmosis and result in tissue swelling.

Several clinical studies have been performed on the changes in the ionic concentration of cerebral tissue after ischemia. During ischemia, there are three main changes that occur to the ionic concentrations in the astrocyte (Mori et al., 2002): (1) the

influx of sodium, Na^+ ions into the cell; (2) the efflux of potassium, K^+ ions into the extracellular space (ECS); and (3) lactic acid accumulation that leads to pH drops in the tissue. In addition to this, cerebral ischemia may cause excessive accumulations of calcium, Ca^{2+}ions in the neurons leading to the release of excitatory amino acids, such as glutamate into the ECS. As ischemia causes a reduction in the cell metabolism, it also causes a limited reuptake of glutamate through an energy-dependent process in the presynaptic neurons, which causes an accumulation of glutamate in the ECS (Dirnagl et al., 1999), resulting in a water homeostasis imbalance in the neuron. However, the focus of this chapter is only the ion movements between the astrocyte and ECS. This is because the net flow of water through the neuron is zero since it has no aquaporin-4 (AQP4) and the water can only flow through the membrane of the neuron and hence, the change of ionic concentration in the neuron will cause less significant effect towards the overall tissue swelling.

The changes in the ionic concentration in the cerebral tissue can be used to obtain important information for a cerebral ischemic patient. For instance, the Na^+ ion concentration, together with the apparent diffusion coefficient (ADC) and cerebral blood flow (CBF) for a patient, can be used in estimating the time after focal cerebral ischemia occurrence (Wang et al., 2000). Another example is the use of pH weighted imaging and brain cell pH dynamics modelling in quantifying the region of salvageable brain tissue after ischemia (Orlowski et al., 2011). However, to integrate the pH dynamics model of the brain cell with the model developed in this study would incur very significant computational cost as this model contains hundreds of ordinary differential equations (ODEs), which would need to be coupled with the partial differential equations (PDEs) described earlier for each temporal and spatial step. Hence, a simpler way in determining

the effect of cerebral tissue ionic concentration towards the tissue swelling during ischemia-reperfusion is needed.

The ionic concentration in astrocytes can be related to the concentration of the fixed charge density (FCD) molecules such as proteoglycans and DNA (Cowin et al., 2009). These FCDs contribute to a force that drives water into the tissue. The effect of FCD is significant when the cell membrane is damaged and this causes water to enter the cell via the Donnan effect (Elkin et al., 2011). To model this effect, it is normally assumed that there are three phases, which are solid, fluid and ions to coexist in a porous medium (Elkin et al., 2010). The work done by Lang et al. (2014) showed that the brain tissue slice volume changes with the change of the ionic bath concentration. Preliminary studies on the effect of concentration changes with compartmental pressure (see Appendix B) prove that the ionic concentration in the cerebral compartments is not necessarily constant and may vary with the tissue displacement.

Therefore, the objectives of this study are to incorporate the variability of ionic concentration in the cerebral tissue in the model and to observe its effect on tissue swelling during ischemia-reperfusion injury. The compartmental model in Chapter 4 is slightly modified to incorporate the Donnan equilibrium equation, which will be used to study the ionic concentration changes in the cerebral tissue. Water is still assumed to flow osmotically through AQP4 while some water can flow directly through the semi-permeable membrane of the cells but the net flow is very small as compared to the water flow through AQP4 and hence, it is assumed to be zero.

5.2 Incorporation of Donnan Equilibrium to the Previous Model

Figure 5.1 shows a schematic used to represent the effect of FCD in oedema formation after cerebral ischaemia through the Donnan effect. In an injured cerebral tissue

after prolonged ischaemia, the astrocyte metabolism is disrupted and unable to maintain its normal resting membrane potential and thus exposes the FCD. This causes the influx of ions into the astrocyte to balance the effect of FCD (Elkin et al., 2011). The rush of ions into the astrocyte increases its osmotic pressure and consequently results in water influx into the cell through AQP4. Cellular swelling occurs and the ECS will shrink due to compression from the astrocyte.

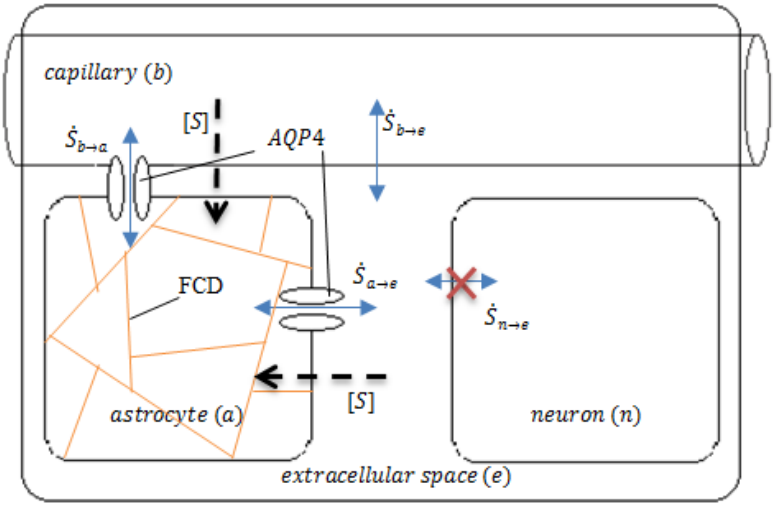

Figure 5.1: The proposed mechanism of the presence of FCD in astrocyte, which can cause the influx of ions $[S]$ from the ECS during cerebral ischaemia.

Assuming that the net water transfer between the neuron and the ECS is zero due to the absence of AQP4 and that the astrocyte is fully immersed in the ECS, then the concentrations of ions in the astrocyte, $[S]_a$, and ECS, $[S]_e$, can be expressed according to the Donnan equilibrium (Cowin et al., 2009) as:

$$\sum_{c=1}^{C}[S_c]_a = c_a = \sqrt{c^{fc^2} + {c_e}^2}, \tag{5.1}$$

$$\sum_{c=1}^{C}[S_c]_e = c_e. \tag{5.2}$$

Here, the summation represents the total concentration of the different ions, $c = 1, \dots, C$ present within the compartment. These include mobile ions such as Na^+, K^+, Ca^{2+}, $HCO_3{}^-$, and other non-permeable anions. In the astrocyte, it is assumed that the ions are

distributed such that they are in electrochemical equilibrium and are electroneutral everywhere within, and that the total ionic concentration in the astrocyte can be represented by the Donnan equilibrium as shown in eqn. (5.1) with the term c^{fc} representing the FCD in the astrocyte.

Meanwhile, to keep the analysis simpler, the total ionic concentration in the ECS is assumed constant with a value c_e, but this will be varied later to see its effect on cerebral tissue swelling. Replacing the osmotic pressure terms for the astrocyte and ECS in the system of eqns. (4.19) to (4.22) with eqn. (4.39), which relates the osmotic pressure of a compartment with its ionic concentration, the following governing equations are obtained:

$$0 = \nabla^2 u - \frac{2}{r^2}u - \frac{1-2v}{2G(1-v)}\left(\alpha_e \frac{\partial P_e}{\partial r} + \alpha_a \frac{\partial P_a}{\partial r} + \alpha_n \frac{\partial P_n}{\partial r}\right), \tag{5.3}$$

$$\begin{aligned}\frac{1}{Q_e}\frac{\partial P_e}{\partial t} = {} & k_e \nabla^2 P_e + 2\bar{n}_b \frac{L_p}{R_c}\left(\frac{L_e}{L_c}\right) f[(P_b - P_e) - \sigma \Pi_b\,] \\ & + F n_{AQP4e}\left(\frac{\bar{A}_a \bar{n}_a}{V_a}\right)\left[\frac{2}{E_a}(P_a - P_e) + 1\right][P_a - P_e - RT(c_a - c_e)],\end{aligned} \tag{5.4}$$

$$\begin{aligned}\frac{1}{Q_a}\frac{\partial P_a}{\partial t} = {} & k_a \nabla^2 P_a - F n_{AQP4e}\left(\frac{\bar{A}_a \bar{n}_a}{V_a}\right)\left[\frac{2}{E_a}(P_a - P_e) + 1\right][P_a - P_e - RT(c_a - c_e)\,] \\ & + 2 n_{AQP4b} \bar{n}_b \frac{F}{R_c}\left(\frac{L_a}{L_c}\right) f[P_b - P_a - (\Pi_b - RT c_a)\,],\end{aligned} \tag{5.5}$$

$$\frac{1}{Q_n}\frac{\partial P_n}{\partial t} = k_n \nabla^2 P_n. \tag{5.6}$$

The term c^{fc} can be related to its initial value, c_o^{fc}, tissue strain, ε and the volume fraction of astrocyte, $\bar{n}_g$ as given below (Lang et al., 2014):

$$c^{fc} = \frac{\bar{n}_g c_o^{fc}}{\varepsilon^3 + 3\varepsilon^2 + 3\varepsilon + \bar{n}_g}. \tag{5.7}$$

The strain $\boldsymbol{\varepsilon}$ is related to the tissue displacement vector, $\boldsymbol{u}$ by the following relationship:

$$\boldsymbol{\varepsilon} = \frac{1}{2}(\nabla \boldsymbol{u} + (\nabla \boldsymbol{u})^T). \tag{5.8}$$

However, for the one-dimensional case, this relationship can be reduced to:

$$\varepsilon = \nabla u. \tag{5.9}$$

The system of eqns. (5.3) to (5.6) is then non-dimensionalised. These equations have the same characteristic parameters as described in Chapter 4. The system of equations also has similar initial and boundary conditions as the model in Chapter 4 and is solved using the 1D parabolic-elliptic PDE solver in MATLAB.

Modification of the model introduces two new parameters, which are c_e and c_o^{fc}, and these have baseline values of 296.0 mM (Orlowski et al., 2013) and 2 mM (Elkin et al., 2010), respectively. The value of c_o^{fc} used has a unit in mEql^{-1} and is first converted to the unit mM using eqn. (2.2) in (Elkin et al., 2010), together with the total charge number of 2 for the substance studied using the 1,9 dimethylmethylene blue (DMMB) assay. The substance used in the study was one of the sulphated types of glycosaminoglycan (GAG), chondroitin sulphate, which according to (Azeloglu et al., 2008) has two negative charges.

5.3 Results

Throughout this section, the tilde ($\sim$) symbol represents the non-dimensionalised form of the variables, as discussed in Chapter 4. Figure 5.2 shows the non-dimensionalised cerebral tissue displacement, ECS and astrocyte pressures plotted against non-dimensionalised time and radius. The patterns are similar to those obtained in Chapter 4. However, the values of maximum displacement and pressures are slightly different for the cases of $n_{AQP4b} = 1$ and $n_{AQP4e} = 1$ but not for the case of no AQP4. For the case of $n_{AQP4b} = 1$, the difference can be seen for the astrocyte pressure and tissue displacement, being 0.12% and 0.46% less than the results in Chapter 4. Meanwhile, for the case of $n_{AQP4e} = 1$, the difference is 0.08%, 0.05% and 0.78%, for the astrocyte pressure, ECS pressure and tissue displacement, respectively. For the latter case, there is

a reduction in ECS pressure due to the presence of parenchymal AQP4. However, the differences calculated are very small.

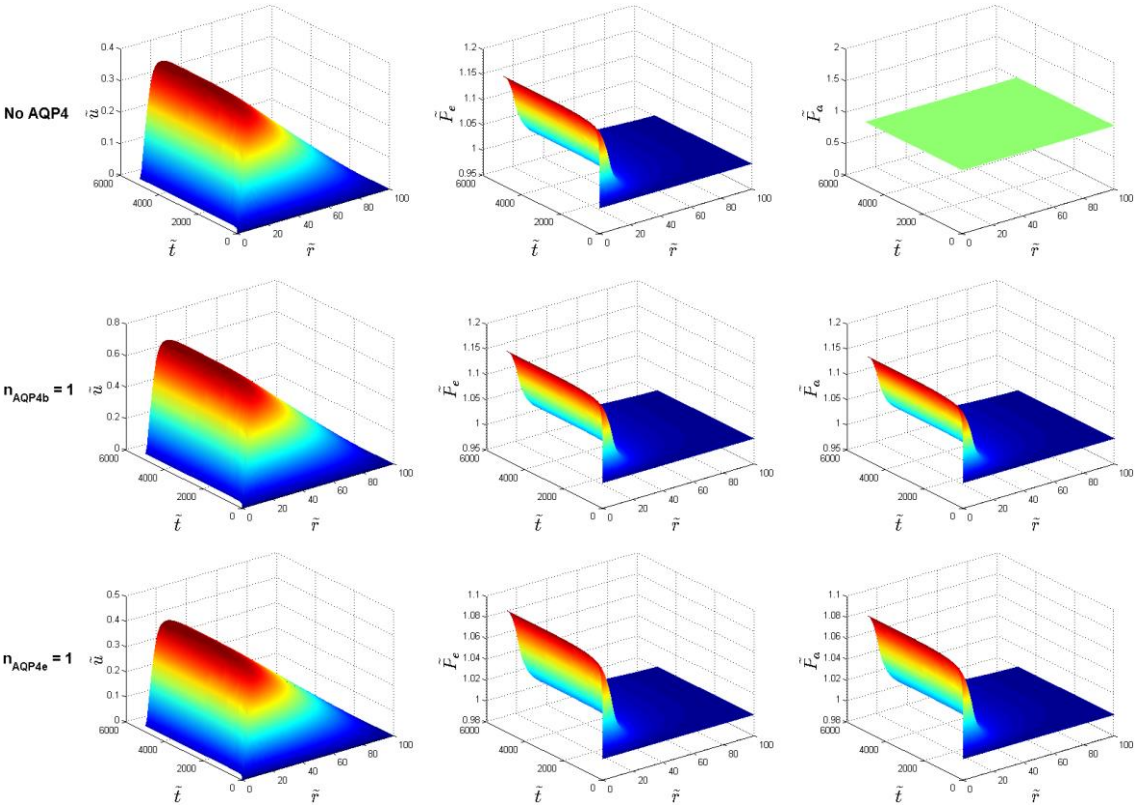

Figure 5.2: Time varying behaviour of the tissue under baseline parameters values with three different AQP4 ratio: (Top) No AQP4; (Middle) $n_{AQP4b} = 1$ and (Bottom) $n_{AQP4e} = 1$.

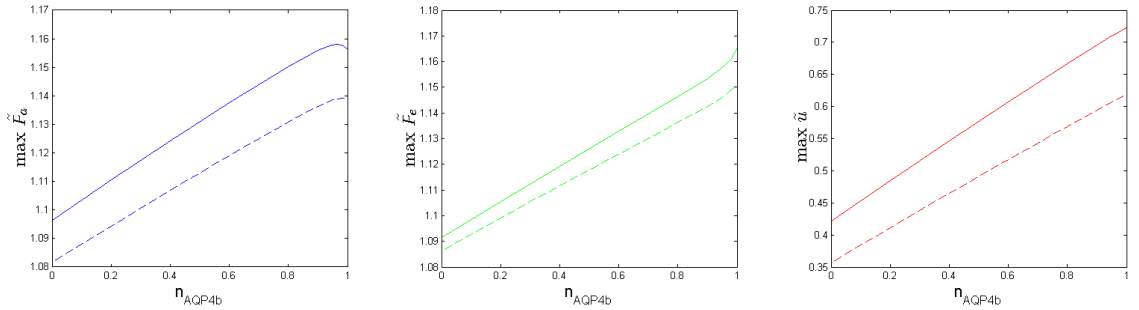

Figure 5.3: Comparison of the tissue behaviour with varying n_{AQP4b} for the model developed here and in Chapter 4. The solid and dashed lines represent the results from Chapter 4 and Chapter 5, respectively.

Figure 5.3 shows the comparison between the values obtained in this chapter and those in Chapter 4. It can be seen that the results obtained here are smaller than those obtained in Chapter 4. The differences are roughly 1.85%, 0.37% and 21.43% for astrocyte pressure, ECS pressure and tissue displacement respectively. Although the

differences for the pressures are not large, their combined effect on the tissue displacement is large. In addition, the trends of the fluid pressures and tissue displacement obtained here are more linear than those obtained in Chapter 4.

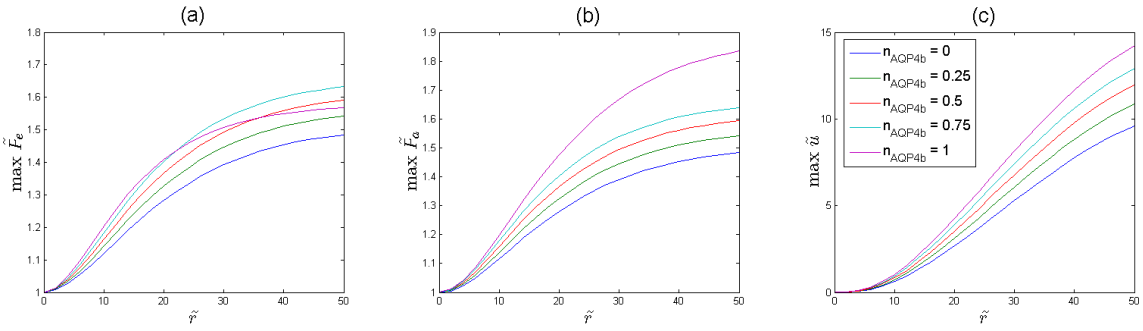

Figure 5.4: Tissue behaviour with varying core radius for 5 different n_{AQP4b} ratios: (a) ECS pressure; (b) astrocyte pressure; and (c) tissue displacement.

The effect of core radius variation towards the changes in the cerebral tissue displacement and fluid pressures can be observed in Figure 5.4. Generally, the trends obtained here are similar to those obtained in Chapter 4. Meanwhile, Figure 5.5 shows the behaviour of the cerebral tissue with different values of ECS concentrations. The differences in the ECS pressure, astrocyte pressure and tissue displacement are not significant at a very small n_{AQP4b} value of about 0 to 0.2. Further, the astrocyte pressures obtained here show an increasing value when the ionic concentration of ECS is increased, while it was shown previously in Chapter 4 that astrocyte pressure behaves otherwise.

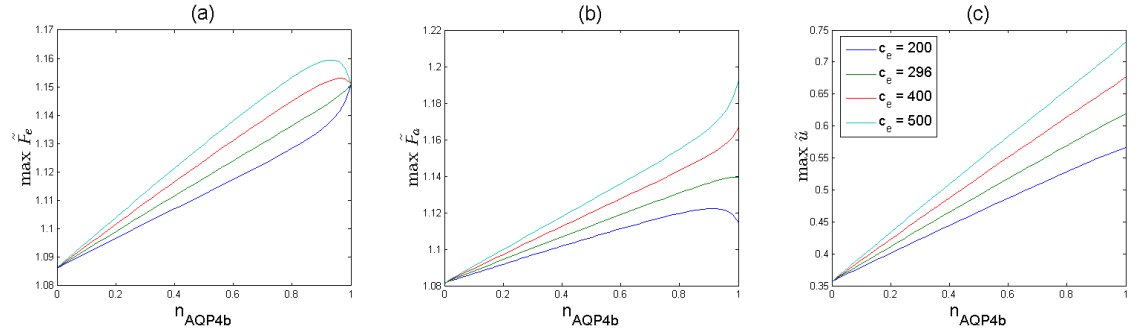

Figure 5.5: Tissue behaviour with varying n_{AQP4b} for 4 different ionic concentrations of ECS, c_e: (a) ECS pressure; (b) astrocyte pressure; and (c) tissue displacement. The unit of the concentrations are in mM.

There is no significant difference when the FCD concentration c_o^{fc} is varied. This is shown in Figure 5.6. There are not many literature sources that provide approximate values of c_o^{fc}; the only available values are $c_o^{fc} = 4$ mEq/l (Elkin et al., 2010), which was obtained through a series of experiments and $c_o^{fc} = 11.6$ mEq/l (Lang et al., 2014), which was obtained by fitting the experimental data with a mathematical model. Using these values in the model produces no difference in the compartmental pressures and tissue displacement. This is because these values are relatively small compared to the value of the ECS concentration, c_e. This effect can be seen from the relationship of the ionic concentration of astrocyte and ECS, which, when expanded using a first order Taylor expansion gives the following relationship:

$$c_a = \sqrt{{c^{fc}}^2 + {c_e}^2} \approx c_e \left(1 + \frac{1}{2}\frac{{c^{fc}}^2}{{c_e}^2}\right). \tag{5.10}$$

Using values of $c^{fc} = 2$ mM and $c_e = 296.0$ mM gives an approximation of $\frac{c_e}{c^{fc}} \gg 1$, thus $c_a \approx c_e$, for a very small value of c^{fc}. To see a significant difference in the tissue displacement and the compartmental pressures, c_o^{fc} is varied to up to 300 mM. The variations for ECS pressure, astrocyte pressure and tissue displacement when varying the c_o^{fc} from 0 to 300 mM are about 2.75%, 4.63% and 14.29%, respectively.

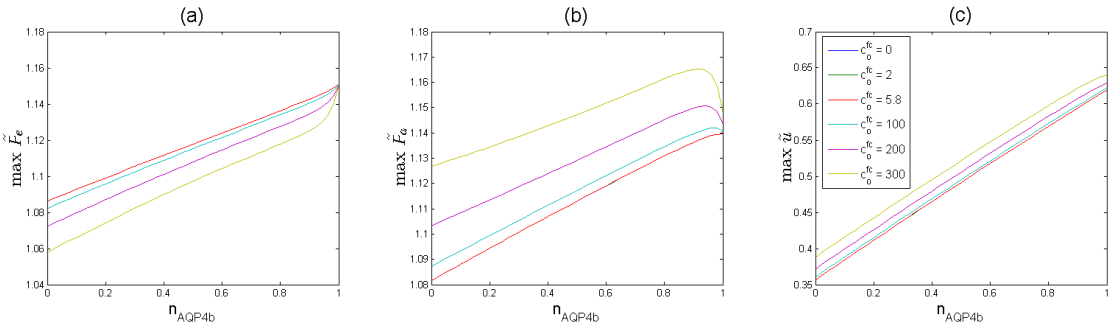

Figure 5.6: Tissue behaviour with varying core radius for 6 different FCD concentrations, c_o^{fc}: (a) ECS pressure; (b) astrocyte pressure; and (c) tissue displacement. The unit of the concentrations are in mM.

5.4 Discussion

The purpose of the model developed here is to study the effect of varying ionic concentration in the astrocyte and ECS towards cerebral swelling during ischaemia-reperfusion injury. It is found that the ionic concentration does not play a significant effect in the cerebral tissue swelling. To cause a significant tissue swelling, the c_o^{fc} value must be greater than approximately 100 mM, as shown from the results obtained. However, the only c_o^{fc} value available was obtained through experiments done on cerebral tissue slices of rat, and is less than 20 mM (Elkin et al., 2010). These values are lower compared to the ionic concentration of ECS that can give a significant effect towards the cerebral tissue displacement during ischaemia-reperfusion. These values are also in agreement with the range of concentrations found in other soft tissue such as the articular cartilage, which has a range 10 – 30 mEq^{-1} (Lu et al., 2008).

It should be noted that the FCD concentration value found by (Elkin et al., 2010) is probably less than the actual value present in the cerebral tissue because there are many other macromolecules that can contribute towards the effect of FCD, such as DNA and another type of GAG, heparin sulphate (Elkin et al., 2011). Removing certain amounts of FCD can be a useful treatment method for cerebral tissue swelling. For example, the use of the enzyme chondroitinase ABC in digesting the chondroitin sulphate proteoglycans was shown to effectively reduce the cerebral tissue swelling in rats (Elkin et al., 2011) and also helps in the process of axon regeneration after central nervous system (CNS) injury (Lin et al., 2008). In addition, GAG is also important in the early development of human brain (Margolis et al., 1975).

The study presented here adds Donnan equilibrium to the existing model which simplifies the analysis considerably without having to couple the existing model with

models that are used in the study of cerebral ion dynamics, such as the cerebral metabolism model (Cloutier et al., 2009) and the cell membrane potential model (Endresen et al., 2000). The model developed by (Orlowski et al., 2013) to study the volume changes of the cerebral cell during ischaemia incorporates cerebral cell dynamics and ion diffusion in the extracellular matrix. However, this model does not consider the mechanical property of the cerebral tissue. The work developed here uses a linear elastic model to represent the material property of the cerebral tissue. Other material property models such as the Fung elastic model (Ateshian et al., 2009) have been used to study the swelling of cerebral tissue (Lang et al., 2014; Lang et al., 2015), which can describe the hyperelastic properties of biological soft tissue. However, at very small values of strain, the Fung elastic model can be approximated to the linear elastic model (see Appendix A), thus concluding that the use of the linear elastic model is sufficient to model the material properties of the cerebral tissue during ischaemia-reperfusion.

Although the results obtained here show that there is no significant effect of varying ionic concentration on the cerebral oedema, the importance of the changes of the ion concentrations such as sodium and potassium in the elevation of cerebral tissue osmolality is widely known (Kawamata et al., 2007). For instance, oedema formation is found to correlate with the increase in Na^+ and the decrease in K^+ ion concentrations, which results in the net gain of water into the cerebral tissue (Menzies et al., 1993). The study done by Lo et al. (1987) suggested that the increase in the cerebral Na^+ concentration during ischaemia is due to the reduction in the clearance of that ion from the brain. In a different study, it has been hypothesized that K^+ ions play a role in glutamate-induced astrocyte swelling and are dependent on Na^+ activation of the Na^+/K^+ pump (Bender et al., 1998), which causes the influx of water. In the studies done by Nielsen et al. (1997) and Amiry-Moghaddam et al. (2003), it was found that AQP4 plays

a role in sustaining the clearance of K^+ and water from swelling astrocytes during oedema elimination.

A different approach to investigating the effects of ionic concentration in cerebral swelling would be to implement a mechanoelectrochemical model, which consists of three primary variables: the solid displacement, the fluid pressure and the ion concentration (Acartürk et al., 2004). The ion concentrations are assumed to be dependent on each other and also depend on the electrochemical potential across the cell membrane. However, the model developed in this study only considers two ions; anion and cation, while as mentioned, the interaction between several ions in the tissue might contribute to the swelling. To further study how these ions contribute to the overall tissue swelling will require the use of a fully multiscale approach, which is beyond the scope of this study.

5.5 Summary

The ionic concentrations of the astrocyte and ECS play a role in the formation of cerebral tissue swelling in ischaemia-reperfusion injury as found by many previous studies. However, it has been shown in the model developed here that varying the ionic concentration does not result in a significant difference in the formation of cerebral oedema. In addition, the FCD concentration is also important in determining cerebral tissue swelling and could provide an alternative in treating this disease. A multiscale modelling approach will be required to further understand the importance of these ions in cerebral tissue swelling during ischaemia-reperfusion.

Chapter 6

Finite Element Analysis of Cerebral Ischaemia-Reperfusion Injury using Simplified Geometry

6.1 Introduction

Brain oedema due to cerebral ischaemia-reperfusion can be observed in medical imaging modalities such as computed tomography (CT) and magnetic resonance imaging (MRI) by the formation of cerebral herniation or the displacement of part of the swollen cerebral tissue in one hemisphere into another part of the brain (Bešenski, 2002). The herniation will usually cause the compression of cerebral microvessels resulting in blockage and leading to the occurrence of secondary ischaemia and compression of the brain ventricles. Another indicator is an increase in intracranial pressure (ICP), although this is not always associated with the occurrence of brain oedema (Fishman, 1975). The rise in ICP can only be observed after cerebral blood flow (CBF) is restored after prolonged ischaemia. Prolonged ischaemia may cause the permeability of blood-brain barrier (BBB) to increase. Reperfusion of CBF after ischaemia then allows a net increase of water into the cerebral tissue through the compromised BBB leading to vasogenic oedema and elevated ICP (Unterberg et al., 2004).

The formation of brain herniation and the elevation of ICP can both be studied by solving the models developed previously using a finite element analysis on a simplified cerebral geometry. This geometry can be drawn to mimic approximately the shape of an actual brain, using a simple closed curve for a 2D geometry such as a circle for an ellipse, and a simple closed surface for a 3D geometry such as a sphere or an ellipsoid. Solving the models using these geometries is very useful in providing general information

regarding the model behaviour before actually solving the models using a more sophisticated realistic patient-specific geometry. In addition, the use of a patient-specific geometry may require larger computational resources and modifications compared to the existing models.

The objective of this chapter is to solve the models developed in Chapter 3 and Chapter 4, which were solved previously in 1D, in both 2D and 3D using a simplified geometry. The models are solved using finite element analysis software, ELMER, and the results are then compared between the two models and also between the results obtained with different dimensions.

6.2 Single Compartment Model

The single compartment model is as developed previously in Chapter 3. In this model, there are two fluid compartments which are blood and the tissue interstitial space, which consists primarily of water. Based on the assumption of the homogeneity of blood pressure throughout the cerebral space, only the changes in water pressure in the interstitial space will contribute to cerebral tissue swelling. In addition, the difference between the water pressure and blood pressure will determine the compressibility of the cerebral vessels during the ischaemia-reperfusion process.

6.2.1 Governing Equations

The governing equations of the single compartment model can be described as:

$$\nabla \cdot \sigma_{ij} - \alpha_w \nabla P_w = 0, \tag{6.1}$$

$$\frac{1}{Q_w}\frac{\partial P_w}{\partial t} - k_w \nabla^2 P_w - \dot{S}_{b\to w} = 0, \tag{6.2}$$

where σ_{ij} is the total stress of the tissue, P_w is the interstitial water pressure, α_w is the Biot parameter for water, Q_w is the relative compressibility of water, $k_w \left(= \frac{\kappa_w}{\mu_w}\right)$ is the permeability of water, t is time and the term $\dot{S}_{b\to w}$ is the water transfer from the capillary space into the cerebral interstitial space due to capillary filtration.

The total stress, σ_{ij}, is linearly related to the strain, ε_{ij}, as given by (Terzaghi, 1943):

$$\sigma_{ij} = 2G\varepsilon_{ij} + \frac{2Gv}{1-2v}\varepsilon_{ii}, \tag{6.3}$$

where G, and v are the shear modulus and Poisson's ratio, respectively, of the cerebral tissue. The term ε_{ij} is the tissue strain, which is related to the tissue displacement, u_i, by the following relationship:

$$\varepsilon_{ij} = \frac{1}{2}\left(\nabla u_i + \nabla u_j\right). \tag{6.4}$$

Meanwhile, the term $\dot{S}_{b\to w}$ is given by:

$$\dot{S}_{b\to w} = 2\bar{n}_b \frac{L_p}{R_c} f[(P_b - P_w) - \sigma\Pi_b\,]. \tag{6.5}$$

where $\bar{n}_b$ is the baseline volume fraction of the blood, L_p is the hydraulic permeability of the capillary, R_c is the baseline value of capillary radius, σ is the reflection coefficient, Π_b is the osmotic pressure in the capillary and P_b is the blood pressure, which has been assumed constant. Lastly, the term f represents the fraction of vessels that remain open after the reperfusion and swelling process at each point in space and time. This has been described in more detail in Chapter 3.

6.3 Two-Compartment Model

The two-compartment model is as developed in Chapter 4. The cerebral space is divided into 4 fluid compartments which are blood, extracellular space (ECS), astrocytes

and neurons. By using the same assumptions for blood pressure homogeneity, the blood pressure is assumed to be spatially constant throughout the swelling process. Meanwhile, aquaporin-4 (AQP4) is assumed to be present on the astrocyte interfaces with the ECS and the cerebral vessel but not on the neuron interfaces. This results in the neuron pressure being approximately constant throughout the process because the net water flow into the neuron is approximately constant since water can only flow through the membrane of the neuron, more slowly than through the AQP4.

6.3.1 Governing Equations

The governing equations for the two-compartment model are described by the system of equations below:

$$\nabla \cdot \sigma_{ij} - (\alpha_e \nabla P_e + \alpha_a \nabla P_a + \alpha_n \nabla P_n) = 0, \tag{6.6}$$

$$\frac{1}{Q_e}\frac{\partial P_e}{\partial t} - k_e \nabla^2 P_e - \dot{S}_{b\to e} - \dot{S}_{a\to e} = 0, \tag{6.7}$$

$$\frac{1}{Q_a}\frac{\partial P_a}{\partial t} - k_a \nabla^2 P_a + \dot{S}_{a\to e} - \dot{S}_{b\to a} = 0, \tag{6.8}$$

$$\frac{1}{Q_n}\frac{\partial P_n}{\partial t} - k_n \nabla^2 P_n = 0. \tag{6.9}$$

The subscripts e, a, and n represent ECS, astrocytes and neurons, respectively. Meanwhile, P, α, Q, and k are the fluid pressure, Biot constant, relative compressibility of the fluid and the fluid permeability, respectively. Here, the stress term σ_{ij} is the same as in the eqn. (6.3).

The fluid transfers between the compartments, $\dot{S}_{b\to a}$, $\dot{S}_{a\to e}$ and $\dot{S}_{b\to e}$, which have been described in more detail in Chapter 4, have the following relationships:

$$\dot{S}_{b\to a} = 2n_{AQP4b}\bar{n}_b \frac{F}{R_c}\left(\frac{L_a}{L_c}\right) f[P_b - P_a - (\Pi_b - \Pi_a)\,], \tag{6.10}$$

$$\dot{S}_{a\to e} = F n_{AQP4e}\left(\frac{\bar{A}_a \bar{n}_a}{V_a}\right)\left[\frac{2}{E_a}(P_a - P_e) + 1\right][P_a - P_e - (\Pi_a - \Pi_e)\,]. \tag{6.11}$$

$$\dot{S}_{b\to e} = 2\bar{n}_b \frac{L_p}{R_c}\left(\frac{L_e}{L_c}\right) f[(P_b - P_e) - \sigma\Pi_b\ ], \tag{6.12}$$

In these equations, the terms Π represents the osmotic pressure of the fluid. The additional terms are the AQP4 ratio along the astrocyte endfeet, n_{AQP4b} and $n_{AQP4e} = 1 - n_{AQP4b}$, the baseline volume ratio of astrocyte, $\bar{n}_a$, the hydraulic permeability through AQP4, F, the ratio of surface area of capillary covered with astrocyte, L_a/L_c and the ratio of the capillary surface covered with ECS, $L_e/L_c = 1 - L_a/L_c$, the baseline surface area of astrocyte, $\bar{A}_a$, and volume of the astrocyte, V_a. Again, in these equations, the term f represents the fraction of vessels that stays open after the reperfusion.

6.4 Geometry and Meshing

The cerebral geometry was drawn according to the realistic brain geometry as proposed by (Hakim et al., 1976), in which the brain is approximated as a sphere. For the 2D geometry, the brain is modelled as a circle that consists of a circular core in the middle that represents the brain ventricle. Meanwhile, for the 3D geometry, the brain is modelled as a perfect hemisphere with a semispherical core in the middle to represent the ventricle. The brain radius is about 65 to 67 mm (Cosgrove et al., 2007), hence the outer radius is taken here to be approximately as 80 mm. The circular core that represent the ventricle has the radius of 24 mm, taken to be about 30% of the brain radius (Smillie et al., 2005). The brain tissue is assumed to be homogeneous, thus there is no difference between the white and grey matter. The inner and outer boundaries of the brain geometry are named as the ventricular layer and the subarachnoid layer, respectively.

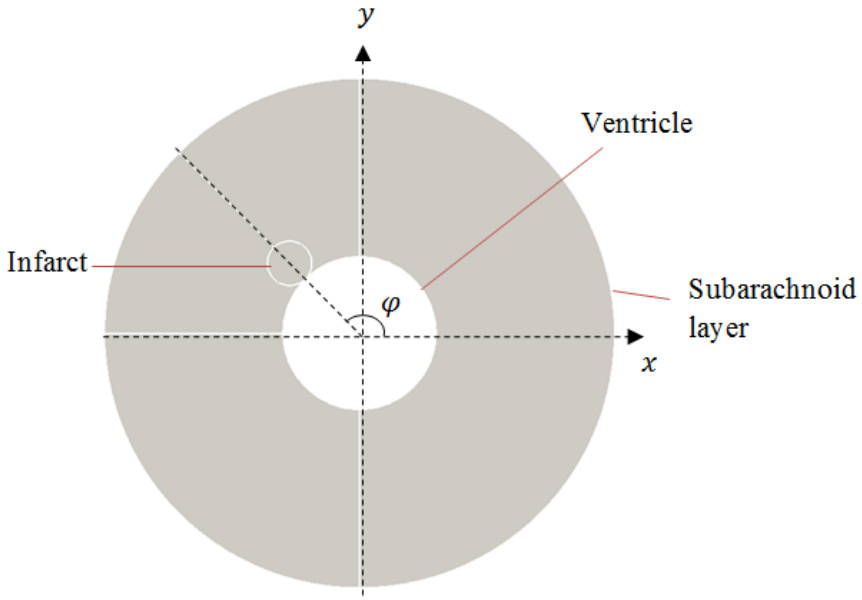

Figure 6.1: Example of the 2D cerebral geometry with a circular infarct of radius 7 mm located at $\varphi = 135^{o}$.

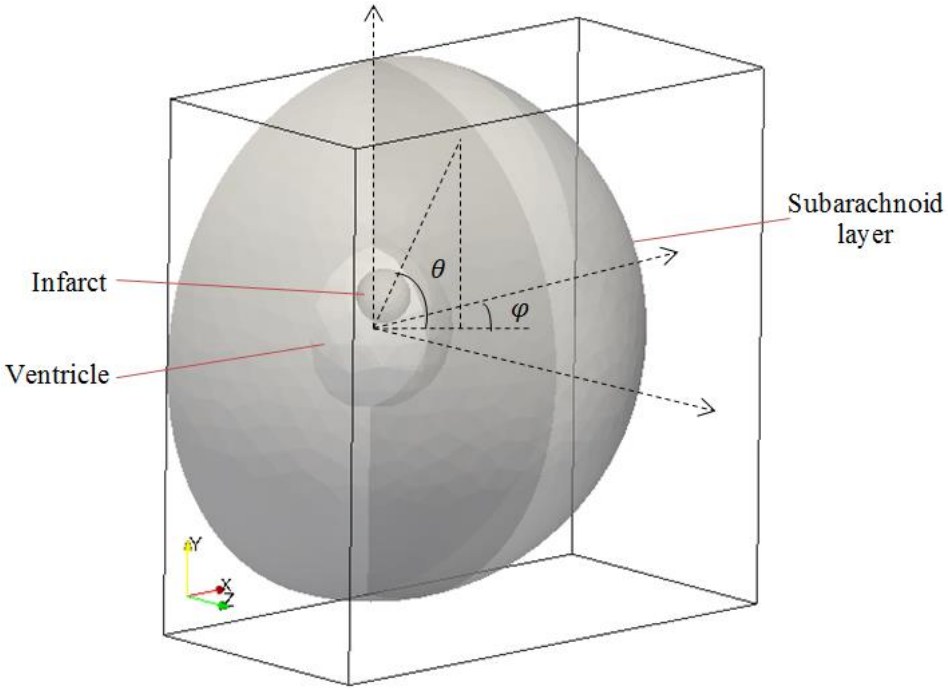

Figure 6.2: Example of the 3D cerebral geometry with a spherical infarct of radius 7 mm located at $\varphi = 135^{o}$ and $\theta = 45^{o}$.

To model the effects of ischaemia, a small infarcted region is drawn within the geometry. The infarct size is varied in the range 7 mm to 28 mm radius to study the effect of size on cerebral swelling. For the 2D geometry, the infarct is drawn as a circle which is located along the line that makes an angle $\varphi = 135^{o}$, where φ is the angle measured

counterclockwise from the *x*-axis, as shown in Figure 6.1. Meanwhile, for 3D geometry, the infarct is drawn as a perfect sphere and is located along the line with angle $\varphi = 135^{o}$ and $\theta = 45^{o}$, where θ is the angle measured clockwise from the *z*-axis as shown in Figure 6.2. In the regions other than the infarct, the eqns. (6.5), (6.10), (6.11), and (6.12) are equal to zero to represent no ischaemia-reperfusion damage.

For both of the geometries, the infarcted region and region near it are discretised using a finer mesh than the rest of the part of the geometry. The number of elements varies depending on the sizes of the infarct. There are about 2000 to 5000 elements for the 2D geometry and 17,000 to 47,000 elements for the 3D geometry. All of the geometries are drawn and meshed using the open source finite element grid generator with built-in CAD software Gmsh (Geuzaine et al., 2009).

6.5 Model Parameters and Numerical Procedure

Most of the parameters and their respective values can be found in Chapters 3 and 4. For some simulations of the two-compartment model, the parenchymal and perivascular AQP4 ratios are assumed to have a fixed value of $\frac{n_{AQP4b}}{n_{AQP4e}} = 10$ (Nagelhaus et al., 1998) and this is done here for the sake of simplification.

For the single compartment model, the initial conditions at $t = 0$ are:

$$u(x, 0) = 0, \tag{6.13}$$

$$P_w(x, 0) = 1330 \text{ Pa}, \tag{6.14}$$

where the initial pressure is equal to the intracranial pressure and the tissue is assumed to have zero displacement. Meanwhile, for the boundary conditions, the subarachnoid and ventricular layers are fixed at zero displacement and the pressure is set at the same value as the ICP. Simulations are performed transiently for 3600 seconds (1 hour) with a time step increment of 1 second.

For the two-compartment model, the initial conditions are:

$$u(x,0) = 0, \tag{6.15}$$

$$P_e(x,0) = P_a(x,0) = P_n(x,0) = 1330 \text{ Pa}, \tag{6.16}$$

in which the tissue is initially stationary and the initial pressures are equal to baseline ICP. The boundary conditions are set so that the skull and ventricle are assumed to remain at their initial conditions, which are zero displacement and pressures equal to baseline ICP. All of the simulation results are solved using open source finite element software, ELMER, and are analysed using open source data analysis and visualisation software ParaView (Henderson, 2007).

6.6 Results

In this section, the results for the two models under investigation are presented separately. For each model, the results for the 1D simulation, which was done in previous chapters, 2D and 3D simulations are compared to see the difference in the cerebral tissue displacement and the fluid pressures. It should be noted that the results obtained for the 1D simulation are in non-dimensionalised form and therefore, must be first converted to dimensionalised form before comparisons can be made.

6.6.1 Single Compartment Model

This section will describe the results obtained for the simulations using the single compartment model. Before the analysis begins, it should be noted that the relationship for the minimum pressure, P_c, required for capillary collapse to occur is as given in Chapter 3:

$$P_c = \bar{P} + \text{E}, \tag{6.17}$$

where $\bar{P}$ and E are the ICP and the capillary stiffness, respectively. By using the parameter values shown in

Table 3.2, the value of this pressure is found to be $P_c = 2194.5$ Pa. This is the value of pressure at which capillary vessels will collapse and capillary filtration will stop. In addition, the occurrence of capillary collapse is an indication that a secondary ischaemic attack may occur.

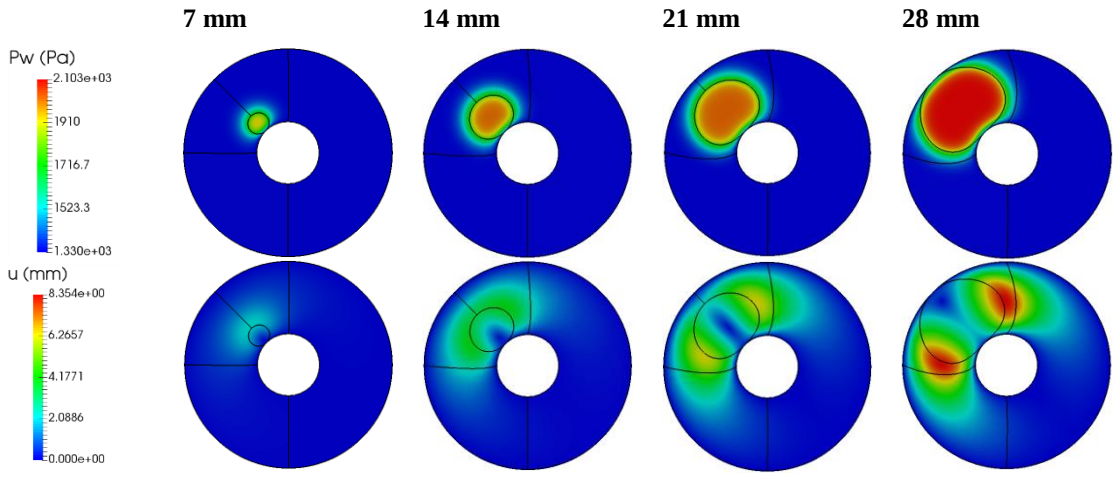

Figure 6.3: Cerebral interstitial pressure, P_w and tissue displacement, u for the different infarct sizes solved in 2D geometry.

Figure 6.3 shows the cerebral interstitial pressure and tissue displacement for the 2D simulations for the infarct located near the ventricle. The tissue displacement starts to develop at the outermost radius of the infarct before slowly spreading to the inside and outside of the infarct. Meanwhile, the pressure starts to rise in the centre of the core and then spreads in the direction of the infarct radius. However, due to the boundary conditions imposed at the subarachnoid and ventricular layers, the displacement and pressure gradually decrease near these layers. The tissue displacement pushes the other side of the cerebral tissue as indicated by the deformation of the middle line to the right side. The deformation of this line increases as the size of the infarct becomes larger.

The changes in maximum displacement and maximum pressure when the infarct distance from the ventricle is varied are shown in Figure 6.4. The maximum displacement

increases when the distance from the ventricle increases except for the case of the infarct radius at 7 mm. For this infarct size, there is a slight drop in the maximum displacement for the infarct distance from 7 mm to 21 mm and the infarct distance from 42 mm to 49 mm. Meanwhile, for the maximum pressure, there is no substantial difference when the distance is varied with the exception of the case for a 7 mm infarct radius, although the difference for this case is only about 25 Pa from the other cases. This difference is due to the 'edge effect', in which the infarct is located near the subarachnoid and ventricle layer that have constant displacement and pressure values.

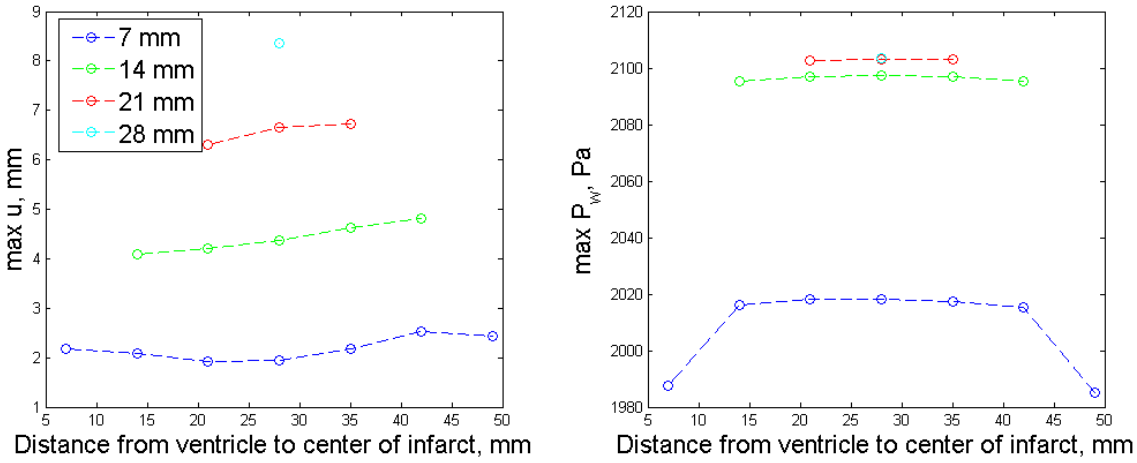

Figure 6.4: Variation of the maximum tissue displacement and interstitial pressure of the cerebral with the infarct location for 2D geometry.

Figure 6.5 shows the results obtained for the 3D simulations. Here, only the results of the infarcts located in the middle between the subarachnoid layer and the ventricle are shown. The geometry is separated into seven equidistant slices to simplify the analysis. The interstitial pressure develops locally and spreads to the region near the ischaemic core. Meanwhile, the tissue displacement starts to develop around the circumference of the core and is propagated through the other regions of the cerebral space. Depending on the size of the ischaemic core, the tissue swelling pushes the non-ischaemic side of the cerebral space from every direction as opposed to what is shown in the 2D results where the swelling pushes the non-ischaemic side significantly only at the top part. Hence,

cerebral swelling after ischaemia reperfusion may also cause the non-affected side of the brain to be damaged as well.

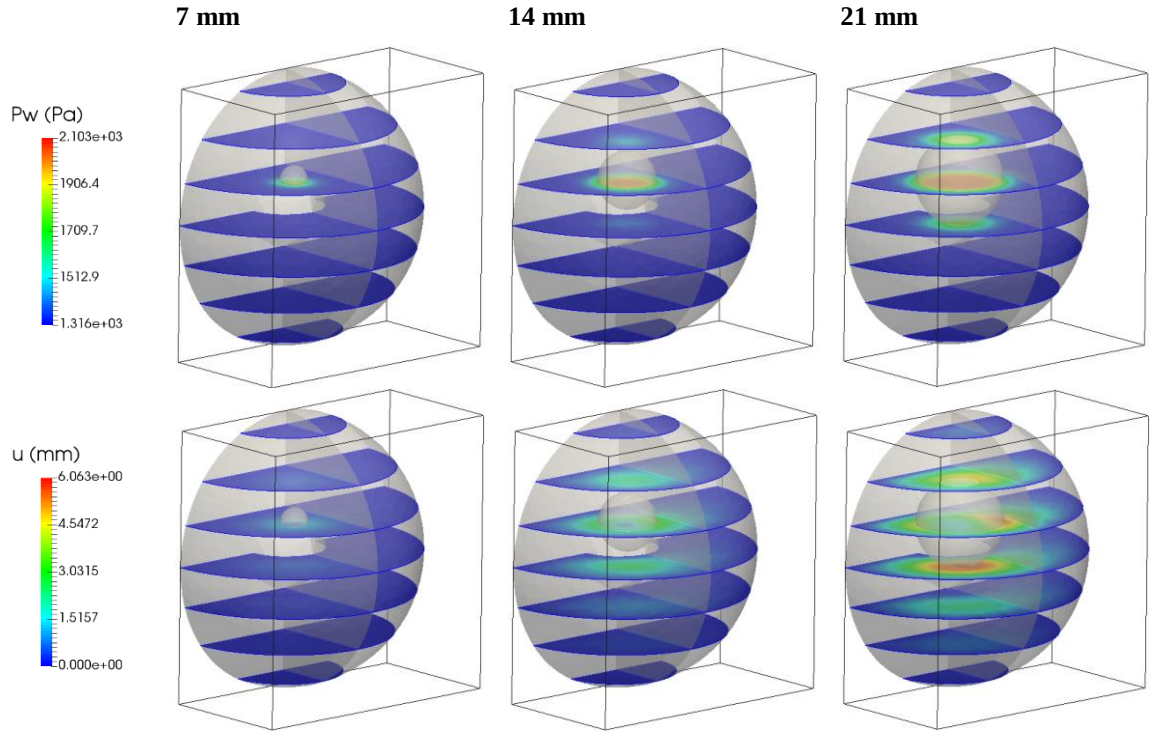

Figure 6.5: Cerebral interstitial pressure, P_w and tissue displacement, u for the different infarct sizes solved in 3D geometry.

Figure 6.6 shows the variations in interstitial pressure and tissue displacement dependent on the location of the ischaemic core for the model solved in 3D. For the interstitial pressure, the variation with infarct location is approximately at 2090 Pa and 2110 Pa for infarct radii of 14 mm and 21 mm, respectively. Meanwhile for an infarct radius of 7 mm, the pressure is constant at a value of about 1960 Pa, with an exception for when the infarct is located near the ventricle and subarachnoid layer, where the pressure is slightly lower at about 1940 Pa. For the tissue displacement, both infarct radii of 14 mm and 21 mm show increasing tissue displacement with increasing distance of infarct from the ventricle. Meanwhile, for an infarct size of 7 mm radius, the tissue displacement is roughly similar independent of the varying distance from the ventricle, being in the range of 1.2 to 1.5 mm.

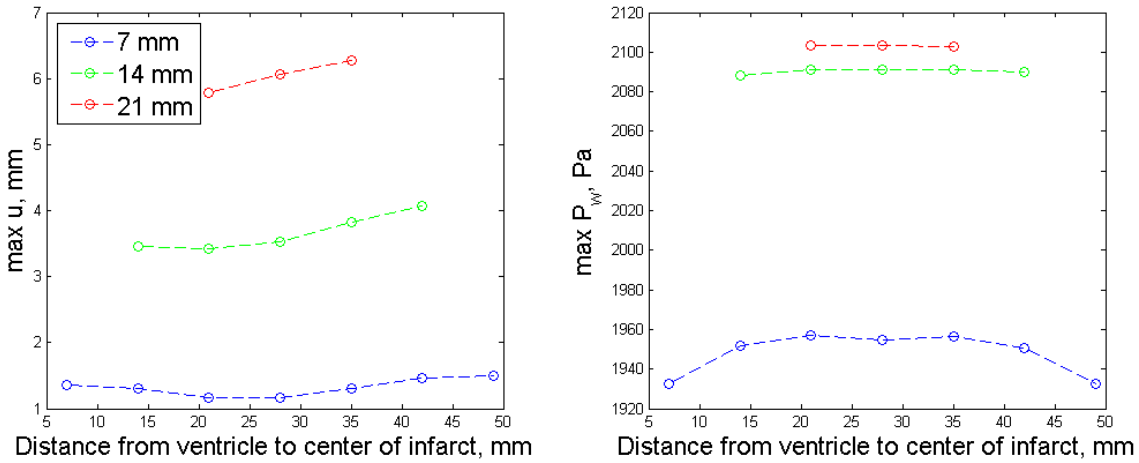

Figure 6.6: Variation of the maximum tissue displacement and interstitial pressure of the cerebral space with the infarct location for 3D geometry.

Figure 6.7 shows the comparison of the maximum cerebral interstitial pressure and tissue displacement with varying infarct size for the model when solved in 1D, 2D and 3D. The results obtained from the 1D simulation give the lowest values of pressure and displacement; meanwhile the 2D simulation results give the highest. The difference in the interstitial pressure for all of the three types of simulation is more noticeable for infarct size of 7 mm as compared to larger infarct sizes, while the difference in the tissue displacement is quite similar for all infarct sizes. Despite these differences, these two variables show a constantly increasing trend as the infarct size becomes larger.

In addition, the interstitial pressure for all of the three simulations reaches a constant value at about 2100 Pa as the infarct size becomes larger. This trend might indicate that the interstitial pressure will increase only a little for larger infarct sizes and this is lower than the predicted collapse pressure, which was previously found to be 2194.5 Pa. Nonetheless, the pressure value obtained is only about 4.3% less than the collapse pressure down to the size of infarct of 14 mm. Although the value obtained is less than the predicted value of collapse pressure, the predicted value is entirely dependent on the vessel properties such as the stiffness and sizes, which still indicates a potential risk of secondary ischaemia attack.

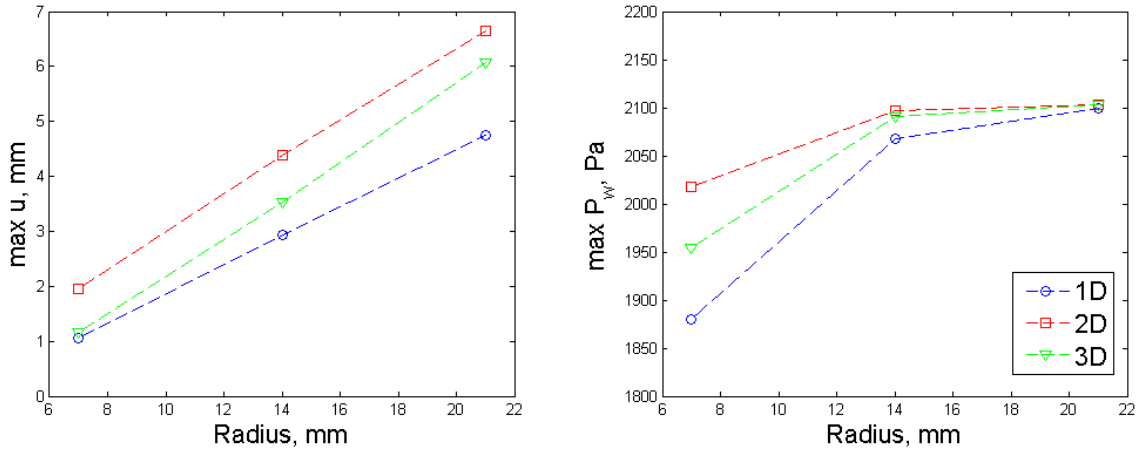

Figure 6.7: Comparison of the maximum cerebral interstitial pressure, P_w and tissue displacement, u between the results obtained in 1D, 2D and 3D.

6.6.2 Two-Compartment Model

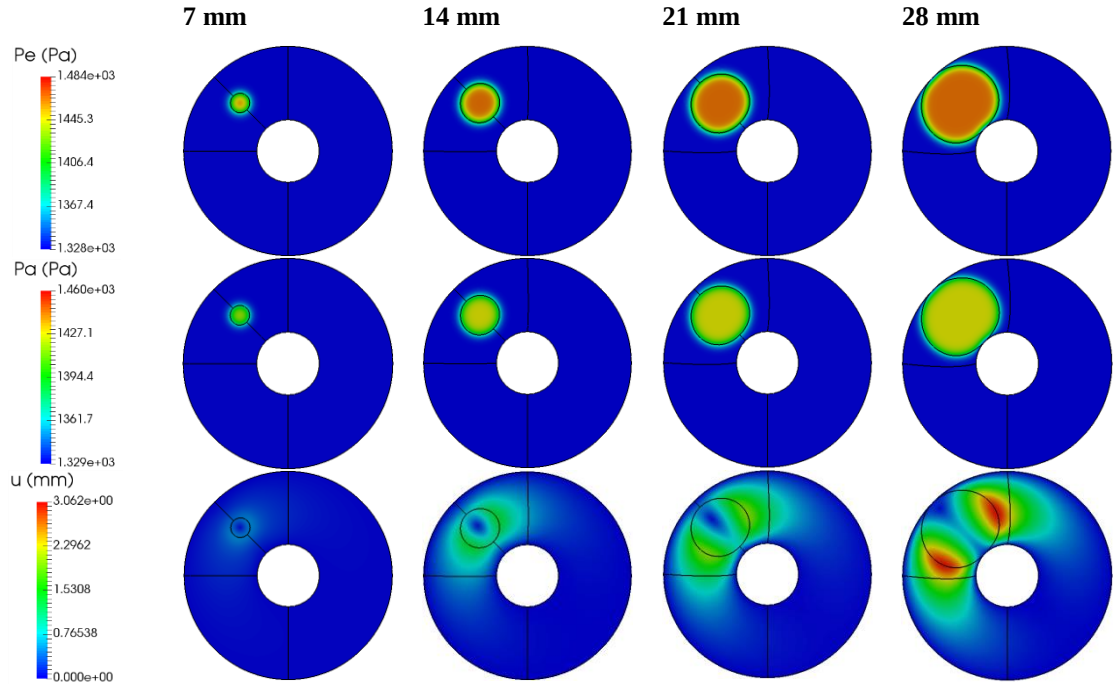

Figure 6.8: Cerebral ECS pressure, P_e, astrocyte pressure, P_a, and tissue displacement, u for the different infarct sizes with $\frac{n_{AQP4b}}{n_{AQP4e}} = 10$, solved in 2D geometry.

The two-compartment model also has the minimum pressure that can cause capillary vessels to collapse, which is similar to the single compartment model. Figure 6.8 shows the cerebral tissue displacement, ECS and astrocyte fluid pressure distributions in the 2D idealised geometry for the case when the infarct is located in the midpoint

between the ventricle and subarachnoid layer. The tissue displacement develops at the circumference of the infarct and spreads radially. Meanwhile, the ECS pressure is higher than the astrocyte pressure although both of these fluid pressures start to develop within the core before spreading radially throughout the infarct. The ECS pressure can, however, only reach up to 1480 Pa, which is 32.6% less than the minimum critical pressure that can cause capillary vessel collapse.

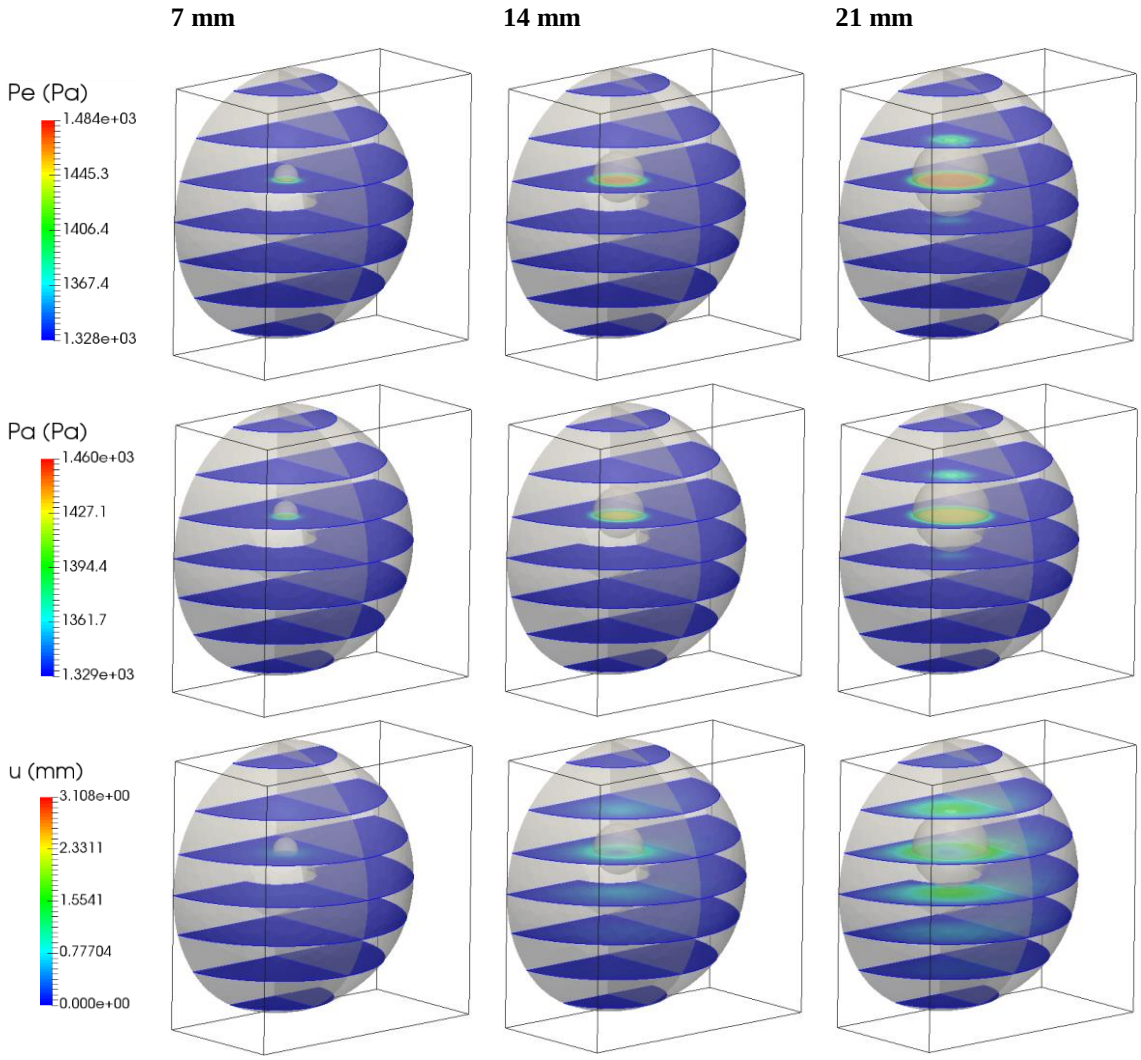

Figure 6.9: Cerebral ECS pressure, P_e, astrocyte pressure, P_a, and tissue displacement, u for the different infarct sizes with $\frac{n_{AQP4b}}{n_{AQP4e}} = 10$ and are solved in 3D geometry.

On the other hand, Figure 6.9 shows the cerebral fluid pressures and tissue displacement distributions obtained using a 3D idealised geometry. Again, the results

show here are for the case when the infarct is located in the middle between the ventricle and the subarachnoid layer. The ECS pressure is again higher than the astrocyte pressure and both develop initially at the centre of the infarct and then spread radially. Meanwhile, the tissue displacement also starts to develop at the circumference of the infarct before spreading outwards from the infarct core.

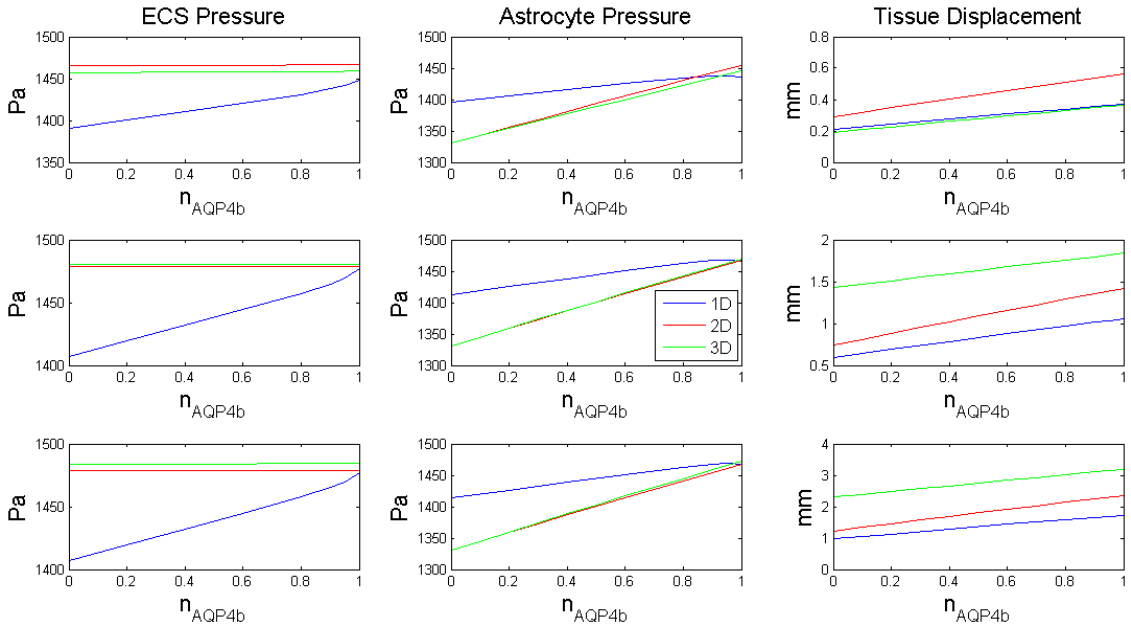

Figure 6.10: Comparison of the variation of the cerebral ECS pressure, P_e, astrocyte pressure, P_a, and tissue displacement, u with n_{AQP4b} for infarct radii of 7 mm (top), 14 mm (middle), and 21 mm (bottom) between the model solved in 1D, 2D and 3D.

Figure 6.10 compares the variations of the cerebral ECS pressure, astrocyte pressure and tissue displacement with the perivascular AQP4 ratio for the 1D, 2D and 3D simulations for infarct radii of 7 mm, 14 mm, and 21 mm. The ECS pressure obtained in 2D and 3D simulations is approximately constant with varying AQP4 ratio for all of the infarct sizes, while the ECS pressure increases linearly with the rate of about 70 Pa/n_{AQP4b} for the 1D simulation. On the other hand, the astrocyte pressure obtained from 2D and 3D shows a linear relationship between the pressure and n_{AQP4b}. However, this is not the case for the 1D simulation where the astrocyte pressure varies linearly up to $n_{AQP4b} = 0.8$ and then starts dropping slightly until $n_{AQP4b} = 1.0$. Meanwhile, the tissue

displacement obtained in the 3D simulations is the highest for the infarct sizes of 14 mm and 21 mm radius. For the case of the 7 mm infarct radius, the tissue displacement obtained in the 2D simulation is the highest. In general, the tissue displacement obtained in the 1D simulation is the smallest in all of the three cases.

6.6.3 Comparison between the Two Models

The two models developed here; the single compartment model and the two-compartment model are compared specifically for the results obtained through 3D simulation as shown in Figure 6.11. Both the tissue displacement and the interstitial pressure obtained using the single compartment model are higher than the two-compartment model for all infarct sizes. The differences are about 50% for both of the variables measured. It should be noted that only the ECS pressure is considered here as representing the interstitial pressure in the two-compartment model, which can contribute to the occurrence of capillary collapse.

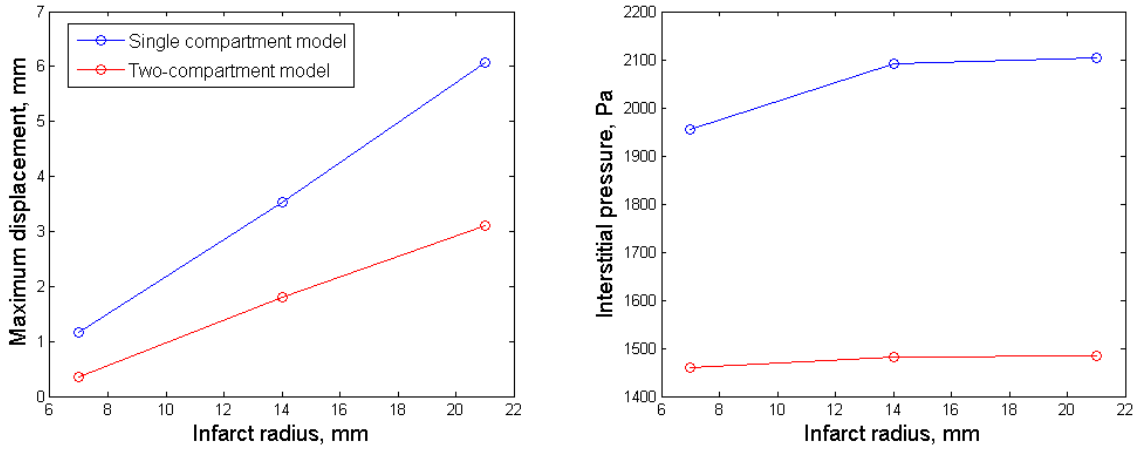

Figure 6.11: Comparison between the two models for simulations in 3D.

6.7 Discussion

The single compartment model and two-compartment model, which were developed previously, have been applied here using 2D and 3D finite element analysis.

One of the noticeable features of the results is that the cerebral swelling due to ischaemia-reperfusion on one side of the cerebral space causes the brain tissue to shift noticeably into the non-infarcted side of the cerebral space. This can be seen clearly from the deflection of the middle line and plane, respectively in the 2D and 3D geometries during the swelling process. The progression of the cerebral swelling is due to the pressure gradient developed within the cerebral space. This can be seen from the elevation of the fluid pressure within the infarcted area as compared to the other non-infarcted region. It was shown in an earlier study (Frank, 1995) that the elevation of the ICP within the cerebral space is the main cause of brain tissue shift during cerebral swelling. This shift in the brain tissue may cause significant neurologic deterioration, brain ventricular compression and cerebral vascular compression.

It is also observable from the results that the single compartment model gives a higher value of cerebral tissue displacement and interstitial pressure than the two-compartment model. This is because the volume ratio for ECS as revised in the two-compartment model is 20% (Go, 1997; Nicholson et al., 1998). Meanwhile, in the single compartment model, the water volume ratio is taken to be 80% accounting for all volume of water within the cerebral space. It is assumed here that it is only the ECS pressure that causes the cerebral microvessel to collapse. In fact, the swelling of the astrocyte endfeet may also cause the compression of the vessel during ischaemia-reperfusion (Verkhratsky et al., 2007) although its effect on vessel compression was described previously (Chiang et al., 1968) as being a combined effect, together with other cerebral components such as the ECS, neuronal swelling and capillary endothelial cell swelling. Because of this complexity in describing the effect of astrocyte swelling on vessel compression, it is omitted from the model for now.

It has also been assumed here that the fluid pressures and tissue displacement at the subarachnoid layer are fixed at baseline ICP and zero displacement respectively. Such an assumption is in accordance with the fact that there is a system of short strands that fix the subarachnoid layer with the skull (Wirth et al., 2006) and hence, this layer can be treated as rigid. However, care should be taken that this can only be applied to adults because infant skulls are usually flexible and can easily deform, as in the case of infantile hydrocephalus (Wirth et al., 2006). A different approach has been suggested in a previous study of a finite element model of a head injury (Canaple et al., 2003) by making the subarachnoid layer to be the interface between the skull and the brain with a low shear modulus to allow relative motion between the cerebral space and the skull.

Meanwhile, the ventricle has been assumed to have a fixed shape and position to simplify the analysis, while in fact, it can be compressed due to tissue swelling and also dilated due to the development of a cerebrospinal fluid (CSF) pressure gradient, especially in the case of hydrocephalus. The compression of the ventricle is also a good indicator of cerebral swelling in CT images (Zimmerman et al., 1978). As obtained in the results here, swelling can also be observed by the deformation of the middle line that divides the two cerebral hemispheres. It is known that the existence of AQP4 at the interface of the ventricle and the cerebral space can help in the clearance of oedematous fluid (Papadopoulos et al., 2013). Thus, a further improvement to the model could be made by incorporating a pressure gradient (Taylor et al., 2004) and stress-free boundary conditions (Liu et al., 2009) at the ventricle to see how the presence of this fluid cavity affects the progression of cerebral swelling and fluid pressure development. Additionally, the ventricle actually has a concave shape and it is found that this shape allows the converging of the direction of the compressive forces on the cerebral tissue (Peña et al., 1999). The study could thus also be extended by using a cerebral geometry drawn with a

more realistic ventricle shape as previously done by Wirth et al. (2006). A probability-based formulation of a finite element model developed by Martin et al. (1994) has been used to determine the deformation of the ventricle in both normal and pathological human brains and the results show that the ventricle is indeed a complicated structure which varies depending on the brain disease and overall brain shape of a patient.

In the finite element model developed here, it has been assumed that the cerebral tissue property is homogeneous throughout the geometry. In reality, the cerebral tissue material properties are different for those located in the white and grey matter of the cerebral space. Oedema is less likely to develop in the grey matter area due to its twisted structure and it has a low tissue compliance as compared to white matter (Kimelberg, 2004). The study done by Smillie et al. (2005) also assumed that the mechanical properties of white and grey matter are the same due to the lack of data available. However, they use different fluid permeability values within these two cerebral structures. Meanwhile, the model developed by Nagashima et al. (1990) used two different cerebral tissue hydraulic conductivity values to account for their different properties. Therefore, by incorporating the different properties in the white and grey matter into the models, the results could be improved as well as the prediction of cerebral swelling progression in the brain during ischaemia-reperfusion.

Solving the models in 2D and 3D requires more computational resources compared to solving in 1D. However, it can be seen from the 2D and 3D simulations that the ischaemia-reperfusion causes the tissue in the infarcted region to compress the unaffected cerebral hemisphere causing brain herniation, which cannot be seen in 1D simulation. This can be seen by the deflection of the middle line and plane that divide the 2D and 3D cerebral geometries, respectively. Despite this, it can be seen from Figure 6.7 and Figure 6.10 that the trend for the tissue displacement and fluid pressures are

approximately similar although with several exceptions. For example, in Figure 6.7, the maximum interstitial pressure varies greatly for infarct size of 7 mm of radius but the variations are lesser for bigger infarct sizes. This is probably due to the different shapes of the geometry used in each of the 1D, 2D and 3D simulations. Another example is in Figure 6.10 where the variation of fluid pressures with n_{AQP4b} obtained in 1D simulation varies greatly compared to 2D and 3D simulations, and this difference is also due to the different shapes of geometry used. However, the models developed here are expected to be solved in 2D and 3D as these are comparable with the actual brain geometry obtained through imaging modalities such as MRI or CT scan.

6.8 Summary

The finite element analysis of the single compartment and two-compartment models has been done here in both 2D and 3D geometries and the results compared with the results obtained in Chapter 3 and Chapter 4, which were solved in 1D. The results obtained here provide further useful information such as: (1) the importance of making the ventricle structure movable for better quantification of the brain tissue swelling; and (2) confirms the occurrence of herniation during brain tissue swelling. This information are useful before the models can be applied to the actual patient data for validation purposes.

Chapter 7

Model Validation

7.1 Introduction

Brain herniation is a condition when the brain tissue, cerebrospinal fluid (CSF) and blood vessels are compressed and displaced from the original position. It is one of the effects of reperfusion treatment after ischaemic stroke that can most readily be observed from MRI and CT scans of patients (Berrouschot et al., 1998; Koudstaal et al., 1988; Wunderlich et al., 2007). The presence of brain herniation may indicate the elevation of intracranial pressure (ICP) and it may cause permanent neurological problems and even fatality. Intensive action is taken to treat brain herniation by reducing the ICP using osmotherapeutics such as mannitol (Adams et al., 1994; Hacke et al., 2000) and decompressive surgery (Cushing, 1905).

Other indicators of the increase in ICP are the midline shift of the brain, the change in ventricular shape and size, and the loss of distinction between the grey and white matters (Lee et al., 2005). These indicators can be caused by various brain pathological conditions such as traumatic brain injury, stroke, and haematoma (Gruen, 2002). These indicators, may not however provide early indication of cerebral swelling (Tomura et al., 1988; von Kummer et al., 1994); they may be more evident at later stages of cerebral oedema (von Kummer, R. et al., 1997). However, ventricle compression can be used as a method of validating the mathematical models developed in Chapter 3 and 4.

In this chapter, the mathematical models developed will be validated with magnetic resonance imaging (MRI) images of stroke patients. The images will first be processed to remove unwanted artefacts and then reconstructed to form a 3D geometry. The mathematical models will then be solved for each geometry using finite element analysis (FEA). Validation will be done by comparing FEA simulation results with the MRI images of the patient taken before and after admission to the hospital. From the validation, the models can then be further improved to make them applicable in understanding brain tissue swelling after ischaemia-reperfusion.

7.2 Patient Selection and Image Acquisition

The images used here were obtained from two patients with acute ischaemic stroke that were admitted to Seoul National University Bundang Hospital between November 2010 and July 2013. Both patients selected for this study met the following eligibility criteria: (1) have the first symptoms witnessed within one hour from the last-seen-well time; (2) have MRI scanning within 24 hours from admission; (3) showing the presence of arterial occlusion in the middle cerebral artery (MCA), particularly in main stem (M1) or in the terminal superior and inferior divisions (M2); (4) there are no contralateral occlusions, i.e. the occlusion only occurred in one side of the brain; (5) patient has successfully undergone recanalisation treatment upon diagnosis and receiving modified Treatment In Cerebral Infarction (mTICI) score of 2b or higher; (6) the infarct size is large and located near the brain ventricles, so that a significant ventricle compression is observable for validation purposes; and (7) there must be no occurrence of haemorrhagic transformation on the patient after the reperfusion treatment.

The outcomes of the treatment received by the patients are measured using two commonly used scores for stroke patient, namely: (1) the National Institutes of Health Stroke Scale (NIHSS); which describes the severity of stroke; and (2) the modified Rankin Scale (mRS); which describes the degree of disability and dependency in daily activities after stroke (Rankin, 1957). In addition, the mTICI score is used by the clinicians to evaluate the effectiveness of the recanalisation treatment and this is based on the score used in a study done by IMS II Trial Investigators (2007). Grade 2b means that there is perfusion through more than 50% of the MCA distribution.

The imaging was performed on either Philips Intra 1. 5T, Achieva 3.0T or Ingenia 3.0T MRI scanners. The patients must have gone through medical imaging scanning at two different time points, which are at: (1) the presentation time (PT), which was done immediately after admission to the hospital; and at (2) the follow-up time (FUT), which was done before the patient is discharged. The following types of MRI images were taken during the FUT: (1) structural T2 MRI, which will be used to develop the brain and the ventricle geometries; (2) diffusion-weighted (DWI) MRI, which will be used to determine the infarct location and size, and also to develop the infarct geometry; and (3) fluid-attenuated inversion recovery (FLAIR) MRI, which was taken at FUT in addition to DWI MRI and to be used as validation purposes. The next section will describe the characteristic of each patient used for this study.

7.2.1 Patients Characteristics

Table 7.1 below lists the characteristics, the diagnosis time, and the type of treatments received for both patients during their admission at the hospital. Both patients are female and of ages 49 and 56, respectively. Patient 1 has blood pressure value recorded during admission, which showed that this patient has Stage 2 hypertension

according to the scale defined by the American Heart Association. Meanwhile, patient 2 has normal blood pressure. Both patients have no history of stroke occurrence and both currently are smokers. Further, both patients have a left MCAO infarct, which is shown in the MRI images in more detail in the next sections.

Table 7.1: Characteristics of each patient selected for this study.

	Patient 1	**Patient 2**
Gender	Female	Female
Age	49	56
Weight, kg	70	57.3
Height, cm	168	170
Systolic blood pressure, mmHg	169	112
Diastolic blood pressure, mmHg	108	91
Past stroke occurrences	No	No
Last known time without stroke symptoms	23rd March 2013 at 19:00 p.m.	10th March 2012 at 19:00 p.m.
Time of arrival to hospital	23rd March 2013 at 20:47 p.m.	10th March 2012 at 23:54 p.m.
Presentation time	23rd March 2013 at 21:26 p.m.	11th March 2012 at 00:13 a.m.
Follow-up time	27th March 2013 at 15:24 p.m.	12th March 2012 at 21:37 p.m.
Time of discharge from hospital	28th March 2013	17th March 2012
Treatment received	IV and IA	IA

Table 7.2: The NIHSS, mRS, and mTICI scores received by both patients.

	NIHSS	**mRS**	**mTICI**
Patient 1			
During admission	22 (Severe stroke)	-	-
During discharge	8 (Moderate stroke)	3 (Moderate disability. Requires some help, but able to walk unassisted.)	2b
Patient 2			
During admission	0 (No stroke symptoms)	-	-
During discharge	2 (Minor stroke)	1 (No significant disability. Able to carry out all usual activities, despite some symptoms.)	2b

The stroke time window both patients are 2:26 hours and 5:13 hours, respectively, which is calculated by finding the difference between the presentation time and last known time without stroke symptoms. The treatment received by the patients is either intravenous (IV), intra-arterial (IA) or both. The outcome of the treatment is listed in Table 7.2, which is indicated by NIHSS, mRS, and mTICI scores.

7.3 Image Processing and Geometry Development

Three different types of MRI images; the T2 images, the DWI images, and the FLAIR images were taken from the patients. The T2 images were used to differentiate anatomical structures within the brain; meanwhile the DWI and FLAIR images were used to assess the infarct formed before and after cerebral ischaemia-reperfusion. The images were viewed and processed using open-source MRI images viewing tool, FSL (Jenkinson et al., 2012) and MATLAB.

7.3.1 Brain Images Extraction and Segmentation

The cerebral image was extracted from the PT T2 images to remove unwanted structures such as the skull, scalp surfaces, eyes and face using a brain extraction tool, BET (Smith, 2002). The cerebral image was then segmented into different tissue types such as the grey matter, white matter and cerebrospinal fluid (CSF) using an automated segmentation tool, FAST (Zhang et al., 2001). This segmentation process is important in determining the approximate shape and location of the brain ventricles. However, only the lateral ventricles were taken into consideration during the geometry development because their compressions are readily visible from the MRI images. The final image obtained from these T2 images then became the basis for the brain geometry development. Figure 7.1 illustrates the steps involved in the processing of the PT T2 images.

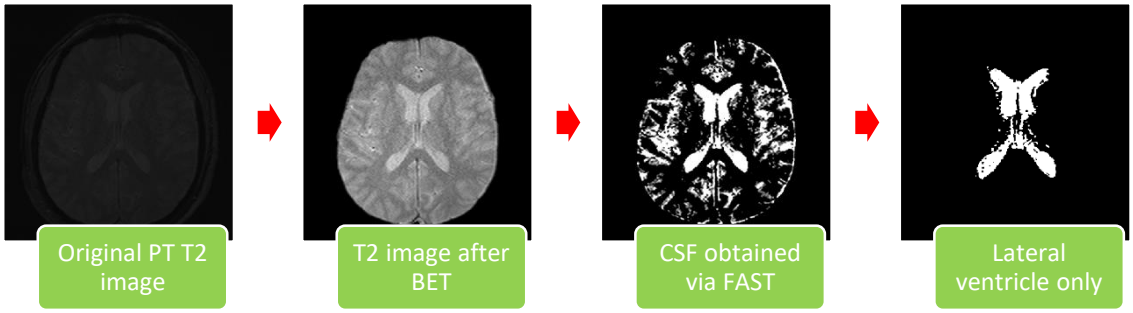

Figure 7.1: Steps involved in obtaining the lateral ventricle image from PT T2 images.

Meanwhile, the DWI and FLAIR images were used to determine the infarct shape and location. The images must first undergo image registration processes to realign the images into the same coordinate system as in the original PT T2 images. This was done using a fully automated linear brain image registration tool, FLIRT (Jenkinson et al., 2002; Jenkinson et al., 2001). Then, the brain extraction processes were performed from the realigned DWI images using BET. The infarcted tissue region was then segmented from the extracted DWI and FLAIR images using a semi-automatic interactive segmentation tool (Levman et al., 2014). This tool utilises a supervised machine learning algorithm to classify each voxel based on the intensity of the signal training voxels. Figure 7.2 shows an example of an ischaemic infarct obtained from DWI images.

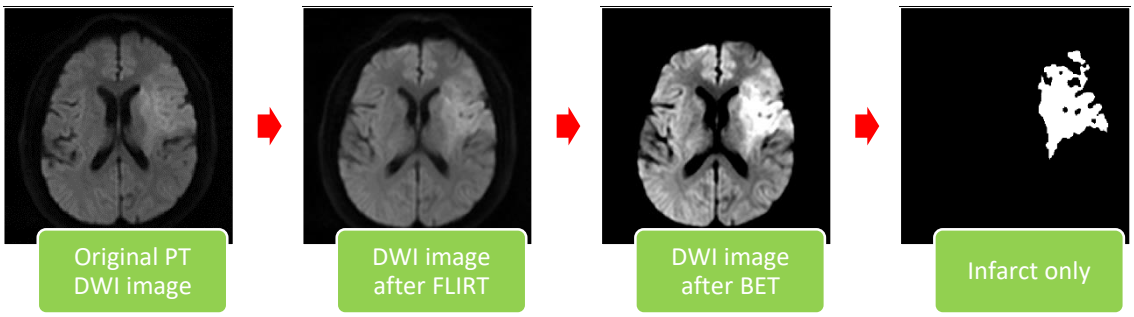

Figure 7.2: Steps involved in obtaining the infarct image from PT DWI images.

For the FUT images, the images first underwent registration process using FLIRT before going through the brain extraction processes using BET. The FUT images were then used to compare the progression of tissue swelling obtained from the patients and the simulation. The tissue swelling can be quantified by measuring the compression on

the lateral ventricles. All of the images obtained from these processing steps were saved in NIfTI format. To summarise the segmentation processes, Figure 7.3 shows the steps involved in the processes of the FUT images.

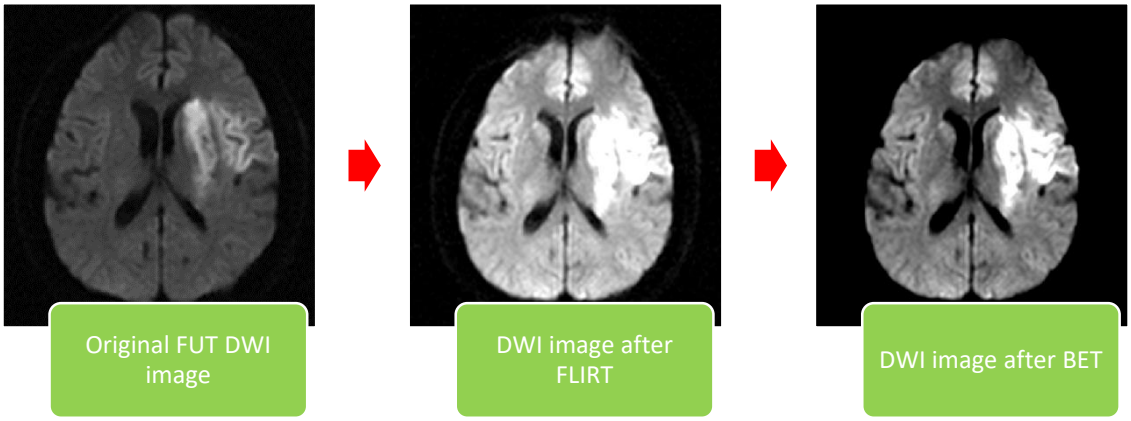

Figure 7.3: Steps involved in processing the FUT images with DWI images as examples.

7.3.2 Brain Geometry Development and Meshing

The brain, ventricle and infarct images obtained in the previous steps were again segmented using open-source 3D semi-automatic segmentation software, ITK-SNAP (Yushkevich et al., 2006), to obtain better approximation of these structures, which is illustrated in Figure 7.4. ITK-SNAP utilises a method called snake evolution which determines the boundaries of the different structures based on the image intensities. ITK-SNAP also provides the capability to readily convert the segmented image into surface meshes, which is useful for volume mesh generation for FEA simulations. The segmented geometries were saved as surface mesh in StereoLithography (.stl) file format.

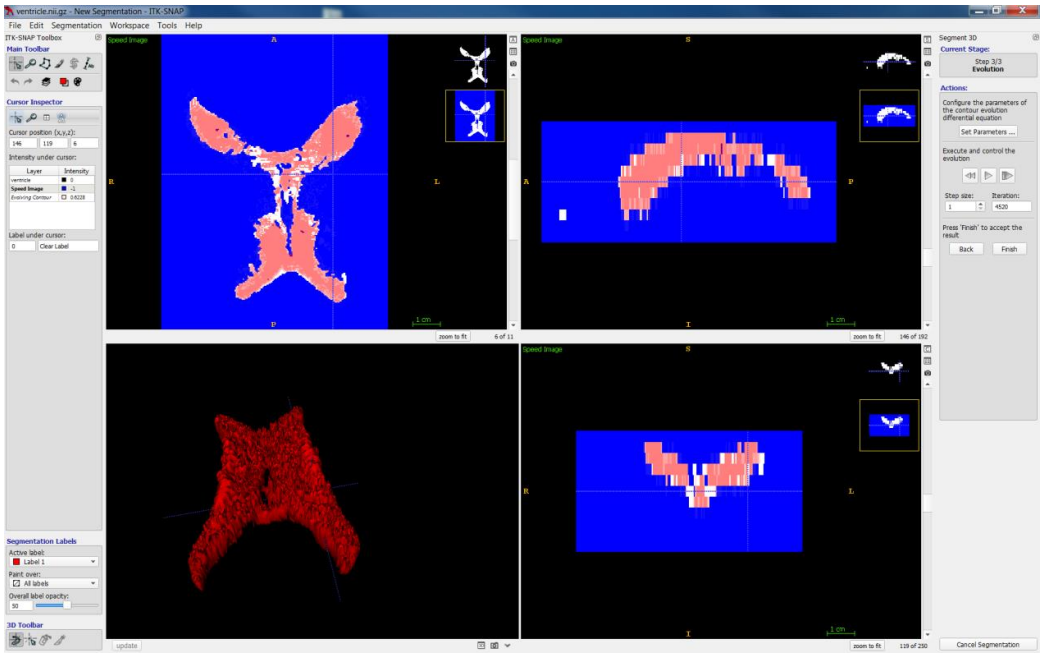

Figure 7.4: Automatic segmentation process using ITK-SNAP to produce surface meshes of the brain geometry.

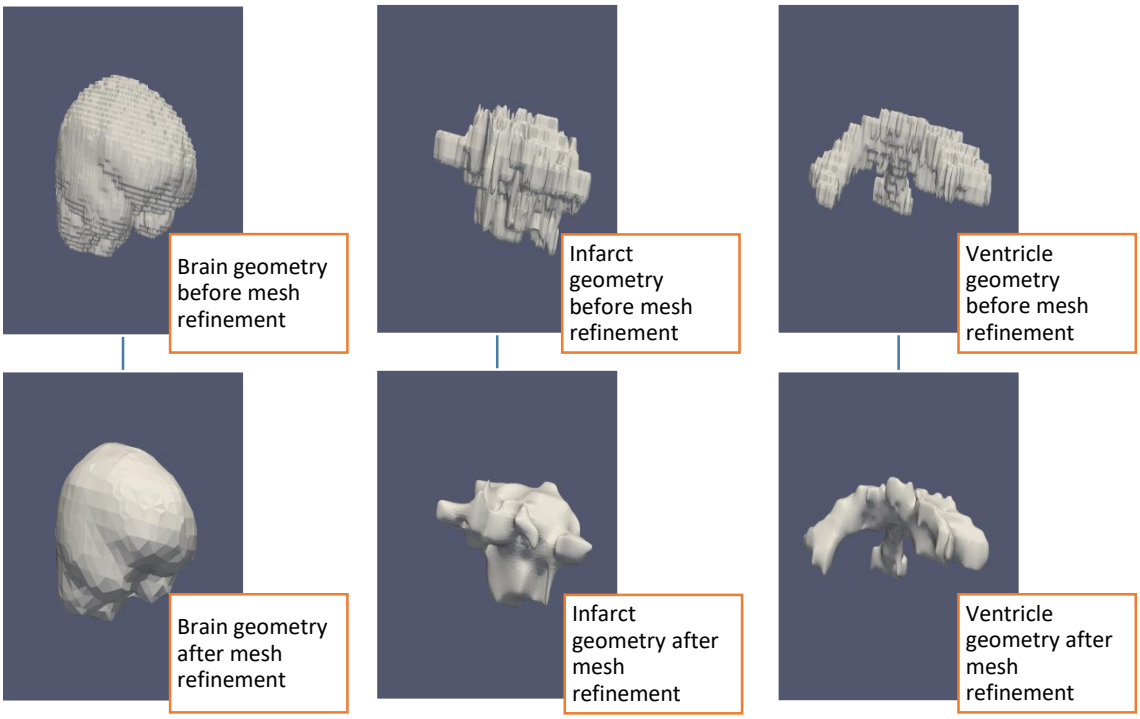

Figure 7.5: Geometries obtained before and after mesh refinement processes.

The mesh refinement process of the surface meshes was carried out using open-source 3D graphics software, Blender. Figure 7.5 shows the brain geometry produced from MRI image segmentation and mesh refinement processes. Mesh refinement is a step

to produce a necessary amount of surface meshes to obtain reasonable results and to save the computational cost. Then, volume meshes were created using open-source mesh generation software, Gmsh (Geuzaine et al., 2009). The meshes produced are finer in the infarct and the ventricle surfaces compared to the other regions in the brain geometry. The final geometries for both patients had approximately 580,000 – 900,000 tetrahedral elements. Figure 7.6 shows the surface meshes of all the geometry combined. The simulation results obtained using this geometry were then compared with the FUT T2 images.

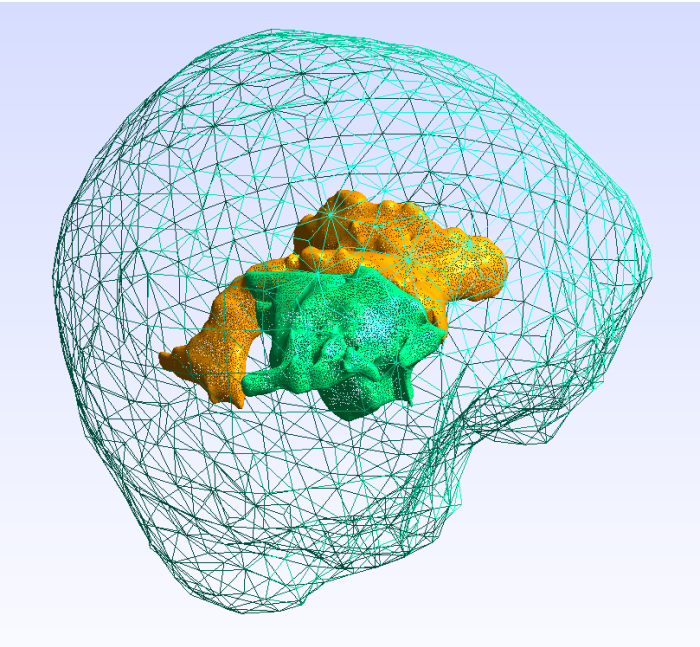

Figure 7.6: Surface mesh of the three structures that make up the overall brain geometry for FEA. The yellow structure is the ventricle. Meanwhile, the inner green structure is the infarct and the outer green structure is the brain.

7.3.3 Comparison between the MRI Images and the Geometry

This section will compare the geometry developed and the original MRI images. Only slices that contain the ventricles will be compared. It is worth noting that the MRI images and the geometry shown here are not in similar scales. The slices are shown from the top to the bottom of the brain where slices at the top are marked with larger numbers.

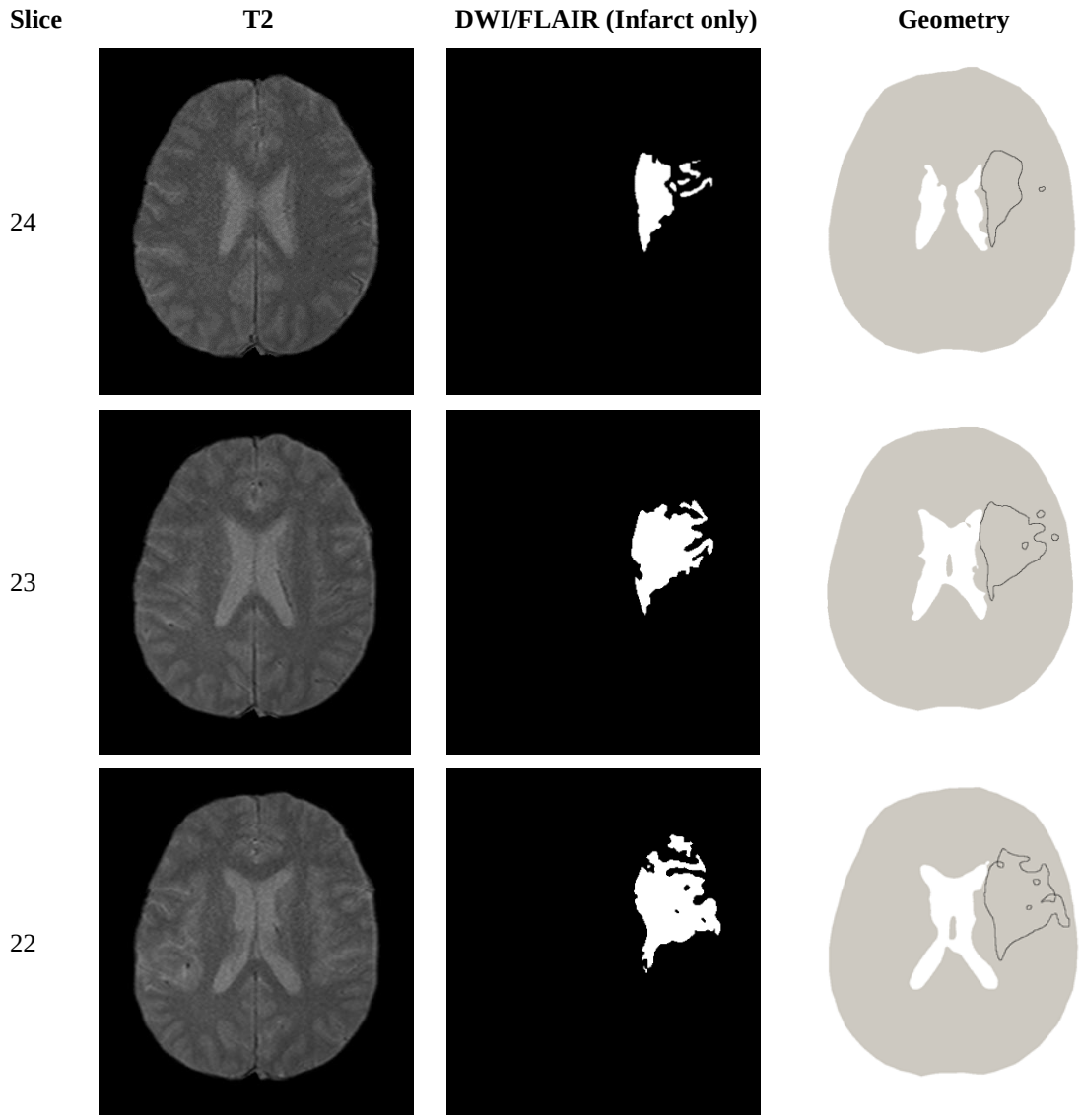

Figure 7.7: The MRI images and geometry of slices 22 to 24 of patient 1.

It is important to point out that the 3D geometry produced is only an approximation to the actual brain. Therefore, only selected slices are chosen for ventricle compression analysis. The chosen slices are based on these criteria: (1) have approximately a similar ventricle shape with their associated MRI image slices, and (2) have a full continuous and distinguishable ventricle. Improvements to the image processing technique will be necessary to obtain a better approximation of the geometry, which will be the subject of future work.

The brain ventricles for patient 1 can be found in slices 17 to 25. Out of these 9 slices, only slices 22, 23 and 24 were chosen for the analysis, as shown in Figure 7.7. On the other hand, patient 2 also has the brain ventricles in slices 17 to 25. Slices 22 to 24 were again chosen for analysis, as shown in Figure 7.8. Other slices were not chosen because: (1) the ventricles are not clearly observable in both the image and the geometry slices; (2) the ventricles produced in the geometry slices are discontinuous, thus rendering them difficult to analyse; and (3) only small portions of the ventricles are present in the slices. The full lists of the slices with the ventricles present are presented in Appendix C.

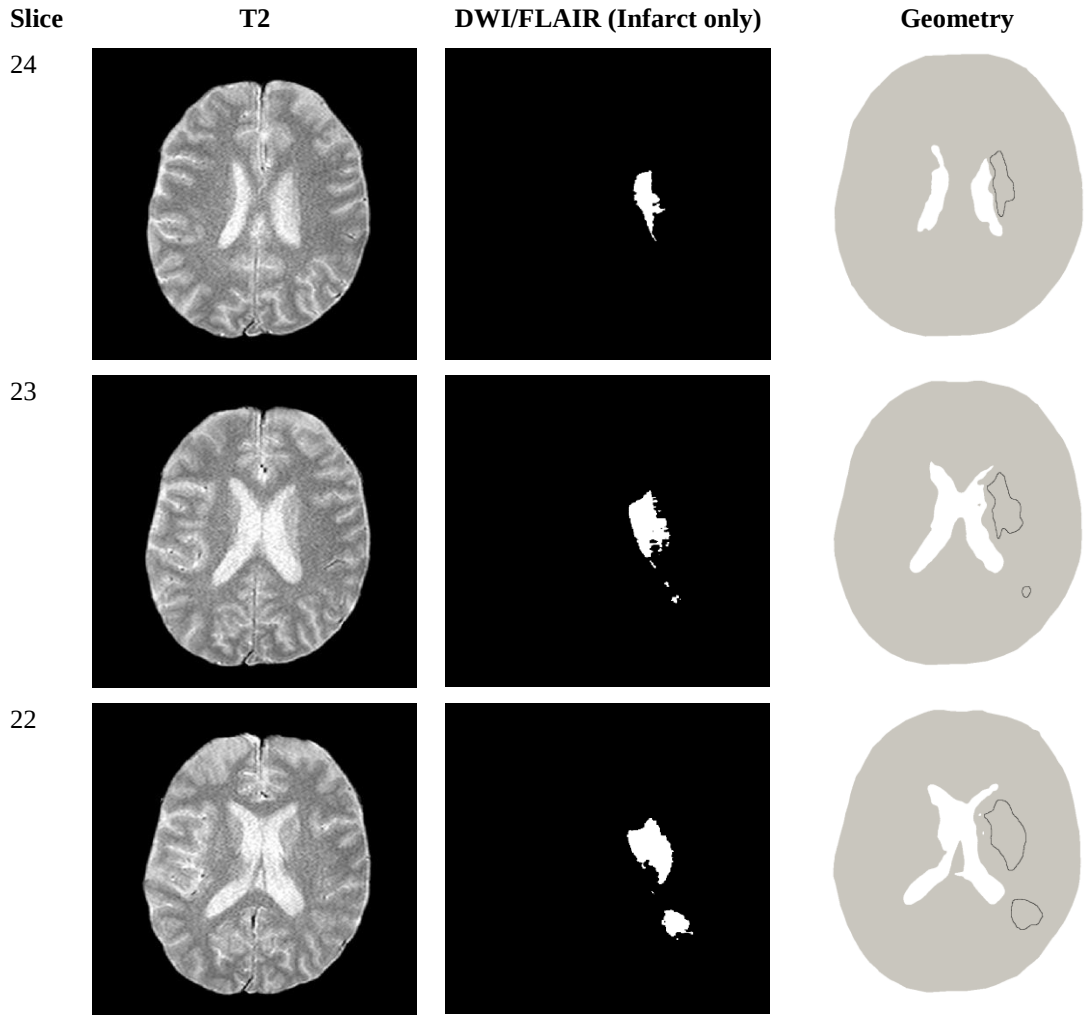

Figure 7.8: The MRI images and geometry of slices 22 to 24 of patient 2.

7.4 Model Implementation

The brain tissue is assumed homogeneous throughout the geometry, where there is no distinction between the white and grey matters in terms of their mechanical properties. In addition, the microvessel distribution in the infarct is also assumed homogeneous, thus the capillary filtration is assumed to occur homogeneously within the infarct. The models are solved on the brain geometry developed using open-source FEA software, ELMER. The models are solved until the fluid pressures reach a steady state. The results are then analysed using open-source visualisation software, ParaView.

7.5 Single Compartment Model

The governing equations for the single compartment model are as described in the section 6.2. The parameters for this model are as described in Chapter 3. The initial condition of the model is given as:

$$u(x, 0) = 0, \tag{7.1}$$

$$P_w(x, 0) = \overline{P}, \tag{7.2}$$

which means that the water pressure , P_w is equal to the intracranial pressure (ICP), and the tissue is initially static.

The water pressure and tissue displacement at the skull boundary, R_S are set as:

$$u(R_S, \mathrm{t}) = 0, \tag{7.3}$$

$$P_w(R_S, \mathrm{t}) = \overline{P}. \tag{7.4}$$

On the other hand, the boundary conditions at the ventricle surface, R_V, is set to allow for the movement of the ventricle during tissue swelling (Liu et al., 2009). Thus, the total tissue stress σ_{ij} on R_V is set as:

$$\sigma_{ij}(R_V, \mathrm{t}) \cdot \mathbf{n} = -P_w(R_S, 0)\mathbf{n}, \tag{7.5}$$

where **n** is the outward unit normal vector of the ventricle surface.

7.5.1 Ventricle Compression, δ_V

One way to validate the model with the available data is by comparing the ventricle compression, δ_V. The ventricle compression is estimated by measuring the horizontal distance from the end of one ventricle to the other. The ventricle end is defined as the point on the ventricle with maximum displacement, which is determined from the simulations. The value of δ_V obtained from the simulations is then compared with the one measured in the FUT images. The measurement procedure is illustrated in detail in Figure 7.9. Here, only the T2 images are shown because the ventricle is clearer on these compared to other images.

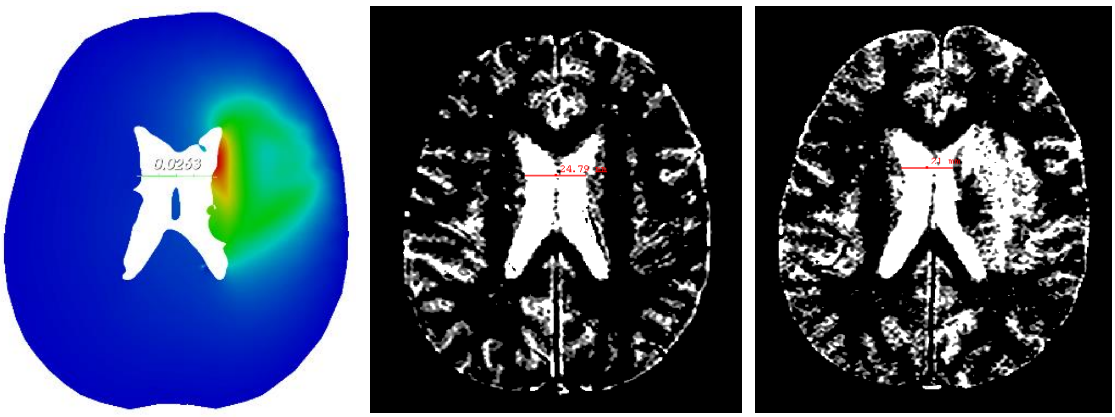

Figure 7.9: Example of ventricle compression, δ_V measurement.

7.5.2 Results for Single Compartment Model

The simulations are carried out until the fluid pressure and tissue displacement reach a steady-state value. Figure 7.10 shows the graphs of maximum P_w and maximum u for both patients. Here, the maximum P_w for both patients reached a steady value of approximately 2100 Pa at about 3 hours after reperfusion, although patient 2 has a slightly lower steady-state P_w value. Meanwhile, the steady-state values for the maximum u for both patients were about 11.5 mm and 12.0 mm and were reached at about 6 hours for

patient 1 and 9 hours for patient 2 after reperfusion. One possible reason for the long time taken for patient 2 to reach a steady value of maximum u is probably due to the fact that the patient has two infarcted regions of different sizes, as previously illustrated in Figure 7.8. Therefore, the infarct swelling might yield a combined effect to the overall tissue swelling and hence, only slowly reaching stability.

Figure 7.11 and Figure 7.13 illustrate the tissue displacement obtained from the simulations for time 1, 3, 5, 7, 10, and 12 hours, for patient 1 and 2, respectively. Also shown in the figures are the cerebrospinal fluid (CSF) contents of the T2 images in presentation and follow-up for side-by-side comparison. From the simulation results of the patient 1, it is clearly evident that the ventricle is overly compressed by the tissue swelling and that this compression is larger than the one observed from the T2 images. Further, it can also be observed here that the region near the ventricle has higher tissue displacement indicating that higher tissue stresses are applied on the ventricles. The same observations can also be seen for the simulation results of patient 2. The figures also show that the left ventricles for both patients are almost totally compressed, see slice 24 of patient 1 and slices 24 and 23 of patient 2.

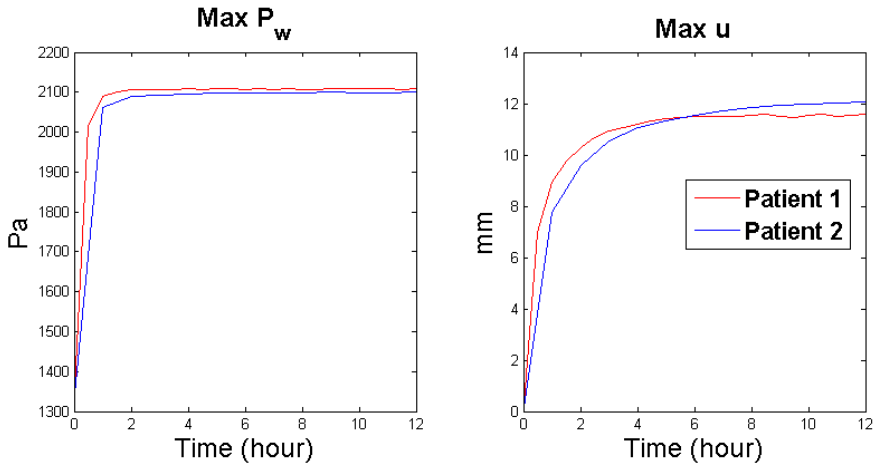

Figure 7.10: Graph of maximum P_w and u against time for the case of Young's modulus of 584 Pa for patient 1 and patient 2.

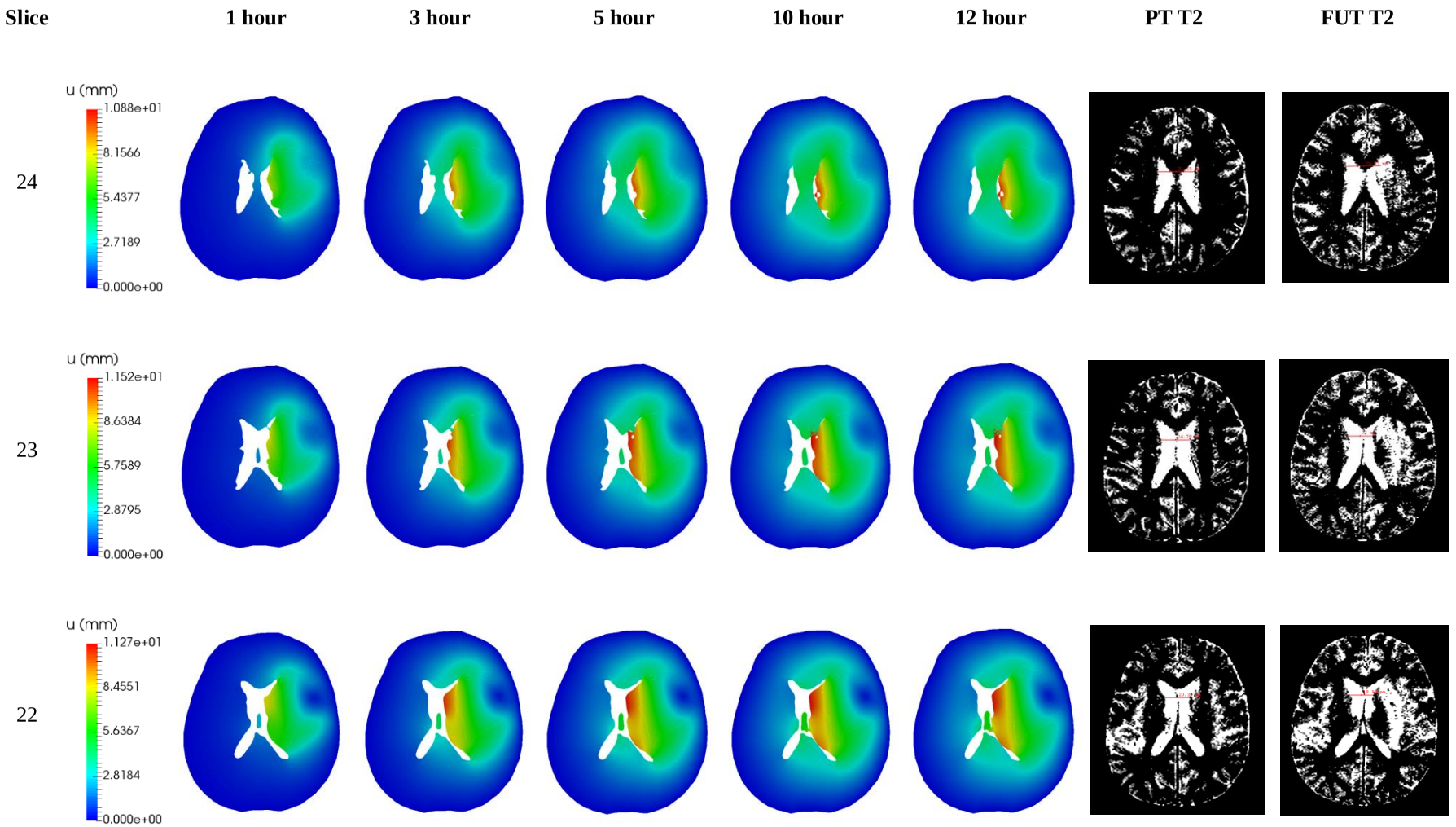

Figure 7.11: Tissue displacement distribution and MRI images for patient 1 with cerebral tissue stiffness of 584 Pa. The δ_V values are 2.41 mm, 3.78 mm, and 1.38 mm for slices 24, 23, and 22, respectively.

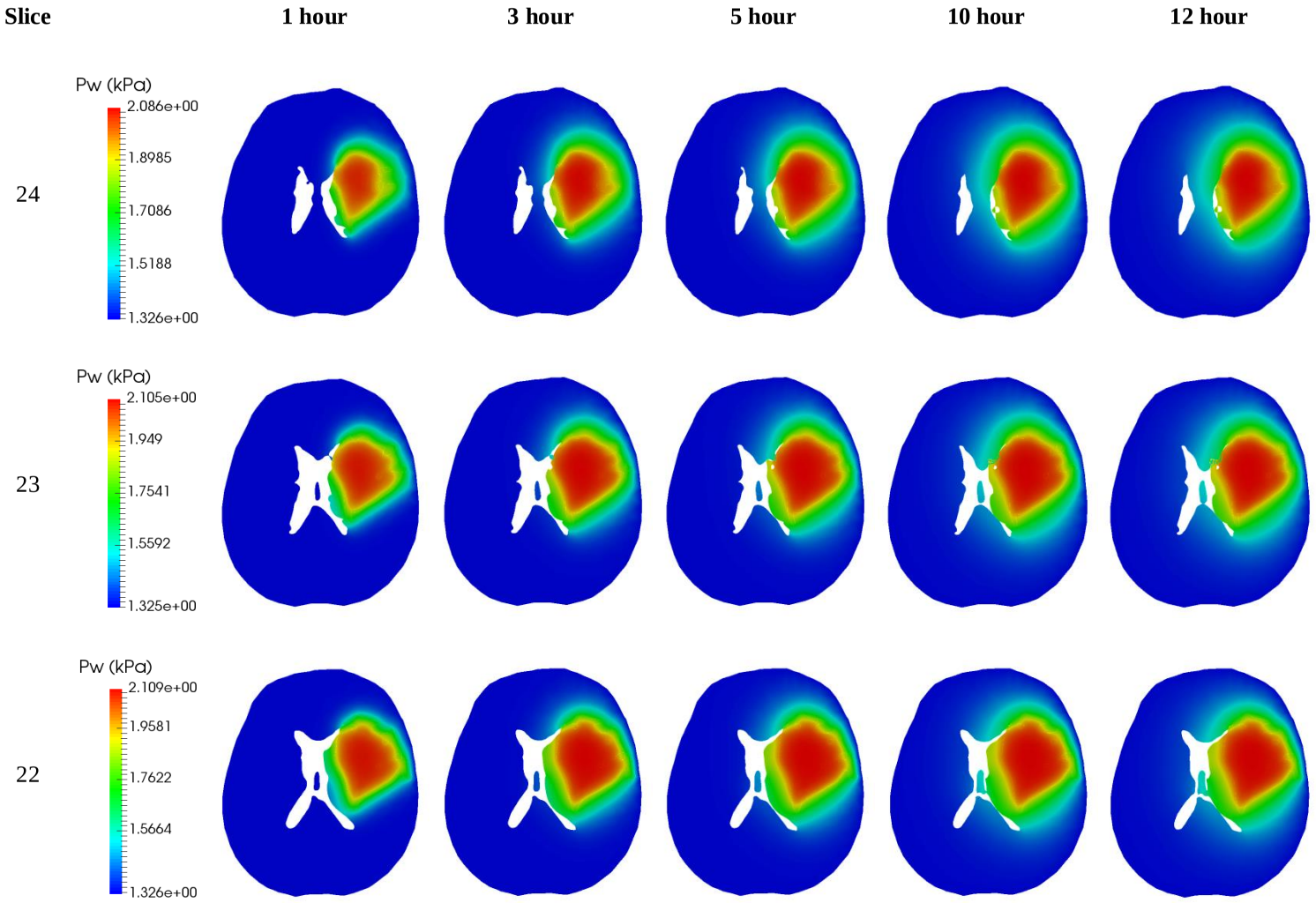

Figure 7.12: Water pressure distribution for patient 1 with cerebral tissue stiffness of 584 Pa.

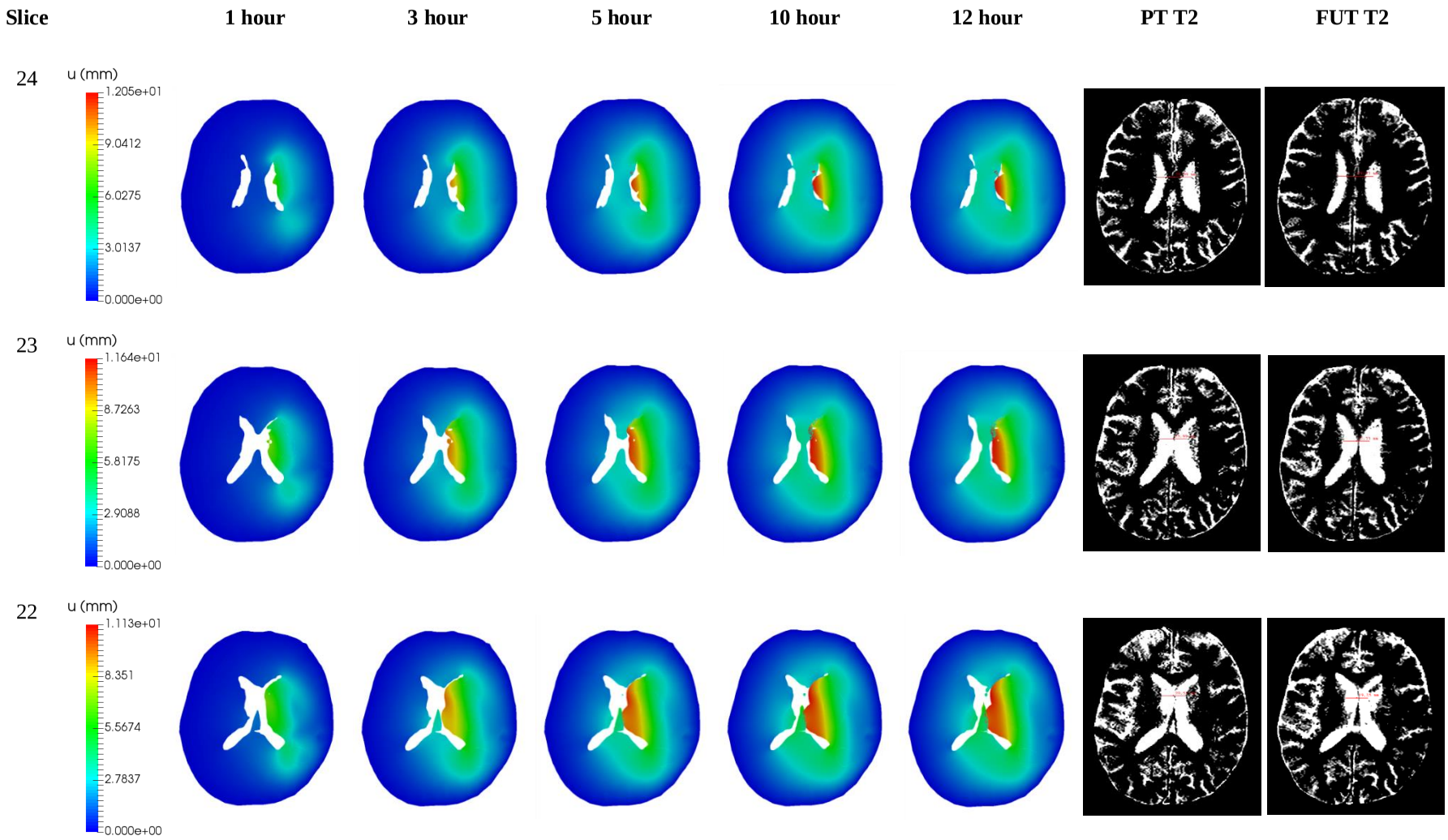

Figure 7.13: Tissue displacement distribution and MRI images for patient 2 with cerebral tissue stiffness of 584 Pa. The δ_V values are 0.32 mm, 1.26 mm, and 1.27 mm for slices 24, 23, and 22, respectively.

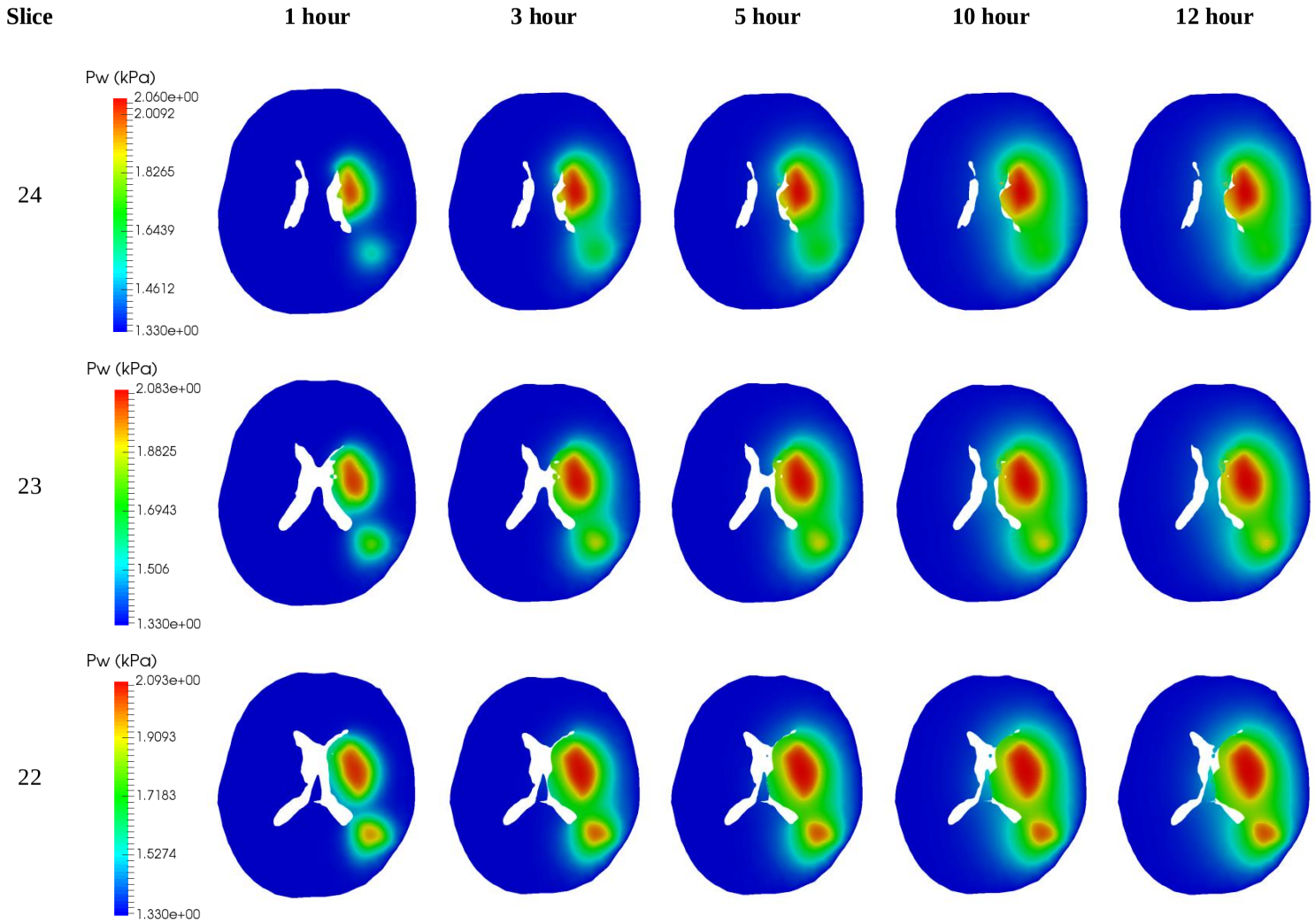

Figure 7.14: Water pressure distribution for patient 2 with cerebral tissue stiffness of 584 Pa.

The water pressure distribution is presented in Figure 7.12 and Figure 7.14 for patients 1 and 2, respectively. The P_w starts to develop from the centre of the infarct and then, it progresses towards the infarct outer layer. As the infarct grows, P_w increases and it progresses along the direction of the infarct growth until reaching a steady-state value of about 2100 Pa as previously shown in Figure 7.10. Although the fluid pressure reached a constant value, as the infarct grows larger due to tissue swelling, the region with the increment of pressure grows as well and will cause the tissue to swell further.

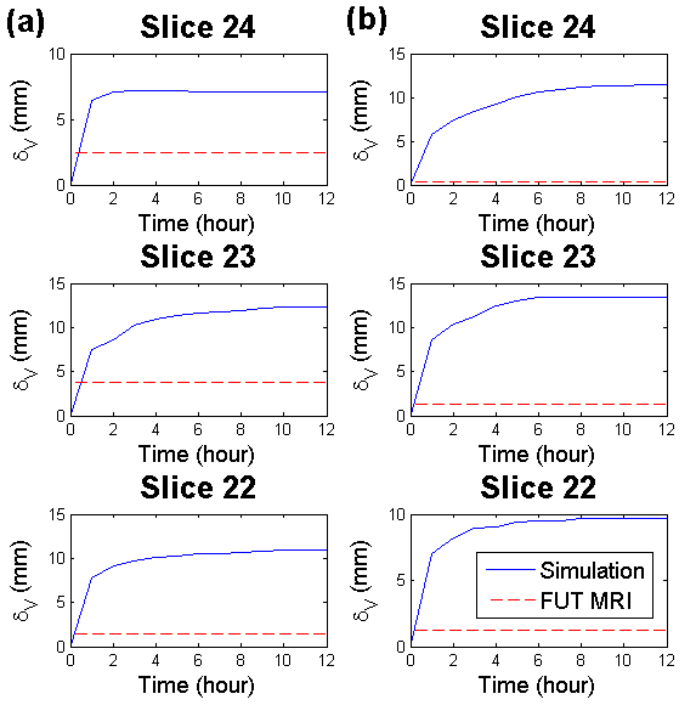

Figure 7.15: Comparison slice-by-slice of δ_V for: (a) patient 1; and (b) patient 2 under baseline cerebral tissue properties.

Finally, Figure 7.15 compares the ventricle compression obtained from the simulations and the MRI images for patient 1 and 2, respectively. It is readily noticeable that δ_V obtained through the simulations is overestimated for both patients. For patient 1, the values of δ_V estimated from the simulations for slices 24, 23, and 22 are approximately 1.8, 2.0, and 7.5 times greater than the MRI images. For patient 2, on the other hand, the δ_V values measured from the simulations and MRI images show marked difference in all

of the three slices. From these observations, it is evident that the model has overestimated the ventricle compression and modification of certain parameters is necessary to achieve a more similar estimation of δ_V.

One may speculate that the overestimation may be due to the small value of cerebral tissue stiffness of 584 Pa. Low values of Young's modulus will produce higher tissue displacements under external forces. This tissue stiffness value was taken from the calculation done on the study of brain hydrocephalus (Taylor et al., 2004). This Young's modulus value of 584 Pa was calculated through the assumption that hydrocephalus occurs at a very low strain rate. This is based on the fact that hydrocephalus is a very slow process, which usually takes few days to fully develop. However, other studies on the mathematical models of the brain utilise a larger Young's modulus value in the range of 10^3 to 10^4 Pa (Kaczmarek et al., 1997; Nagashima et al., 1987; Peña et al., 1999).

On that basis, different values of Young's modulus ranging from 600 to 1500 Pa were then applied to the model to quantify the effects of cerebral tissue stiffness on the ventricle compression during ischaemia-reperfusion cerebral tissue swelling. Figure 7.16 shows the variations of maximum P_w and maximum u when the value of Young's modulus is increased. It can be observed here that the tissue will reach similar maximum P_w but produce less swelling when the tissue stiffness is increased, thus, smaller ventricle compression is expected.

Figure 7.17 shows the change of δ_V against time for five different Young's modulus for both patients. It can be seen here that δ_V can nearly match the measurement made from MRI images when using higher Young's modulus than previously used. The only δ_V values that nearly match the MRI measurements are those from slices 24 and 23

of patient 1. This signifies that a higher Young's modulus will be needed for the model to produce similar δ_V with the available MRI data.

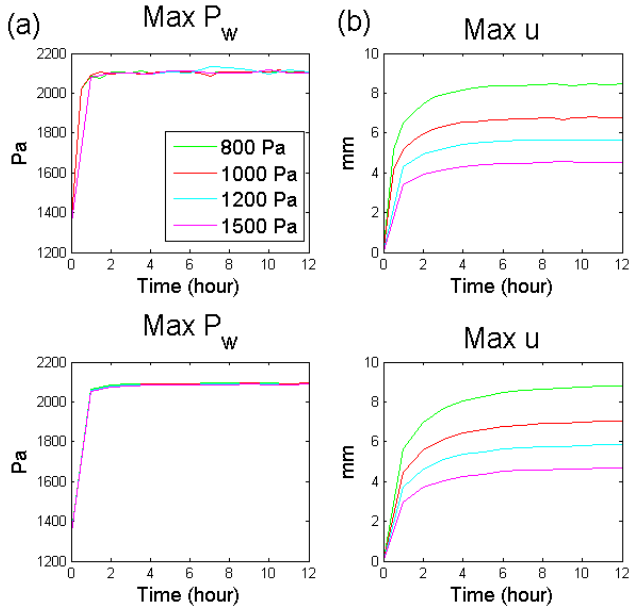

Figure 7.16: Graphs of P_w and u against time for different Young's modulus values for: (a) patient 1; and (b) patient 2.

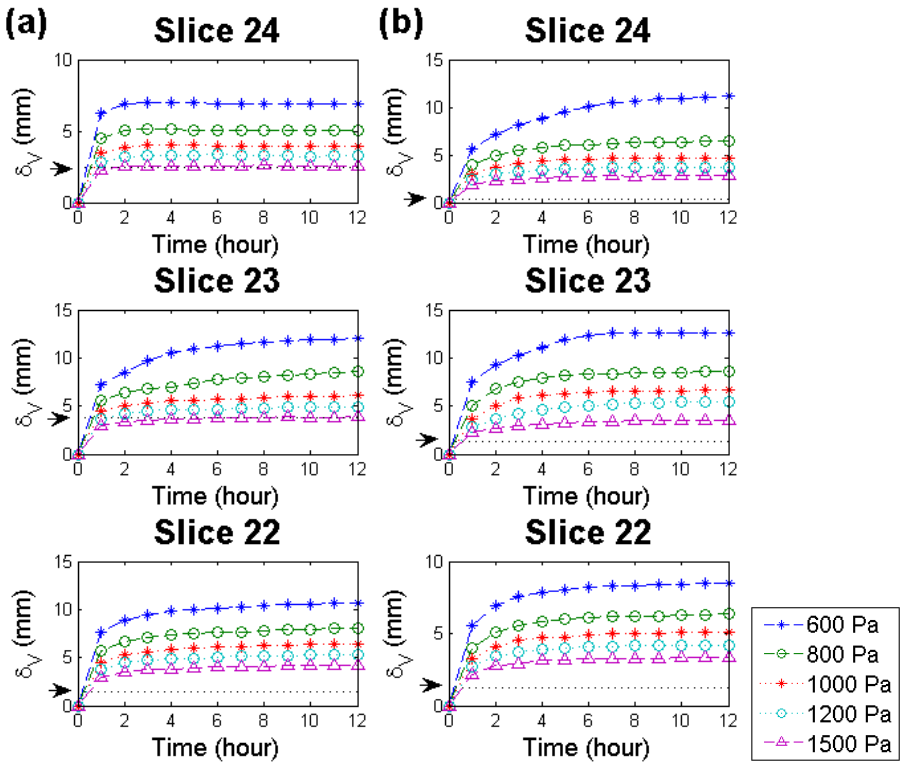

Figure 7.17: Graph of δ_V against time for various Young's modulus values for: (a) patient 1; and (b) patient 2. The black dotted lines and arrows represent the δ_V measured in the FUT MRI.

Figure 7.18 shows the variation in δ_V when the Young's modulus is further increased. The δ_V for slices 24 and 23 of patient 1 matched the MRI measurement when the Young's modulus was in the range 1500 to 2000 Pa. Meanwhile, patient 2 has a value of δ_V matching the MRI measurement when the tissue stiffness is in the range 3000 to 4000 Pa. Despite these, slice 22 of patient 1 and slice 24 of patient 2 did not have values δ_V to match the MRI measurement. In addition, the δ_V almost exponentially decreases with Young's modulus, thus indicating that slice 22 of patient 1 and slice 24 of patient 2 might require a very high Young's modulus to match the MRI measurement. It is also worth noting that the different Young's modulus values required for different brain slices might indicate that cerebral tissue swelling has anisotropic mechanical behaviour.

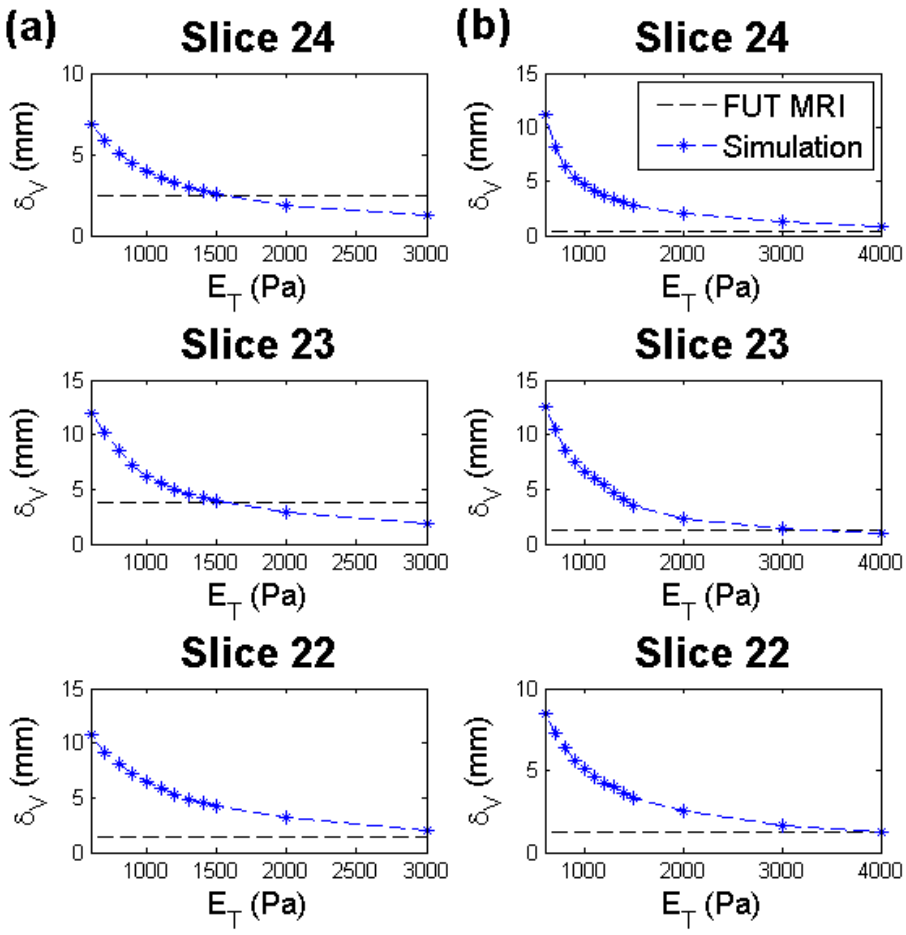

Figure 7.18: Graph of δ_V against Young's modulus at 12 hours and Young's modulus estimation for: (a) patient 1; and (b) patient 2.

7.6 Two-Compartment Model

The two-compartment model has governing equations as described in the section 6.3 and the model parameters have been described in Chapter 4. Initially, the tissue displacement is zero, while the astrocyte pressure, P_a, extracellular space (ECS) pressure, P_e, and neuron pressure, P_n are assumed to be equal to the ICP pressure. These initial conditions are as given below:

$$u(x,0) = 0, \tag{7.6}$$

$$P_a(x,0) = P_e(x,0) = P_n(x,0) = \overline{P}. \tag{7.7}$$

At the skull boundary, R_S, the variables have the following conditions:

$$u(R_S,t) = 0, \tag{7.8}$$

$$P_a(R_S,t) = P_e(R_S,t) = P_n(R_S,t) = \overline{P}. \tag{7.9}$$

Meanwhile, the boundary conditions at the ventricle surface, R_V are set as:

$$\sigma_{ij}(R_V,t) \cdot \mathbf{n} = -\big(P_a(R_V,t) + P_e(R_V,t) + P_n(R_V,t)\big)\mathbf{n}. \tag{7.10}$$

The two-compartment model has slightly different forms of total tissue stress, σ_{ij}, and thus, the total stress acting on the inner ventricle surfaces is equal to the total fluid pressure acting on the outer ventricle surfaces.

7.6.1 AQP4 Ratio Variation

The two-compartment model is next used to investigate the effect of AQP4 in the formation and elimination of cerebral oedema during ischaemia-reperfusion. The general results of the effect of the AQP4 ratio variation on cerebral tissue swelling have been discussed thoroughly in Chapter 4 and Chapter 6. Therefore, to simplify the analysis of the two-compartment model using the patient-specific geometry, only four types of AQP4 ratio are used, which are: (1) no AQP4 (labelled as b0e0); (2) only parenchymal AQP4 present (b0e1); (3) only perivascular AQP4 (b1e0); and (4) baseline AQP4 ratio

(baseline), which has a value of $\frac{n_{AQP4b}}{n_{AQP4e}} = 10$ according to (Nagelhaus et al., 1998). In addition to the AQP4 ratio variation, the cerebral tissue Young's modulus is also varied using values of 584 Pa, 1500 Pa, 2000 Pa (for patient 1), and 3000 Pa (for patient 2).

7.6.2 Results for Two-Compartment Model

Figure 7.19 shows the variation of the fluid pressures, P_e and P_a, and the cerebral tissue displacement with time. One noticeable observation is that the time taken for the fluid pressures and the tissue displacement to reach a constant is fairly long, approximately 40 hours after the reperfusion treatment. The reason is because the characteristic time as calculated in Chapter 4 for the two-compartment model is about 5 times higher than the single compartment model. Another noticeable observation is the significant difference in the steady state values of u for baseline and b1e0 AQP4 ratios are about as twice as high as for b0e0 and b0e1 for all different values of cerebral tissue Young's modulus. This is because of the combined effect of the build-up of astrocyte and ECS fluid pressure in the baseline and b1e0 AQP4 conditions.

The steady-state P_e values for the case of baseline and b1e0 AQP4 ratios are slightly higher than for b0e0 and b0e1, with the exception for cerebral tissue stiffness of 2000 Pa for patient 1 and 3000 Pa for patient, where the P_e values are relatively similar. In addition, P_a remains at baseline value for AQP4 ratios of b0e1 and b0e0 for all Young's modulus values used. This shows that the influence of water transfer between the astrocyte and ECS is not as significant in causing the change in P_a compared to water transfer between the cerebral capillary and astrocyte. From these observations, it can be deduced that the water transfer between the ECS and astrocyte will only occur in the presence of perivascular AQP4.

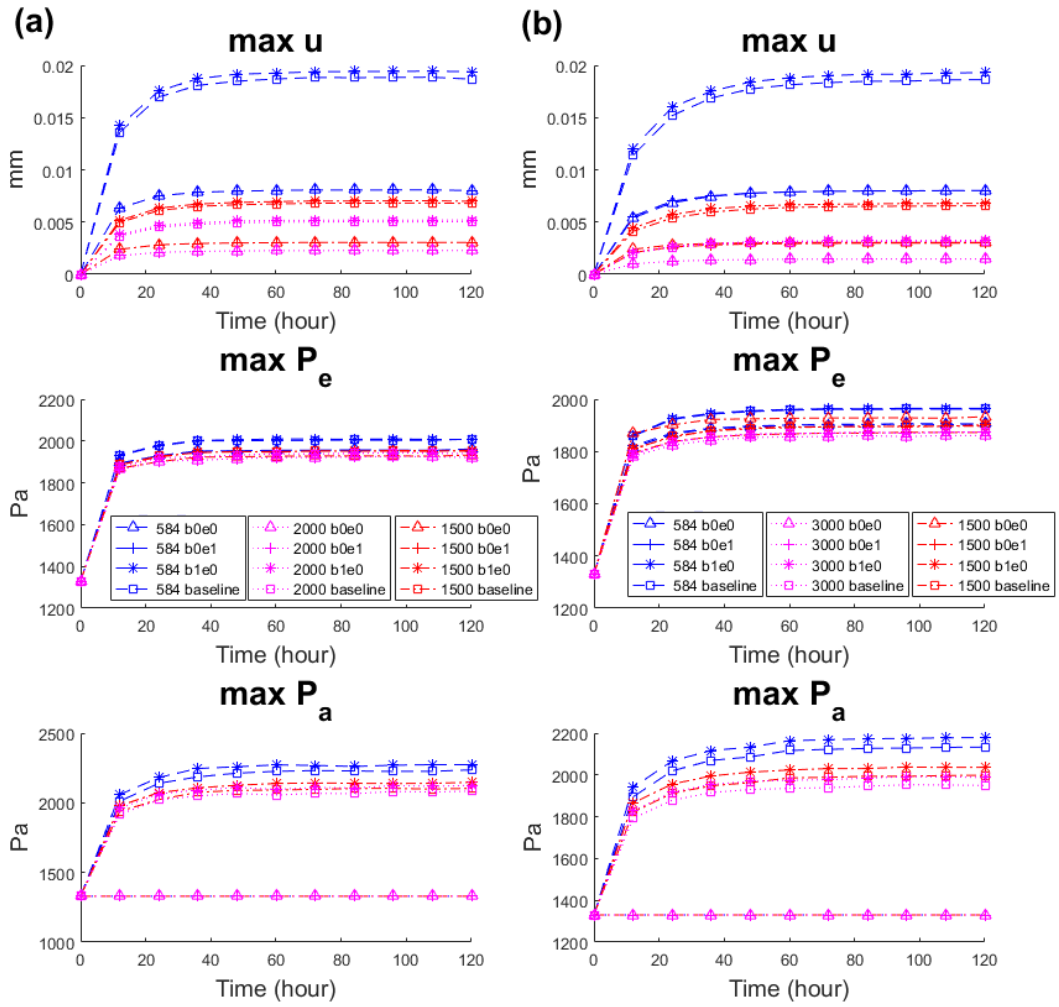

Figure 7.19: Graph of maximum P_e, P_a, and u against time for three different Young's moduli for: (a) patient 1; and (b) patient 2.

The patients are discharged at about 90 hours and 46 hours after the reperfusion treatment. The two-compartment model also predicted that the P_e, P_a, and u may have reached a steady value for patient 1 but not for patient 2. From the simulation, patient 2 only shows about 90% of the steady-state value of the tissue swelling predicted at 46 hours after reperfusion. Although the patient outcome is favourable as seen in Table 7.2, she may be at risk of experiencing further tissue swelling after the discharge from the hospital. Therefore, it would be worth to further validate the two-compartment model by having a second follow-up MRI scan a few days after the patient has discharged.

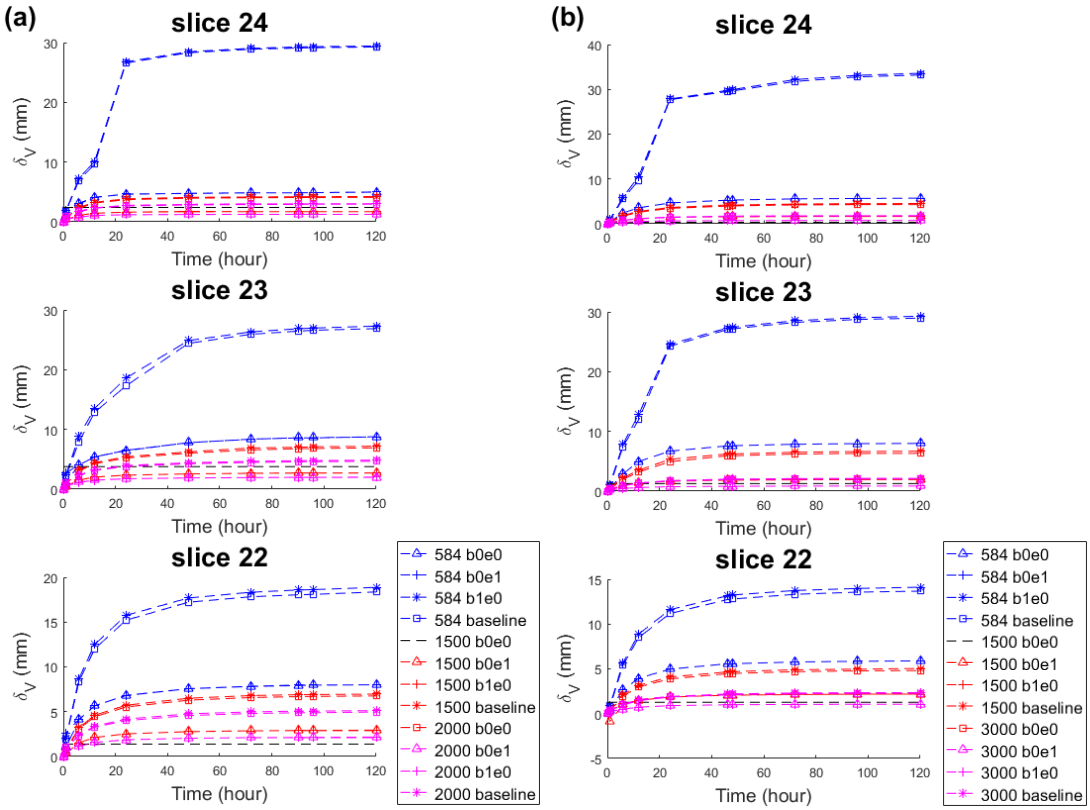

Figure 7.20: Graph of δ_V against time for various Young's modulus values and different AQP4 ratios for: (a) patient 1; and (b) patient 2. The black arrows and black dash lines show the δ_V measured from the FUT MRI.

The ventricle compression, is again used here to validate the two-compartment model. Figure 7.20 shows the δ_V values obtained from the simulations. For the case of baseline and b1e0 AQP4 ratios when the cerebral tissue stiffness is 584 Pa, δ_V is very large, reaching values of about 15 to 30 mm for both patients. Observing the simulation results closely as shown in Figure 7.21 and Figure 7.22, the ventricle is almost completely compressed for the baseline and b1e0 AQP4 ratios. This shows that the tissue swelling is very large for both of these cases, thus the choice of Young's modulus of 584 Pa to represent the tissue stiffness for this model is not suitable. Furthermore, the mesh elements overlap for these two cases, while in reality this is unlikely to occur. This is due to the limitation of the finite element software used which will be discussed further later.

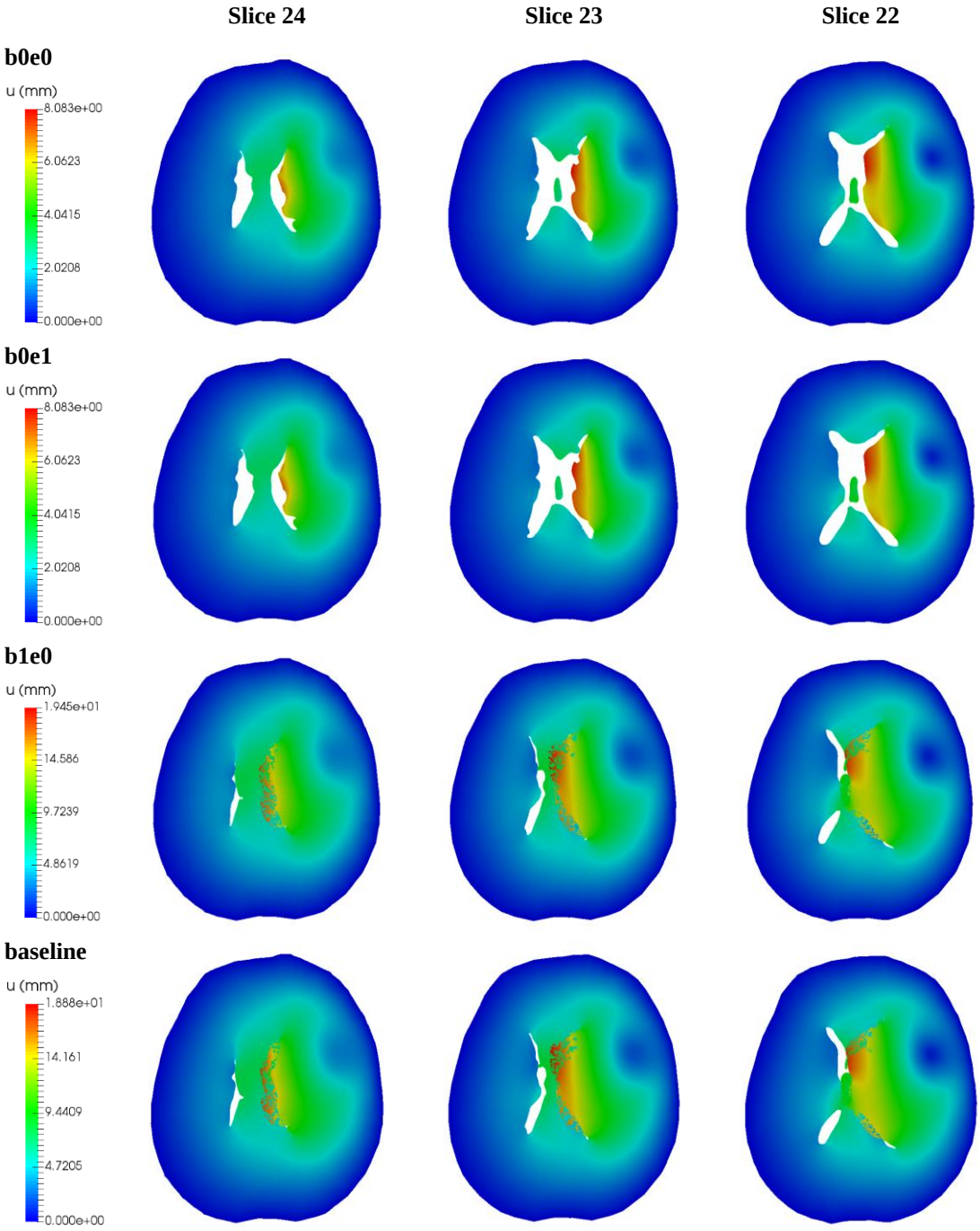

Figure 7.21: Tissue displacement distribution at 90 hours after reperfusion of brain slices 24, 23, and 22 of patient 1 of different AQP4 ratios with the cerebral tissue Young's modulus of 584 Pa.

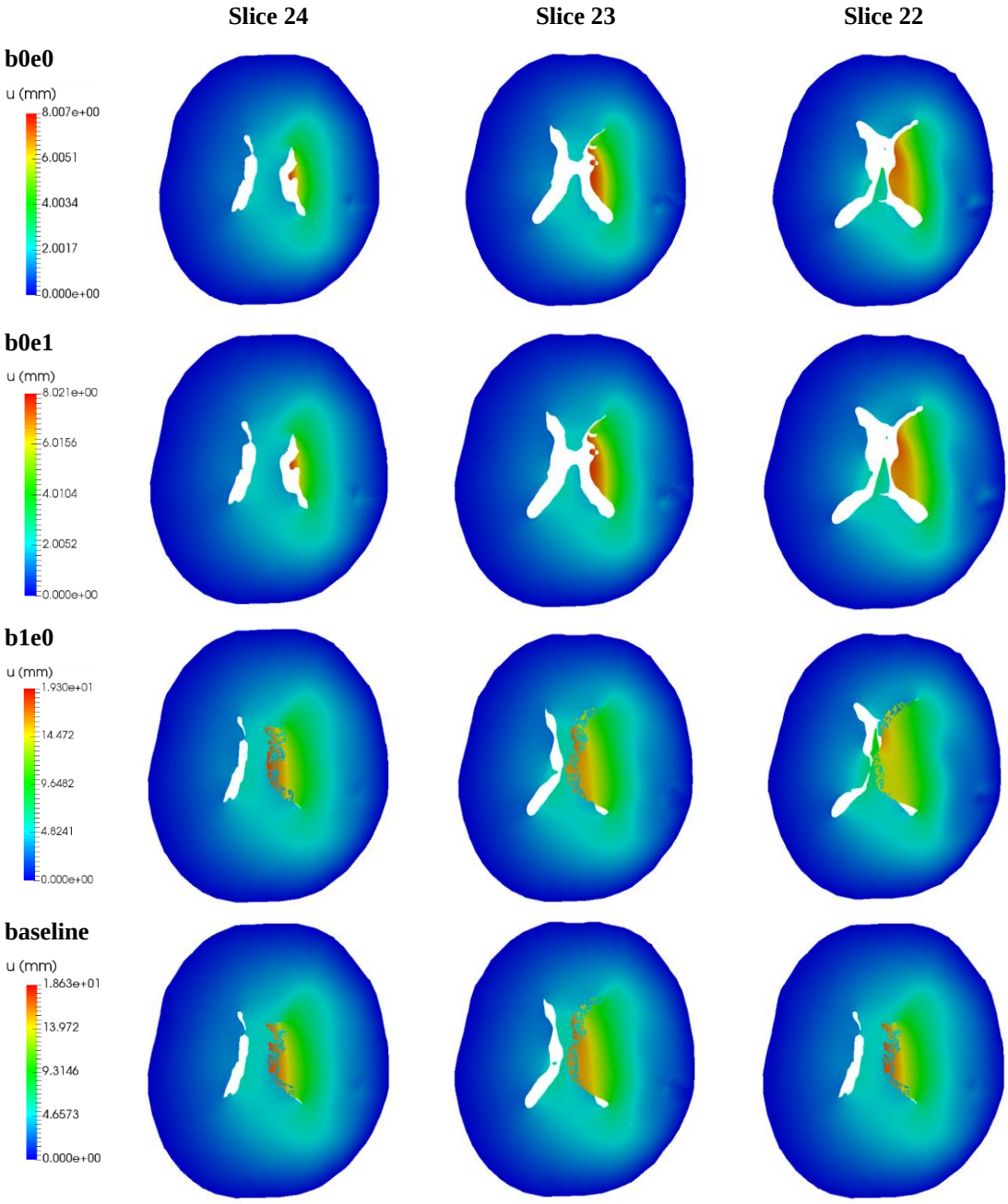

Figure 7.22: Tissue displacement distribution at 46 hours after reperfusion of brain slices 24, 23, and 22 of patient 2 of different AQP4 ratios with the cerebral tissue Young's modulus of 584 Pa.

Meanwhile, Figure 7.23 shows the variation of δ_V with cerebral tissue Young's modulus for each patient at discharge time. One distinction of the δ_V value obtained from the two-compartment model compared to the single compartment model is that it requires a smaller value of Young's modulus to match the δ_V value measured in the FUT MRI. The δ_V value obtained from simulations matches the MRI measurement for slices 24 and 23 of patient 1, and slices 23 and 22 of patient 2. The Young's modulus value is in the

range of 1000 to 1500 Pa for patient 1, and 2000 to 3000 Pa for patient 2. These values are lower than as predicted for the single compartment model. Besides, it can be clearly seen that δ_V values obtained when AQP4 ratios at baseline and b1e0 are higher than for the AQP4 ratios in cases b0e0 and b0e1.

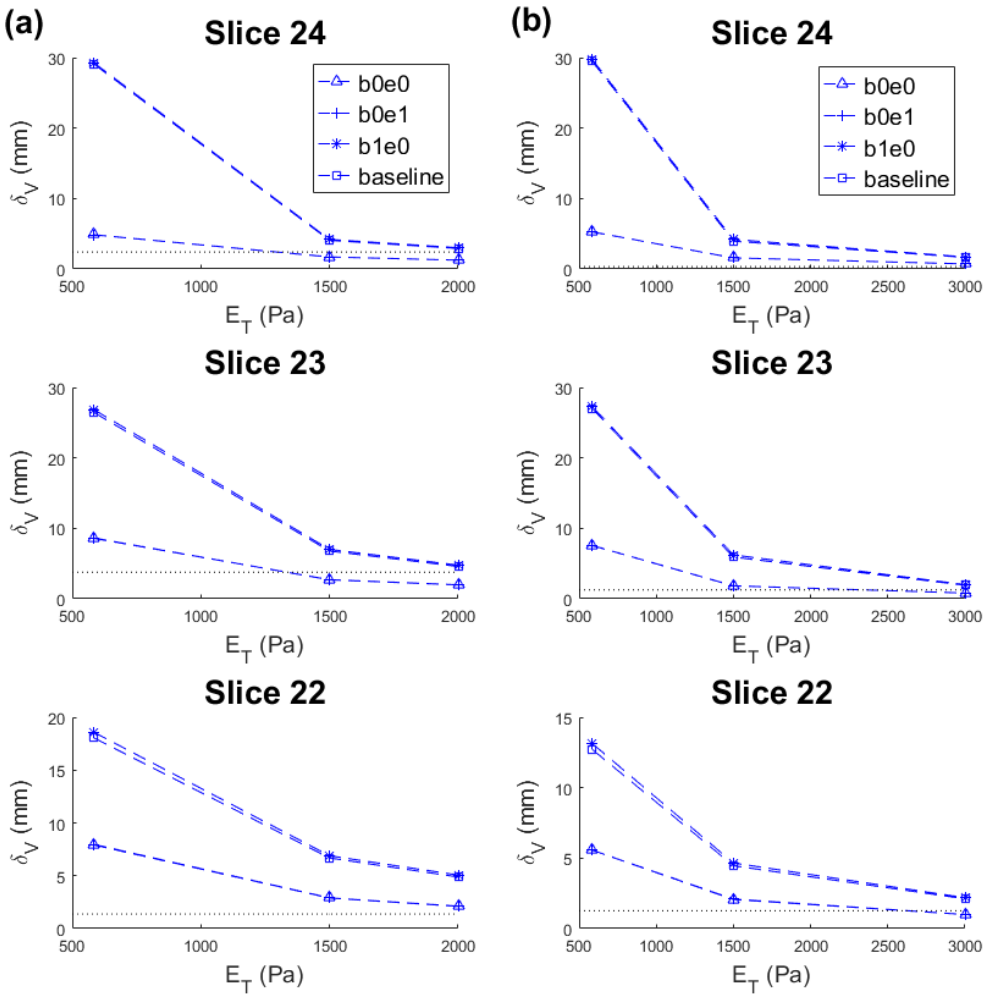

Figure 7.23: Graph of δ_V against Young's modulus at discharge time for: (a) patient 1; and (b) patient 2.

7.7 Discussion

This section will discuss the methods used in simulating the model using patient-specific data and reasons the model could not produce similar brain tissue swelling as obtained in the MRI data. This section is divided into three subsections, namely: (1) section 7.7.1, which discuss the data of the patients used and the limitation of the ventricle compression measurement method with possible improvement; (2) section 7.7.2, which discuss about the results obtained from the simulation of single-compartment model; and (3) section 7.7.3, that discuss the results of the two-compartment model and its significant.

7.7.1 MRI Data and Method Limitation

The single compartment and two-compartment models have been validated here using available ischaemic stroke patient MRI data and FEA techniques. The validation procedures require the development of brain geometry from a set of MRI images. In this study, sets of MRI images from two ischaemic stroke patients were obtained from a hospital in South Korea. The images were first processed to develop a 3D geometry for the FEA. Three important structures are built from the MRI images, namely the brain, the ventricles, and the infarct. It should be noted here that only the lateral ventricles are included in the analysis due to them being easily observable in the MRI images for any ventricle movement during cerebral tissue swelling and also being the largest among all of the ventricles. In addition, the inclusion of only the lateral ventricles makes the analysis simpler.

Other than the lateral ventricles, there are two other ventricular structures present in the brains, which are the third and fourth ventricles. The ventricles are important structures that are responsible for in the circulation of CSF. The third and fourth ventricles

are excluded from this study because: (1) the MRI data used in this study have low image resolution, thus making it difficult to distinguish between the different fluids present in the brain of the patients; and (2) the inclusion of these ventricles will require the addition of CSF circulation in the model, which is not the primary focus of this study. Higher quality imaging data will be required to allow for the inclusion of the third and fourth ventricles. However, these are the only data available at the moment and we hope to acquire more data from ischaemic stroke patients to further improve the model validation in the future.

Both of the patients in this study have undergone reperfusion treatments after about 2.5 and 5.25 hours after ischaemic attack, respectively. According to the acute ischaemic stroke (AIS) protocol outlined by the hospital, two kinds of reperfusion treatments would be given to the patients depending on the time window of the stroke onset, namely IV and IA. IV is usually administered within 3 to 4.5 hours of stroke onset, instead, if the patient is beyond this time window, IA treatment is given. Thus, patient 1 is given both IA and IV, while patient 2 received only IA. A randomised trial on the efficacy of IV rtPA has shown that this treatment provides favourable benefits if given within 3 hours of stroke onset (Hacke et al., 2004) and is more effective if given immediately. On the other hand, the IA treatments are still beneficial even when given within 6 hours of stroke onset with reasonable haemorrhage risks (Furlan et al., 1999). The outcomes of the patients during the follow-up time (FUT) are described by the NIHSS, mRS, and mTICI scores, as listed in Table 7.2. Here, patient 1 suffers from moderate disability, while patient 2 shows almost no disability. However, it is difficult to estimate the effect of ischaemia-reperfusion after the FUT because the outcomes after the patients are discharged are not available. Further, both of these patients have shown a

remarkable amount of ventricle movement in the FUT MRI images, indicating the occurrence of significant cerebral tissue swelling.

Ventricle compression is chosen as a method to quantify the degree of cerebral tissue swelling here because it can be easily measured from the simulations and the MRI data. This method does not account for the overall movement of the ventricle relative to the midline of the brain and it only accounts for the compression at the location of maximum tissue swelling. However, this measurement is suitable for this study as it provides quick validation of the models with the MRI images. There are various other methods available to quantify brain tissue movement. The lateral displacement of the pineal body has been used to investigate brain herniation in various consciousness levels in humans (Ropper, 1986). Meanwhile, measuring the volume change of the brain ventricles in MRI images has been used in studying of brain deformation during neurosurgery, (Hartkens et al., 2003), in Alzheimer patients (Nestor et al., 2008), and in schizophrenic patients (Gaser et al., 2001; Mathalon et al., 2001). A more rigorous measurement of the brain ventricle deformation will be required to improve the validation, however.

7.7.2 Single-Compartment Model

From the results of the single compartment model, the water pressure for both patients reached a steady value of 2100 Pa about 3 hours post-ischaemia-reperfusion. Meanwhile, the tissue displacement reached a steady-state value 3 hours after the water pressure. These observations show a rapid occurrence of cerebral tissue swelling after ischaemia-reperfusion. The actual time taken for oedema to reach its maximum varies from study to study. The study by Baird et al. (1997) on 28 ischaemic stroke patients found that cerebral tissue lesions can continuously grow after 6, 12, and 24 hours after

stroke onset. Meanwhile, a study on the time course of the apparent diffusion coefficient (ADC) in ischaemic human patients suggested that vasogenic oedema may occur up to 4 days of stroke onset (Schlaug et al., 1997). Our findings on the time taken for the swelling to reach steady-state likely signify the pathophysiological variability amongst the patients such as the degree of blood-brain barrier (BBB) breakdown, the size of infarct, and the number of microvessels affected by ischaemia. The assumptions previously made in our models regarding the homogeneity of microvessels distribution and mechanical properties could be changed to further study these variability.

The validation of the single compartment model has revealed the importance of using the right values of cerebral tissue stiffness parameters. In the models developed here, two tissue stiffness parameters have been used, namely the Young's modulus and Poisson's ratio. The baseline Young's modulus value was taken from a study of cerebral hydrocephalus (Taylor et al., 2004), which is thought to occur under a low strain rate condition. However, it was found from our study that a higher Young's modulus is needed for the ischaemia-reperfusion model. A higher Young's modulus value ranging from 10^3 to 10^4 Pa has been used in many mathematical modelling studies on brain tissues (Kaczmarek et al., 1997; Nagashima et al., 1987; Peña et al., 1999). These values were taken from mechanical tests done on various mammals such as monkeys (Metz et al., 1970), cattle (Guillaume et al., 1997), dogs (Flexner et al., 1932; Walsh et al., 1976), and humans (Galford et al., 1970). Our findings have shown that the Young's modulus should have a value of at least between 1500 to 4000 Pa, which is still however within bands as provided by the previous studies.

Poisson's ratio is another cerebral tissue stiffness parameter that can be varied. A value of 0.5 indicates the tissue to be an incompressible material. However, a lower Poisson's ratio value of 0.35 has been used for brain tissue to allow for fluid displacement

within the solid matrix, thus giving the material a slight compressibility (Guillaume et al., 1997; Taylor et al., 2004). Thus, we decided to fix this parameter at $v = 0.35$.

From the ventricle compression δ_V measurements of the single compartment model, it is also found that different brain slices need to have different Young's modulus value to fit with the data. One possible explanation is that the brain tissue might possess anisotropy. Moreover, anisotropy can also occur in the tissue swelling due to the distribution of the microvessels. It has been assumed in this study that the microvessel distribution is homogeneous and that all microvessels have similar mechanical properties. However, different vessels may have different level of BBB damage which may contribute to the anisotropy of cerebral tissue swelling. MRI scans of the brain have shown that water diffusion is anisotropic (Doran et al., 1990; Hajnal et al., 1991; Moseley et al., 1990). Anisotropy of brain water diffusion also has been shown to provide additional information to understand stroke progression using DWI (Yang et al., 1999). Further, anisotropy in the white matter has been incorporated into mathematical models to evaluate its effect on brain pathology (Basser, 1992; Shahim et al., 2010; Stoverud et al., 2012). Therefore, incorporating anisotropy might shed light on the progression of cerebral tissue swelling during ischaemia-reperfusion.

7.7.3 Two-Compartment Model

The two-compartment model is also simulated here using the geometry developed here. This model has provided insights regarding the function of AQP4 in the formation and resolution of oedema during ischaemia-reperfusion. It is found that when the cerebral tissue stiffness is 584 Pa, the ventricle is almost totally compressed, especially for the case of baseline AQP4 and when only perivascular AQP4 is present. This value of Young's modulus is too small; although it has been used to study hydrocephalus (Taylor

et al., 2004; Tully et al., 2011), it seems from the results shown here that this value is not suitable in the context of ischaemia-reperfusion cerebral tissue swelling.

Complete brain ventricle effacement or compression is observed in the two-compartment model in the form of overlapping of meshes. However, it is not being accurately modelled. Complete ventricle compression can happen, for example, in traumatic brain (Yuh et al., 2008). Incorporating complete ventricle effacement will require the application of contact analysis. The addition of contact analysis will help to understand the effect of forces caused by the compression of one ventricle to the other, which in the current studies is not taken into consideration. One reason is that the open source software ELMER does not have the capability of solving contact problems and thus this will be the subject of future work.

The time taken for the fluid pressures, P_e and P_a, and tissue displacement, u, to reach steady-state values are longer compared to the single compartment model. This is because the characteristic time of the two compartment model is about 5 times higher than the single compartment model. On top of that, the relative compressibility of fluid, Q^a is assumed to be lower than the single compartment model, making the fluid pressure slower to reach a constant value. Although the Q^a term can be varied to see its effect on the formation of tissue swelling, this is not considered here. The reasons are: (1) the time taken for tissue swelling to stop growing and remain constant is not known; and (2) varying Q^a may increase the computational cost because it will take a longer time for the model to solve.

From the two-compartment model results, the tissue displacement u and subsequently the ventricle compression δ_V are found to be higher in the cases of baseline and b1e0 AQP4 ratios compared to b0e0 and b0e1 AQP4 ratios. The baseline and b1e0

AQP4 ratios signify the existence of perivascular AQP4. In these two cases, water flows into the astrocyte via AQP4 due to the pressure gradient between the intracellular space and the blood circulation (Papadopoulos et al., 2013). Hence, it is proven here that oedema might not be cleared through blood circulation, instead it might be removed via the CSF circulation (Ohata et al., 1990) possibly at the ventricle and subarachnoid interfaces (Papadopoulos et al., 2013). Our model does not include CSF circulation, thus to further understand oedema clearance through CSF circulation will require modification of the existing model.

It has been shown that the removal of AQP4 at the early stage of ischaemia may hinder cytotoxic oedema occurrence. However, the deletion of AQP4 at a later stage of ischaemia may slow down vasogenic oedema clearance (Amiry-Moghaddam et al., 2003). From the two-compartment model, it is suggested that deleting perivascular AQP4 may improve the outcome of ischaemia-reperfusion by reducing cerebral tissue swelling. Perivascular AQP4 is associated with a specific protein known as α-syntrophin (Amiry-Moghaddam et al., 2003; Neely et al., 2001). Targeting the α-syntrophin gene to remove perivascular AQP4 could be a treatment strategy to reduce cerebral tissue swelling.

7.8 Summary

Both single-compartment and two-compartment models have been validated by comparing the simulation results using patient-specific geometry with MRI data of ischaemic stroke patients. It was found that both of the models have overestimated the ventricle compression when using baseline mechanical properties. A higher cerebral tissue stiffness is needed for these models as indicated in many previous clinical studies on brain tissue stiffness.

For the two-compartment model, it was found that removing perivascular AQP4 reduces the tissue swelling and thus, can be used as a potential treatment method to reduce brain swelling. Oedema clearance through AQP4 may occur at CSF interfaces such as at the ventricle and subarachnoid space. Therefore, modifications of these models to include the CSF circulation effect, anisotropy of brain tissue, and microvessels distribution, together with more data from ischaemic stroke patients will be needed to further validate these models.

Chapter 8

Conclusion and Future Directions

8.1 Thesis Summary

Vasogenic oedema is one brain ischaemia-reperfusion injury, which is formed through a series of complex mechanisms. Cerebral blood flow (CBF) that carries oxygen and nutrients to the tissue is reduced during ischaemic stroke, which causes blood-brain barrier (BBB) breakdown to occur. This increases the permeability of the cerebral capillaries and allows the filtration of protein plasma and ions into the cerebral tissue extracellular space (ECS), which creates osmotic pressure and draws water into the ECS. Accumulation of water in the ECS or vasogenic oedema causes brain tissue swelling and elevates the intracranial pressure (ICP), which might cause the compression of cerebral microvessels contributing to the no-reflow phenomenon.

The mathematical model developed in Chapter 3 was used to describe this phenomenon by utilising several existing models such as filtration equation, tube law, and poroelastic theory. From the model, the filtration of proteins causes water flux and subsequently results in tissue swelling and increased interstitial pressure. Also, tissue swelling can be shown to cause the cerebral vessel to collapse but it can only occur at high value of reperfusion pressure, high blood osmotic pressure, high cerebral capillary permeability and low cerebral capillary stiffness. This model has become the foundation for the subsequent works to further understand this complex phenomenon.

The presence of aquaporin-4 (AQP4) in the brain has been shown in many clinical studies (Amiry-Moghaddam et al., 2003; Papadopoulos et al., 2007) to play a role in the

formation and elimination of cerebral oedema. A mathematical model has been developed here to understand the role of AQP4 in cerebral oedema, especially during ischaemia-reperfusion. The cerebral space is assumed to be made up of four fluid compartments namely the astrocyte, neuron, ECS and blood microvessels, with the brain tissue as the solid matrix. AQP4 are located along the astrocyte, which allows the movement of water between the astrocyte into the microvessels and ECS. This is done by modifying the model developed in Chapter 3 by implementing the concept of multiple-network poroelastic theory (Tully et al., 2011). From the model, it has been found that the presence of AQP4 during ischaemia-reperfusion injury helps to reduce vasogenic oedema but that it is compensated for by the increase in astrocyte pressure, leading to the formation of cytotoxic oedema. In addition, the inhibition of AQP4 function could possibly become a new treatment to reduce brain oedema as proposed by Marmarou (2007). However, from this model, it is found that this technique must be applied appropriately to balance out carefully the effect of tissue swelling and oedema.

One of the major concerns of the model developed in Chapter 4 is the assumption used for the ionic concentration in astrocytes. It is assumed that the concentration is constant for the sake of simplicity of the simulation. Chapter 5 dealt with this by applying the Donnan equilibrium to study the effect of fixed charge density (FCD) on cerebral tissue swelling. When cerebral tissue is damaged due to ischaemia and the cell membrane starts to function abnormally, this will expose the FCD and cause an influx of ions from the ECS into the cell to balance out the effect of FCD charges. As a result, an osmotic pressure difference is created between the ECS and the astrocyte that might lead to tissue swelling. From the results, it was found that for the FCD to give a substantial effect in cerebral tissue swelling, the concentration of FCD should be higher than 100 mM. However, the only available values of FCD concentration found from experiments by

Elkin et al. (2010) is about 2 mM, which is a lot smaller than the required value obtained from the simulations. These findings show that the ionic concentration changes in the astrocyte might not play a significant role towards the cerebral tissue swelling after ischaemia-reperfusion, but it is undeniable of course that ionic concentration does play a role in the cell function.

Chapter 6 uses the models developed here in 2D and 3D finite element analysis using both idealised and patient-specific models. Results clearly show that there is a deflection of the middle line and plane that divides the two cerebral hemispheres due to cerebral tissue swelling. However, the brain ventricle has been assumed fixed and has a round shape, while in reality, the ventricle can be compressed due to tissue swelling. It was found from the results that it is necessary to make some modifications to the boundary conditions for the validation chapter.

Validating the models is the final objective of this thesis and has been thoroughly discussed in Chapter 7. MRI data of two ischaemic stroke patients were used for the validation. Two 3D geometries were developed from the MRI data using sophisticated image processing technique. Again, finite element analysis was applied on these geometries to evaluate the cerebral tissue swelling and the results compared with the follow-up MRI data. It was found that the models require higher cerebral tissue stiffness values than previously used in Chapters 3 and 4. Furthermore, it was also found that the presence of perivascular AQP4 may worsen the tissue swelling. Thus, removing perivascular AQP4 is recommended to reduce the effect of cerebral oedema. However, more data are needed to help improving the models.

8.2 Future Works

Future works are needed to improve the existing models. In addition to collecting more data in ischaemic stroke patients, several modifications of the models will be necessary. The formation of brain oedema depends on many factors as previously discussed. Several future works are suggested here, including the modelling of BBB breakdown, AQP4 expression and astrocyte-neuron interaction during ischaemia. These works are also useful in the development of an improved treatment strategy for cerebral ischaemia. However, these future works will require the use of a more sophisticated modelling technique and will also involve laboratory experiments to acquire relevant information. These proposed works are described as follows.

8.2.1 BBB Breakdown Modelling

The BBB breakdown has a complex mechanism. The mechanism starts during ischaemia and hypoxia, which involves a series of molecular cascades (Yang et al., 2011). Cerebral ischaemia activates matrix metalloproteinase-9 (MMP9) and 2 (MMP2), the enzymes of which are secreted to weaken the extracellular matrix in tissue remodelling processes (Murphy et al., 1997). In cerebral ischaemia, the production of MMPs causes BBB damage and subsequently an increase in BBB permeability (Rosenberg et al., 1996). Clinical studies suggest that MMP9 are produced from the infiltration of leukocytes into the infarcted region as an inflammatory response (Gidday et al., 2005; Rosell et al., 2008). Modelling this mechanism will require further understanding of the pathways involved in the production of MMPs and the actions involved in the BBB breakdown. Besides, this model can further verify previous clinical studies on the potential treatment of brain oedema through inhibition of MMPs action (Rosenberg et al., 1997).

The BBB breakdown causes the loss of the integrity of the tight junctions between the endothelial cells and allows the entrance of fluid into the tissue space creating vasogenic oedema. Further damage due to ischaemia may cause disruption of the basal lamina of cerebral microvessels (Hamann et al., 1995) and may lead to haemorrhage transformation (Hamann et al., 1996). Haemorrhagic transformation is a common concern during and after an ischaemic stroke attack. It is also well known that the use of thrombolytic treatment beyond the suggested time window may cause haemorrhagic damage to the brain. Modelling the development of haemorrhagic transformation may allow a better understanding on the suitability of thrombolytic treatment applied outside the time window.

In addition, it is worth studying the extent of BBB opening, which is thought to depend on the time taken for reperfusion. Early reperfusion may be able to fix the BBB damage (Brouns et al., 2009), meanwhile late reperfusion, usually more than one day after the stroke onset, may cause irreversible BBB damage (Yang et al., 2011). Modelling the period of BBB opening will help to provide understanding of the optimum time for reperfusion after stroke. This also will definitely involve the simultaneous formation of cytotoxic and vasogenic oedema, which might also give insights into the role of AQP4 during cerebral ischaemic damage.

8.2.2 Modelling Cells Interactions during Ischaemia

The effective time window between the stroke onset and treatment is very narrow, and treatment given beyond this time window may reduce the chance of full recovery. The mismatch between perfusion-weighted MRI (PWI) and diffusion-weighted MRI (DWI) has been identified as a region of tissue at risk of infarction (Schlaug et al., 1999). It has been hypothesised that patients with PWI/DWI mismatch have higher odds to

benefit from thrombolytic treatment compared to those without the mismatch (Olivot et al., 2008). However, a systematic review showed that infarct growth can still occur even if the mismatch is not present (Kane et al., 2007). This might depend on the cell-cell interaction.

The process might involve various cell behaviours and interactions such as cell signalling, cell movement, cell growth and death. The Cellular Potts Model (CPM) is an example of a computational modelling method that simulates cellular interactions, which was developed by Graner et al. (1992) to study cell sorting and also has been used in describing various biological phenomena, for example tumour growth (Chen et al., 2007), tumour invasion into healthy tissue (Szabo et al., 2013), and progenitor cell sorting (Krieg et al., 2008). Implementation of CPM to model the cell-cell interactions during cerebral ischaemia may provide a better understanding of infarct formation and in the determination of salvageable tissue.

8.2.3 AQP4 Expression during Stroke

It has been discussed earlier that the amount of AQP4 expression depends on the duration of ischaemia. AQP4 expression during early ischaemia is lesser compared to after a prolonged ischaemia. AQP4 is strongly expressed after the BBB starts to break down, which has been shown to help in eliminating oedematous fluid (Amiry-Moghaddam et al., 2003). In addition, a study also shows that there is a strong AQP4 expression during the start of BBB breakdown and when BBB function begins to recover (Tomás-Camardiel et al., 2005).

To fully study the function of AQP4 during ischaemia will require the understanding of the factors that cause its expression. The mechanism of the regulation of AQP4 expression is still not fully understood. Recent studies have showed that AQP4

expression depends on a protein kinase C (PKC), which is an enzyme that controls the function of the proteins (Kleindienst et al., 2006; Nakahama et al., 1999). Using mathematical models specifically developed to evaluate the function of PKC might help in directing the research towards understanding the mechanism of AQP4 regulation.

8.3 Final Remarks

The models developed in this thesis are useful to evaluate the efficacy of reperfusion treatment of ischaemic stroke. Although the models pose several limitations, the recommended future works will hopefully help to improve the models for their application in assisting clinicians and researchers to further understand ischaemia-reperfusion injury.

Appendix A

Comparison between Linear and Fung Elastic Constitutive Models in Cerebral Swelling Model

A.1 Introduction

One of the poroelastic theory assumptions is that the stress-strain relationship to has linear relationship (Terzaghi, 1943) due to the strain being assumed to be relatively small. In the work done by Elkin et al. (2010) and Lang et al. (2014) on cerebral tissue swelling, they implemented a triphasic theory and used a nonlinear stress-strain relationship based on the Fung model. Therefore, the purpose of this section is to compare these constitutive models in the application of cerebral swelling during ischemia-reperfusion injury and to validate the model selection made throughout this study.

A.2 Linear Elastic Constitutive Equation

The elastic model used in previous chapters has the Cauchy stress, $\boldsymbol{\sigma}$, of the form:

$$\boldsymbol{\sigma} = 2G_p\boldsymbol{\varepsilon} + \lambda_p \mathrm{Tr}(\boldsymbol{\varepsilon})\boldsymbol{I} - \sum_{a=1}^{A} \alpha^a P^a \boldsymbol{I}, \tag{A.1}$$

where G_p and λ_p are the Lamé constants as defined in Chapter 3, while α^a and P^a are the Biot parameter and hydrostatic pressure for the fluid compartments $a = 1, \dots, A$ present in the tissue. The other remaining terms; $Tr(\boldsymbol{\varepsilon})$ is the sum of the diagonal element of the tensor $\boldsymbol{\varepsilon}$. The term $\boldsymbol{\varepsilon}$ is known as the infinitesimal strain or Cauchy strain, which is related to the displacement vector $\boldsymbol{u}$:

$$\boldsymbol{\varepsilon} = \frac{1}{2}(\nabla \boldsymbol{u} + (\nabla \boldsymbol{u})^T), \tag{A.2}$$

in which the operations T and ∇ are the transpose and gradient operators, respectively. The Cauchy strain can also be expressed in terms of the deformation gradient tensor $\boldsymbol{F}$, which measures the deformation of a body from a reference configuration to a current configuration, as given below:

$$\boldsymbol{\varepsilon} = \frac{1}{2}(\boldsymbol{F} + \boldsymbol{F}^T) - \boldsymbol{I}. \tag{A.3}$$

For the case of pure homogeneous, isotropic deformation and one-dimension, $\boldsymbol{F}$ can be expressed in terms of the stretch ratio λ:

$$\boldsymbol{F} = \lambda \boldsymbol{I}. \tag{A.4}$$

The stretch ratio λ measures the ratio of the extension from the current to the reference configuration to the initial length. The relationship between $\boldsymbol{\varepsilon}$ and λ thus can be obtained:

$$\lambda = \varepsilon + 1, \tag{A.5}$$

where $\boldsymbol{\varepsilon} = \varepsilon \boldsymbol{I}$. Assuming that the tissue is immersed in a solution bath and allowed to swell, under free-swelling boundary conditions (Elkin et al., 2010), the stress of the tissue must be equal to the pressure exerted by the solution bath. Thus, the pressure difference Δp can be described in terms of ε:

$$\Delta p = 3K_p \varepsilon, \tag{A.6}$$

where $K_p = 2G_p + 3\lambda_p$, is the bulk modulus.

A.3 Fung Elastic Constitutive Equation

The Cauchy stress, $\boldsymbol{\sigma}$, for the Fung elastic model has the following form (Ateshian et al., 2009):

$$\boldsymbol{\sigma} = \frac{1}{2J} e^{Q} [\lambda_S (\mathrm{Tr}\boldsymbol{B} - 3)\boldsymbol{B} + 2\mu_S (\boldsymbol{B}^2 - \boldsymbol{B})] - \sum_{a=1}^{A} \alpha^a P^a \boldsymbol{I}. \quad \text{(A.7)}$$

Here, the strain is defined in terms of Left Cauchy-Green tensor, $\boldsymbol{B} = \boldsymbol{F}\boldsymbol{F}^T$. The terms λ_S and μ_S are the Lamé constants as defined by (Lang et al., 2014) and $J = \det(\boldsymbol{F})$ is equal to the local change in volume. The stress-strain relationship is nonlinear with the presence of the exponential term with an extra material coefficient, c, also known as the strain stiffening elastic parameter with a unit of stress, which is defined in the term Q given by:

$$Q = \frac{1}{4\mathrm{c}} [\lambda_S (\mathrm{Tr}\boldsymbol{B} - 3)^2 + 2\mu_S (\mathrm{Tr}(\boldsymbol{B}^2) - 2\mathrm{Tr}\boldsymbol{B} + 3)]. \quad \text{(A.8)}$$

Under the same assumptions as used for linear elastic model, the pressure difference, Δp, can be simplified as:

$$\Delta p = \left[\frac{3K_S(\lambda^2 - 1)}{2\lambda}\right] e^{\left[\frac{9K_S}{4c}(\lambda^2 - 1)^2\right]}, \quad \text{(A.9)}$$

where $K_S = 3\lambda_S + 2\mu_S$ is the bulk modulus. Expressing Δp in terms of ε to obtain the following relationship:

$$\Delta p = \left[\frac{3K_S(\varepsilon^2 + 2\varepsilon)}{2\varepsilon + 2}\right] e^{\left[\frac{9K_S}{4c}(\varepsilon^4 + 4\varepsilon^3 + 4\varepsilon^2)\right]}. \quad \text{(A.10)}$$

Further mathematical analysis can be done for the case of small deformations to show that the Fung elastic model can be reduced to a linear model as given below:

$$\Delta p \approx \left[\frac{3K_S(\varepsilon^2 + 2\varepsilon)}{2\varepsilon + 2}\right] = 3K_S\varepsilon, \quad \text{(A.11)}$$

by assuming that all the higher powers of ε are approximately zero and that $\varepsilon + 1 \approx 1$.

A.4 Model Comparison and Analysis

Table A.1 below lists the material parameters used for both of the elastic material types. The bulk modulus, K_S, used for the Fung elastic model is taken from curve fitting between experimental data of white matter under unconfined compression with a

poroviscoelastic model (Cheng et al., 2007). On the other hand, the bulk modulus, K_S, used for the linear elastic model, is taken from (Taylor et al., 2004). Both of these bulk moduli are suitable for small strain simulations such as hydrocephalus and also for the case in the current study. Meanwhile, the value of the strain stiffening constant, c, of a normal biological tissue is taken from (Lang et al., 2014).

Table A.1: Material parameters for the linear and Fung elastic material models.

Linear elastic		**Fung elastic (Elkin et al., 2010)**	
Parameter	**Value**	**Parameter**	**Value**
Bulk modulus, K_p	648.9 Pa	Bulk modulus, K_S	380 Pa
		Strain stiffening, c	1000 Pa

By using the parameters above, graphs of Δp against ε are plotted for each type of material model, as shown Figure A.1. Both the linear and Fung models will be comparatively the same when ε is small, using the same bulk modulus. In this figure, the symbol (*) represents the point where the percentage Δp difference between the two models is 1% and has values ε of 0.09 and 0.135, for bulk moduli of 684.9 Pa and 380 Pa, respectively. This shows that the Fung model is approximately linear for small strains and that a small bulk modulus will produce a closer approximation between the two models. Furthermore, from the work in Chapter 3, the maximum ε value obtained was 0.1949, which is for the ischemic core radius of 38.95 mm. At this maximum strain, the percentage difference of Δp is about 21.3% and 8.0% for the two bulk moduli. However, these differences are within an acceptable range and an ischemic lesion is unlikely to have a size more than 38.95 mm. From the results predicted here, it can be concluded that using the linear elastic model is sufficient to represent cerebral tissue elasticity accurately.

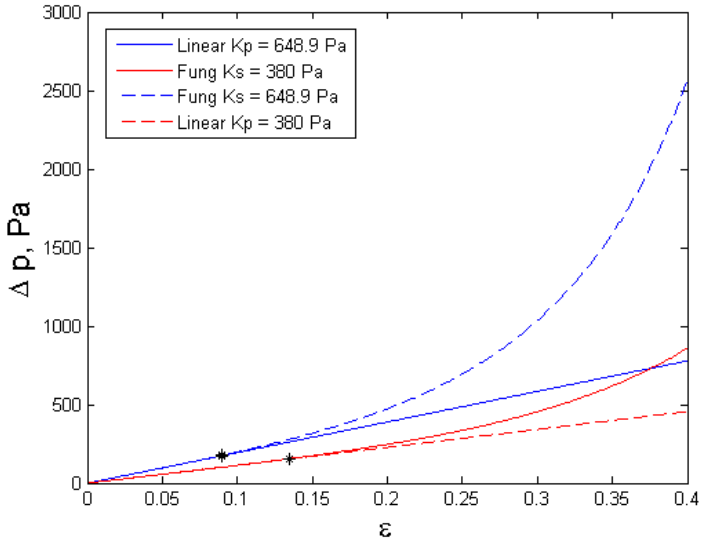

Figure A.1: Comparison between linear and Fung elastic models with different bulk modulus value.

Appendix B

Validating the Assumption of Constant Ion Concentrations in Cerebral Tissue during Ischaemia

B.1 Introduction

The diffusion of ions between biological tissue and a salt solution will cause fluid flow by osmosis and will stop until an equilibrium concentration of water is reached. Overflow of fluid from the solution into the tissue will cause the tissue to swell, which usually occurs in an unhealthy tissue state such as after cerebral ischemia. The Donnan effect is assumed to provide the driving force that causes the swelling and this is due to the presence of fixed charge molecules, known as fixed charge density (FCD) (Elkin et al., 2010). The osmotic pressure, Δp_{osm}, that drives the fluid between the tissue and the solution can be determined through the Donnan equilibrium (Cowin et al., 2009):

$$\Delta p_{osm} = RT\left[\sqrt{{c^{fc}}^2 + {c^*}^2} - c^*\right], \tag{B.1}$$

where RT is the gas constant and room temperature, while c^{fc} and c^* are the concentrations of FCD and the salt solution, respectively.

The term c^{fc} can be related to its initial value c_o^{fc} and the tissue strain ε according to the following relationship (Lang et al., 2014):

$$c^{fc} = \frac{\emptyset_o^w c_o^{fc}}{\varepsilon^3 + 3\varepsilon^2 + 3\varepsilon + \emptyset_o^w}, \tag{B.2}$$

where $\emptyset_o^w$ represents the volume fraction of water in the tissue during stress-free condition. Assuming that the tissue behaves as a linear elastic solid, Δp_{osm} also follows the relationship (A.6). Substituting this into eqn. (B.2) gives a concentration-strain relationship:

$$c^* = \frac{1}{2}\left[\frac{RT}{3K_p\varepsilon}\left(\frac{\emptyset_o^w c_o^{fc}}{\varepsilon^3 + 3\varepsilon^2 + 3\varepsilon + \emptyset_o^w}\right)^2 - \frac{3K_p\varepsilon}{RT}\right], \tag{B.3}$$

B.2 Modification and Analysis of Concentration-Strain Relationship

From the results of the study done by Lang et al. (2014), there must exist a residual strain and that the volume change at a high salt solution concentration is zero. To account for this, the eqn. (B.1) is slightly modified as below:

$$\Delta p_{osm} = RT\left[\sqrt{c^{fc^2} + c^{*2}} - c^*\right] = 3K_p(\varepsilon + \bar{\varepsilon}), \tag{B.4}$$

where the term $\bar{\varepsilon} = \frac{RT}{3K_p}\left[\sqrt{c_o^{fc^2} + c^{*2}} - c^*\right]$ represents the residual strain term. Rearranging eqn. (B.4) gives:

$$c^* = \sqrt{\left(\frac{RT}{6K_p\varepsilon}\right)^2\left(c_o^{fc^2} - c^{fc^2}\right) - \frac{1}{2}\left(c_o^{fc^2} + c^{fc^2}\right) + \left(\frac{3K_p}{2RT}\varepsilon\right)^2}. \tag{B.5}$$

Table B.1 below lists the parameter values involved in eqn. (B.5) and Figure B.1 illustrates this equation graphically. The curves represent the ECS salt concentration and tissue strain relationship by assuming that the astrocyte is immersed in the ECS, with a value of the volume fraction of the astrocyte of 0.25. From these curves, it can be seen that the strain can reach zero at a certain solution concentration. This concentration can be determined by calculating the limit of the strain as it approaches zero for eqn. (B.5). The concentrations obtained are 79.2 $\mathrm{mEqL^{-1}}$ and 254 $\mathrm{mEqL^{-1}}$ for the different volume fractions of $\emptyset_o^w$ and $\bar{n}_g$ respectively. For strain in the range 0 to 0.1, the solution

concentration drops about 38% and 68%, respectively, for the two volume fractions. It is also obvious that as the volume fraction decreases, the changes in solution concentration with strain are larger. These observations show that the changes in the ionic concentration of tissue may have an effect on the tissue displacement and that a slight modification can be made to improve the previous work in which the assumption of constant ionic concentration of the tissue has been made.

Table B.1: Parameter values for the concentration-strain relationship.

Parameter	**Value**	**Reference(s)**
Initial FCD concentration, c_o^{fc}	4 $\mathrm{mEqL^{-1}}$	(Elkin et al., 2010)
Initial volume fraction of tissue, $\emptyset_o^w$	0.8	(Hrabětová et al., 2002)
Initial volume fraction of astrocyte, $\bar{n}_g$	0.25	(Cloutier et al., 2009)

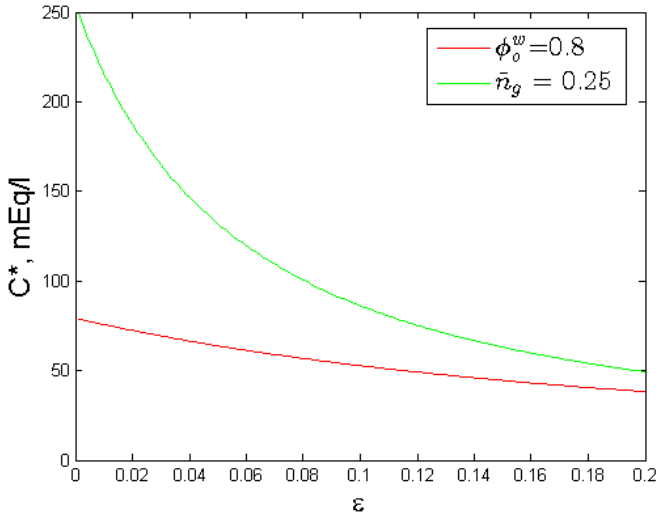

Figure B.1: Concentration-strain relationship of eqn. (B.5) with different volume fraction of water.

Appendix C

Patient-Specific Geometry

C.1 Introduction

This section lists the MRI and geometry slices that have the brain ventricles present in them. As discussed in Chapter 7, slices 22 until 24 are used for the model analysis for both of the patients. The chosen slices are based on these criteria: (1) these have approximately a similar ventricle shape with their associated MRI image slices, and (2) they have a full continuous and distinguishable ventricle.

Other slices are not chosen because: (1) the ventricles are not clearly observable in both the image and the geometry slices; (2) the ventricles produced in the geometry slices are discontinuous, thus rendering it difficult to analyse; or (3) only small portions of the ventricles are present in the slices. Further improvement of the image processing techniques is required to produce a better quality brain geometry, which will be the subject of the future works. The slices are as shown in the following sections.

C.2 Patient 1

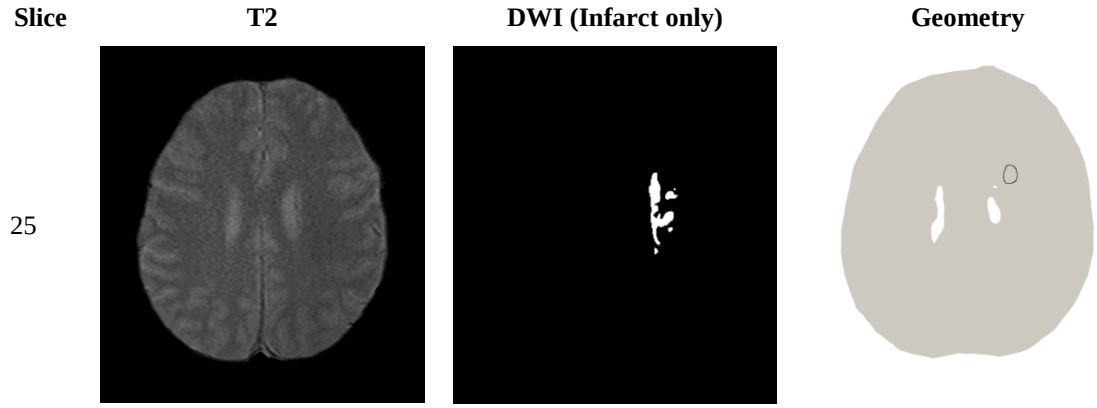

Figure C.1: Slice 25 of patient 1. It is not chosen because of unclear ventricles.

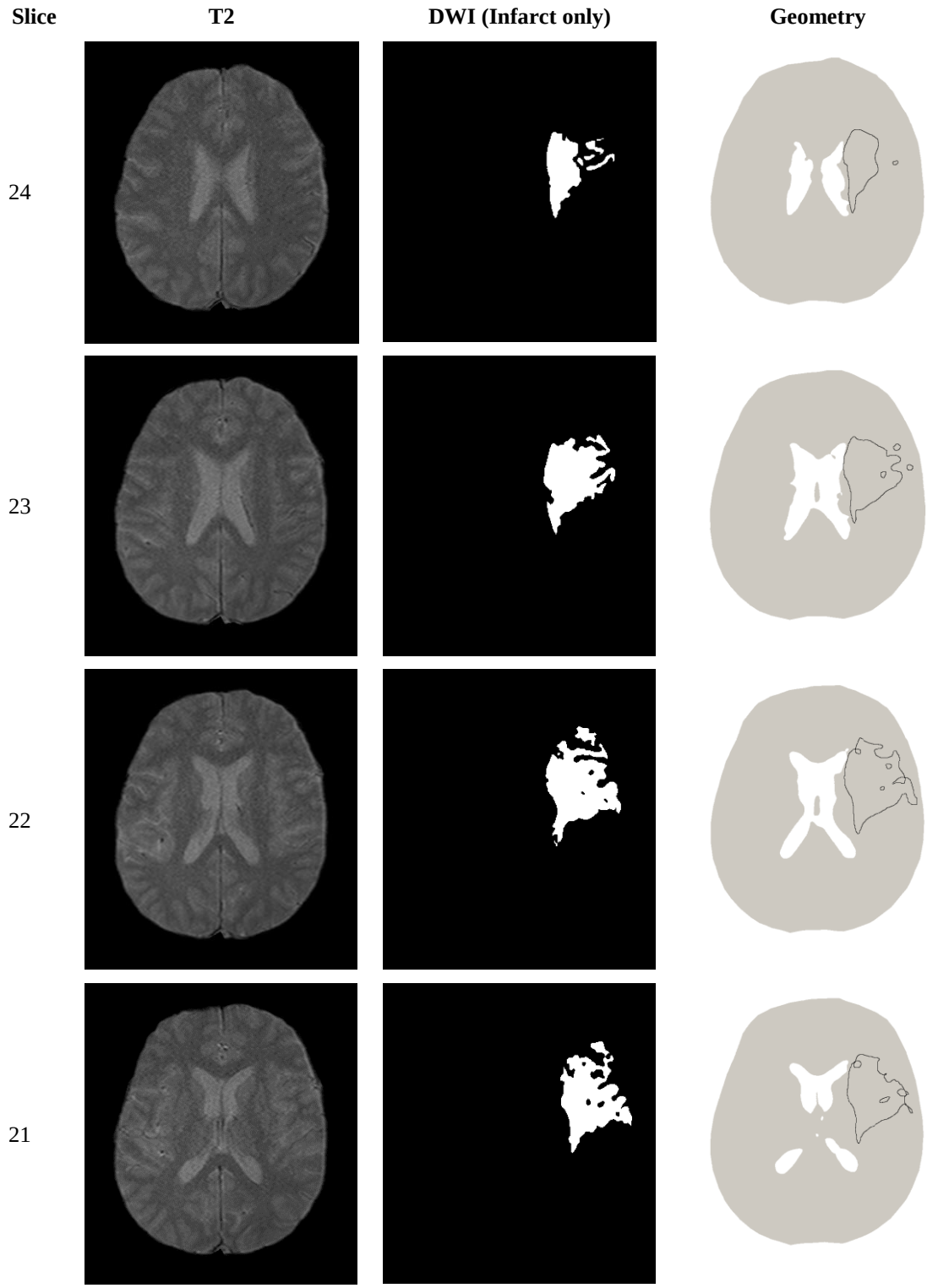

Figure C.2: Slices 21 to 24 of patient 1. Only slice 21 was not selected for analysis because the ventricles present in this slice are discontinuous.

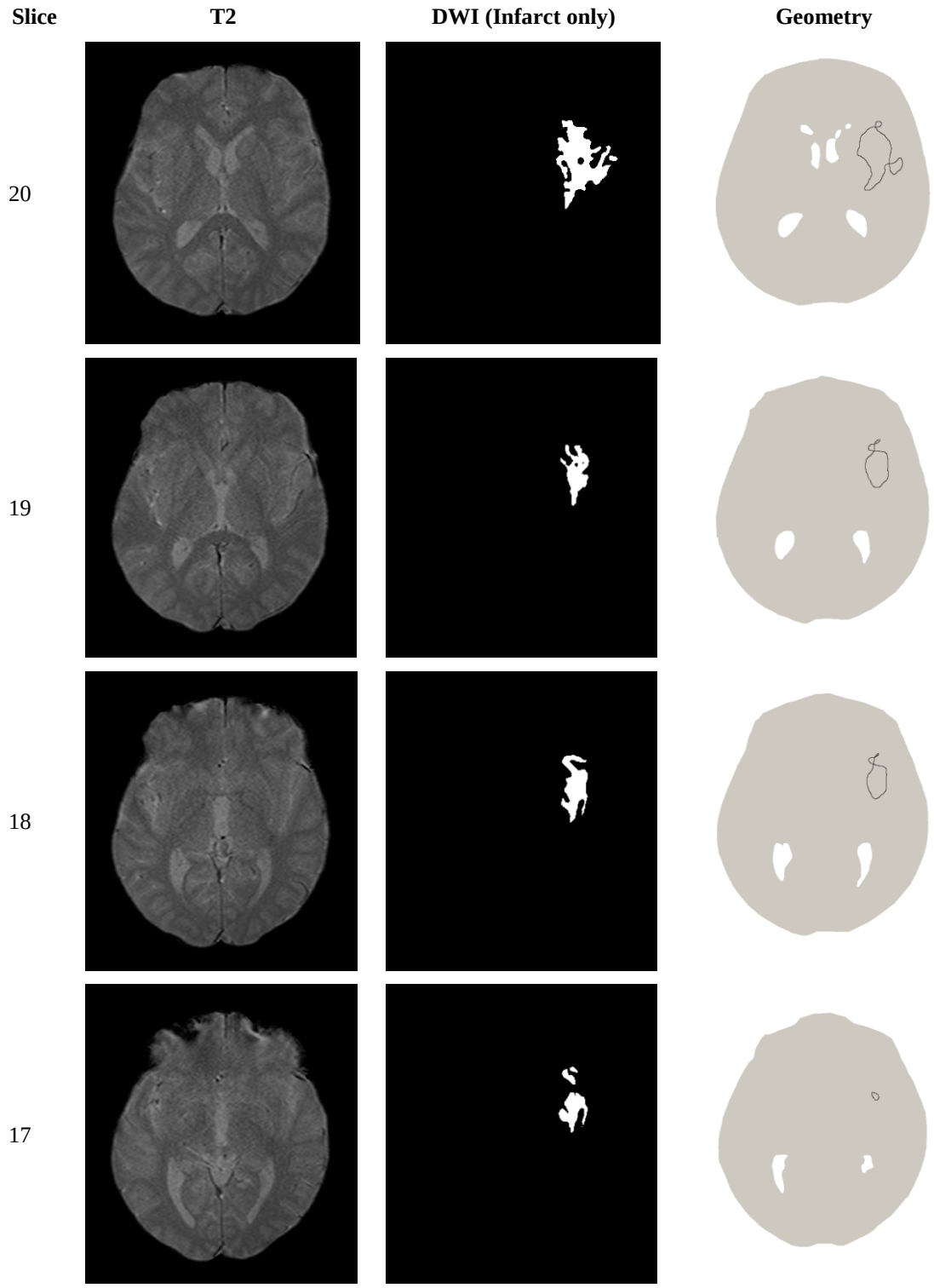

Figure C.3: Slices 17 to 20 of patient 1. None of these slices were chosen for the analysis because they are discontinuous and only small portions of the ventricles are present in these slices.

C.3 Patient 2

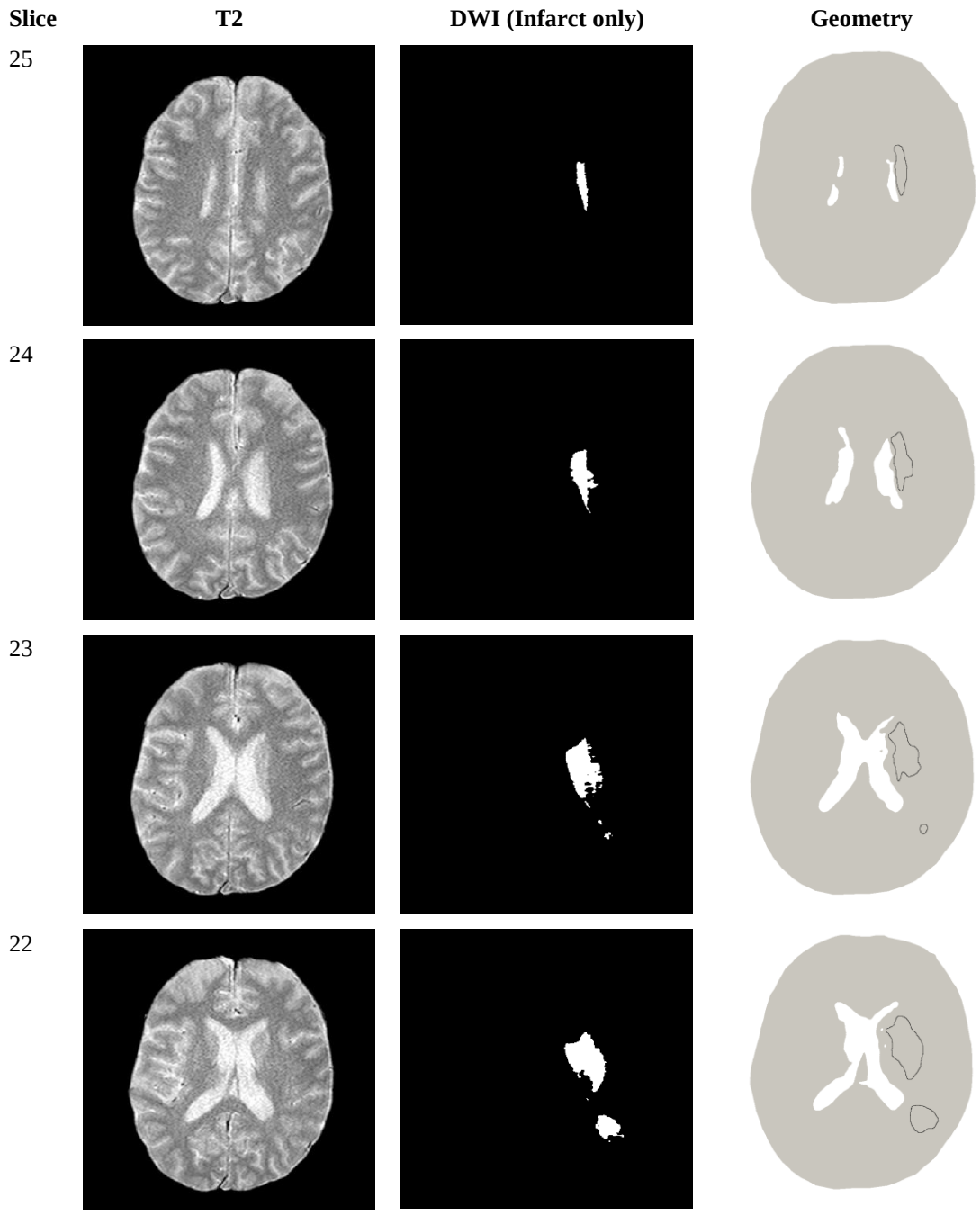

Figure C.4: Slices 22 to 25 of patient 2. Only slice 25 was not chosen because the ventricles present in this slice are not clear.

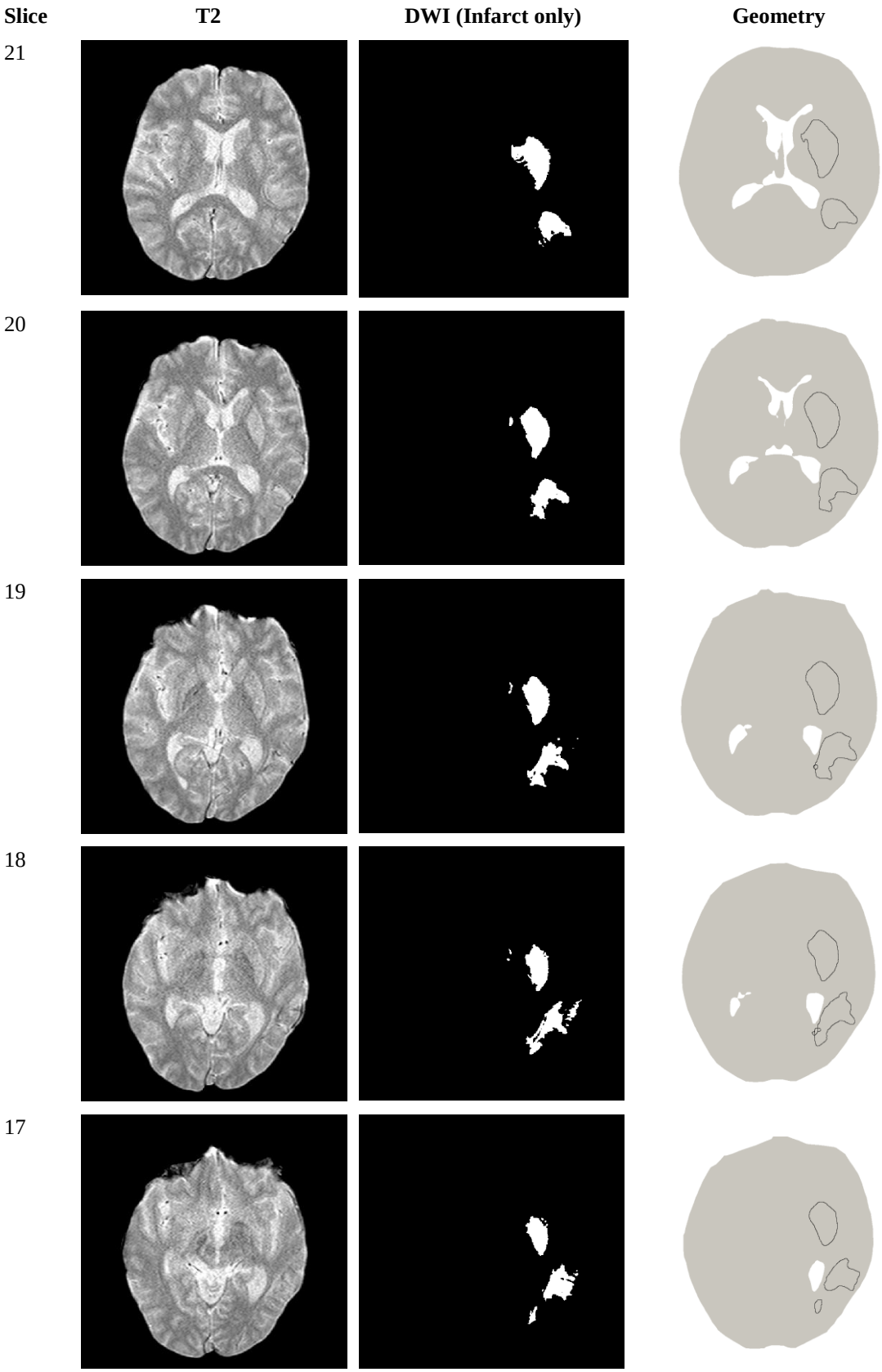

Figure C.5: Slices 17 to 21 of patient 2. None of these slices were chosen for the analysis because they are discontinuous and only small portions of the ventricles are present in these slices.

References

Aarabi, B., et al. (2006). Outcome following decompressive craniectomy for malignant swelling due to severe head injury. *J. Neurosurg., 104*, 469-479.

Abbott, N. J., et al. (2010). Structure and function of the blood-brain barrier. *Neurobiol. Dis., 37*, 13-25.

Abbott, N. J., et al. (2006). Astrocyte-endothelial interactions at the blood-brain barrier. *Nat. Rev. Neurosci., 7*, 41-53.

Abo-Ramadan, U., et al. (2009). Post-ischemic leakiness of the blood–brain barrier: A quantitative and systematic assessment by Patlak plots. *Exp. Neurol., 219*, 328-333.

Acartürk, A., et al. (2004). Modelling of swelling phenomena in charged hydrated porous media. *PMM-J. Appl. Math. Mech., 4*(1), 296-297.

Adams, H. P., et al. (1994). Guidelines for the management of patients with acute ischemic stroke: A statement for healthcare professionals from a special writing group of the Stroke Council, American Heart Association. *Stroke, 25*(9), 1901-1914.

Agre, P. (2006). The aquaporin water channels. *Proc. Am. Thorac. Soc., 3*, 5-13.

Aifantis, E. C. (1980). On the problem of diffusion in solids. *Acta Mech., 37*, 265-296.

Akins, P. T., et al. (2014). Complications of endovascular treatment for acute stroke in the SWIFT Trial with Solitaire and Merci Devices. *AJNR Am. J. Neuroradiol., 35*, 524-528.

Akins, P. T., et al. (2008). Sinking skin flaps, paradoxical herniation, and external brain tamponade: A review of decompressive craniectomy management. *Neurocrit. Care, 9*, 269-276.

Ames, A., et al. (1968). Cerebral ischemia: II. The no-reflow phenomenon. *Am. J. Pathol., 52*, 437-453.

Amiji, M., et al. (2003). *Applied physical pharmacy*. New York: McGraw-Hill Medical.

Amiry-Moghaddam, M., et al. (2003). An α-syntrophin-dependent pool of AQP4 in astroglial end-feet confers bidirectional water flow between blood and brain. *Proc. Natl. Acad. Sci. USA, 100*(4), 2106-2111.

Amorim, R. L., et al. (2014). Improved hemodynamics parameters in middle cerebral artery infarction after decompressive craniectomy. *Stroke, 45*, 1375-1380.

Andersen, K. K., et al. (2009). Hemorrhagic and ischemic strokes compared: Stroke severity, mortality, and risk factors. *Stroke, 40*, 2068-2072.

Aoki, T., et al. (2002). Bllod-brain barrier disruption and matrix metalloproteinase-9 expression during reperfusion injury: Mechanical versus embolic focal ischemia in spontaneously hypertensive rats. *Stroke, 33*, 2711-2717.

Araujo, R. P., et al. (2004). A history of the study of solid tumour growth: The contribution of mathematical modelling. *B. Math. Biol., 66*, 1039-1091.

Aries, M. J. H., et al. (2010). Cerebral autoregulation in stroke: A review of transcranial doppler studies. *Stroke, 41*, 2697-2704.

Astrup, J., et al. (1981). Thresholds in cerebral ischemia - The ischemic penumbra. *Am. Heart. Assoc., 12*(6), 723-725.

Ateshian, G. A., et al. (2009). A frame-invariant formulation of Fung elasticity. *J. Biomech., 42*, 781-785.

Ayata, C., et al. (2002). Ischaemic brain oedema. *J. Clin. Neurosci., 9*(2), 113-124.

Azeloglu, E. U., et al. (2008). Heterogeneous transmural proteoglycan distribution provides a mechanism for regulating residual stresses in the aorta. *Am. J. Physiol. Heart Circ. Physiol, 294*, H1197-H1205.

Badaut, J., et al. (2004). Distribution of Aquaporin 9 in the adult rat brain: Preferential expression in catecholaminergic neurons and in glial cells. *Neuroscience, 128*, 27-38.

Bai, M. (1993). Multiporosity/multipermeability approach to the simulation of naturally fractured reservoirs. *Water Resour. Res., 29*(6), 1621-1633.

Baird, A. E., et al. (1997). Enlargement of human cerebral ischemic lesion volumes measured by diffusion-weighted magnetic resonance imaging. *Ann. Neurol., 41*, 581-589.

Baish, J. W., et al. (1997). Transmural coupling of fluid flow in microcirculatory network and interstitium in tumors. *Microvasc. Res., 53*, 128-141.

Balestreri, M., et al. (2006). Impact of intracranial pressure and cerebral perfusion pressure on severe disability and mortality after head injury. *Neurocrit. Care, 4*, 8-13.

Barber, P. A., et al. (1999). Identification of major ischemic change: Diffusion-weighted versus computed tomography. *Stroke, 30*, 2059-2065.

Barber, P. A., et al. (2000). Validity and reliability of a quantitative computed tomography score in predicting outcome of hyperacute stroke before thrombolytic therapy. *Lancet, 355*, 1670-1674.

Barber, P. A., et al. (2005). Imaging of the brain in acute ischaemic stroke: Comparison of computed tomography and magnetic resonance diffusion-weighted imaging. *J. Neurol. Neurosurg. Psychiatry, 76*, 1528-1533.
Barber, P. A., et al. (2001). Why are stroke patients exclued from TPA therapy? *Neurology, 56*(8), 1015-1020.
Basser, P. J. (1992). Interstitial pressure, volume and flow during infusion into brain tissue. *Microvasc. Res., 44*, 143-165.
Bender, A. S., et al. (1998). Ionic mechanisms in glutamate-induced astrocyte swelling: Role of K^+ influx. *J. Neurosci. Res., 52*, 307-321.
Bereczki, D., et al. (2000). Cochrane report: A systematic review of mannitol therapy for acute ischemic stroke and cerebral parenchymal hemorrhage. *Stroke, 31*, 2719-2722.
Berrouschot, J., et al. (1998). Mortality of space-occupying ('malignant') middle cerebral artery infarction under conservative intensive care. *Intens. Care Med., 24*(6), 620-623.
Bešenski, N. (2002). Traumatic injuries: Imaging of head injuries. *Eur. Radiol., 12*, 1237-1252.
Biot, M. A. (1941). General theory of three dimensional consolidation. *J. Appl. Mech., 12*, 155-164.
Biot, M. A. (1956). Theory of propagation of elastic waves in a fluid-saturated porous solid. I: Low-frequency range. *J. Acoust. Soc. Am., 28*(2), 168-178.
Biot, M. A. (1961). Generalized theory of acoustic propagation in porous dissipative media. *J. Acoust. Soc. Am., 34*(5), 1254-1264.
Biot, M. A. (1962). Mechanics of deformation and acoustic propagation in porous media. *J. Appl. Mech., 33*, 1482-1498.
Biot, M. A., et al. (1957). The elastic coefficients of the theory of consolidation. *J. Appl. Mech., 24*, 594-601.
Bloch, O., et al. (2005). Aquaporin-4 gene deletion in mice increases focal edema associated with staphylococcal brain abscess. *J. Neurochem., 95*, 254-262.
Bouma, G. J., et al. (1992). Blood pressure and intracranial pressure-volume dynamics in severe head injury: Relationship with cerebral blood flow. *Neurosurg., 77*, 15-19.
Brant-Zawadzki, M., et al. (1986). MR imaging of acute experimental ischemia in cats. *AJNR Am. J. Neuroradiol., 7*, 7-11.
Brouns, R., et al. (2009). The complexity of neurobiological processes in acute ischemic stroke. *Clin. Neurol. Neurosur., 111*, 483-495.
Busza, A. L., et al. (1992). Diffusion-weighted imaging studies of cerebral ischemia in gerbils: Potential relevance to energy failure. *Stroke, 23*, 1602-1612.
Canaple, B., et al. (2003). Towards a finite element head model used as a head injury predictive tool. *Int. J. Crashworthines., 8*(1), 41-52.
Candelise, L., et al. (1975). Therapy against brain swelling in stroke patients: A retrospective clinical study on 227 patients. *Stroke, 6*(4), 353-356.
Cassot, F., et al. (2006). A novel three-dimensional computer-assisted method for a quantitative study of microvascular networks of the human cerebral cortex. *Microcirculation, 13*, 1-18.
Chen, N., et al. (2007). A parallel implementation of the Cellular Potts Model for simulation of cell-based morphogenesis. *Comput. Phys. Commun., 176*(11-12), 670-681.
Cheng, S., et al. (2007). Unconfined compression of white matter. *J. Biomech., 40*, 117-124.
Chiang, J., et al. (1968). Cerebral ischemia: III. Vascular changes. *Am. J. Pathol., 52*(2), 455-476.
Clark, A. G., et al. (2011). Mechanics and regulation of cell shape during the cell cycle. In J. Z. Kubiak (Ed.), *Cell cycle in development*. Germany: Springer Berlin Heidelberg.
Cloutier, M., et al. (2009). An integrative dynamic model of brain energy metabolism using in vivo neurochemical measurements. *J. Comput. Neurosci., 27*, 301-414.
Cosgrove, K. P., et al. (2007). Evolving knowledge of sex differences in brain structure, function and chemistry. *Biol. Psychiat., 62*(8), 847-855.
Cowin, S., et al. (2009). *Tissue Mechanics*. Berlin, Germany: Springer.
Cushing, H. (1905). The establishment of cerebral hernia as a decompressive measure for inaccessible brain tumors: with the description of intermuscular methods of making the bone defect in temporal and occipital regions. *Surg. Gynecol. Obstet., 1*, 297-314.
Czosnyka, M., et al. (2005). Age, intracranial pressure, autoregulation, and outcome after brain trauma. *Neurosurg., 102*, 450-454.
del Zoppo, G. J., et al. (2003). Cerebral microvessel responses to focal ischemia. *J. Cereb. Blood Flow Metab., 23*, 879-894.
del Zoppo, G. J., et al. (1991). Polymorphonuclear leukocytes occlude capillaries following middle cerebral artery occlusion and reperfusion in baboons. *Stroke, 22*, 1276-1283.
Detre, J. A., et al. (1992). Perfusion imaging. *Magnet. Reson. Med., 23*, 37-45.

Dirnagl, U., et al. (1999). Pathobiology of ischemic stroke: An integrated view. *Trends Neurosci., 22*, 391-397.
Doczi, T. (1993). Volume regulation of the brain tissue - A survey. *Acta Neurochir. (Wien), 121*, 1-8.
Donkin, J. J., et al. (2010). Mechanisms of cerebral edema in traumatic brain injury: Therapeutic developments. *Curr. Opin. Neurol., 23*, 293-299.
Donnan, F. G. (1924). The theory of membrane equilibria. *Chem. Rev., 1*(1), 73-90.
Doran, M., et al. (1990). Normal and abnormal white matter tracts shown by MR imaging using directional diffusion weighted sequences. *J. Comput. Assist. Tomo., 14*(6), 865-873.
Drake, J. M., et al. (1996). Realistic simple mathematical model of brain biomechanics for computer simulation of hydrocephalus and other brain abnormalities. *Can. J. Neurol. Sci., 23*, S5.
Drapaca, C. S., et al. (2012). A mechano-electrochemical model of brain neuro-mechanics: Application to normal pressure hydrocephalus. *Int. J. Num. Anal. Mod. Ser. B., 3*(1), 82-93.
Drzewiecki, G., et al. (1997). Vessel growth and collapsible pressure-area relationship. *Am. J. Physiol. Heart Circ. Physiol, 42*, H2030-H2043.
Elkin, B. S., et al. (2010). Fixed negative charge and the Donnan effect: A description of the driving forces associated with brain tissue swelling and oedema. *Phil. Trans. R. Soc. A., 368*, 585-603.
Elkin, B. S., et al. (2011). Chondroitinase ABC reduces brain tissue swelling in vitro. *J. Neurotraum., 28*, 2277-2285.
Endresen, L. P., et al. (2000). A theory for the membrane potential of living cells. *Eur. Biophys. J., 29*, 90-103.
Eyster, H. C. (1943). Osmosis and osmotic pressure. *Bot. Rev., 9*(5), 311-324.
Feigin, V., et al. (2003). Stroke epidemiology: A review of population based studies of incidence, prevalence, and case-fatality in the late 20th century. *Lancet Neurol., 2*, 43-53.
Feigin, V. L., et al. (2014). Global and regional burden of stroke during 1990-2010: findings from the Global Burden of Disease Study 2010. *Lancet, 383*(9913), 245-254.
Fenstermacher, J., et al. (1988). Structural and functional variations in capillary systems within the brain. *Ann. NY. Acad. Sci., 529*(1), 21-30.
Fink, J. N., et al. (2002). The stroke patient who woke up: Clinical and radiological features, including diffusion and perfusion MRI. *Stroke, 33*, 988-993.
Fischer, E. G., et al. (1977). Reassessment of cerebral capillary changes in acute global ischemia and their relationship to the "no-reflow phenomenon". *Stroke, 8*(1), 36-39.
Fischer, E. G., et al. (1979). Cerebral blood flow immediately following brief circulatory stasis. *Stroke, 10*, 423-427.
Fishman, R. A. (1975). Brain Edema. *New Engl. J. Med., 293*(14), 706-711.
Flexner, L. B., et al. (1932). The elasticity of the dural and its contents. *Am. J. Physiol., 101*(2), 292-303.
Floyd, R. A. (1990). Role of oxygen free radicals in carcinogenesis and brain ischemia. *FASEB J., 4*, 2587-2597.
Fodstad, H., et al. (1984). Effect of cranioplasty on cerebrospinal fluid hydrodynamics in patients with the syndrome of the trephined. *Acta Neurochir., 70*, 21-30.
Fotheringham, A. P., et al. (2000). Oedema and glial cell involvement in the aged mouse brain after permanent focal ischaemia. *Neuropath. Appl. Neuro., 26*, 412-423.
Frank, J. I. (1995). Large hemispheric infarction, deterioration, and intracranial pressure. *Neurology, 45*, 1286-1290.
Fraser, P. A., et al. (1990). Measurement of filtration coefficient in single cerebral microvessels of the frog. *J. Physiol., 423*, 343-361.
Frijns, A. J. H., et al. (1997). A validation of the quadriphasic mixture theory for intervertebral disc tissue. *Int. J. Engng. Sci., 35*(15), 1419-1429.
Furlan, A., et al. (1999). Intra-arterial prourokinase for acute ischemic stroke. The PROACT II study: a randomized controlled trial. Prolyse in Acute Cerebral Thromboembolism. *JAMA-J. Am. Med. Assoc., 282*(21), 2003-2011.
Furlan, A. J., et al. (2003). Thrombolytic therapy in acute ischemic stroke. *Curr. Treat. Options Cardiovasc. Med., 5*, 171-180.
Galford, J. E., et al. (1970). A viscoelastic study of scalp, brain, and dura. *J. Biomech., 3*(2), 211-221.
Gaser, C., et al. (2001). Deformation-based morphometry and its relation to conventional volumetry of brain lateral ventricles in MRI. *Neuroimage, 13*(6 Pt 1), 1140-1145.
George, M. G., et al. (2009). Paul Coverdell National Acute Stroke Registry Surveillance - four states, 2005-2007. *MMWR Surveill. Summ., 58*(7), 1-23.
Gerriets, T., et al. (2001). Sonographic monitoring of midline shift in space-occupying stroke: An early outcome predictor. *Stroke, 32*, 442-447.

Gerriets, T., et al. (1999). Sonographic monitoring of midline shift in hemispheric infarctions. *Neurology, 52*, 45-49.
Geuzaine, C., et al. (2009). Gmsh: A three-dimensional finite element mesh generator with built-in pre- and post- processing facilities. *Int. J. Numer. Method Eng., 0*, 1-24.
Gidday, J. M., et al. (2005). Leukocyte-derived matrix metalloproteinase-9 mediates blood-brain barrier breakdown and is proinflammatory after transient focal cerebral ischemia. *Am. J. Physiol. Heart Circ. Physiol, 289*, H558-H568.
Go, K. G. (1997). The normal and pathological physiology of brain water. *Adv. Tech. Stand. Neurosurg., 23*, 47-142.
Gonzalez, R. G., et al. (1999). Diffusion-weighted MR imaging: Diagnostic accuracy in patients imaged within 6 hours of stroke symptom onset. *Radiology, 210*, 155-162.
Graner, F., et al. (1992). Simulation of biological cell sorting using a two-dimensional extended Potts Model. *Phys Rev Lett, 69*(13), 2013-2017.
Green, A. E., et al. (1969). On basic equations for mixtures. *Quart. J. Mech. Appl. Math., 22*(4), 427-438.
Greenwood, J. (1991). Mechanisms of blood-brain barrier breakdown. *Neuroradiology, 33*, 95-100.
Gruen, P. (2002). Surgical management of head trauma. *Neuroimaging Clin N Am, 12*(2), 339-343.
Guillaume, A., et al. (1997). Effects of perfusion on the mechanical behavior of the brain exposed to hypergravity. *J. Biomech., 30*(4), 383-389.
Hacke, W., et al. (2004). Association of outcome with early stroke treatment: pooled analysis of ATLANTIS, ECASS, and NINDS rt-PA stroke trials. *Lancet, 363*(9411), 768-774.
Hacke, W., et al. (1995). Intravenous thrombolysis with recombinant tissue plasminogen activator for acute hemispheric stroke: The European Cooperative Acute Stroke Study (ECASS). *JAMA, 274*(13), 1017-1025.
Hacke, W., et al. (2000). European Stroke Initiative (EUSI) recommendations for stroke management: The European Stroke Initiative Writing Committee. *Eur J Neurol, 7*, 607-623.
Hacke, W., et al. (1996). 'Malignant' middle cerebral artery territory infarction: Clinical course and prognostic signs. *Arch. Neurol., 53*, 309-315.
Hajnal, J. V., et al. (1991). MR imaging of anisotropically restricted diffusion of water in the nervous system: Technical, anatomic, and pathological considerations. *J. Comput. Assist. Tomo., 15*(1), 1-18.
Hakamata, Y., et al. (1995). Long-term high-colloid oncotic therapy for ischemic brain edema in gerbils. *Stroke, 26*, 2149-2158.
Hakim, S., et al. (1976). The physics of the cranial cavity, hydrocephalus, and normal pressure hydrocephalus: Mechanical interpretation and mathematical model. *Surg. Neurol., 5*, 187-210.
Haley Jr, E. C., et al. (1993). Pilot randomized trial of tissue plasminigen activator in acute ischemic stroke. The TPA Bridging Study Group. *Stroke, 24*, 1000-1004.
Hamann, G. F., et al. (1996). Hemorrhagic transformation and microvascular integrity during focal cerebral ischemia/reperfusion. *J. Cereb. Blood Flow Metab., 16*, 1373-1378.
Hamann, G. F., et al. (1995). Microvascular basal lamina antigens disappear during cerebral ischemia and reperfusion. *Stroke, 26*, 2120-2126.
Hartkens, T., et al. (2003). Measurement and analysis of brain deformation during neurosurgery. *IEEE Trans Med Imaging, 22*(1), 82-92.
Hauck, E. F., et al. (2004). Capillary flow and diameter changes during reperfusion after global cerebral ischemia studied by intravital video microscopy. *J Cereb Blood Flow Metab, 24*(4), 383-391.
Hawkins, B. T., et al. (2005). The blood-brain barrier/Neurovascular unit in health and disease. *Pharmacol. Rev., 57*, 173-185.
Heiss, W.-D., et al. (1997). Repeat positron emission tomographic studies in transient middle cerebral artery occlusion in cats: Residual perfusion and efficacy of postischemic reperfusion. *J. Cereb. Blood Flow Metab., 17*, 388-400.
Henderson, A. (2007). *The ParaView Guide: A Parallel Visualization Application*: Kitware Inc.
Hofmeijer, J., et al. (2009). Surgical decompression for space-occupying cerebral infarction (the Hemicraniectomy After Middle Cerebral Artery infarction with Life-threatening Edema trial [HAMLET]): a multicentre, open, randomised trial. *Lancet Neurol., 8*, 326-333.
Honeybul, S. (2008). Decompressive craniectomy: A new complication. *J. Clin. Neurosci., 16*, 727-729.
Hossmann, K.-A. (1976). Development and resolution of ischemic brain swelling. In H. M. Pappius, et al. (Eds.), *Dynamics of brain edema* (pp. 219-227). Berlin/Heidelberg/New York: Springer-Verlag.
Hossmann, K.-A. (1997). Reperfusion of the brain after global ischemia: Hemodynamic disturbances. *Shock, 8*(2), 95-101.
Hrabětová, S., et al. (2002). Water compartmentalization and spread of ischemic injury in thick-slice ischemia model. *J. Cereb. Blood Flow Metab., 22*, 80-88.

Huang, J., et al. (2006). Inflammation in stroke and focal cerebral ischemia. *Surg. Neurol., 66*, 232-245.
Iliff, J. J., et al. (2012). A paravascular pathway facilitates CSF flow through the brain parenchyma and the clearance of interstitial solutes, including amyloid β. *Sci. Trans. Med., 4*(147), 1-11.
IMS II Trial Investigators. (2007). The Interventional Management of Stroke (IMS) II Study. *Stroke, 38*(7), 2127-2135.
Ito, H., et al. (2001). Arterial fraction of cerebral blood volume in humans measured by positron emission tomography. *Ann. Nucl. Med., 15*(2), 111-116.
Ito, U., et al. (1979). Brain edema during ischemia and after restoration of blood flow: Measurement of water, sodium, potassium content and plasma protein permeability. *Stroke, 10*(5), 542-547.
Jansen, O., et al. (1995). Thrombolytic therapy in acute occlusion of the intracranial internal carotid artery bifurcation. *AJNR Am. J. Neuroradiol., 16*, 1977-1986.
Janzer, R. C. (1993). The blood-brain barrier: Cellular basis. *J. Inher. Metab. Dis., 16*, 639-647.
Jenkinson, M., et al. (2002). Improved optimisation for the robust and accurate linear registration and motion correction of brain images. *Neuroimage, 17*(2), 825-841.
Jenkinson, M., et al. (2012). FSL. *Neuroimage, 62*, 782-790.
Jenkinson, M., et al. (2001). A global optimisation method for robust affine registration of brain images. *Med. Image Anal., 5*(2), 143-156.
Jensen, O. E., et al. (1989). The existence of steady flow in a collapsed tube. *J. Fluid Mech., 206*, 339-374.
Jiang, H., et al. (2013). Cellular pressure and volume regulation and implications for cell mechanics. *Biophys. J., 105*, 609-619.
Jiménez-Conde, J., et al. (2007). Does sleep protect against ischemic stroke? Less frequent ischemic strokes but more severe ones. *J. Neurol., 254*, 782-788.
Jin, B.-J., et al. (2012). Aquaporin-4-dependent K^+ and water transport modeled in brain extracellular space following neuroexcitation. *J. Gen. Physiol., 141*(1), 119-132.
Jordan, J. D., et al. (2012). Cerebral autoregulation and acute ischemic stroke. *Am. J. Hypertens., 25*(9), 946-950.
Joseph, V., et al. (2009). Syndrome of the trephined. *J. Neurosurg., 111*, 650-652.
Kaczmarek, M., et al. (1997). The hydromechanics of hydrocephalus: Steady-state solutions for cylindrical geometry. *Bulletin of Mathematical Biology, 59*(2), 295-323.
Kan, P., et al. (2006). Outcomes after decompressive craniectomy for severe traumatic brain injury in children. *J. Neurosurg. (5 Suppl Pediatrics), 105*, 337-342.
Kane, I., et al. (2007). Magentic resonance perfusion diffusion mismatch and thrombolysis in acute ischaemic stroke: A systematic review of the evidence to date. *J. Neurol. Psychiatry, 78*, 485-490.
Kawamata, T., et al. (2007). Tissue hyperosmolality and brain edema in cerebral contusion. *Neurosurg. Focus, 22*(5), 1-8.
Keir, S. L., et al. (2000). Systematic review of diffusion and perfusion imaging in acute ischemic stroke. *Stroke, 31*, 2723-2731.
Kimelberg, H. K. (1995). Current concepts of brain edema: Review of laboratory investigations. *J. Neurosurg., 83*, 1051-1059.
Kimelberg, H. K. (2004). Water homeostasis in the brain: Basic concepts. *Neuroscience, 129*, 851-860.
Klatzo, I. (1987). Pathophysiological aspects of brain edema. *Acta Neuropathol., 72*, 236-239.
Kleindienst, A., et al. (2006). Modulation of AQP4 expression by the protein kinase C activator, phorbol myristate acetate, decreases ischemia-induced brain edema. *Acta Neurochir. [Suppl], 96*, 393-397.
Knepper, M. A., et al. (2004). Peter Agre, 2003 Nobel Prize winner in Chemistry. *J. Am. Soc. Nephrol., 15*, 1093-1095.
Kniesel, U., et al. (2000). Tight junctions of the blood-brain barrier. *Cell. Mol. Neurobiol., 20*(1), 57-76.
Koenig, M., et al. (1998). Perfusion CT of the brain: Diagnostic approach for early detection of ischemic stroke. *Radiology, 209*, 85-93.
Koudstaal, P. J., et al. (1988). Fatal ischemic brain edema after early thrombolysis with tissue plasminogen activator in acute stroke. *Brit Med J, 297*(6663), 1571-1574.
Krieg, M., et al. (2008). Tensile forces govern germ-layer organization in zebrafish. *Nat Cell Biol, 10*(4), 429-436.
Krueger, M., et al. (2010). CNS Pericytes: Concepts, misconceptions, and a way out. *Glia, 58*, 1-10.
Kurbel, S. (2008). Are extracellular osmolality and sodium concentration determined by Donnan effects of intracellular protein charges and of pumped sodium? *J. Theor. Biol., 252*, 769-772.
Kuroiwa, T., et al. (1994). Is the swelling in brain edema isotropic or anisotropic? *Acta Neurochir. Suppl. (Wien), 60*, 155-157.
Kuroiwa, T., et al. (1990). Accummulation of oedema fluid in deep white matter after cerebral cold injury. *Acta Neurochir. Suppl. (Wien), 51*, 84-86.

Kyriacou, S. K., et al. (2002). Brain mechanics for neurosurgery: Modeling issues. *Biomechan. Model. Mechanobiol., 1*, 151-164.
Lang, G. E., et al. (2014). Is the Donnan effect sufficient to explain swelling in brain tissue slices? *J. R. Soc. Interface, 11*, 1-8
Lang, G. E., et al. (2015). Propagation of damage in brain tissue: Coupling the mechanics of oedema and oxygen delivery. *Biomech. Model Mechanobiol., 14*(6), 1197-1216.
Lansberg, M. G., et al. (2000). Comparison of diffusion-weighted MRI and CT in acute stroke. *Neurology, 54*, 1557-1561.
Lansberg, M. G., et al. (2009). Efficacy and safety of tissue plasminogen activator 3 to 4.5 hours after acute ischemic stroke: A metaanalysis. *Stroke, 40*, 2438-2441.
Leaf, A. (1959). Maintenance of concentration gradients and regulation of cell volume. *Ann. NY. Acad. Sci., 72*(12), 396-404.
Lee, B., et al. (2005). Neuroimaging in traumatic brain imaging. *NeuroRx, 2*(2), 372-383.
Levick, J. R., et al. (2010). Microvascular fluid exchange and the revised Starling principle. *Cardiovasc. Res., 87*, 198-210.
Levman, J., et al. (2014). Semi-automatic region-of-interest segmentation based computer-aided diagnosis of mass lesions from dynamic contrast-enhanced magnetic resonance imaging based breast cancer screening. *J Digit Imaging, 27*(5), 670-678.
Li, G., et al. (2010). A model for the blood-brain barrier permeability to water and small solutes. *J. Biomech., 43*, 2133-2140.
Lin, R., et al. (2008). Chondroitinase ABC has a long-lasting effect on chondroitin sulphate glycosaminoglycan content in the injured rat brain. *J. Neurochem., 104*(400-408).
Lindenberg, R. (1955). Compression of brain arteries as pathogenetic factor for tissue necroses and their areas of predilection. *J. Neuropath. Exp. Neur., 14*(3), 223-243.
Liu, F., et al. (2009). Model-based estimation of ventricular deformation in the cat brain. *Med. Image. Comput. Comput. Assist. Interv., 12(Pt 2)*, 308-315.
Lo, W. D., et al. (1987). Transport of sodium from blood to brain in ischemic brain edema. *Stroke, 18*, 150-157.
Lodder, J. (1984). CT-detected hemorrhagic infarction; relation with the size of the infarct and the presence of the midline shift. *Acta Neurol. Scand., 70*(5), 329-335.
Lozano, R., et al. (2012). Global and regional mortality from 235 causes of death for 20 age groups in 1990 and 2010: a systematic analysis for the Global Burden of Disease Study 2010. *Lancet, 380*(9859), 2095-2128.
Lu, X. L., et al. (2008). Biomechanics of articular cartilage and determination of material properties. *Med. Sci. Sport. Exer., 40*(2), 193-199.
Lucas, C. (2013). *An anatomical model of the cerebral vasculature and blood flow.* (D. Phil.), Oxford Univ., Oxford.
Manley, G. T., et al. (2004). New insights into water transport and edema in the central nervous system from phenotype analysis of aquaporin-4 null mice. *Neuroscience, 129*, 983-991.
Margolis, R. U., et al. (1975). Glycosaminoglycans of brain during development. *Biochemistry, 14*(1), 85-88.
Marmarou, A. (2007). A review of progress in understanding the pathophysiology and treatment of brain edema. *Neurosurg. Focus, 22*(5), 1-10.
Marshall, J. (1977). Diurnal variation in occurrence of strokes. *Stroke, 8*, 230-231.
Martin, J., et al. (1994, June). *Shape analysis of brain structures using physical and experimental modes.* Paper presented at the Proceedings of the IEEE Conf. on Computer Vision and Pattern Recognition (CVPR), Seattle, WA.
Masugata, H., et al. (1998). Mitral valve tissue characterization using acoustic microscopy. *J. Cardiol., 31*(Suppl. 1), 45-51.
Mathalon, D. H., et al. (2001). Progressive brain volume changes and the clinical course of schizophrenia in men: a longitudinal magnetic resonance imaging study. *Arch Gen Psychiatry, 58*(2), 148-157.
Mayer, T. E., et al. (2000). Dynamic CT perfusion imaging of acute stroke. *AJNR Am. J. Neuroradiol., 21*, 1441-1449.
Mendis, S., et al. (2015). Organizational update: the world health organization global status report on noncommunicable diseases 2014; one more landmark step in the combat against stroke and vascular disease. *Stroke, 46*(5), e121-122.
Menzies, S. A., et al. (1993). Contributions of ions and albumin to the formation and resolution of ischemic brain edema. *J. Neurosurg., 78*, 257-266.
Menzies, W. F. (1893). Thrombosis of inferior cerebellar artery. *Brain, 16*(3), 436-439.

Metz, H., et al. (1970). A comparison of elasticity of live, dead, and fixed brain tissue. *J. Biomech., 3*(4), 453-458.
Miga, M. I., et al. (2000). In vivo quantification of a homogeneous brain deformation model for updating preoperative images during surgery. *IEEE T. Biomed. Eng., 47*(2), 266-273.
Miller, J. D., et al. (1973). Cerebral blood flow regulation during experimental brain compression. *J. Neurosurg., 39*, 186-196.
Miller, K. (1999). Constitutive model of brain tissue suitable for finite element analysis of surgical procedures. *J. Biomech., 32*, 531-537.
Mintorovitch, J., et al. (1991). Comparison of diffusion- and T2-weighted MRI for the early detection of cerebral ischemia and reperfusion in rats. *Magnet. Reson. Med., 18*, 39-50.
Mohr, J. P., et al. (1995). Magnetic resonance versus computed tomographic imaging in acute stroke. *Stroke, 26*, 807-812.
Mokri, B. (2001). The Monro-Kellie hypothesis: Applications in CSF volume depletion. *Neurology, 56*, 1746-1748.
Molina, C. A., et al. (2005). Extending reperfusion therapy for acute ischemic stroke: emerging pharmacological, mechanical, and imaging strategies. *Stroke, 36*(10), 2311-2320.
Mori, K., et al. (2002). Temporal profile of changes in brain tissue extracellular space and extracellular ion (Na^+, K^+) concentrations after cerebral ischemia and the effects of mild cerebral hypothermia. *J. Neurotraum., 19*(10), 1261-1270.
Moseley, M. E., et al. (1990). Diffusion-weighted MR imaging of anisotropic water diffusion in cat central nervous system. *Radiology, 176*(2), 439-445.
Murphy, G., et al. (1997). Relating matrix metalloproteinase structure to function: Why the "Hemopexin" domain? *Matrix Biol., 15*, 511-518.
Murray, C. J., et al. (2012). Disability-adjusted life years (DALYs) for 291 diseases and injuries in 21 regions, 1990-2010: a systematic analysis for the Global Burden of Disease Study 2010. *Lancet, 380*(9859), 2197-2223.
Nagashima, T., et al. (1990). A two-dimensional, finite element analysis of vasogenic brain edema. *Neurol. Med. Chir., 30*, 1-9.
Nagashima, T., et al. (1987). Biomechanics of hydrocephalus - A new theoretical model. *Neurosurgery, 21*(6), 898-904.
Nagelhaus, E. A., et al. (2013). Physiological roles of aquaporin-4 in brain. *Physiol. Rev., 93*, 1543-1562.
Nagelhaus, E. A., et al. (1998). Aquaporin-4 water channel protein in the rat retina and optic nerve: Polarized expression in Müller cells and fibrous astrocytes. *J. Neurosci., 18*(7), 2506-2519.
Nakahama, K.-I., et al. (1999). Effect of TPA on aquaporin 4 mRNA expression in cultured rat astrocytes. *Glia, 25*, 240-246.
Nau, R. (2000). Osmotherapy for elevated intracranial pressure: A critical reappraisal. *Clin. Pharmacokinet., 38*(1), 23-40.
Naugebauer, H., et al. (2014). Hemicraniectomy for malignant middle cerebral artery infarction: Current status and future directions. *Int. J. Stroke, 9*(4), 460-467.
Neely, J. D., et al. (2001). Syntrophin-dependent expression and localization of aquaporin-4 water channel protein. *Proc. Natl. Acad. Sci. USA, 98*(24), 14108-14113.
Nestor, S. M., et al. (2008). Ventricular enlargement as a possible measure of Alzheimer's disease progression validated using the Alzheimer's disease neuroimaging initiative database. *Brain, 131*, 2443-2454.
Ng, I., et al. (2004). Effects of head posture on cerebral hemodynamics: Its influences on intracranial pressure, cerebral perfusion pressure, and cerebral oxygenation. *Neurosurg., 54*, 593-598.
Nicholson, C., et al. (1998). Extracellular space structure revealed by diffusion analysis. *Trends Neurosci., 21*, 207-215.
Nielsen, S., et al. (1997). Specialized membrane domains for water transport in glial cells: High-resolution immunogold cytochemistry of aquaporin-4 in rat brain. *J. Neurosci., 17*(1), 171-180.
Nielsen, S., et al. (1993). Distribution of the aquaporin CHIP in secretory and resorptive epithelia and capillary endothelia. *Proc. Natl. Acad. Sci. USA, 90*, 7275-7279.
Ohata, K., et al. (1990). An immunocytochemical study of protein clearance in brain infusion edema. *Acta Neuropath., 81*, 162-177.
Oldendorf, W. H., et al. (1977). The large apparent work capability of the blood-brain barrier: A study of the mitochondrial content of capillary endothelial cells in brain and other tissues of the rat. *Ann. Neurol., 1*, 409-417.
Olivot, J.-M., et al. (2008). Relationship between infarct growth, clinical outcome, and early recanalization in diffusion and perfusion imaging for understanding stroke evolution (DEFUSE). *Stroke, 39*, 2257-2263.

Orlowski, P., et al. (2011). Modelling of pH dynamics in brain cells after stroke. *Interface focus, 1*, 408-416.
Orlowski, P., et al. (2013). Modelling of the physiological response of the brain to ischaemic stroke. *Interface focus, 3*, 1-8.
Oshio, K., et al. (2005). Reduced cerebrospinal fluid production and intracranial pressure in mice lacking choroid plexus water channel Aquaporin-1. *FASEB J., 19*, 76-78.
Pan, J., et al. (2007). Reperfusion injury following cerebral ischemia: pathophysiology, MR imaging, and potential therapies. *Neuroradiology, 49*(2), 93-102.
Panickar, K. S., et al. (2005). Astrocyes in cerebral ischemic injury: Morphological and general considerations. *Glia, 50*, 287-298.
Papadopoulos, M. C., et al. (2004). Aquaporin-4 facilitates reabsorption of excess fluid in vasogenic brain edema. *FASEB J., 18*, 1291-1293.
Papadopoulos, M. C., et al. (2005). Aquaporin-4 gene disruption in mice reduces brain swelling and mortality in pneumococcal meningitis. *J. Biol. Chem., 280*, 13906-13912.
Papadopoulos, M. C., et al. (2007). Aquaporin-4 and brain edema. *Pediatr. Nephrol., 22*, 778-784.
Papadopoulos, M. C., et al. (2008). Potential utility of aquaporin modulators for therapy of brain disorders. *Prog. Brain Res., 170*, 589-601.
Papadopoulos, M. C., et al. (2013). Aquaporin water channels in the nervous system. *Nat. Neurosci., 14*, 265-277.
Patlak, C. S., et al. (1985). Graphical evaluation of blood-to-brain transfer constants from multiple-time uptake data. Generalizations. *J. Cereb. Blood Flow Metab., 5*, 584-590.
Patlak, C. S., et al. (1983). Graphical evaluation of blood-to-brain transfer constants from multiple-time uptake data. *J. Cereb. Blood Flow Metab., 3*, 1-7.
Payne, S. J. (2006). A model of the interaction between autoregulation and neural activation in the brain. *Mathematical Biosciences, 204*(2), 260-281.
Peña, A., et al. (1999). Effects of brian ventricular shape on periventricular biomechanics: A finite-element analysis. *Neurosurg., 45*(1), 107.
Perlmutter, L. S., et al. (1990). Microangiopathy, the vascular basement membrane and Alzheimer's Disease: A review. *Brain Res. Bull., 24*, 677-686.
Preston, E., et al. (1997). Evidence for pore-like opening of the blood-brain barrier following forebrain ischemia in rats. *Brain Res., 761*, 4-10.
Preston, G. M., et al. (1991). Isolation of the cDNA for erythrocyte integral membrane protein of 28 kilodaltons: Member of an ancient channel family. *Proc. Natl. Acad. Sci. USA, 88*, 11110-11114.
Prichard, J. W., et al. (1999). New reasons for early use of MRI in stroke. *Neurology, 52*(9), 1733-1736.
Rankin, J. (1957). Cerebral vascular accidents in patients over the age of 60. II. Prognosis. *Scott. Med. J., 2*(5), 200-215.
Rapoport, S. I. (1978). A mathematical model for vasogenic brain edema. *J. Theor. Biol., 74*, 439-467.
Rash, J. E., et al. (1998). Direct immunogold labeling of aquaporin-4 in square arrays of astrocyte and ependymocyte plasma membranes in rat brain and spinal cord. *Proc. Natl. Acad. Sci. USA, 95*, 11981-11986.
Reinhard, M., et al. (2012). Dynamic cerebral autoregulation associates with infarct size and outcome after ischemic stroke. *Acta Neurol. Scand., 125*, 156-162.
Reulen, H. J., et al. (1977). Role of pressure gradients and bulk flow in dynamics of vasogenic brain edema. *J. Neurosurg., 46*, 24-35.
Reulen, H. J., et al. (1978). Clearance of edema fluid into cerebrospinal fluid: A mechanism for resolution of vasogenic brain edema. *J. Neurosurg., 48*, 754-764.
Rippe, B., et al. (1994). Transport of macromolecules across microvascular walls: The two-pore theory. *Physiol. Rev., 74*(1), 163-219.
Ropper, A. H. (1986). Lateral displacement of the brain and level of consciousness in patients with an acute hemispheral mass. *N Engl J Med, 314*(15), 953-958.
Ropper, A. H., et al. (1984). Brain edema after stroke: Clinical syndrome and intracranial pressure. *Arch. Neurol., 41*, 26-29.
Rosell, A., et al. (2008). MMP-9 - Positive neutrophil infiltration is associated to blood-brain barrier breakdown and basal lamina type IV collagen degradation during hemorrhagic transformation after human ischemic stroke. *Stroke, 39*, 1121-1126.
Rosenberg, G. A., et al. (1996). Effect of steroids on CSF matrix metalloproteinases in multiple sclerosis: Relation to blood-brain barrier injury. *Neurology, 46*, 1626-1632.
Rosenberg, G. A., et al. (1997). Metalloproteinase inhibition blocks edema in intracerebral hemorrhage in the rat. *Neurology, 48*, 921-926.

Saadoun, S., et al. (2003). Water transport becomes uncoupled from K^+ siphoning in brain contusion, bacterial meningitis, and brain tumours: Immunohistochemical case review. *J. Clin. Pathol., 56*, 972-975.
Sandercock, P., et al. (2012). The benefits and harms of intravenous thrombolysis with recombinant tissue plasminogen activator within 6 h of acute ischaemic stroke (the third international stroke trial [IST-3]): a randomised controlled trial. *Lancet, 379*(9834), 2352-2363.
Santambrogio, S., et al. (1978). Is there a real treatment for stroke? Clinical and statistical comparison of different treatments in 300 patients. *Stroke, 9*(2), 130-132.
Schellinger, P. D., et al. (2007). MRI-based and CT-based thrombolytic therapy in acute stroke within and beyond established time windows: an analysis of 1210 patients. *Stroke, 38*(10), 2640-2645.
Schlaug, G., et al. (1999). The ischemic penumbra: Operationally defined by diffusion and perfusion MRI. *Neurology, 53*, 1528-1537.
Schlaug, G., et al. (1997). Time course of the apparent diffusion coefficient (ADC) abnormality in human stroke. *Neurology, 49*(1), 113-119.
Sedlakova, R., et al. (1999). Ultrastructure of the blood-brain barrier in the rabbit. *J. Submicrosc. Cytol. Pathol., 31*(1), 149-161.
Serena, J., et al. (2003). Stroke on awakening: Looking for a more rational management. *Cerebrovasc Dis, 16*, 128-133.
Shahim, K., et al. (2010). Finite element analysis of normal pressure hydrocephalus: Influence of CSF content and anisotropy in permeability. *App. Bionics Biomech., 7*(3), 187-197.
Shaw, C.-M., et al. (1959). Swelling of the brain following ischemic infarction with arterial occlusion. *A. M. A. Arch. Neurol., 1*, 53-69.
Siemkowicz, E. (1980). Cerebrovascular resistance in ischemia. *Pflugers Arch., 388*, 243-247.
Smillie, A., et al. (2005). A hydroelastic model of hydrocephalus. *J. Fluid Mech., 539*, 417-443.
Smith, S. M. (2002). Fast robust automated brain extraction. *Hum. Brain Mapp., 17*(3), 143-155.
Smith, W. S., et al. (2008). Mechanical thrombectomy for acute ischemic stroke: Final Results of the Multi MERCI Trial. *Stroke, 39*, 1205-1212.
Smith, W. S., et al. (2005). Safety and efficacy of mechanical embolectomy in acute ischemic stroke. *Stroke, 36*, 1432-1438.
Soinne, L., et al. (2014). Malignant hemispheric infarction: Diagnosis and management by hemicraniectomy. *Stroke, 45*, e185-e187.
Solenov, E., et al. (2003). Sevenfold-reduced osmotic water permeability in primary astrocyte cultures from AQP-4-deficientmice, measured by a fluorescence quenching method. *Am. J. Physiol. Cell Physiol., 286*, C426-C432.
Starling, E. H. (1896). On the absorption of fluids from the connective tissue spaces. *J. Physiol., 19*(4), 312-326.
Steiner, L. A., et al. (2006). Monitoring the injured brain: ICP and CBF. *Brit. J. Anaesth., 97*(1), 26-38.
Steiner, T., et al. (2001). Treatment options for large hemispheric stroke. *Neurology, 57*(Suppl. 2), S61-S68.
Stolz, E., et al. (1999). Comparison of transcranial color-coded duplex sonography and cranial CT measurements for determining third ventricle midline shift in space-occupying stroke. *AJNR Am J Neuroradiol, 20*, 1567-1571.
Stoverud, K. H., et al. (2012). Modeling concentration distribution and deformation during convection-enhanced drug delivery into brain tissue. *Transp. Porous Med., 92*, 119-143.
Su, S. W. (2011). *Modelling blood flow and oxygen transport in the human cerebral cortex.* (D. Phil.), Oxford Univ., Oxford.
Sun, P. Z., et al. (2010). Early experience of translating pH-weighted MRI to image huma subjects at 3 Tesla. *Stroke, 41[suppl 1]*, S147-S151.
Sun, P. Z., et al. (2007). Detection of the ischemic penumbra using pH-weighted MRI. *J. Cereb. Blood Flow Metab., 27*, 1129-1136.
Swanson, K. R., et al. (2003). Virtual and real brain tumors: using mathematical modeling to quantify glioma growth and invasion. *J. Neurol. Sci., 216*, 1-10.
Szabo, A., et al. (2013). Cellular potts modeling of tumor growth, tumor invasion, and tumor evolution. *Front Oncol, 3*, 1-12.
Taniguchi, M., et al. (2000). Induction of aquaporin-4 water channel mRNA after focal cerebral ischemia in rat. *Mol. Brain. Res., 78*, 131-137.
Taylor, Z., et al. (2004). Reassessment of brain elasticity for analysis of biomechanisms of hydrocephalus. *J. Biomech., 37*, 1263-1269.
Terzaghi, K. (1943). *Theoretical soil mechanics*. New York: John Wiley.

The National Institute of Neurological Disorders and Stroke rt-PA Stroke Study Group. (1995). Tissue Plasminogen Activator for Acute Ischemic Stroke. *New England Journal of Medicine, 333*(24), 1581-1588.
The NINDS t-PA Stroke Study Group. (1997). Intracerebral hemorrhage after intravenous t-PA therapy for ischemic stroke. *Stroke, 28*(11), 2109-2118.
Tinevez, J.-Y., et al. (2009). Role of cortical tension in bleb growth. *P. Natl. Acad. Sci. USA, 106*(44), 18581-18586.
Todd, N. V., et al. (1986). Reperfusion after cerebral ischemia: influence of duration of ischemia. *Stroke, 17*(3), 460-466.
Tomás-Camardiel, M., et al. (2005). Blood-brain barrier disruption highly induces aquaporin-4 mRNA and protein in perivascular and parenchymal astrocytes: Protective effect by estradiol treatment in ovariectomized animals. *J. Neurosci. Res., 80*, 235-246.
Tomura, N., et al. (1988). Early CT finding in cerebral infarction: obscuration of the lentiform nucleus. *Radiology, 168*(2), 463-467.
Tortora, G. J., et al. (2009). *Principle of anatomy and physiology* (12th ed.). NJ, USA: John Wiley & Sons.
Tourdias, T., et al. (2011). Differential aquaporin 4 expression during edema build-up and resolution phases of brain inflammation. *J. Neuroinflamm., 8*, 143-160.
Traupe, H., et al. (1982). Reperfusion of focal ischemia of varying duration: Postichemic hyper- and hypo-perfusion. *Stroke, 13*(5), 615-622.
Traystman, R. J., et al. (1991). Oxygen radical mechanisms of brain injury following ischemia and reperfusion. *J. Appl. Physiol., 71*(4), 1185-1195.
Tully, B., et al. (2009). Coupling poroelasticity and CFD for cerebrospinal fluid hydrodynamics. *IEEE T. Biomed. Eng., 56*(6), 1644-1651.
Tully, B., et al. (2011). Cerebral water transport using multiple-network poroelastic theory: Application to normal pressure hydrocephalus. *J. Fluid Mech., 667*, 188-215.
Unterberg, A. W., et al. (2004). Edema and brain trauma. *Neuroscience, 129*, 1021-1029.
Vahedi, K., et al. (2007). Early decompressive surgery in malignant infarction of the middle cerebral artery: a pooled analysis of three randomised controlled trials. *Lancet Neurol, 6*(3), 215-222.
Verkhratsky, A., et al. (2007). *Glial Neurobiology*: John Wiley & Sons.
Verkman, A. S., et al. (2000). Role of water channels in fluid transport studied by phenotype analysis of aquaporin knockout mice. *Exp. Physiol., 85S*, 233S-241S.
Vizuete, M. L., et al. (1999). Differential upregulation of aquaporin-4 mRNA expression in reactive astrocytes after brain injury: Potential role in brain edema. *Neurobiol. Dis., 6*, 245-258.
von Kummer, R., et al. (1997). Acute stroke: Usefulness of early CT findings before thrombolytic therapy. *Neuroradiology, 205*, 327-333.
von Kummer, R., et al. (1994). Sensitivity and prognostic value of early CT in occlusion of the middle cerebral artery trunk. *AJNR Am J Neuroradiol, 15*, 9-15.
von Kummer, R., et al. (1997). Brain and vascular imaging in acute ischemic stroke: The potential of computed tomography. *Neurology, 49*(suppl 4), S52-S56.
Vorbrodt, A. W., et al. (1985). Ultrastructural observations on the transvascular route of protein removal in vasogenic brain edema. *Acta Neuropath. (Berl), 66*, 265-273.
Walsh, E. K., et al. (1976). Elastic behavior of brain tissue in vivo. *Am. J. Physiol., 230*(4), 1058-1062.
Wang, X., et al. (2004). Mechanisms of hemorrhagic transformation after tissue plasminogen activator reperfusion therapy for ischemic stroke. *Stroke, 35 [Suppl I]*, 2726-2730.
Wang, Y., et al. (2000). Brain tissue sodium is a ticking clock telling time after arterial occlusion in rat focal cerebral ischemia. *Stroke, 31*, 1386-1392.
White, H., et al. (2008). Cerebral perfusion pressure in neurotrauma: A review. *Anesth. Analg., 107*, 979-988.
Williams, V., et al. (1980). Volume and surface area estimates of astrocytes in the sensorimotor cortex of the cat. *Neuroscience, 5*, 1151-1159.
Wilson, A. J., et al. (2010). Aquaporin-1 in blood vessels of rat circumventricular organs. *Cell Tissue Res., 340*, 159-168.
Wirth, B., et al. (2006). An axisymmetric and fully 3D poroelastic model for the evolution of hydrocephalus. *Math. Med. Biol., 23*, 363-388.
Wolman, M., et al. (1981). Evaluation of the Dye-Protein Tracers in Pathophysiology of the Blood-Brain Barrier. *Acta Neuropath. (Berl), 54*, 55-61.
World Health Organization. (2014). *Injuries and violence: The facts 2014*. Geneva: World Health Organization Retrieved from http://www.who.int/iris/handle/10665/149798.
Wunderlich, M. T., et al. (2007). Recanalization after intravenous thrombolysis: Does a recanalization time window exist? *Neurology, 68*(17), 1364-1368.

Yamane, Y., et al. (2000). Quantitative analyses of topography and elasticity of living and fixed astrocytes. *J. Electron Microsc., 49*(3), 463-471.
Yamaura, A., et al. (1977). Neurological deficits in the presence of the sinking skin flap following decompressive craniectomy. *Neurol. Med. Chir. (Tokyo), 17*, 43-53.
Yang, G.-Y., et al. (1994). Reperfusion-induced injury to the blood-brain barrier after middle cerebral artery occlusion in rats. *Stroke, 25*, 1658-1665.
Yang, Q., et al. (1999). Serial study of apparent diffusion coefficient and anisotropy in patients with acute stroke. *Stroke, 30*(11), 2382-2390.
Yang, X. F., et al. (2008). Surgical complications secondary to decompressive craniectomy in patients with a head injury: A series of 108 consecutive cases. *Acta Neurochir., 150*, 1241-1248.
Yang, Y., et al. (2011). Blood-brain barrier breakdown in acute and chronic cerebrovascular disease. *Stroke, 42*, 3323-3328.
Yuh, E. L., et al. (2008). Computer-aided assessment of head computed tomography (CT) studies in patients with suspected traumatic brain injury. *Journal of Neurotrauma, 25*(10), 1163-1172.
Yushkevich, P. A., et al. (2006). User-guided 3D active contour segmentation of anatomical structures: Significantly improved efficiency and reliability. *Neuroimage, 31*(3), 1116-1128.
Zador, Z., et al. (2009). Role of aquaporin-4 in cerebral edema and stroke. *Handbook Exp. Pharm., 190*, 160-167.
Zhang, X., et al. (2006). A 1-D model to explore the effects of tissue loading and tissue concentration gradients in the revised Starling principle. *Am. J. Physiol. Heart Circ. Physiol, 291*, H2950-H2964.
Zhang, Y., et al. (2001). Segmentation of brian MR images through a hidden Markov random field model and the expectation-maximization algorithm. *IEEE Trans. Med. Imag., 20*(1), 45-57.
Zienkiewicz, O. C. (1982). Basic formulation of static and dynamic behaviours of soil and other porous media. *Appl. Math. Mech. -Engl., 3*(4), 457-468.
Zienkiewicz, O. C., et al. (1990). Static and dynamic behaviour of soils: A rational approach to quantitative solutions. I. Fully saturated problems. *Proc. R. Soc. Lond. A, 429*, 285-309.
Zienkiewicz, O. C., et al. (1984). Dynamic behaviour of saturated porous media; The generalized Biot formulation and its numerical solution. *Int. J. Numer. Anal. Met., 8*, 71-96.
Zimmerman, R. A., et al. (1978). Computed tomography of pediatric head trauma: Acute general cerebral swelling. *Radiology, 126*, 403-408.
Zornow, M. H. (1996). Hypertonic saline as a safe and efficacious treatment of intracranial hypertension. *J. Neurosurg. Anesth., 8*(2), 175-177.